DOCTOR OF SCIENCES

Investigating slow photon effect in inverse opal photonic structures for photocatalytic applications

MADANU, Lourdu

Award date:
2024

Awarding institution:
University of Namur

Investigating slow photon effect in inverse opal photonic structures for photocatalytic applications

---

Thesis submitted by

Thomas Lourdu Madanu

as part of the fulfillment of requirements to obtain the degree of

Doctor of Sciences in Chemistry

May 2024

Thesis committee:

Prof. Catherine MICHAUX (UNamur, President)
Prof. Alexandru VLAD (UCLouvain)
Prof. Benoît CHAMPAGNE (UNamur)
Prof. Olivier DEPARIS (UNamur)
Prof. Alain KRIEF (UNamur)
Prof. Yu Li (Wuhan Institute of Technology)
Prof. Bao-Lian SU (UNamur, Supervisor)

UNIVERSITÉ
DE NAMUR

Investigating slow photon effect in inverse opal photonic structures for photocatalytic applications

---

Thesis submitted by

Thomas Lourdu Madanu

CMi
Chemistry of Inorganic Materials

NISM
Namur Institute of Structured Matter

ihs Jésuites
Europe
Occidentale
Francophone

JESUITS
Andhra Province

“The most beautiful thing we can experience is the mysterious. It is the source of all true art and science. He to whom the emotion is a stranger, who can no longer pause to wonder, and stand wrapped in awe, is as good as dead – his eyes are closed.”

Albert Einstein (*attributed)*

Thesis abstract

Photocatalytic hydrogen generation from water is one of the most sustainable and eco-friendly energy conversion processes since it utilizes naturally available resources like sunlight and water, to produce a zero-emission fuel. Significant efforts have been made to actualize this process, but the minimum solar-to-hydrogen conversion efficiency required to implement it at the industrial scale has not been achieved. Reasons for this include insufficient solar light absorption, inefficient exploitation of absorbed light to generate charge carriers, sluggish charge transfer kinetics, and ineffective charge utilization to drive surface redox reactions. The primary challenge in this process is light absorption. Strategies employed so far to improve solar light absorption have focused mainly on the choice and modification of materials. However, the strategy of modifying the propagation of light to enhance light harvesting is underexplored. Photonic structures, thanks to their periodic structures with alternating refractive indices, possess unique ability to modify the propagation of light, particularly the ability to reduce the group velocity of light at specific frequencies and localize it within the structure. These 'slow photons' can be used to enhance light harvesting and photocatalytic activity, especially when their frequencies are tuned to the electronic absorption of the photocatalyst.

In this thesis, we investigate the utilization of slow light in inverse opal TiO_2-based photonic structures to enhance light harvesting in photocatalytic dye degradation and then in hydrogen generation from water, our ultimate objective. Firstly, we synthesized high-quality inverse opal TiO_2 photonic structures and embedded them with visible light responsive $BiVO_4$ nanoparticles. The frequencies of slow photons generated in the TiO_2 photonic structure were tuned through lattice parameter and incidence angle variations to the electronic absorption of $BiVO_4$, to obtain up to a seven-fold increase in photocatalytic dye degradation compared to the non-structured compact films. Secondly, since slow photons are limited to narrow spectral regions, we generated slow photons at multiple spectral regions by synthesizing bilayer inverse opal structures with different periodicities in each layer, to achieve a two-fold increase in photoactivity compared to the monolayer structures. Finally, we employed slow photon-assistance in photocatalytic H_2 generation over inverse opal TiO_2 sensitized with CdS, Au, and Pt nanoparticles, to achieve an 8-fold increase in H_2 evolution, under optimal tuning conditions, compared to that over pristine inverse opal TiO_2.

Acknowledgement

The best things in life are the people we love, the places we've been and the memories we've made along the way. Perhaps, no better words can sum up my sentiments at this juncture. After four and a half years of my research journey, at Namur, Belgium, a place far away from my native country, India, I look back and see with contentment, the wonderful people that I have met, the new places I have been to and the rich memories I carry with me. I take this opportunity to acknowledge those who made this journey memorable.

The journey began with the initial contact I had with Prof. Bao-Lian Su, my advisor. Prof. Su, it was, it is, and it will always be a pleasure for me to interact and discuss with you. The discussions we had were motivating, and filled with positive energy, always searching for what more could be done and how better. The question you repeat very often - 'Why?' - with your unique intonation, will resonate long in my future research. Thank you for welcoming me in the Chemistry of Inorganic Materials (CMI) group, for introducing me to the 'colorful' world of inverse opal photonic structures, and for accompanying me in my research.

My research here would have been impossible without the support of the European Occidentale Francophone (EOF) Jesuit province. I express my deepest gratitude to the EOF province for their consistent support in every way possible. I also acknowledge the profound trust with which the Andhra Jesuit Province, India, of which I am a member, sent me here. It is during my stay here that I completed my 25th year of joining the Society of Jesus, a religious organization committed to the service of faith, service, and social justice. I feel proud and grateful to be a member and I hope this formation will enable me to promote the values the Society upholds and propagates.

One feature that stands out when I think of my CMI group is diversity, both culturally and in research. Having many colleagues from different countries is our greatest asset. I feel privileged to be part of this wonderful group. The best memories I have with you include the discussions in the coffee room, the evening parties, seminars in the academic room, the barbecues, and the team-building activities. It was joyful. It was memorable. Thank you each and every one of you for being part of this journey – Tarek, Marvin, Maxime, Louis, Patrick, Andre, Laroussi, Clotilde, Mateo, Marine, Jing Li, Xikun, Guangying, Liuxi, Yuan, Miao, Runtian, Pengcheng, Ivalina, Lakshmi, Myriam, Maxence, Hongyan, Min Hui, Ying Ying, Yang Ding, Adan, Jamila, Quentin, Cyrille, Benjamin, Silvia, Diogo, Domenico, Valerie. Particularly, I wish to thank you Tarek for your pivotal role. Right from the time I arrived, you have been encouraging me, motivating me, and constantly assuring me of your help. Your presence was reassuring. I remember with gratitude your constant support, and friendly approach. Special mention needs to be made of Isabelle, our laboratory secretary. Isa, I always admire your ‘never-to-worry, always-look-for-a solution’ approach. Your optimistic attitude is calming. I thank you profoundly for all your help in the administrative work.

The second laboratory in which I spent the majority of my research time is the solid-state physics (LPS) laboratory, in the research group of Prof. Oliver Deparis. It was a joy to work with you, Prof. Olivier. I learnt a lot. Your detailed observations, insights and thought-provoking questions helped me to explore deeper into the scientific inquiries and challenges I encountered. Working with you, especially for the articles we published, enriched me in my research. I hope to continue to work with you in the future. Also, I remember with gratitude Sebastien Mouchet from the same unit. Sebastien, it would not be an exaggeration to say that you were a trusted mentor for me. The countless hours you spent, with a lot of patience, helping me in my research were truly invaluable. You are the one I can rely on at any time. Thank you for your precious help.

Apart from the people in the university, numerous people accompanied me on my journey. Particularly, I remember all the Jesuits with whom I stayed during this entire period. It is a community with people of different age groups and from different countries. It is truly befitting to say that I felt at home with all of you. I acknowledge your fraternal affection and your ‘bienveillance’ towards me. At any time of the day, I am confident there will always be someone to whom I can talk to. I express my gratitude to each of you for the memorable time spent in the community. I also acknowledge the precious services rendered by the staff in the house.

Among all the friends I have here at Namur, I wish to single out Marie Christine. I believe the word that can best qualify you is ‘motherly’. Your affection, your constant encouragement, and the ‘positive energy’ which you believe in have touched me profoundly. I believe a simple ‘thank you’ is too little to acknowledge your role. All the same, thank you very much for everything.

There are many others who played an important role in my journey. Although I don’t mention each of them by name, I thank them profoundly for being part of my journey.

I especially remember my parents. Your love and support are unconditional. Words cannot express how deeply I feel grateful to you. Though you are far away from me, I am sure you are always with me in spirit. I also thank my brother and sister and their families for the constant support and love. Special thanks to all my friends back in India who have been constantly supporting me.

And finally, I wish to thank the Almighty who I believe is the silent, invisible hand guiding me all along. The deeper I dwell into research, the greater is the feeling of awe and wonder at the infinite possibilities that the universe offers us to explore and research. One of my favourite pastimes in the laboratory is assembling a butterfly wing alongside the colorful samples I have prepared in the lab and comparing the delicate beauty of nature with the artistic work of science. It fills me with wonder and instigates my scientific curiosity. There is a lot more to unfold in the mystery of the universe. And I believe there is a deeper Mystery behind and beyond what we see and wish to see.

List of abbreviations and symbols

Abbreviations

3-DOM	3-Dimensionally Ordered Macroporous
4-CP	4-chlorophenol
AC	Achieved Commitments
AFM	Atomic force microscopy
ALD	Atomic Layer Deposition
AM	Air Mass
AQE	Apparent Quantum Efficiency
BE	Blue Edge
C	Concentration
CA	Contact angle
CB	Conduction Band
CCT	Colloid Crystal Template
CR	Chemical Reduction
CT	Current Trajectory
CV	Coefficient of Variation
CVD	Chemical Vapour Deposition
D	Diameter
DLS	Dynamic Light Scattering
DMF	Dimethylformamide
DO	Disorder(ed)
DSSC	Dye-Sensitized Solar Cell
EA	Electronic Absorption
EBG	Electronic Band Gap
ECD	Electro-Chemical Deposition
EDX	Energy Dispersive X-ray Spectroscopy
EF	Enhancement Factor
EISA	Evaporation-Induced Self-Assembly
EISSA	Evaporation-Induced Simultaneous Self-Assembly
EJ	Exajoule
eV	Electron-volt
FA	Further Acceleration
fcc	Face-Centred Cubic
FDTD	Finite-difference time-domain
FEM	Finite Element Method
FM	Fading Momentum
GtCO$_2$e	Gigatonnes of carbon dioxide equivalent
HAADF-STEM	High-Angle Annular Dark-Field Scanning Transmission Electron Microscope
HER	Hydrogen Evolution Reaction
HF	Hydrogen fluoride
HOMO	Highest Occupied Molecular Orbital
IO	Inverse Opal
IPCE	Incident Photon-to-Current conversion Efficiency

IR	Infra-red
IUPAC	International Union of Pure and Applied Chemistry
J	Joule
kJ	Kilojoule
LED	Light-emitting diode
LSPR	Localized Surface Plasmon Resonance
LUMO	Lowest Unoccupied Molecular Orbital
MB	Methylene Blue
MJ	Megajoule
mM	Milli-molar
mmol	Milli-mole
MO	Methyl Orange
M-O	Metal oxide
mW	Milli-Watt
NA	Nanoarrays
NC	Nanocrystal (nanocrystalline)
NHE	Normal Hydrogen Electrode
nm	Nanometer
NP	Nanoparticle
NS	Non-structured
OER	Oxygen Evolution Reaction
OM	Optical Microscope(y)
OWS	Overall Water Splitting
P	Power
PBG	Photonic Band Gap
PC	Photonic crystal
PC	Photocatalyst (system)
PEC	Photoelectrochemical (system)
PFO	Pseudo-first order
pH	Potential of Hydrogen
PL	Photoluminescence
PMMA	Polymethyl methacrylate
pPBG	Pseudo-photonic band gap
PS	Polystyrene
PSO	Pseudo-second order
PV-EC	Photovoltaic-electrocatalyst (system)
PVP	Polyvinylpyrrolidone
PWE	Plane Wave Expansion
QD	Quantum Dot
QE	Quantum Efficiency
RCWA	Rigorous Coupled Wave Analysis
RE	Red Edge
RhB	Rhodamine B
RI	Refractive Index
SAED	Selected Area Electron Diffraction
SBG	Stop Band Gap

SC	Semiconductor
SCD	Super-Critical Deposition
SD	Standard deviation
SEM	Scanning Electron Microscope(y)
SERS	Surface-Enhanced Raman Scattering
SILAR	Successive Ionic Layer Adsorption and Reaction
SPE	Slow Photon Effect
SPR	Surface Plasmon Resonance
STH	Solar-to-Hydrogen
SWA	Scalar Wave Approximation
TEM	Transmission Electron Microscope
TEOS	Tetraethyl orthosilicate
THF	Tetrahydrofuran
TiBALDH	Titanium (IV) bis (ammonium lactato) dihydroxide
TIP	Titanium isopropoxide
TMAH	Tetramethyl ammonium hydroxide
TOF	Turn Over Frequency
TON	Turn Over Number
TWh	Terawatt-hours
VB	Valence Band
V	Volt
UV	Ultra-violet
UV-Vis	Ultra-violet Visible
XRD	X-ray diffraction
XPS	X-ray photoelectron spectroscopy

Symbols

η	Conversion efficiency
ΔG	Change in Gibb's free energy
E_g	Electronic band gap
ΔE	Change in internal energy
$\alpha(\lambda)$	Absorption coefficient as a function of wavelength
λ	Wavelength
D	Diffusion coefficient
μ	Drift mobility
τ	Carrier lifetime
L	Diffusion length
ω	Angular frequency
k	Wave vector
$\omega(k)$	Dispersion relation
v_g	Group velocity of wave packet of light
ε	Dielectric permittivity
n	Refractive index
a	Periodicity in the photonic structure
$\mathrm{\mu}$	Magnetic permeability

$1/e$	Inverse of Euler’s number (mathematical constant – 2.71828)
v_{w}	Substrate withdrawal rate in self-assembly
v_{c}	Colloid array growth rate
j_{w}	Water influx in self-assembly
j_{e}	Water evaporation flux in self-assembly
h	Thickness of colloid film
φ	Volume fraction
d_{hkl}	Interplanar spacing
hkl	Miller indices
f	Filling fraction
a	Unit cell parameter
J_{sc}	Short-circuit current density
V_{oc}	Circuit voltage
μM	Micromole
μm	Micrometre
n_g	Number of Fourier components
t	Time
K	Rate constant
R	Regression coefficient

Table of contents

Chapter I

Chapter II

Chapter III

Chapter VI

Chapter VII

Annex

CHAPTER I

Introduction

Overview

This chapter details the fundamentals of photocatalytic water splitting, slow photon effect in photonic structures, and inverse opal photonic crystals, and reviews research advances regarding slow photon utilization in photocatalysis. In the first section, the basic principles, thermodynamics, kinetics, and mechanism of photocatalytic water splitting are presented in detail. Along with this, the challenges involved, and the strategies adopted to tackle these challenges are addressed. In the second section, the theoretical principles underlying light manipulation in photonic crystals, particularly the manifestation of the photonic band gap and slow light, are elaborated upon. This is followed by a discussion on the specific type of photonic crystal used in this work, namely the inverse opal photonic crystal. This sub-section focusses mainly on the intricacies involved in the synthesis of inverse opals, and the optical properties. The final part of the introduction reviews the strategies employed by researchers to explore slow photon assistance in light harvesting applications, particularly in photocatalysis.

1. Introduction

Rise in energy demand, increasing concerns about fuel emissions, and dwindling fossil fuel reserves are driving research to explore alternate renewable, sustainable and non-polluting energy sources. It is estimated that global power demand will more than double from 25,000 terawatt-hours (TWh) to between 52,000 and 71,000 TWh by 2050, at a rate of 2.6-3.8% increase per annum **(Fig. 1a)**[1]. Emissions resulting from the use of energy in 2022 reached an all-time high of 34.4 $GtCO_2e$[2]. The share of renewable energy is expected to grow from 27% in 2022 to 85% in 2050, with 30-40% coming from solar energy (**Fig. 1b**). This scenario of energy and emissions highlights the growing importance of renewable energy, particularly solar energy.

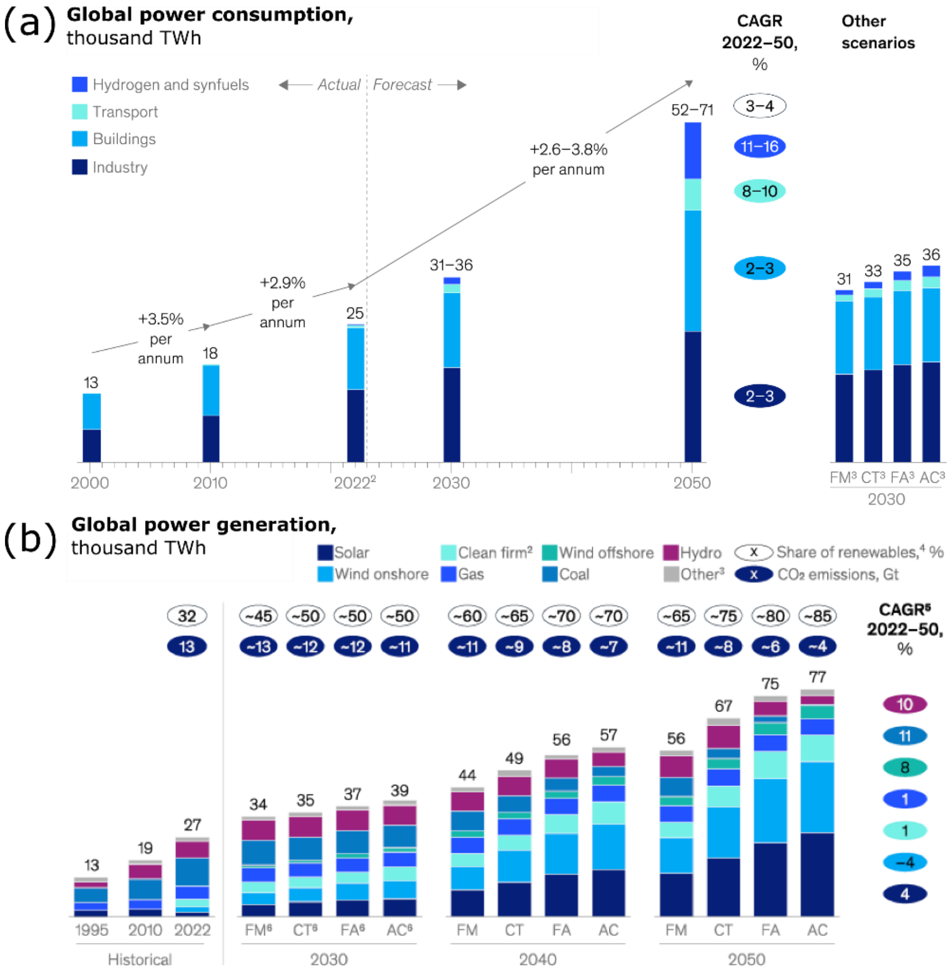

Fig. 1.1: (a) Trend of global power consumption by sector (TWh) up to 2050, showing an increase of 3-4% per year; **(b)** Share of energy sources, indicating the growing share of renewables[1]. Four different scenarios are considered: FM-Fading Momentum, CT-Current Trajectory, FA-Further Acceleration, and AC-Achieved Commitments.

Solar energy is the most abundant energy source on Earth. According to estimates, the surface of the earth receives 3.4×10^5 EJ of energy per year from the sun, seven-to-eight thousand times higher than the annual global energy consumption[3]. However, the percentage of energy converted from this source (0.012%) pales out in comparison with total solar energy reaching the earth. Part of this problem lies in the low energy density of solar energy that necessitates an area of 500×500 km^2 to obtain 8-TW energy based on converting air mass (AM) 1.5-G photon flux at 10% conversion efficiency (η), irrespective of the conversion technology[4]. This calls for finding more efficient methods to collect, convert, store and transport solar energy.

Common methods to harness this abundant potential include photocatalytic, photoelectrocatalytic, photovoltaic, photothermal, photo-bioconversion, and hybrid processes[5], each having its advantages and disadvantages. Among them, the photocatalytic route to convert solar energy to chemical energy is widely studied, owing to its resemblance to natural photosynthesis process[6]. The fact that 21% of oxygen in the atmosphere is mostly from photosynthesis and that the fossil fuel reserves are the result of solar-to-chemical conversion over centuries, proves that chemical bonds are convenient for energy storage, and inspires scientists to develop conversion methods based on similar principles[7].

Photocatalysis is defined, based on the International Union of Pure and Applied Chemistry (IUPAC) glossary of terms, as a process in which a catalyst, upon absorption of light, initiates or promotes chemical transformation of the reaction partners[8]. This broad definition, however, does not distinguish between the strictly termed ‘photocatalytic’ process and the ‘photosynthetic’ process. While both require the absorption of light to generate free photoelectrons and holes that promote chemical reactions at the surface, the fundamental difference lies in their thermodynamics[9]. The process in ‘artificial photosynthesis’ is similar to that in ‘natural photosynthesis’, since both require additional photochemical energy from the light source to drive thermodynamically forbidden ‘up-hill reactions’ ($\Delta G > 0$) **(Fig. 1.2, (a-b))**. Photo-driven water splitting, and CO_2 reduction are examples of this process. The thermodynamic requirements for some common artificial photosynthesis reactions are shown in **Fig. 1.2(b)**. Since light provides additional photochemical energy in this process, it is considered by some authors as one of the reactants[7]. In contrast, in ‘photocatalysis’ (**Fig. 1.2 (c))**, light is used to accelerate a thermodynamically favourable ‘down-hill reaction’ ($\Delta G < 0$) (**Fig. 1.2 (c))**. Photodegradation of pollutants is an example of this process. Such reactions are spontaneous and do not alter the thermodynamics but only the kinetics of the reaction[6].

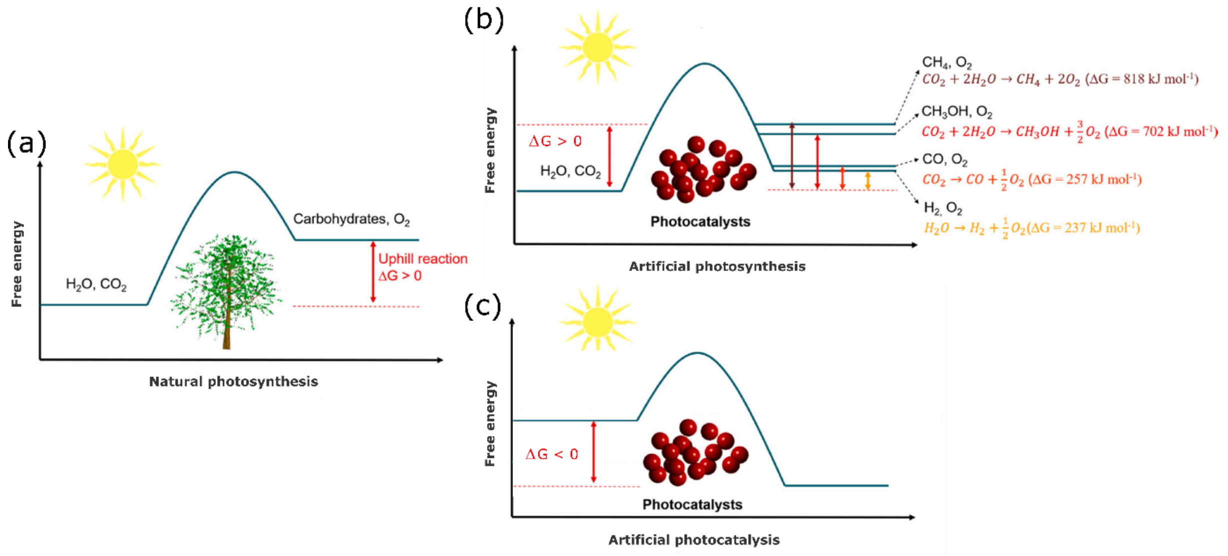

Fig. 1.2: Schematic representation of natural and artificial photo-driven processes: **(a)** natural photosynthesis with Gibb's free energy change ΔG > 0, **(b)** artificial photosynthesis with ΔG > 0, and **(c)**. artificial photocatalysis with ΔG < 0 (adapted from ref[10]).

The origins of photochemical reactions can be dated back to 1901 when the influence of irradiation was studied in photochemical reactions like hydrogen abstraction by carbonyls, oxygenation reactions and double-bond isomerization reactions[11]. The term 'photocatalysis' surfaced for the first time in 1911, to describe the bleaching of Prussian blue pigment under illumination of ZnO[12]. Research progressed ever since but was mostly confined to laboratory experiments, with little promise of practical industrial applications. Scientific interest in photochemical reactions grew manifold since the 1970's after the first report of photoelectrochemical water oxidation on TiO_2 photoanode by Fujishima and Honda[13]. Although an external electrical or chemical bias was used, this work established that semiconductors could convert light energy to chemical energy in thermodynamically unfavourable reactions like water splitting. Also, it intensified research interest in solar-to-fuel photochemical conversion, as the prospect of obtaining hydrogen, a fuel with high mass energy density (142 MJ kg^{-1})[14] and zero emissions[15], became highly promising both for economic and environmental reasons.

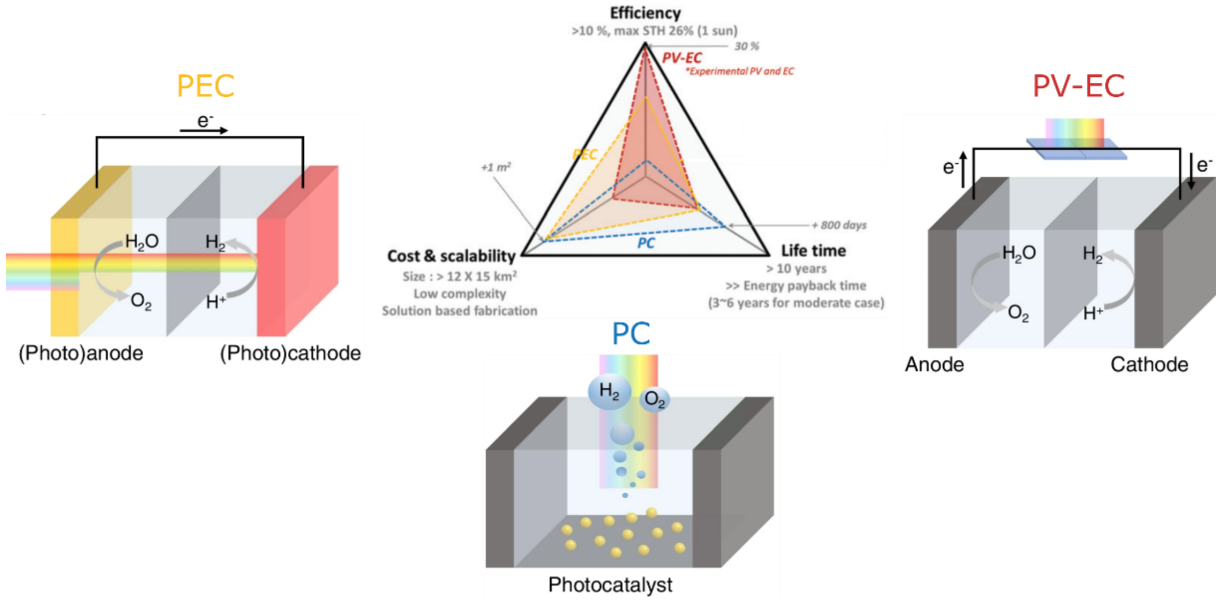

Fig. 1.3: **(a)** Schematic representation of PC, PEC, and PV-EC solar-driven water splitting system, along with a simplified comparative evaluation of their efficiency, cost and scalability, and lifetime (adapted from refs.[16, 17]).

Hydrogen can be obtained from solar-driven photochemical conversions using different approaches, which can be categorized into three systems: (i) photocatalyst system (PC), (ii) photoelectrochemical (PEC) system, and (iii) photovoltaic-electrocatalyst system (PV-EC)[16] **(Fig. 1.3)**. A typical PC system consists of just the photocatalyst (light absorber and/or electrocatalyst) and the reactants, making it the simplest of all the three systems. As shown in **Fig. 1.3**, light is absorbed by the photocatalyst to generate free electrons and holes, which are transported to the surface of the photocatalyst to assist in redox reactions. Redox reactions usually happen on the surface of the same photocatalyst. Hence, the charge transfer pathway is significantly shorter, in the order of a few micrometres, compared to that in other systems. The advantages of this system are the following: (i) No requirement of additional circuits, (ii) No requirement of external bias, (iii) convenience for large-scale application, (iv) high surface area with a high density of active sites. Disadvantages in this process include: (i) Limitation of materials with suitable band gaps that enable overall water splitting (OWS) redox reactions, (ii) Stability of photocatalyst, (iii) Surface charge recombination due to the proximity between oxidation and reduction sites, and (iv) comparatively lower water splitting efficiency[6].

A basic PEC system consists of photoelectrodes, an electrolyte and an external circuit (**Fig. 1.3**). The photoelectrode(s) is in contact with the electrolyte, while the charge collector remains isolated.

When the photoelectrode is irradiated with light having energy greater than that of the bandgap of the material, electrons and holes are separated. A Schottky junction forms between the interface of the semiconductor and the electrolyte, as in the case of an n-type semiconductor photoanode. The excited electrons are collected by the current collector and transported through the external circuit to the site for reduction reaction, while the holes emerge to the interface to carry out the oxidation reaction[16]. H_2 and O_2, in this case, are evolved over different electrodes. Advantages of this system include: (i) facile charge separation, (ii) convenient product separation, (iii) better control over reaction pathways, (iv) ease in supplementing photoenergy by external power supplies[6]. However, the major disadvantages of this system are: (i) relatively poor scalability, (ii) optimization of interface between photoelectrode and current collector, (iii) requirement of membranes to separate products, and (iv) requirement of expensive materials and equipment.

In a PV-EC system, an independent unit generates photocurrent through a photovoltaic (PV) unit, which is then used to drive electrocatalytic redox reactions. Typically, the light absorber is out of water, while the evolution of H_2 and O_2 happens at different electrodes in the electrochemical (EC) unit (**Fig. 1.3**). Advantages of this process include: (i) convenience for separate optimization of light absorption and electrolysis, (ii) facile charge transfer, (iii) stability of light-harvesting material which is out of water, (iv) highest efficiency. Significant disadvantages in this system include: (i) complexity of the system, (ii) technological feasibility, (iii) economic viability[6].

Since the focus of this research is on photocatalytic water splitting (PC), the fundamentals, mechanism, challenges, and strategies involved in this system are discussed in detail.

1.1. Photocatalytic water splitting - fundamentals, challenges, and strategies

Photocatalytic (PC) water splitting, as discussed in the previous section, has the greatest advantage of operating at low cost with greater ease of scalability. However, the process results in low solar-to-hydrogen (STH) conversion efficiency. To improve this efficiency, it is important to understand the basic mechanism, principles, and challenges in this process. The discussion that follows focusses on these aspects while limiting itself to semiconductor PC water splitting.

1.1.1. Thermodynamics of photocatalytic water splitting

Photocatalytic water splitting is a thermodynamically uphill reaction with an overall Gibb's energy change (ΔG) of 237.2 $kJmol^{-1}$, or a potential of 1.23 eV per electron[16]. When a semiconductor photocatalyst absorbs light (with energy greater than its electronic band gap E_g), the electrons in its valence band (VB) are excited to the conduction band (CB), leaving behind holes in the VB. These photogenerated charge carriers migrate to the surface of the photocatalyst and promote redox reactions, namely oxygen evolution reaction (OER) and hydrogen evolution reaction (HER)[18]. The basic process is schematically shown in **Fig. 1.4 (a)**.

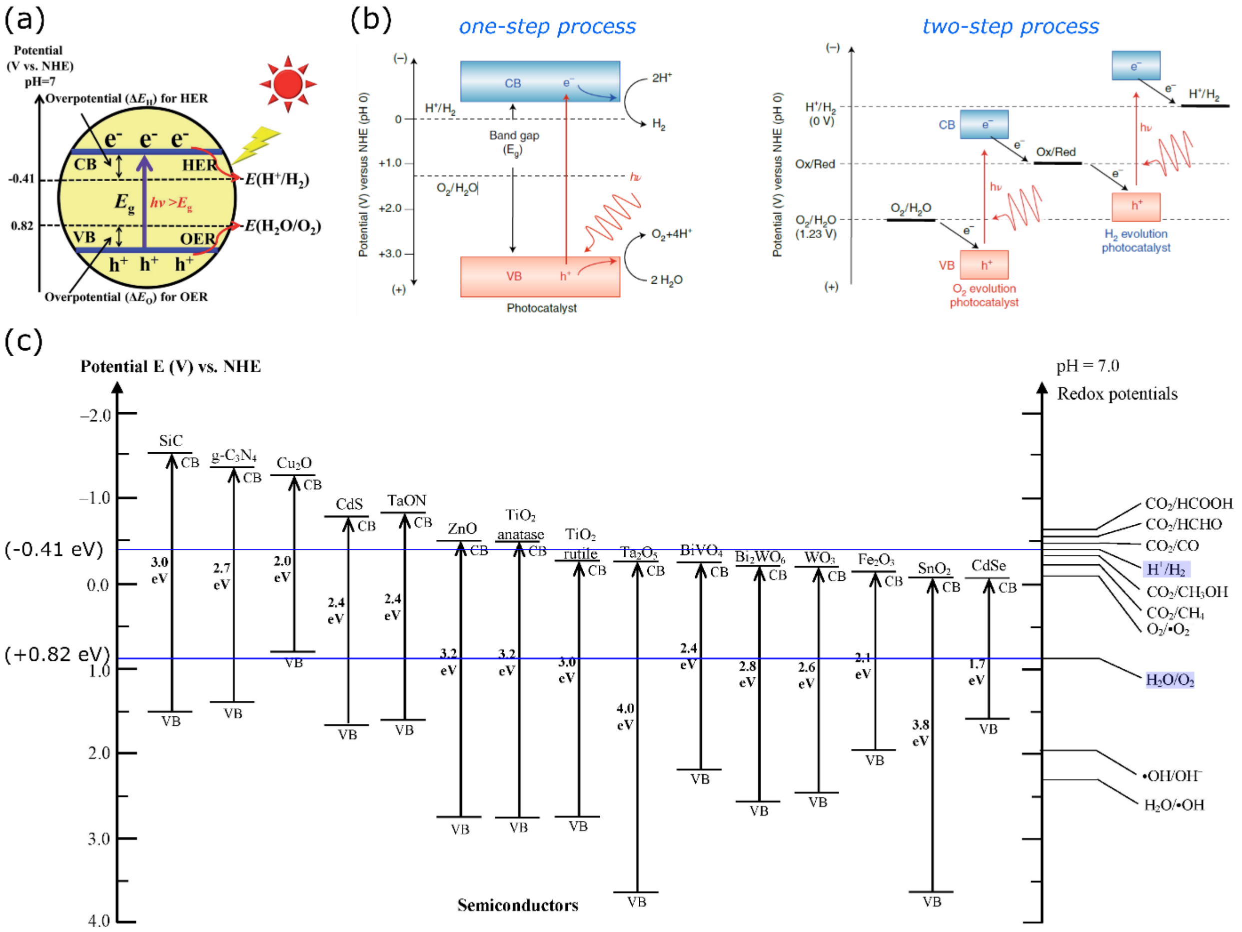

Fig. 1.4: **(a)** Schematic representation of the principles underlying photocatalytic water splitting over semiconductor photocatalyst[19]; **(b)** Energy diagrams of photocatalytic water splitting in one-step and two-step excitation processes[20]; **(c)** Band gap energies (E_g = VB – CB) of various semiconductors and their VB, CB positions relative to the redox potentials of water splitting (indicated in blue), CO_2 reduction, and pollutant degradation at pH 7 (adapted from ref[21]).

The reactions involved in photocatalytic water splitting, along with their corresponding redox potentials at pH=0 are given below[16, 19].

Oxygen evolution reaction (OER) : $2H_2O\ (l) + 4h^+_{vb} \rightarrow O_2\ (g) + 4H^+$ $\Delta E^o = +\ 1.23$ V

Hydrogen evolution reaction (HER) : $2H^+ + 2e^-_{cb} \rightarrow H_2$ $\Delta E^o = 0.00$ V

Overall water splitting (OWS) : $2H_2O\ (l) \rightarrow 2H_2\ (g) + O_2\ (g)$ $\Delta E^o = 1.23$ V

(Note: At pH=7, the O_2 and H_2 evolution potentials change to +0.82 V and -0.41 V respectively.)

The above reactions present a simplified process of photocatalytic water splitting. However, the actual process occurs through intermediate steps, each having a specific potential, forming various intermediate products[22, 23]. The detailed reaction process is presented below.

Photogenerated holes in the VB initiate oxidation reactions to generate $OH^•$ radicals when the valence band of the semiconductor is more positive than the oxidation potentials of OH-/$OH^•$ (1.99 V vs NHE) and H_2O/ $OH^•$ (2.34 V vs NHE).

$$H_2O + h^+_{VB} \rightarrow {}^•OH + H^+$$
$$OH^- + h^+_{VB} \rightarrow {}^•OH$$

In addition to the above, H_2O_2 also can be produced by the direct oxidation of water through the following reaction[24]:

$$2H_2O + 2h^+_{VB} \rightarrow H_2O_2 + 2H^+$$

The H_2O_2 generated can further undergo either oxidation by the photogenerated holes to produce O_2 (1.23 V) or reduction by the photogenerated electrons to produce $^•OH$ and OH^- (1.14 V)[24, 25]:

$$H_2O_2 + 2h^+_{VB} \rightarrow O_2 + 2H^+$$
$$H_2O_2 + e^-_{CB} \rightarrow {}^•OH + OH^-$$

The $^•OH$ radical may be further reduced to OH^- as follows[26]:

$${}^•OH + e^-_{CB} \rightarrow OH^-$$

Photogenerated electrons in the CB initiate reduction reactions to generate OH^- and H_2O_2 when the CB of the semiconductor is positioned at a more negative value than the potential to form OH^- (0.40 V vs NHE[26]) and H_2O_2 (0.70 V vs NHE[26]).

$$O_2 + 2H_2O + 4\ e^-_{CB} \rightarrow 4OH^-$$
$$O_2 + 2H^+ + 2\ e^-_{CB} \rightarrow H_2O_2$$

H_2O_2 formed can undergo further redox reactions as described above. In addition to the above, electrons in CB can react with dissolved oxygen to generate superoxide radical $^{\bullet}O_2^-$ ($^{\bullet}O_2^-/O_2$: 0.33 V vs NHE), which gets protonated and undergoes dissociation to produce $^{\bullet}OH$ radicals.

$$O_2 + e^-_{CB} \rightarrow {}^{\bullet}O_2^-$$
$${}^{\bullet}O_2^- + H^+ \rightarrow HOO^{\bullet}$$
$$2HOO^{\bullet} \rightarrow H_2O_2 + O_2$$
$$H_2O_2 \rightarrow 2OH^{\bullet}$$

The intermediates resulting from the redox reactions at VB and CB (H_2O_2, $^{\bullet}OH$, H^+, OH^-) are highly reactive and can promote the oxygen evolution and hydrogen evolution reactions at the surface of the semiconductor.

It should however be added that the detailed pathway(s) mentioned above includes most of the possible reaction steps in a generalized case. The actual intermediate reactions would depend on the semiconductor(s) employed, the reaction conditions, and the presence of other additional factors like the use of sacrificial agent and/or cocatalyst.

The potentials for O_2 and H_2 evolution reactions imply that, for overall water splitting (OWS) to occur, the VB maximum of the semiconductor should be located at a more positive potential than the oxidation potential of H_2O to O_2 (+0.82 V *vs* NHE at pH 7), while the CB minimum should be located at a more negative potential than the reduction potential of H^+ to H_2 (-0.41 V *vs* NHE at pH 7)[18]. In addition, the semiconductor should have a minimum band gap energy of 1.23 eV (~1000 nm) necessary to drive the photo-redox reactions. Given the energy losses in the process and the kinetic overpotential required for each of the half reactions (ΔE_H for HER and ΔE_O for OER in **Fig. 1.4 (a)**, the E_g of a semiconductor needs to be in the range of 1.5 to 2.5 eV[19].

Not all semiconductors satisfy the above thermodynamic requirements, making the choice of semiconductors for OWS limited. As shown in **Fig. 1.4 (c)**, $BiVO_4$ for instance has sufficient band gap width for water splitting (E_g = 2.4 eV) but the position of its CB is not conducive to HER reaction. Similarly, Cu_2O has the right CB position, but its VB position is not conducive for OER reaction. Very few photocatalysts like TiO_2, CdS, and gC_3N_4 satisfy the thermodynamic requirements for OWS. Among these, photocatalysts like TiO_2, despite having required band gap width and band edge positions, fare poorly in solar water splitting since its band gap width is large, which limits its absorption to UV light which constitutes just ~4% of the solar spectrum. Hence, photocatalysts with a small band width which is greater than the minimum required, and with suitable band edge positions are suitable for solar-driven overall water splitting[27]. Alternatively, photocatalysts with unsuitable band gap positions can also be employed in photocatalytic water splitting as, for instance, in the two-step excitation process **(Fig. 1.4 (b))** in which two photocatalysts are combined to form a heterojunction such that one of them assists in HER while the other assists in OER reaction[14].

1.1.2. Quantification of photocatalytic water splitting efficiency

The most common method for quantification is the solar-to-hydrogen (STH) conversion efficiency (η_{STH}), determined under standard solar irradiation generated with an AM 1.5G filter or one sun (100 mWcm^{-2}) with no applied bias. It is calculated as[16]:

$$\eta_{STH} = \left[\frac{Chemical\ energy\ produced}{Solar\ energy\ input}\right] = \left[\frac{mmol\ H_2\ per\ s\ \times 237000\ J\ mol^{-1}}{P_{total}(mWcm^{-2}) \times Area\ (cm^2)}\right]$$

STH is generally used to evaluate only overall water splitting (OWS) reactions and not half reactions, as in the case of HER assisted by sacrificial agents. In the latter cases, quantitative evaluation can be best done using quantum efficiency (QE), defined as the rate at which molecules undergo a particular transformation with respect to the number of photons absorbed per unit time. In photocatalytic water splitting, it is expressed as the ratio of the number of electrons reacted to the number of absorbed photons. However, in practical conditions, as it is difficult to determine the number of photons absorbed by the photocatalyst, it is usually expressed in terms of apparent quantum efficiency (AQE) calculated as:

$$AQE = \left[\frac{no.of\ reacted\ electrons}{no.of\ incident\ photons}\right] \times 100\%$$

$$\eta_{STH} = \left[\frac{2\ \times no.of\ H_2\ molecules\ evolved}{no.of\ incident\ photons}\right] \times 100\% = \left[\frac{4\ \times no.of\ O_2\ molecules\ evolved}{no.of\ incident\ photons}\right] \times 100\%$$

The wavelength of incident photons is a crucial factor in determining AQE since the photocatalyst exhibits different absorption coefficients at different wavelengths, which strongly influences photocatalytic water splitting[28]. The function of AQE is to solely evaluate the performance of the photocatalyst independently of the reactor, the area, and the amount of the photocatalyst. Concerning the amount of the photocatalyst, it is necessary to optimize it for a specific amount of photon flux, since increasing the photocatalyst amount beyond the optimal point would not increase the yield of products from photocatalytic water splitting[29]. However, to incorporate the amount of photocatalyst in the quantification process, turn over number (*TON*) and turn over frequency (*TOF*) are also used, and are calculated as[30]:

$$TON = \left[\frac{H_2\ evolved\ (mmol)}{photocatalyst\ amount\ (mmol)}\right]$$

$$TOF = \left[\frac{H_2\ evolved\ (mmol)}{photocatalyst\ amount\ (mmol) \times Reaction\ time\ (h)}\right]$$

1.1.3. Kinetics and mechanism of photocatalytic water splitting

The basic principles in the mechanism of photocatalytic water splitting are similar to those in other photocatalytic processes. The process can be elaborated based on the following three steps: (i) photon absorption, (ii) charge separation and transport, and (iii) surface chemical reactions[10]. The three steps are schematically shown in **Fig. 1.5**, along with the timescales involved in each step.

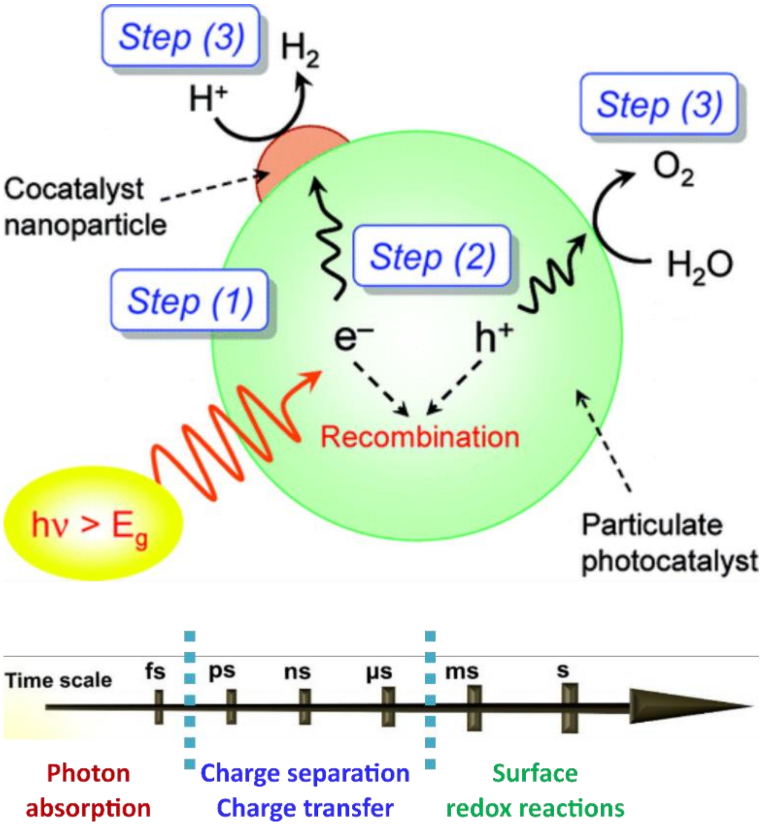

Fig. 1.5: Mechanism of photocatalytic water splitting on a semiconductor photocatalyst[32, 33].

1.1.3.1. Photon absorption – challenges and strategies

Photon absorption is the step that initiates the process of photocatalytic water splitting. When a semiconductor absorbs light, the electrons in VB or the highest occupied molecular orbital (HOMO) are excited to the CB or the lowest unoccupied molecular orbital (LUMO)[31]. This happens in the femtosecond timescale. The rapid relaxation of electrons to the bottom of CB and holes to the top of VB (**Fig. 1.5**) happens on a similar time scale[32].

The absorption properties are based on the electronic structure of the semiconductor. Quantification of light absorption by a semiconductor is done based on the absorption coefficient of the material, $\alpha(\lambda)$, expressed as a function of wavelength, which varies with the bandgap, band positions, and the type of transitions (direct or indirect) in a semiconductor. The reciprocal of this gives the absorption depth, which is the distance below which light intensity is reduced to 1/e of the incident radiation[10]. It is this value that determines the optimal thickness of a photocatalyst film or the optimal amount of photocatalyst suspension that is required to obtain maximum photocatalytic efficiency[32].

Challenges:

The major challenge for photon absorption lies in finding the right material having: (i) sufficiently large band gap (>1.23 eV) with right band gap positions to drive water splitting redox reactions and, (ii) sufficiently small band gap to absorb sunlight that is concentrated in the visible range (~40% from 400 to 700 nm as shown in **Fig. 1.6 (a-b)**).

Techno-economic studies have shown that a minimum of 10% STH (shown by dotted lines in **Fig. 1.6 (b)**) is required for economic feasibility of large-scale industrial photocatalytic H_2 generation[37, 38]. Based on this STH conversion, it was estimated that approximately 10,000 solar plants, each of 25 km^2 area, would be required for photon harvesting to produce 570 tons of H_2 gas per day, which could satisfy one-third of the world's energy requirement (**Fig. 1.6 (c)**)[35].

An example of investigation for such large-area light harvesting can be found in the work of Nishiyama *et al.* who demonstrated H_2 production over a 100 m^2 panel photocatalytic system[36] (**Fig. 1.6 (d)**). However, to obtain maximum H_2 from a minimum area, the light harvesting efficiency of the photocatalyst system needs to be improved.

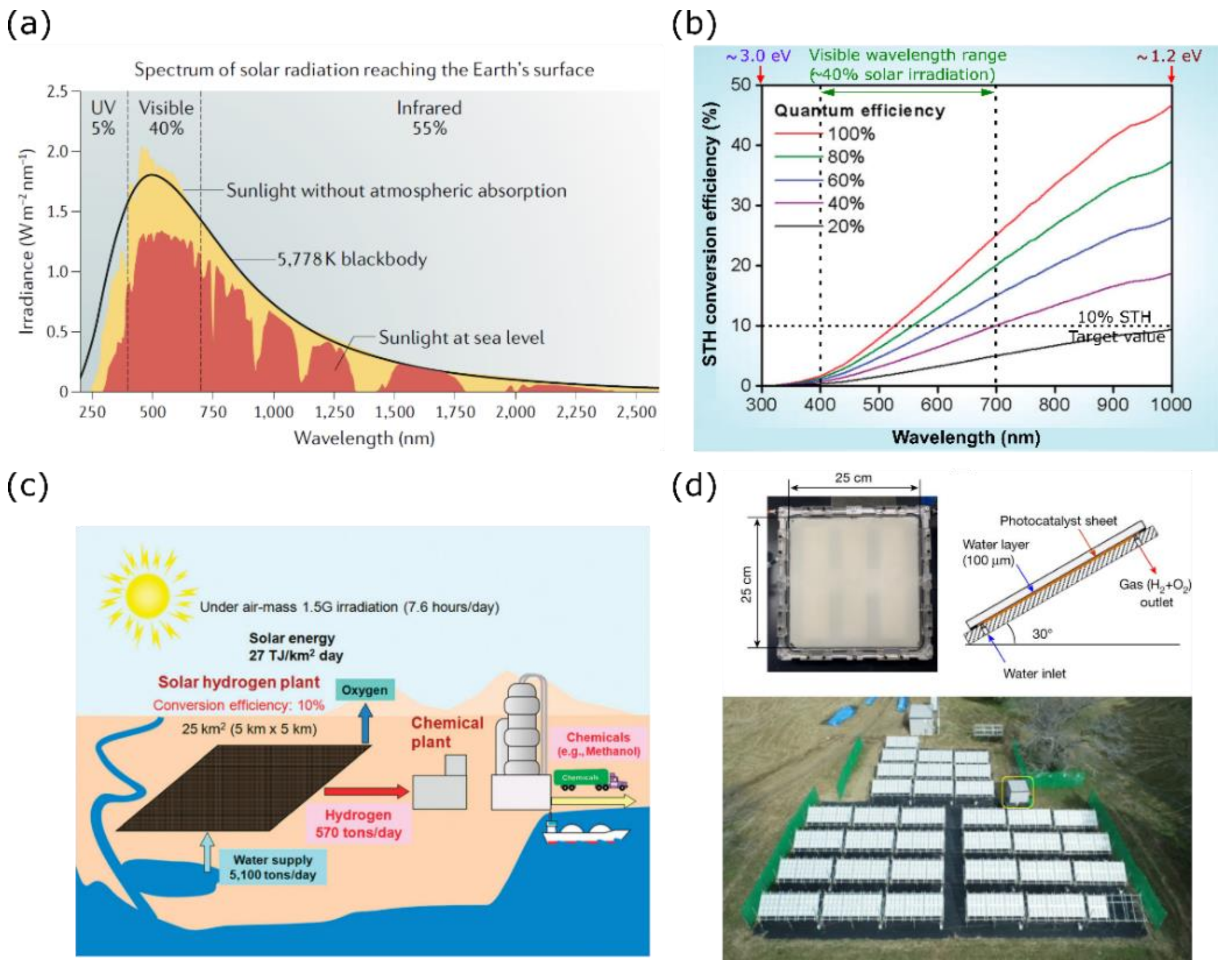

Fig. 1.6: **(a)** The spectrum of solar irradiation at the earth's surface[34]; **(b)** calculated STH values plotted as function of photon wavelengths, assuming AM 1.5G solar irradiation, at different quantum efficiencies. The target STH value required for economic viability and the energy values corresponding to the wavelengths are also indicated (adapted from ref[35]). **(c)** a possible scheme for large-scale water splitting[35]; **(d)** a photographic image of photocatalytic panel reactor, a side-view of the panel structure, and a 100 m^2 solar H_2 production system[36].

This stringent requirement for light harvesting in photocatalytic water splitting can be explained, as shown in **Fig. 1.6 (b)**, based on the calculated STH conversion efficiency values plotted as a function of photon wavelength, at different quantum efficiencies[35]. For example, a large band gap semiconductor like TiO_2 (~3.2 eV for anatase TiO_2), absorbs light only in the visible range (< 400 nm), indicating that even at 100% QE, only ~2% STH values can be attained[39], as can be seen in **Fig. 1.6 (b)**. Drastic increase in STH values is possible for absorption at higher wavelengths (>700 nm). However, currently available semiconductors do not possess band gaps low enough to absorb light beyond 700 nm. In addition, extremely low band gaps reduce the driving forces required for HER and OER[27]. Consider a photocatalyst with an absorption edge at ~520 nm, around 100% QE is required to attain 10% STH (**Fig. 1.6 (b)**), which is practically impossible, since the highest reported QE's do not exceed 60%[10]. Assuming this efficiency, a photocatalyst with absorption edge at ~600 nm is required to attain the desired 10% STH. This requirement calls for finding visible light-responsive photocatalysts for overall water splitting. As seen in **Fig. 1.4 (a)**, very few photocatalysts like CdS and TaON possess simultaneously narrow band gaps to absorb visible light and suitable band gap positions to drive HER and OER reactions. However, they are not stable under aqueous environments and tend to undergo photocorrosion[19]. Hence, to overcome this bottleneck, alternate strategies were explored to improve photon absorption efficiency.

Strategies to improve photon absorption

The strategies related to improving photon absorption are schematically shown in **Fig. 1.7** and are discussed below.

Doping a photocatalyst with metal cations or non-metal anions can enhance the absorption of light in the visible range due to the formation of localized or delocalized electronic states[19]. Besides improving light absorption, this strategy can also improve charge separation efficiency. Metal ion dopants with ionic radii similar to those of the host ions are capable of narrowing the bandgap due to the interaction of cation states with VB or CB, or due to the creation of intra-bandgap levels (**Fig. 1.7 (a)**). Thus, a donor dopant is capable of donating an electron to the CB while an acceptor dopant is capable of accepting an electron from the VB, thereby shifting the band levels and the absorption of the photocatalyst[10]. Unlike metal ion dopants, non-metal dopants like N, C, S, and X (F, Cl, Br) do not form donor levels in the forbidden band but rather shift the valence band edge upward by creating additional electronic states above the VB[18].

Solid solutions formed by combining a wide band gap semiconductor with a narrow band gap semiconductor offer another promising solution for modifying the absorption range (**Fig. 1.7 (b)**). Convenient tuning of bandgaps and energy levels can be attained by varying the proportions of each of the semiconductors[18]. Particularly, solid solutions of isostructural semiconductors are preferable as they can readily undergo orbital hybridization and/or distortion of metal-oxygen octahedral/tetrahedral units, causing changes in band structures. However, the downside of solid solutions is that they are often prepared by a high temperature solid state reaction, leading to low surface area and poor activity[19].

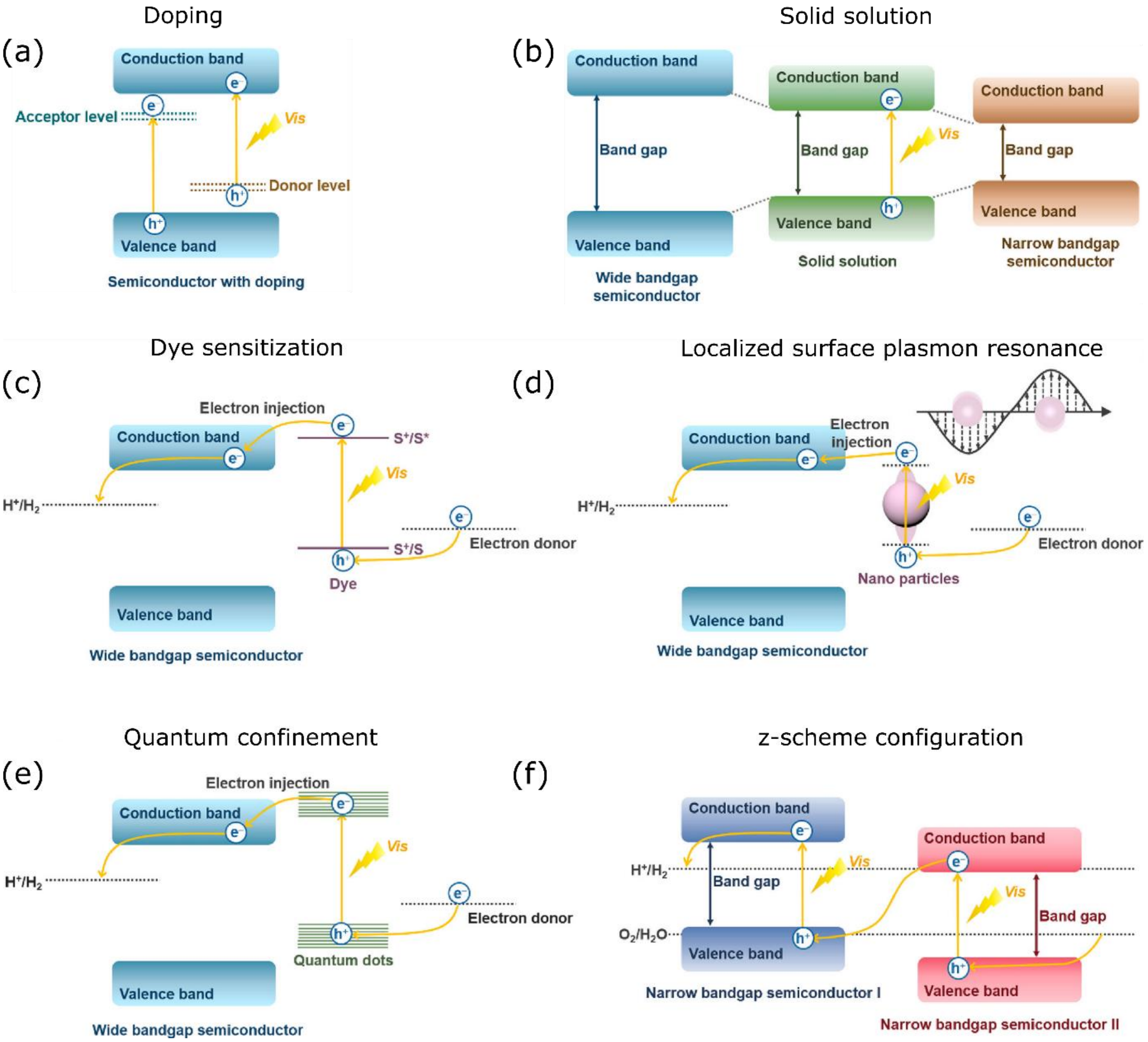

Fig. 1.7: Band diagrams illustrating different strategies employed for improving light harvesting efficiency of the photocatalyst system[10].

Dye sensitization of a photocatalyst improves the absorption efficiency as the dye assists in light absorption and causes excitation of the electrons which can be injected into the CB of the semiconductor (**Fig. 1.7 (c)**)[18]. For this strategy to be successful in photocatalytic OWS, the CB minimum of the semiconductor should be located between the oxidation energy level of the excited dye (E_{S^+/S^*}) and the H^+/H_2 reduction potential[10].

Localized surface plasmon resonance effect (LSPR), contrary to other methods discussed so far, is an optical phenomenon observed in metal nanoparticles (NPs). LSPR is the collective oscillation of electric charges (collective electron oscillations) observed when light interacts with metal NPs whose size is less than or comparable to the wavelength of light[40]. This charge oscillation generates an electric field localized on the metal NP, that reaches a maximum under resonant frequency conditions[41], resulting in strong spectral absorption. This phenomenon can be exploited to increase light absorption of another material coupled to the metal NP or to assist photochemical transformations on the surface of the metal NP through the transfer of excited electrons[42] (**Fig. 1.7 (d)**). When coupled with a semiconductor photocatalyst, LSPR-sensitization of metal NPs enhances light absorption of the photocatalyst through amplification of local electric field and excitation of active charge carriers[43, 44].

Quantum confinement effect, obtained by sensitizing the photocatalyst semiconductor with quantum dots, is also proved to be efficient for improving light harvesting. A quantum dot is a particle with a size smaller than its Bohr exciton diameter, which can enable charge carriers to be spatially confined such that the energies of photogenerated electrons and holes are increased[34]. This confers it with unique electronic characteristics and large absorption coefficients. The most striking effect is that the band gap energy and the positions can be easily modified by modifying the quantum dot size[10]. As shown in **Fig. 1.7 (e)**, the photoexcited electrons can be injected into the CB of a wide band gap semiconductor, providing charge carriers for redox reactions.

Z-scheme configuration is based on a two-step photoexcitation process (**Fig. 1.7 (f)**) and involves an H_2 evolution semiconductor and an O_2 evolution semiconductor[14]. This strategy is particularly useful when using photocatalysts whose bandgap positions enable them to be active only for proton reduction or water oxidation. In this system, visible light irradiation excites electrons from VB to CB in both photocatalyst semiconductors. The HER reaction is promoted over hydrogen evolution semiconductor while the OER reaction is promoted over oxygen evolution semiconductor. Visible light utilization is more efficient over a z-scheme system than over a single photocatalyst since energy requirement to drive each half-reaction is lower than the energy requirement to drive the overall water-splitting reaction[45].

1.1.3.2. Charge separation and transport – challenges and strategies

The second step in the mechanism of photocatalytic water splitting is the separation of photogenerated charges and their transport to the active sites. The separation of charges in the electron-hole pair (exciton) happens in the picosecond time scale[4]. The efficiency of charge separation depends on the dielectric properties of the materials that are determined by the electronic structures of the semiconductors[46]. Based on the dielectric properties and the exciton binding energy, two types of excitons can be distinguished. Wannier-Scott excitons, which are typical of semiconductor materials with high dielectric constant, are those in which the distance between electron and hole is larger than the lattice spacing, and hence can be easily dissociated. Frenkel excitons, which are typical of organic polymers with low dielectric constant, are those in which Coulomb interaction between electron and hole is strong, and hence dissociation is difficult[4]. The binding energies of these two excitons are typically less than 0.01 and 1 eV, which must be overcome to realize charge separation[47].

After separation, the charges need to migrate from the bulk of the semiconductor to the active sites at the surface to carry out redox reactions. This happens in the nanosecond to microsecond time scale. Carrier transport can be quantified based on the diffusion coefficient (D) and the drift mobility (μ)[10]. Diffusion of charges is driven by concentration gradient while drift of charges is driven by the electric field. Important factors that influence charge transport efficiency are carrier lifetime and carrier mobility[4]. The carrier lifetime (τ) together with the diffusion coefficient determines the diffusion length (L), which is defined as the average distance a carrier diffuses before it recombines with another carrier. Carrier lifetime is typically short ranging from picosecond to nanosecond[10]. The quality of the semiconductor is crucial for carrier lifetime since defects and surface states can act as recombination centres and reduce carrier lifetime and diffusion length. Carrier mobility is driven by the potential gradient generated at the interfaces (space charge layers) and is dependent on the effective mass of the carriers, the electronic structure of the semiconductor, and its purity[4].

***Challenges*:**

The major hurdle in effectively using photogenerated electrons and holes is their recombination. This can happen by radiative means (band-to-band) or through traps (defects or impurity states in the forbidden gap). The former is common in direct band gap semiconductors while the latter is common in indirect bandgap semiconductors[47]. Recombination is also possible at surface states, significantly observed in nanoparticle (NP) suspensions[10]. Another hurdle for the separation of charges is the trapping of electrons in energy levels distributed across the forbidden gap. Although this could prolong the charge lifetime from pico-nanoseconds to microseconds, it could also decrease the carrier energetics and mobility[10].

***Strategies*:**

Particle size reduction is a convenient method to reduce recombination since it decreases the distance of migration for charge carriers and increases the surface to volume ratio. For this, synthesis methods can be optimized to obtain the desired particle size of the photocatalyst.

Defect engineering is another approach to reduce charge recombination. It has been shown that high crystallinity with low defects results in high water splitting efficiency due to higher mobility and lower recombination of excited charges. However, some defects like oxygen vacancies were proven to improve carrier transfer by serving as trapping sites or active sites[19]. As the presence of defects is double-edged, careful engineering of defects is required for this strategy to be effective.

Interface engineering is a strategy that involves the formation of a junction in or with a semiconductor. Theoretical studies have revealed that charge separation is governed by separation potential gradients which are concentrated on the semiconductor surface and not the bulk. Hence, the creation of a junction with potential gradient is highly efficient in charge separation. These include homojunctions as in the case of rutile-anatase TiO_2 junction, semiconductor-semiconductor junction as in the case of a z-scheme configuration, and semiconductor-metal junction as in the case of Au, Pt in contact with TiO_2. In these cases, the alignment of semiconductor band gap positions and metal work functions are crucial for charge separation[48].

1.1.3.3. Surface chemical reactions – challenges and strategies

The electrons and holes which are transported to the active sites assist in electrocatalytic redox reactions. This happens in the microsecond to millisecond scale. As shown in **Fig. 1.5**, since the timescale between charge transport and redox reactions is significantly high, charges must be consumed quickly to ensure product formation. Charge consumption efficiency is directly related to the efficiency of electrochemical redox reactions. In thermodynamically uphill processes like water splitting, the redox reactions tend to be sluggish since they involve a high activation energy or overpotential[10]. Particularly, in the overall water splitting process, it was found that O_2 evolution, which takes place in the seconds time scale was kinetically slower than H_2 evolution, which takes place on the microseconds time scale, since O_2 evolution requires four electrons to be transferred from two adsorbed water molecules to the semiconductor surface, compared to two electrons required for H_2 evolution[49]. For electrocatalytic reactions to take place efficiently, the presence of a metal-semiconductor or a semiconductor-semiconductor interface and the presence of a cocatalyst can turn out to be productive for charge separation and consumption[4]. In addition to the above three steps, the mass transfer of reactants and products also plays an important role, since back reaction involving the recombination of evolved H_2 with O_2 decreases the quantum efficiency. Mass transfer depends mainly on the electrolyte, particularly the pH, and the reaction conditions, particularly the temperature of the reaction[4].

Challenges:

The first challenge in this final step is the occurrence of back reactions. In photocatalytic water splitting, either molecular oxygen can undergo a reduction reaction ($O_2 + 4H^+ + 4e^- \rightarrow 2H_2O$) or the evolved H_2 and O_2 can recombine ($H_2 + O_2 \rightarrow H_2O$) to form water. A second challenge is the occurrence of competing side reactions on the photocatalyst, as in the case of S^{2-} anions in CdS photocatalyst being preferentially oxidized ($CdS + 2h^+ \rightarrow Cd^{2+} + S$) compared to water oxidation. This not only results in the decrease of water splitting efficiency but also causes photocorrosion of the photocatalyst.

Strategies:

Cocatalysts are known to reduce the activation energy or overpotential for redox reactions on semiconductor surfaces, particularly for the O_2 evolution reaction which is kinetically more sluggish[50]. In the presence of a cocatalyst, photogenerated electrons from the CB can be transferred to the H_2 evolution cocatalyst or holes from the VB can be transferred to the O_2 evolution cocatalyst. For this to happen, the relative energy levels at the hetero junction are crucial. Also, a short distance between the semiconductor and cocatalyst is necessary for efficient charge transfer. Thus, cocatalysts not only increase water splitting efficiency but also prevent photocorrosion of the semiconductor photocatalyst[50].

Surface engineering is another important strategy to improve overall water splitting efficiency since redox reactions occur on the surface of the semiconductor. One method is to remove the inactive surface layer of the photocatalyst which can act as a recombination centre. Removal of surface layer could also reduce the surface defects and promote charge transfer and redox reactions. Another method is to passivate the surface of an unstable semiconductor with a layer of stable material, which not only prevents photocorrosion of semiconductor but also serves as an electrocatalyst in the water splitting redox reaction.

Having discussed the basic principles, challenges, and strategies involved in improving photocatalytic water splitting, the strategy of modulating the propagation of light by reducing its group velocity using photonic structures to improve photon absorption, which is the focus of this thesis, is discussed in the following section.

1.2. Slow light in inverse opal photonic crystals for light harvesting

As discussed earlier, the first step in solar-driven photocatalytic water splitting is light absorption. Strategies to improve solar light absorption have so far focussed mainly on the choice and modification of materials and their composites[51]. However, in the past three decades, owing to recent advances in photonic principles, light management for solar energy conversion started being ever-increasingly explored. Photonic methods to improve light harvesting include antireflective coatings for minimizing reflection losses[52, 53], surface texturing for minimizing transmission losses[54, 55], back reflectors to recycle light[56], photon up-conversion and down-conversion to utilize a broader wavelength of solar spectral range[57, 58], optical filters for selective and efficient light utilization particularly in thermophotovoltaics[59], plasmonic structures[60-62], light scattering structures[63, 64], and photonic crystals[65-67].

Among them, photonic crystals (PCs) are unique, as they can mould the propagation of light and slow it down at certain frequencies, which can be potentially used for enhancing light harvesting. Slow light, described as the propagation of an electromagnetic wave at an extremely low group velocity than that in free space[68, 69], can be attained by several mechanisms: stimulated Brillouin scattering arising from the scattering of a laser field from a retreating sound wave[70-72]; coherent population oscillations[73, 74]; electromagnetically induced transparency[75]; quantum weak values, quantities investigated in quantum physics and involving a shift in the pointer of a measuring device under pre- and post-selection of the quantum state of a system[76-78]; twisted optical phase front shaping[79]; or structural dispersion mechanisms e.g., taking place in some coupled resonator structures[80, 81], negative permeability metamaterials[82, 83], metamaterials with negative permittivity and permeability[84], twisted bilayer graphene[85], and photonic crystals such as photonic crystal waveguides[86-88], periodic multilayers i.e., one-dimensional (1D) photonic crystals)[89-91], two-dimensional (2D) photonic crystals[92], and three-dimensional (3D) photonic crystals such as inverse opals[92-94]. These mechanisms could potentially be used in slow-photon enhanced light-harvesting applications. However, some of them require the use of powerful laser beams that make them less energy efficient, while others are difficult to apply in practical solar-to-energy conversion. Photonic crystals, on the other hand, have emerged as promising structures for slow photon assisted light harvesting enhancement, thanks to the research progress in the past four decades on the principles and the fabrication of PC structures.

1.2.1. Photonic crystals and slow light

Photonic crystals are periodic dielectric structures that create a range of forbidden frequencies, called a photonic band gap (PBG), for which light cannot propagate through the medium[95-97]. This can be understood by drawing a parallelism with the propagation of electrons in a semiconductor (SC). In a SC ‘electronic crystal’, the atomic lattice offers a periodic potential to an electron such that Bragg-like diffraction from the atoms creates a gap in allowed energies for which the electron is forbidden to propagate in any direction. Similarly, in a PC, the dielectric lattice offers the periodic potential such that Bragg scattering from the dielectric interfaces creates a gap in allowed frequencies for which the photon is forbidden to propagate in any direction[95].

Nature offers us many examples of such structures[99] like opal gemstones[100], some flowers, insects, birds, fish, plant leaves, berries and algae[98], all of which are characterized by their period structures and iridescent structural colours **(Fig. 1.8)**. PCs can be either 1D, 2D, or 3D periodic structures, as shown in **Fig. 1.8**.

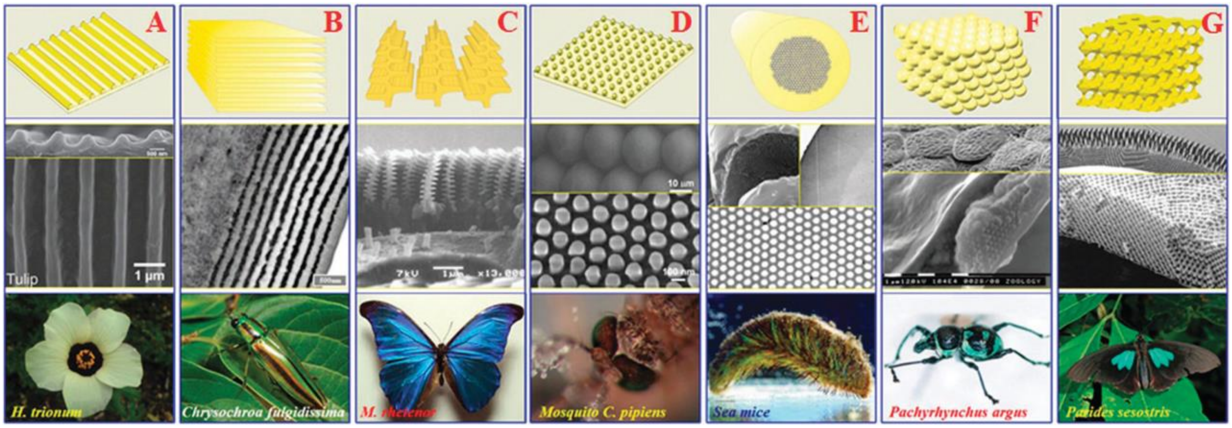

Fig. 1.8: Photonic nanostructures exhibiting structural colours in nature[98].

The origin of studies on artificial PCs can be traced back to the 19th century when Rayleigh initiated the theoretical work on periodic multi-layer dielectric stacks that can influence light propagation in one dimension[101]. Theoretical investigation progressed in the 20th century with works by Bykov on the spontaneous emission from an excited atom or molecule in a 1D periodic structure[102] and by Ohtaka on the energy band of photons in a model 3D system of dielectric spheres[103]. However, the pioneering works by Yablonovitch[104] and John[105] in 1987 laid strong theoretical foundations for the manipulation of light in periodic 3D structures. The former proposed the strong inhibition of spontaneous emission in a 3D periodic dielectric structure due to the presence of an electromagnetic band gap, while the latter elaborated on the idea that periodic structures affect photon localization due to a random refractive index variation. These studies, combined with the quest to render devices smaller and faster by replacing electrons with photons as information carriers, accelerated research on PCs in the 21st century. Today, PCs, with their remarkable ability to reflect, bend, diffract, guide, and slow down light, find applications in diverse fields like optics, optoelectronics, computing, lasers, displays, sensors, medical, biological and energy systems[106].

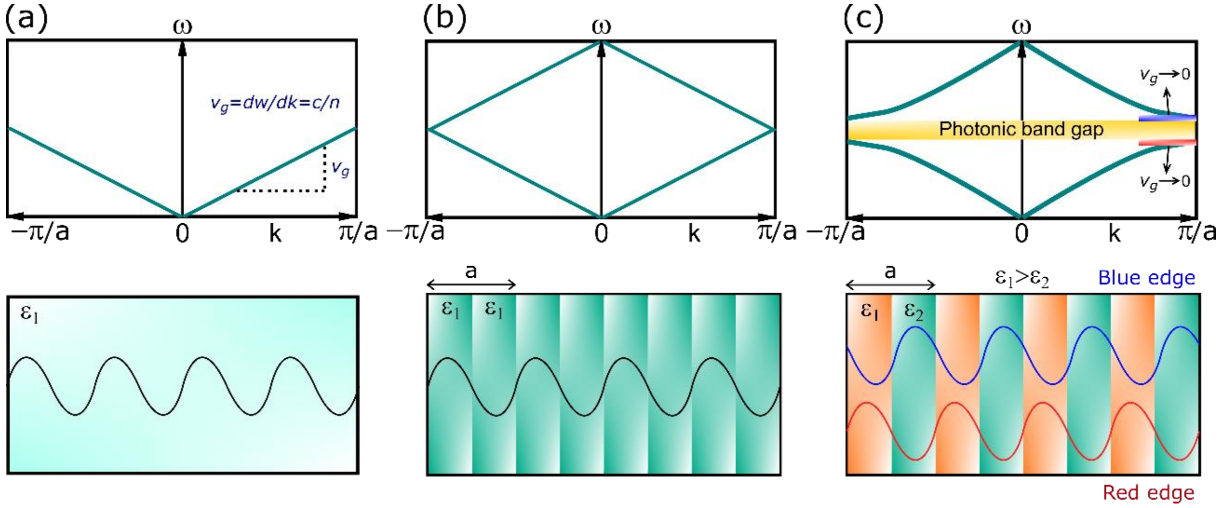

Fig. 1.9: The periodicity and the contrast in refractive index give rise to the opening of photonic bandgap in photonic crystals. When light propagates through a homogeneous medium with a refractive index equal to $n_1 = \sqrt{\varepsilon_1 \mu_1}$, where ε_1 is the dielectric permittivity and μ_1, the *magnetic permeability* that may reasonably be assumed equal to 1, the angular frequency ω is proportional to the norm of the wavevector k as described by the dispersion relation $\omega(k) = ck/n_1$ **(a).** Introducing theoretically a periodicity a to the medium leads to the folding of the dispersion relation at the edge of the first Brillouin zone **(b)**. The illustrated case corresponds to a one-dimensional periodicity. If a modulation of the dielectric constant is added to the periodic medium, bandgaps open in the band structure, leading to band flattening at the edge of the bandgap, and hence to slow photons **(c)**.

Photonic band gap: The most interesting property of PCs in modifying the propagation of an electromagnetic wave is the photonic band gap. This can be explained by the relation between the angular frequency ω of the photon and its wavevector $k = 2\pi/\lambda$, called the dispersion relation $\omega(k)$, derived from Maxwell's equations governing macroscopic electromagnetism and Floquet-Bloch theorem concerning periodic dielectric media. When light propagates through a homogeneous medium with uniform dielectric function, there exists a linear dependence between angular frequency and wave vector, where the slope is equal to the phase velocity $v = c/n$, or the group velocity of the wave packet v_g. As shown in **Fig. 1.9 (a)**, this can be represented as $\omega = ck/n$ where n is the refractive index of the medium that is related to the permittivity ε by $n = \sqrt{\varepsilon}$ (assuming magnetic permeability μ to be 1). The band structure obtained from the dispersion relation as a plot of ω against k represents all the frequencies in which the optical modes are allowed for a given wave vector k. The range of ω for which there are no propagating solutions for any k is called the photonic band gap.

When an artificial periodicity a is introduced to this homogeneous medium, the dispersion relation folds at the edge of the Brillouin zone, as shown in **Fig. 1.9 (b) (**in the case of one-dimensional periodicity). If a modulation of the dielectric constant is added to the periodic medium, bandgaps open in the band structure, causing the band to flatten at the edge of the bandgap (**Fig. 1.9 (c)**). In this case, due to the periodic dielectric function, the forward moving waves are partially reflected at every dielectric interface. At frequencies fulfilling the Bragg condition (at the boundaries of the first Brillouin zone $k = \pm\pi/a$), interference of backward propagating waves (due to reflection from the interfaces) and forward propagating waves, results in a standing wave at the edge of the Brillouin zone. Subsequently, a gap in the dispersion relation opens, called the photonic band gap, due to the splitting of the $\pm\pi/a$ planewaves into $cos\ (\pi x/a)$ and $sin\ (\pi x/a)$ standing waves by the different effective RIs and the difference in photon energies. Photons of all frequencies pertaining to the PBG are forbidden from propagating through the material.

Three conditions need to be fulfilled for a periodic structure to exhibit a PBG. Firstly, the periodicity of the PC should be in the order of the wavelength of light[107]. This implies that to have a PC working in the visible or near-IR region, where most of the solar radiation is concentrated, the periodicity should be in the order of a few hundred nanometres to 1 μm. Secondly, as can be deduced from the above discussion on PBG formation, the refractive index contrast between the two dielectric components should be sufficiently high. Ideally, it should be greater than 2.8, for the manifestation of a complete PBG, as reported in some works[108, 109]. Thirdly, to manifest an omni-directional PBG, it should be a 3D PC, as only 3D PCs are capable of manifesting a complete PBG[110]. The term omni-directional PBG or complete PBG refers to frequencies wherein light is forbidden to propagate at all angles. In the case where light propagation is forbidden in only certain directions or angles, it is called a pseudo-photonic band gap (pPBG) or stop band gap (SBG).

Slow light and light absorption enhancement: Slow light in PCs is the most attractive property for light-harvesting applications. At the edges of PBG, the bands tend to flatten, causing v_g to tend to zero. Propagating light is hence slowed down. This phenomenon can be understood as the stationary wave arising from the interaction between wave packets reflected by the PBG and the wave packets with wavelengths just outside the PBG. This stationary wave packet has a very low v_g that is equal to zero, from a theoretical point of view. Light propagating at the red edge of the PBG (namely, at an angular frequency just below the PBG) has an intensity higher in the material of the photonic crystal with a higher RI (n_1), whereas light propagating at the blue edge (namely, at an angular frequency just below the PBG) corresponds to a higher intensity in the low RI material (n_2)[101]. Light propagating in these spectral regions with reduced group velocity is termed as slow light or slow photons, with those at the blue edge called blue edge (BE) slow photons and those at the red edge called red edge (RE) slow photons. The reduced group velocity of light in a photonic crystal implies a longer lifetime and a longer optical pathlength of photons in the structure[109]. When a light-harvesting material is present in the photonic structure, this can result in enhanced photon absorption.

1.2.2. Inverse opal photonic crystals – synthesis, properties, and applications

Different types of PCs have been either theoretically proposed or synthesized[111]. Initially, diamond and diamond-like structures were theoretically studied and proposed to be the most favourable among PCs to manifest a complete PBG (between the second and third photonic bands), owing to their weak directional isotropy for light propagation[112]. It was reported that an RI contrast as small as 1.9 is sufficient to create a complete PBG in such structures[113]. The first 3D PC possessing a complete PBG in the microwave region was fabricated by Yablonovitch in 1991 using a lithographic method to create a diamond symmetry[114]. Later, in 1998, a woodpile PC operating in the infrared region was prepared using layer-by-layer microelectronics fabrication technology[115].

Although, both the above PCs exhibited a complete PBG, the practical realization of such structures proved to be complex and challenging. In contrast to top-down approaches like lithography, bottom-up approaches like self-assembly started gaining attention, primarily due to the ease of synthesis and cost-effectivness[116]. Self-assembled structures were first investigated for their photonic properties in opal colloid photonic structures[117, 118]. However, opal colloidal PCs do not manifest a complete PBG due to insufficient RI contrast[101]. Instead, they manifest a pseudo-photonic band gap (pPBG), also called stop band gap (SBG), between the second and third bands for wave propagation along the [111] crystal direction in real space, which forbids wavelengths in certain directions only. Also, opal PCs are not practically applicable in light-harvesting applications due to the difficulty of fabricating monodisperse spheres of photoactive materials[51]. Hence, research shifted towards the inverted structure of the opal called the inverse opal (IO).

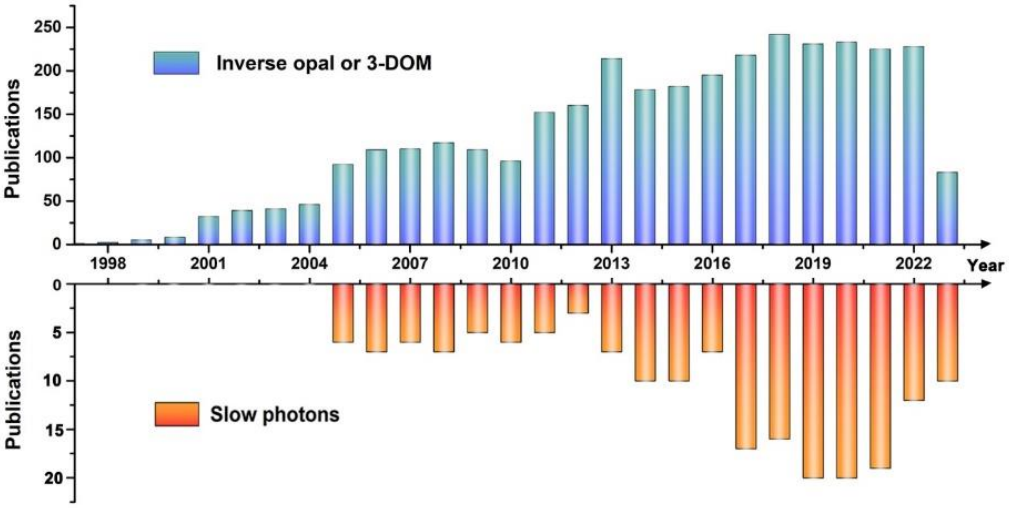

Fig. 1.10: The number of publications on 3-dimensionally ordered macroporous (3-DOM) materials for light harvesting applications and the publications among them that exclusively discuss the impact of slow photons for light harvesting enhancement. The data was derived from Scopus search using the search terms "inverse opal*" OR "3*DOM" OR "3*dimensionally ordered macroporous" OR "3D ordered macroporous" and "slow photon*" respectively.

Inverse opal (IO) PCs are a class of 3-dimensionally ordered macroporous (3-DOM) structures with close-packed array of spherical voids, synthesized by infiltration of the templating colloid opal structure with a high RI material, followed by the removal of the templating colloids[119]. The IO PC consists of a face-centred cubic (*fcc*) lattice of air spheres in the background of the infiltrated material. The *fcc* structure is a result of the close packing of templating colloids into the *fcc* arrangement which is thermodynamically the most stable packing of identical spheres [120, 121]. IO PCs are capable of manifesting a full PBG between the eighth and ninth photonic bands only when the RI contrast is high and losses due to the material's absorption are low[122]. One of the earliest studies on PBG formation in IO structures was carried out by Sajeev and John[108], with the conclusion that a complete PBG spanning 10% and 15% of the PBG centre is possible by inverting the opal structure infiltrated with high RI materials of Si and Ge respectively. Among all the PCs, IO PCs are the most employed for light harvesting applications, owing to their optical and structural properties, the relative ease of fabrication, and the cost-effectiveness[123]. **Fig. 1.10** shows the number of research articles that have been published in the past two decades on IOs and on slow photon effect in IOs for light-harvesting applications, which highlights the growing research interest in inverse opals.

1.2.2.1. Synthesis of inverse opals – three-step approach

Initial breakthrough in IO synthesis came in the late 90's with the synthesis of IO SiO_2[124], which was later extended to the synthesis of other IO metal oxides like TiO_2, ZrO_2, and Al_2O_3[125, 126]. IO synthesis involves three steps: (i) opal assembly of monodisperse templating colloids, (ii) infiltration of the opal structure with the material, (iii) removal of templating colloids (**Fig. 1.11)**.

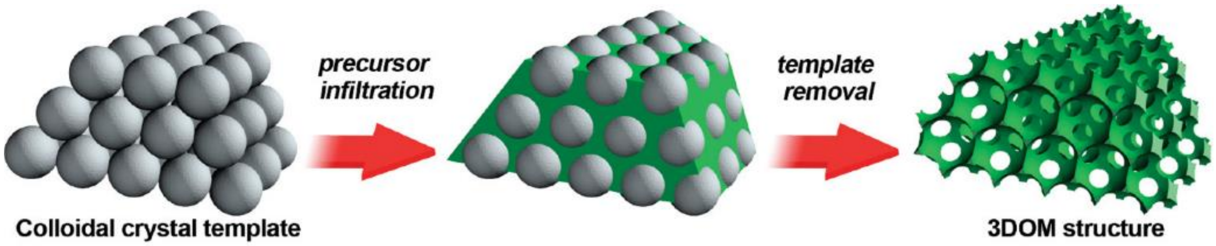

Fig. 1.11: Schematic illustration of the synthesis of IO structures[127].

The first two steps in this process can be combined into a single step, as in the coassembly method, which will be discussed later in this section.

(i) Colloid crystal template (CCT): Constructing a CCT is a bottom-up approach that involves the ordered assembly of colloidal building blocks. Spherical colloids are the most employed building blocks due to the ease and controllability of their synthesis. Building blocks of other morphologies, despite being complex and challenging, have also been successfully employed to create ordered structures[128, 129]. For IO synthesis, spherical colloids of amorphous materials like silica and polymers were often used. Silica colloids were one of the first inorganic monodisperse spherical particles that were synthesized in 1968 by Stober[130]. Silica templating colloids can be synthesized with high monodispersity and are naturally charge-stabilized. However, their removal after material infiltration requires the use of harmful reagents.

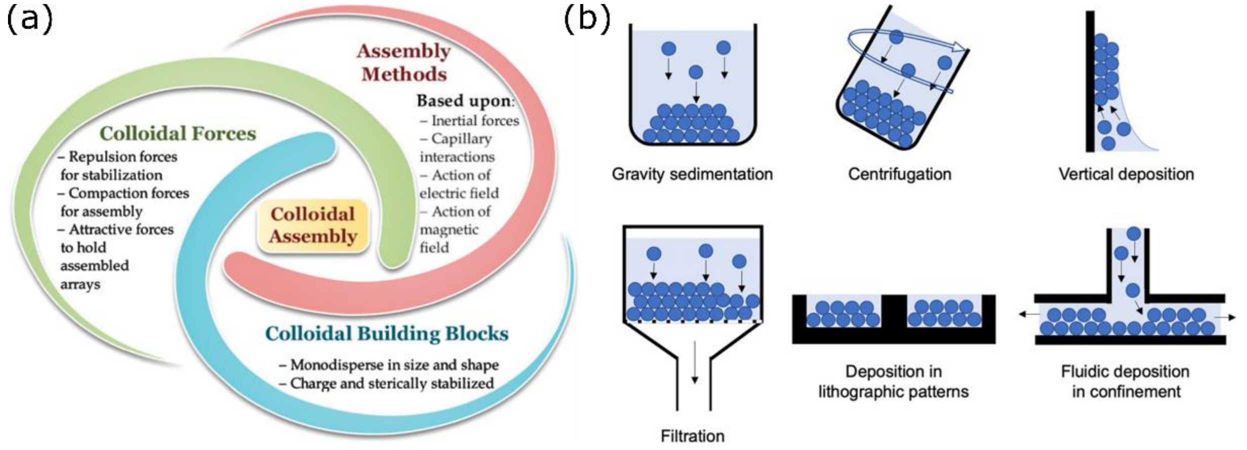

Fig. 1.12: (a) Representation of the key factors involved in colloid assembly[131]; **(b)** representative methods of colloid assembly[132].

Common polymer colloids employed to form a colloidal crystal include polystyrene (PS) and polymethyl methacrylate (PMMA). The ease with which the particle size, surface potential and colloid stability can be controlled and their facile elimination after infiltration with material, make them highly applicable in colloid crystal assembly[131]. To have an IO PC operating in the visible/infra-red region where most of the solar irradiation is concentrated, it is necessary to synthesize colloid particles in the size range of ~100 nm to ~1000 nm. Also, to have an IO PC with excellent photonic properties, the colloid crystal must be a highly ordered opal PC. The first condition to obtain an ordered PC is the monodispersity of templating colloids. Some simulation studies concluded that high quality colloidal PCs can be formed if colloid size distribution is within 2% of standard deviation (SD), and that the SBG completely disappears if the SD is greater than 5%[116, 133]. Generally, polymer colloids are prepared by emulsion or dispersion polymerization. The size, monodispersity and surface charge are controlled by various factors like monomer concentration, initiator concentration, stabilizer, emulsifier, surfactant, reaction temperature and reaction time[134].

In addition to the monodispersity, a balance between various forces needs to be attained to obtain highly ordered CCTs. The various parameters involved in colloid assembly and the forces at play in the assembly process are shown in **Fig. 1.12 (a)**.

The first important requirement in colloid assembly is to have a stable colloid suspension. Sufficient repulsion forces between colloids are required to overcome van der Waal's forces and other interactions that can cause undesired agglomeration. Repulsion forces include electrostatic repulsion resulting from charge stabilization in polar solvents and steric repulsions resulting from solvated adsorbed layers[131]. In addition to these forces, the mass of colloids can play a role in the sedimentation of colloids under the influence of gravity, especially in the case of larger colloids. Hence, a balance between the attractive and repulsive forces is required to have a stable colloid suspension.

Assembly of colloids into an ordered structure can occur spontaneously due to the gain in free energy after assembly. However, to attain control over the assembly process, various driving forces are employed, which determine the classification of assembly processes. Colloid assembly methods like sedimentation, centrifugation, spin-coating, Langmuir-Blodgett method and shear ordering rely on gravity or inertial forces, while methods like evaporation-induced self-assembly (EISA), dip coating, and assembly at liquid-liquid interfaces rely on capillary forces driven by the surface tension of evaporating solvent[131]. Other external forces like electric and magnetic fields can also be used to drive colloids into an ordered structure. **Fig. 1.12 (b)** shows representative examples of the external forces and methods applied to assemble colloids.

***Evaporation-induced self-assembly (EISA)*:** Among the various methods of colloid self-assembly[135], EISA offers numerous advantages, , like high structural order, large size-fabrication, versatility and low cost[136-138]. As this method has been used in this research work, it is discussed here in detail. EISA is particularly used to prepare colloid films. In a typical synthesis, a substrate is immersed in a colloidal suspension and the suspension medium is allowed to evaporate, causing the colloidal particles to be driven to the meniscus by evaporation-induced fluid flow and to self-assemble on the substrate (**Fig. 14, a-c**). In general, due to favourable entropy, the colloids assemble into an *fcc* lattice structure with the [111] plane parallel to the substrate[139].

The mechanism of EISA in colloid suspensions is more complex than it seems to be at the outset. One of the earliest studies on EISA mechanism was done by Dimitrov *et al*. in 1996[140]. The primary driving force is the convection force provided by the evaporation of water molecules. As shown in **Fig. 1.13 (a-b)**, when water starts evaporating, a pressure gradient is created from the suspension towards the wetting film due to evaporation, producing a suspension influx from the bulk suspension towards the wetting suspension film. This influx comprises the water component (j_w) and the particle flux component (j_p). During evaporation, the water evaporation flux is compensated by the water and particle flux components. This flux along with the capillary forces between the substrate and the colloidal suspension results in the assembly of colloidal spheres on the substrate[141]. One of the competing forces working against colloidal assembly is sedimentation due to gravity, especially in the case of larger spheres. This can be tackled for example by increasing the convective flow through the increase of the rate of evaporation[142].

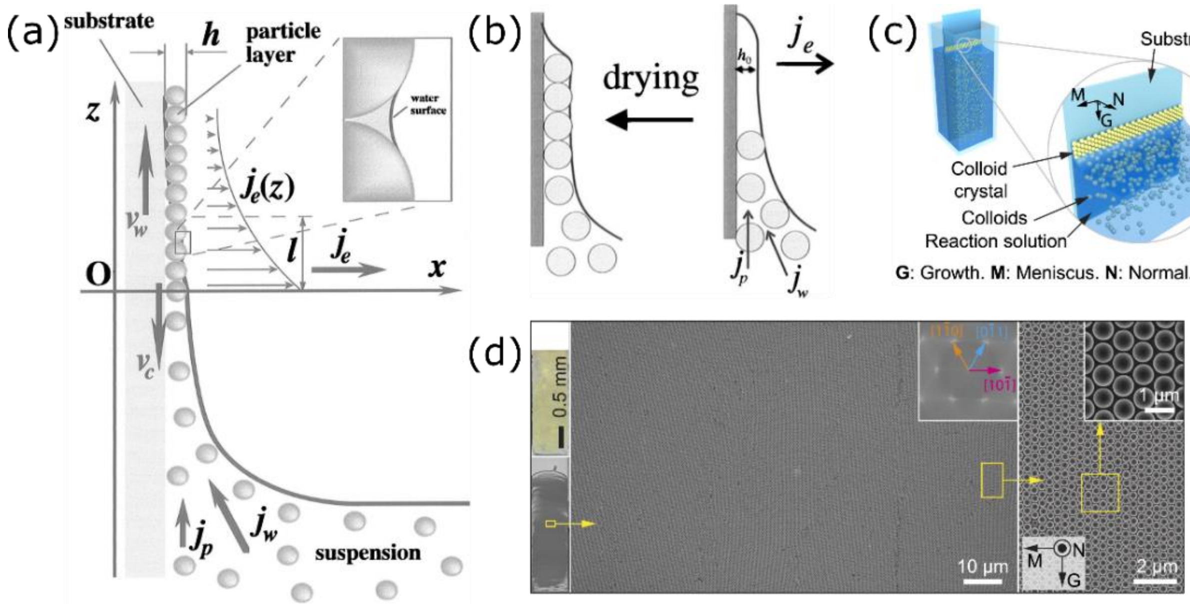

Fig. 1.13: (a-b) Schematic representation showing the growth of colloid arrays on a substrate by **(a)** withdrawal of substrate from the colloid suspension and **(b)** evaporation of the suspension medium (EISA), with v_w representing the substrate withdrawal rate, v_c the array growth rate, j_w the water influx, j_e the water evaporation flux and h the thickness of the colloid film[140]; **(c)** schematic representation of evaporation-induced colloidal coassembly process with G, M and N representing growth, meniscus and normal directions respectively; **(d)** SEM of an optical images along with Fourier Transform of the colloid assembly[139].

Recent studies have revealed the mechanism behind the preferential [110]-oriented growth in the EISA method of colloid crystal assembly (**Fig. 1.13 (c)**)[139]. Initially, the convective force of evaporation nucleates a poly-crystalline colloidal monolayer along the horizontal meniscus direction *M* in which the close-packed direction is often parallel to the local meniscus orientation. As the number of layers increases, the grains in the colloidal crystal gradually rotate due to tensile stress along the meniscus direction caused by the mismatch between the colloid crystal shrinkage due to drying and the rigid substrate. This rotation occurs in the range of several hundred micrometres until the close-packed region aligns with the growth direction *G*. Following this alignment, the colloidal crystal grows uniformly with [110] orientation. **Fig. 1.13 (d)** shows the SEM and optical microscope images of the colloidal crystal film grown over a large area for this study, along with the Fourier transform and the crystallographic orientation[139].

Various factors influence colloid assembly by the EISA process. These include the contact between the meniscus and the substrate (influenced in part by the hydrophilicity of the substrate), the bulk volume of colloid particles (φ_b) which should be greater than a critical concentration (φ_c), the rate of evaporation (influenced by the temperature and humidity)[123], choice of solvent, choice of substrate and the angle of the substrate relative to the direction of convection[119]. A careful control of these factors can result in large-area, highly ordered colloidal opal PCs[143]. EISA of colloids is a highly promising method in IO synthesis as it can produce IO films with excellent photonic properties over a large area.

Challenges in CCT formation: Synthesizing CCTs over a large area and with minimum defects is a serious challenge. Common defects include point defects like a vacancy and Frenkel effect, vacancy associations, dislocations, stacking faults and cracks. The most pertinent among them is the development of cracks. Cracks in the opal template are carried over to the inverse opal structure and are detrimental to their photonic properties causing undesirable light scattering effects[144]. Cracks usually form during the drying process. Evaporation of the solvated layer around the colloids and the shrinkage of the colloids during drying results in tensile stress. The tensile stresses constrained by the rigid substrate give rise to capillary stresses, which are then mitigated through crack formation in the films[145, 146]. Methods employed to reduce defect formation in colloid templates include using highly charged colloids[147, 148] and highly monodisperse colloids[149, 150], modifying the dispersion medium in the colloidal suspension[151, 152], regulating the rate of evaporation by controlling the temperature[142, 153], controlling the experimental conditions like humidity and volume fraction[143], and using substrates that can relieve stresses[154-156].

(ii) Infiltration of colloid crystal template with material:

Infiltration of CCT can be done either by dry methods like atomic layer deposition (ALD) and chemical vapour deposition (CVD) or by wet methods like liquid-phase infiltration, electrochemical deposition (ECD), supercritical deposition (SCD), and chemical reduction

(CR)[116]. Gas-phase infiltration methods like ALD and CVD offer better infiltration with high filling fraction but they are experimentally demanding and require the optimization of various parameters. Methods like ECD, SCD, and CR, although efficient, are limited in their scope of application, as infiltration with a wide variety of materials is challenging[131].

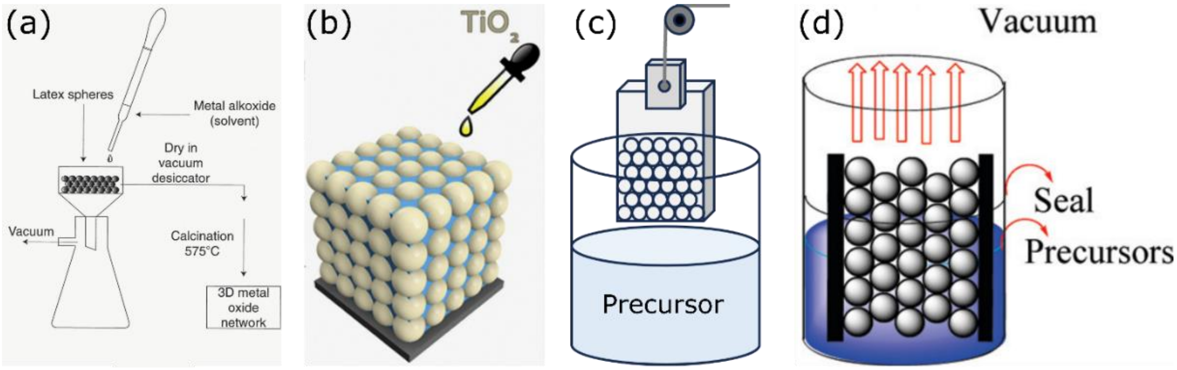

Fig. 1.14: Schematic representation of selected methods of infiltrating the IO matrix material into the interstices of the colloidal crystal template: **(a)** vacuum infiltration (adapted from ref.[125]), **(b)** drop infiltration (adapted from ref.[157]), **(c)** dip infiltration, **(d)** sandwich vacuum infiltration (adapted from ref.[158]).

The frequently used method among the above is the liquid-phase infiltration method, which can be carried out by various methods like suction method[125], dip method, template immersion, drop method, lift-off turn-over technique[159], capillary infiltration[160], and sandwich infiltration[158]. Representative examples of liquid infiltration are shown in **Fig. 1.14.** Various materials can be used for infiltration like sol-gel precursors[161-163], salt solutions[164], and nanocrystal suspensions[165]. A typical sol-gel approach involves the infiltration of the opal CCT with a metal alkoxide precursor which undergoes hydrolysis and condensation within the interstices of the opal structure during sintering/calcination to form the metal oxide (MO). Subsequent removal of the template results in MO-IO structure. Various MO-IO structures were synthesized using this approach like those of SiO_2, TiO_2, Al_2O_3, and ZrO_2[162]. The sol-gel method allows the synthesis of a wide range of materials with relatively cost-effective precursors. However, the precursors are often sensitive to moisture rendering their handling difficult and preventing complete infiltration. In the salt precursor approach, a metal salt solution, typically of nitrates or acetates, is dissolved in ethanol or acetic acid and infiltrated in the opal CCT. Subsequent chemical conversion by oxalic acid, for example, followed by calcination, results in the respective MO-IO structures. MOs like ZnO, Fe_2O_3, Cr_2O_3, Mn_2O_3, MgO, and NiO were templated into IO structures using this approach[131].

Alternatively, preformed NPs can also be infiltrated into the opal CCT, which prevents the crystal lattice from being distorted by chemical transformations[165].

Challenges in infiltration process**:** Control over the infiltration process is crucial to obtain ordered IO structures. During the infiltration process, there could be either insufficient infiltration of the precursor leading to defects post-calcination or extra precursor used that could result in the formation of overlayer[166]. Both have a negative impact on IO photonic properties. To improve the infiltration of the precursor, strategies employed involve using external forces such as suction or vacuum, controlling the precursor properties like viscosity and dilution, and improving the wetting interaction between the template and the precursor[119]. Alternatively, 'coassembly' approach has gained prominence not only to reduce crack formation in CCT, but also to improve the filling of the interstices in the opal CCT with the material. This approach will be discussed in the next section in detail, as it is the method employed in this research work.

(iii) Removal of colloids:

Methods to remove templating colloids include calcination, solvent extraction, and chemical etching[167]. The choice of method depends on the nature of the colloid and the IO material involved. Polymer-based colloids like PS and PMMA are usually removed by calcination. Alternatively, they can be removed by solvent extraction using solvents like toluene, dimethylformamide (DMF), and tetrahydrofuran (THF). Using these solvents is not eco-friendly as some of these solvents are toxic, and the recovery of solvents after extraction is complicated. Also, the colloid material may not be completely removed by the solvent, resulting in photonic properties being compromised[168]. In the calcination process, the temperature and ramp rate play a crucial role in the final IO structure. In general, polymer colloids are completely removed above 500°C. Calcination not only removes the colloids but also assists in chemical transformation of the matrix material as in the case of sol-gel precursors. For instance, increasing the calcination temperature much beyond 500°C could favour the formation of the rutile phase of TiO_2 instead of the anatase phase[168]. Calcination temperature could also affect the pore size of the IO structure, as demonstrated in some works[93, 169]. A low ramp rate, typically 1-2°C is generally preferable during calcination, as it permits the removal of colloids without disturbing the structural order. When carbon-based IOs are to be prepared, for instance in the synthesis of IO carbon and IO g-C_3N_4, calcination needs to be carried out in an inert atmosphere, which leaves behind undesirable residues. In such cases, SiO_2 colloids are often used, which are removed by chemical etching with HF, NHF_2, or a strong alkali.

The three-step approach for the synthesis of IO structures allows for a wide range of materials to be synthesized. Particularly, in the case of photocatalytic applications, IO structures of various metal oxide semiconductors like TiO_2, ZnO, WO_3, Fe_2O_3, $BiVO_4$, Bi_2WO_6, $SrTiO_3$, Fe_2TiO_5, Ga_2O_3, $ZnGa_2O_4$, $InVO_4$, CdS, $CuCrO_2$, TaON and g-C_3N_4 were synthesized using this approach (CCT formation, infiltration, template removal). However, the quest for minimizing defects arising from CCT formation or infiltration led to the exploration of alternative and more efficient synthesis strategies.

1.2.2.2. Synthesis of inverse opal – two-step coassembly approach

The two-step coassembly approach involves the simultaneous self-assembly of both the colloids and the material, followed by calcination. The process is schematically represented in **Fig. 1.15 (a)**. The minimization of defects in this approach can be attributed to two reasons. Firstly, the reduction in the number of steps during synthesis implies that difficulties encountered during infiltration in the 3-step process like underfilling and overfilling of the precursor can be reduced. Secondly, tensile stresses between the shrinking colloidal crystal and the rigid substrate during drying are mitigated as the colloids can shift their position in the gelling suspension[123]. **Fig. 1.15 (a)** shows schematically the comparison between the 3-step and the 2-step approach. The corresponding SEM images clearly indicate that the 2-step coassembly approach resulted in more homogeneous structures over a large area with minimum cracks.

The coassembly approach can be classified into three types based on the type of precursor used. As shown in **Fig. 1.15 (c)**, the first method involves the coassembly of the colloids and the sol-gel precursor. The precursor composition and concentration, its compatibility with the colloids, hydrolysis-condensation rate, and the degree of matrix shrinkage on drying and calcination influence the quality of the IO structure[144]. One of the earliest reports of this approach can be found in the work by Wang *et al*. who assembled silica beads in the presence of TEOS precursor by EISA method to synthesize highly ordered, crack-free IO SiO_2 structures[170]. However, the removal of SiO_2 beads in this process required the use of HF which is toxic. Hatton *et al*. replaced SiO_2 beads with PMMA colloids and coassembled them along with TEOS precursor to prepare highly ordered IO SiO_2 structures **(Fig. 1.15 (b))**[171].

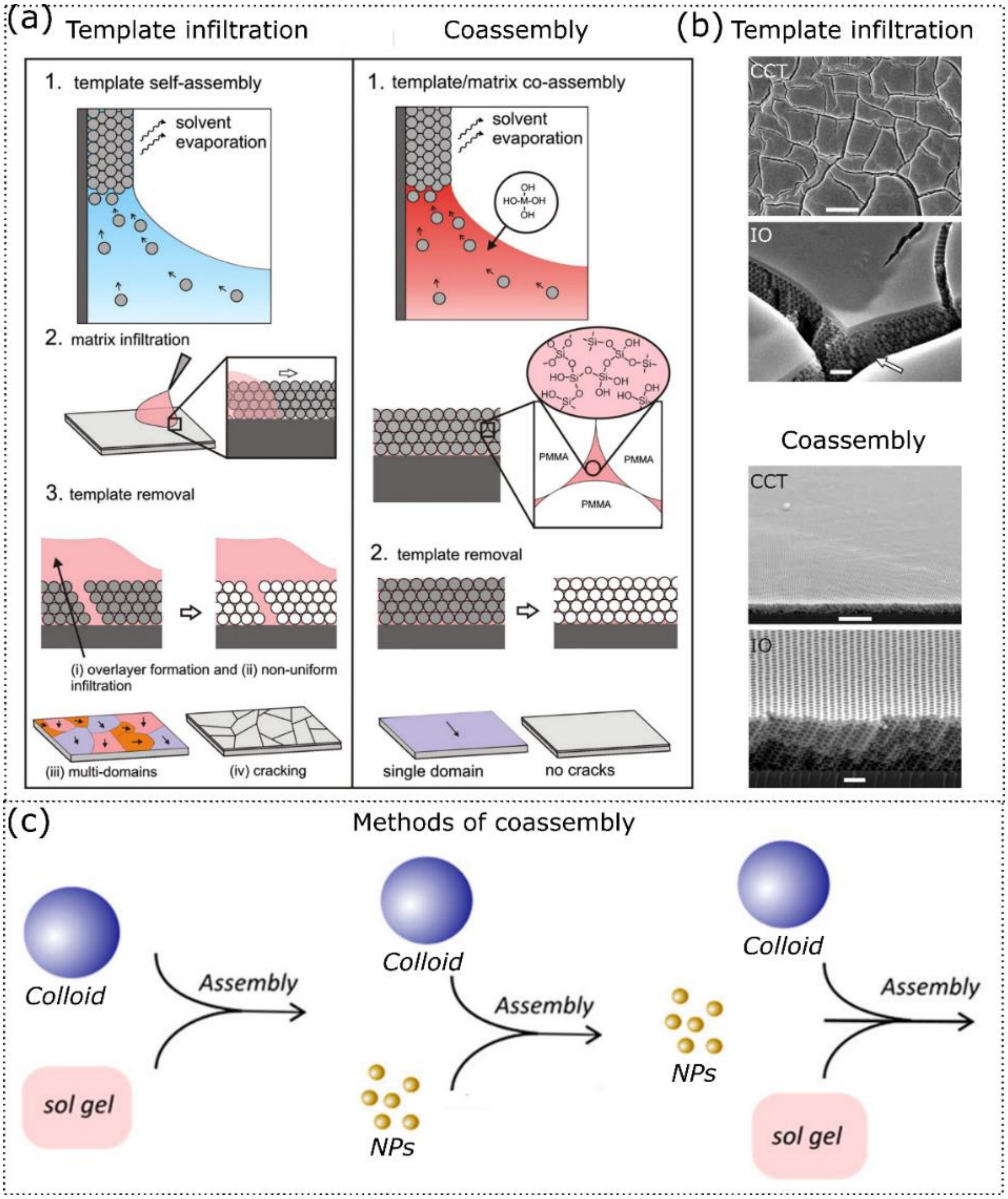

Fig. 1.15: (a) Schematic representation of the comparison between the 3-step infiltration process and the 2-step coassembly process in the synthesis of IO structures in the case of the synthesis of IO SiO_2 using PMMA colloids and TEOS sol-gel precursor; **(b)** the corresponding comparison of CCT and IO SEM images of structures prepared by the two methods, showing the higher degree of order and crack-free structures in the coassembly approach (adapted from ref.[171]); **(c)** different methods of coassembly: colloids along with the sol-gel precursor, colloids along with NPs, and colloids along with sol-gel precursor and NPs (adapted from ref.[123]).

The second method of coassembly approach involves the simultaneous self-assembly of templating colloids and prefabricated NPs (**Fig. 1.15 (c)**). The important factors that need to be considered here are the concentration of the NPs relative to that of the colloids, and the matching between the constitutive sizes of both the particles[123]. Based on the particle fluxes in the case of TiO_2 NPs and PS colloids, an optimal theoretical volume fraction of $\frac{\varphi_{nano}}{\varphi_{PS}} \sim 0.023$ was calculated by Han *et al*. for the ratio of nanocrystal precursor to templating colloids[172]. One of the earliest examples of this approach can be found in the work by Zheng *et al*., who coassembled SiO_2 NPs along with PS colloids to obtain highly ordered IO SiO_2 structures[173]. In addition, with careful control of temperature, they coassembled multimodal structures by co-assembling PS colloids of two different sizes along with SiO_2 NPs. An improvement in this method was proposed by the group of Aizenberg *et al*. who used bi-phase amorphous-crystalline TiO_2 NPs to be self-assembled along with PMMA colloids[174]. Control over the phase of TiO_2 NPs was achieved by controlling the molar ratio of titanium isopropoxide (TIP) to tetramethyl ammonium hydroxide (TMAH) in the peptization process. The crack-free structures obtained in this bio-inspired process, were attributed to the amorphous portion of the TiO_2 precursor diminishing stresses related to the competing forces during evaporation assisted self-assembly, and the crystalline phase reducing shrinkage-related stresses during calcination.

The third method of coassembly approach is a three-phase coassembly that involves the assembly of colloids along with a sol-gel precursor and NPs. Typically, this approach was employed to load plasmonic NPs *in situ* in the metal oxide IO structure. The work by Vasquez *et al*. was one of the first to report this method for the synthesis of IO SiO_2 loaded *in situ* with Au NPs. Colloidal PMMA spheres, Au NP suspension and TEOS sol-gel precursor were mixed according to carefully calculated proportions and left to self-assemble on a glass substrate. Subsequent calcination resulted in highly ordered IO SiO_2-Au structures. In a slightly different approach, Au NPs were loaded *in situ* in IO SiO_2 by a three-phase coassembly of PS colloids, TEOS precursor and $HAuCl_4$ as Au precursor[175]. In this case, Au NPs were fabricated *in situ* instead of using prefabricated NPs. Another slightly different method for obtaining NP-loaded IO structures is by using raspberry particles, wherein the NPs are first loaded onto the surface of the colloids, followed by the self-assembly of the raspberry colloids[176].

IOs of different metal oxides like SiO_2, TiO_2, Al_2O_3, ZrO_2, Fe_2O_3 and WO_3, indium-tin oxide, Zn-doped ferrite were prepared by the coassembly approach[166, 172, 174, 177] to yield highly ordered, homogeneous and crack-free IO structures over a large area. Other variations of this approach were also investigated as in the case of mixed sol-gel precursors to prepare IO SiO_2-TiO_2 hybrids[178], mixed NPs to load Au and Ag NPs in IO SiO_2[179], and shape-controlled NPs to prepare different structures of IO TiO_2[172]. Despite significant progress in the coassembly approach, this method remains to be explored for the synthesis of other IO metal oxides.

1.2.3. Strategies to use slow light in photonic structures for light harvesting

Early research on photonic crystals was motivated by the desire to control the spontaneous emission of light[180], based on the property of photonic band gap. Later on, with advances in research on photonic crystals, the property of slow light (reduction of the group velocity of light at the edges of the photonic band gap) started gaining attention as it offers immense potential in the fields of telecommunication and optical data processing[181] with potential applications in optical devices like lasers, amplifiers, detectors, absorption modulators and wavelength converters[182]. Besides the applications of this property in optics and optoelectronics, this property can also be successfully exploited in light harvesting applications, as the increased optical path length and lifetime of photons favours stronger light-matter interaction, thereby enhancing optical gain and light harvesting[183, 184].

Slow light in inverse opal photonic structures was first investigated for light harvesting applications in a dye-sensitized solar cell (DSSC)[185]. A photoelectrode of nanocrystalline (NC) TiO_2, when coupled with an inverse opal TiO_2 photonic structure, was observed to yield a 26% increase in photocurrent compared to that of pristine NC-film. This was attributed to slow photons at the red edge of the stop band gap (SBG) overlapping with the dye absorption range, thereby enhancing light absorption by the dye and photocurrent. Further experimental[186, 187] and theoretical[188] studies on the same application confirmed slow photon-assisted enhancement. However, it was proposed that the photonic layer acting as a back-reflecting Bragg mirror in the bilayer structure could have played a greater role than the slow photons in this configuration.

Although the above work discussed the impact of slow photons in detail, it remained a claim without ample justification. The first attempt to firmly establish slow photon assistance was made by Ozin's group[189] in a photocatalytic application involving IO TiO_2 for the solid-phase photodegradation of methylene blue (MB). Firstly, seven IO TiO_2 samples having increasing pore diameters, with their SBG and slow photon spectral positions located at increasing wavelengths, were tested for photocatalysis. The sample whose red edge slow photons coincided with TiO_2

electronic absorption (situated at ~370 nm, indicated by the yellow shade in **Fig. 1.16 (a)**, showed the highest activity, two times greater than that of the non-structured NC TiO_2. Secondly, the activities of the samples were tested at varying incidence angles (0°, 10°, and 20°), which changed the spectral positions of pPBG peak and slow photons. The sample with pPBG peak at 370 nm (yellow shade in **Fig. 1.16 (b)**) showed the least activity under normal incidence (0°), since the pPBG peak and not the slow photons overlapped with TiO_2 absorption, which caused reflection losses. The same sample, however, showed the highest activity at 20° incidence angle, as the pPBG position shifted away from TiO_2 absorption edge and the red edge slow photons overlapped with TiO_2 absorption. Finally, the competing effects of pPBG reflection losses and slow photon absorption gains were verified by testing photocatalytic activities under both monochromatic (~370 nm) and polychromatic irradiation.

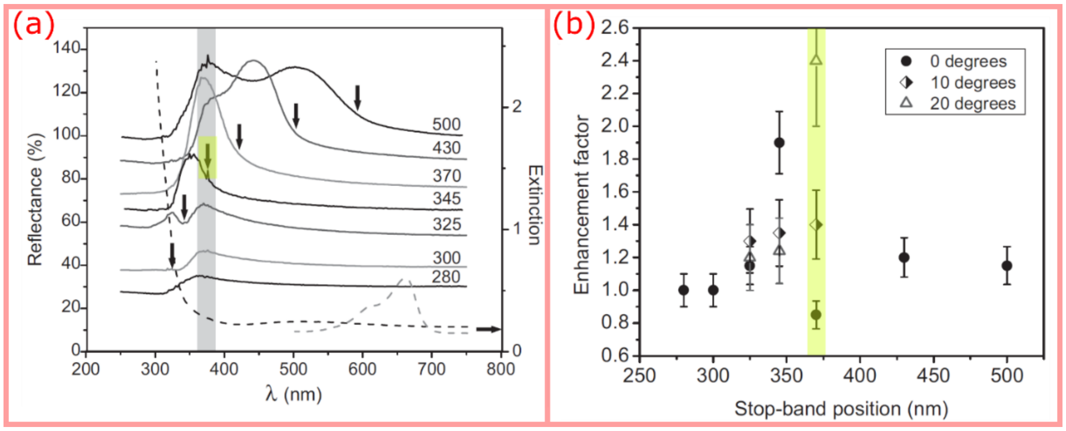

Fig. 1.16: (a) Reflectance measurements of different inverse opal TiO_2 samples with increasing pore diameters (from bottom to top) indicating the positions of their stop band gap edges (arrows) and the TiO_2 absorption region (at ~387 nm indicated by grey shaded region). The dashed lines represent extinction spectra of TiO_2 (dotted black line) and methylene blue (dotted grey line); **(b)** Photocatalytic enhancement factors of the inverse opal structured samples at varying incidence angles relative to the photocatalytic activity of non-structured NC TiO_2 (ref.[189]).

It is to be noted that two strategies were employed in the above work: (i). tuning slow photon wavelengths through lattice parameter and incidence angle variations to overlap with the electronic absorption of the photoactive material and (ii). tuning the incidence light wavelength to the slow photon wavelengths and electronic absorption of the photoactive material.

In addition to the above, the following comparative studies were often carried out to further justify slow photon assistance in activity enhancement: (i) comparing the activity of PCs in slow photon-assisted conditions with that of disordered (DO) porous structures that do not exhibit photonic properties, to discriminate SPE from other contributing factors like increased specific surface area, mass transport and multiple internal reflection of light, (ii) comparing the activity of PCs in slow photon-assisted conditions with that of non-structured (NS) counterparts that do not exhibit photonic properties. Each of these strategies and other strategies employed are discussed in detail in the following subsections with relevant select examples.

1.2.3.1. Tuning slow photons to electronic absorption of material

The fundamental strategy in using slow photons for improving light harvesting lies in tuning the slow photon frequencies to the electronic absorption of the light-harvesting material, which could be the IO skeleton itself, another photoactive material embedded in the IO structure, or the target reactant material **(Fig. 1.17)**.

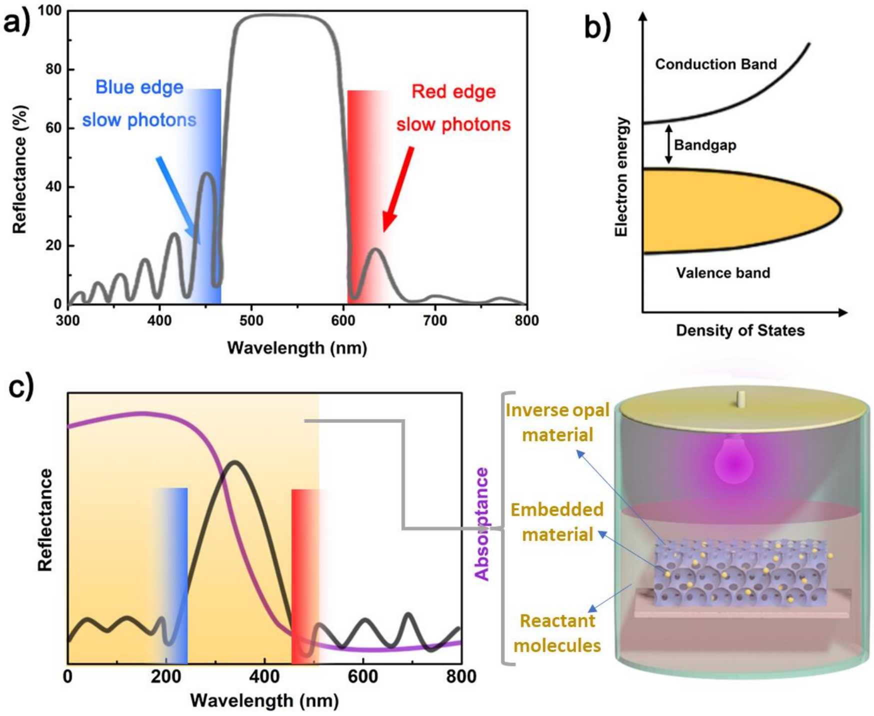

Fig. 1.17: Schematic representation of tuning the slow photon frequencies to the electronic absorption of the light-harvesting material: **(a)** A theoretical reflectance spectrum of an IO photonic structure showing a peak corresponding to the stop band gap and slow photons at either of its edges; **(b)** Energy band diagram of a light harvesting semiconductor; **(c)** A superposed spectrum showing both the reflectance spectrum with the stop band gap (black line) and the absorption spectrum (purple line) along with the absorption region (yellow shade) of either the inverse opal material, embedded material in the inverse opal or the reactant material.

Two factors need to be considered to highlight the importance of accurate tuning of slow photons: (i). photons reflected due to pPBG are counterproductive for photocatalysis, which necessitates precise tuning to avoid pPBG reflection while simultaneously matching the slow photon wavelengths with the electronic absorption of the material, (ii). slow photons at the edges of the pPBG are limited to narrow spectral ranges, which calls for accurate tuning of their wavelengths. As tuning is the key factor here, it is important to consider the various tuning parameters, tuning possibilities, conditions, and strategies employed by researchers to tune slow photon wavelengths in light harvesting applications.

1.2.3.1.1. Tuning parameters

Parameters to modify the spectral position of pPBG and hence that of slow photons[190] can be categorized as follows: i. Lattice parameter (determined from pore diameter of the IO macropore), ii. Effective refractive index (RI of matrix material, RI of void-filling medium, and their respective filling fractions), iii. Angle of light incidence (with respect to the normal of the plane of the IO structure)[191-194].

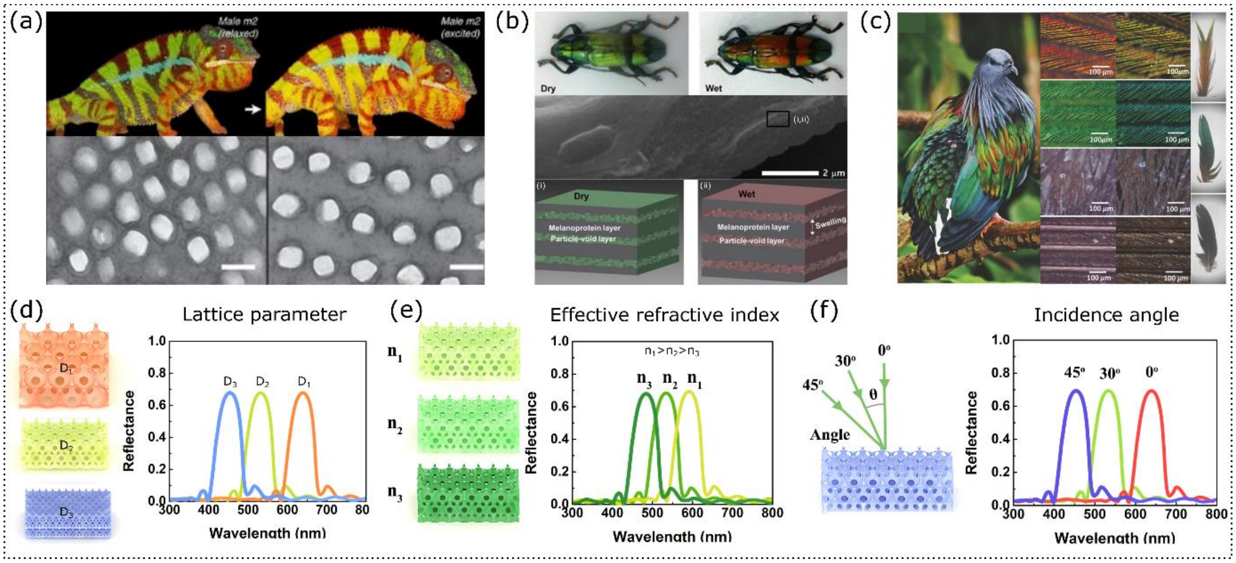

Fig. 1.18: (a-c) Light modulation in living biological photonic structures: **(a)** reversible colour change in panther chameleon between relaxed state and excited state caused by the lattice change of guanine nanocrystals in S-iridophores of the chameleon (scale bar-200 nm)[195]; **(b)** colour change in longhorn beetles from golden-green to red caused by the change in effective RI when the voids between the melanoprotein layers are filled with water[196]; **(c)** structural colours of a Nicobar pigeon whose colours vary with viewing angle[197]; **(d-f)** variation of SBG in IO photonic structures with variation in **(d)** lattice parameter, **(e)** effective refractive index, **(f)** light incidence angle.

Nature provides us with examples of the variation of structural colours (PBG positions) with each of these parameters, as shown in **Fig. 1.18 (a-c)**. In IO photonic structures, the variation of PBG and slow photon wavelengths with each of these parameters is similar, as graphically depicted in **Fig. 1.18 (d-f).** As seen in the figure, the SBG position shifts towards longer wavelengths with an increase in lattice parameter and with an increase in effective refractive index, while it shifts towards shorter wavelengths with an increase in light incidence angle.

The variation of the pPBG spectral position with the change of the above parameters can be estimated using modified Bragg's law that takes into account the reduction in incidence angle when light enters from air medium to the matrix material (Snell's law)[198]:

$$\lambda = \frac{2\, d_{hkl}}{m} \sqrt{n_{eff}^2 - n_{inc}^2\, sin^2\, \theta}$$

where λ is the wavelength of pPBG reflection, d_{hkl} is the interplanar spacing defined in the case of *fcc* lattice as:

$$d_{hkl} = \frac{a}{\sqrt{h^2 + k^2 + l^2}}$$

where a is the unit cell parameter, defined in the case of an IO with pore diameter D as

$$a = \sqrt{2}\, D$$

m is the order of Bragg diffraction, n_{eff} is the effective RI of the PC structure usually calculated by volume-weighted RI approximation as

$$n_{eff}^2 = n_{matrix}^2\, f + n_{void}^2\, (1 - f)$$

with n representing the RI of each medium and f representing their respective filling fractions, n_{inc} representing the RI of incidence medium, and θ the light incidence angle with respect to the normal of the exposed plane. In the case of a planar IO film where the [111] planes of the IO PC are exposed to incident light, the pPBG of first order Bragg diffraction becomes:

$$\lambda = 2 \cdot \sqrt{2/3}\; D\, \sqrt{n_{matrix}^2\, f + n_{void}^2\, (1 - f) - n_{inc}^2\, \sin^2 \theta}$$

Researchers working on slow photon assistance in light harvesting applications often report the close correlation between the spectral positions of experimentally observed pPBG peaks and those calculated from the above equation[199-201], to ratify the photonic properties of the synthesized IO structures. It should however be noted that pPBG peak position calculated from the above equation remains an estimation as it involves the approximation of crucial variables like filling fraction and effective RI that are often not experimentally determined. For instance, the ideal filling fraction in an *fcc* IO structure is 0.26 for the matrix and 0.74 for the void. However, less than ideal filling fractions between 0.1 and 0.2 for the matrix were either presumed or estimated from Braggs equation in previous reports involving slow photon-assisted photocatalysis[200, 202]. Also, the calculation of the actual RI of the matrix becomes complicated especially when it involves planar IO films having composite materials, with additional complication encountered in the case of aqueous phase photocatalysis when incomplete filling of the pores can alter the effective RI. In addition, the Braggs equation does not account for the discrepancies in pPBG spectral position caused by structural imperfection. Nevertheless, Braggs equation serves as an important tool to estimate the size of templating colloids required to generate slow photons in the desired wavelength range. Also, it could serve to estimate pPBG position in conditions wherein experimental measurements could be challenging, like that in aqueous phase applications, and to interpret experimental results of enhanced activity based on slow photon wavelengths calculated from Bragg equation[201, 203].

1.2.3.1.2. Optical gains vs reflection losses

The possibilities of tuning the pPBG peak and slow photon wavelengths in the presence of a photoactive material are shown schematically in **Fig. 1.19**, with the plot representing the pPBG reflectance peak, the blue and red lines representing the blue edge (BE) and red edge (RE) slow photon regions, and the yellow shade representing the electronic absorption (EA) region of the photoactive material. The various tuning possibilities can be categorized under four distinct cases. **Case I:** As seen in **Fig. 1.19 (a),** BE slow photons, pPBG peak and RE slow photons lie within the EA of the material. In this case, light absorption enhancement due to both BE and RE slow photons occurs. However, the detrimental effect of attenuation caused by pPBG reflection also takes place. In this case optical gain due to slow photons and reflection losses due to pPBG compete. **Case II:** As seen in **Fig. 1.19 (b)**, BE slow photons and pPBG peak lie within the EA of the material while RE slow photons are away from the EA of the material. In this case too, competing factors come into play as BE slow photons enhance light harvesting while pPBG reflection undermines it. **Case III:** As seen in **Fig. 1.19 (c)**, BE slow photons are tuned to overlap with the EA of the material while the pPBG peak and the RE slow photons remain outside the EA of the material. Here, BE slow photons enhance light harvesting while simultaneously avoiding the adverse effect of pPBG reflection. **Case IV:** As seen in **Fig. 1.19 (d)**, both the pPBG peak and the slow photons are situated far away from the EA of the photoactive material. In this case, the photoactive material cannot harvest energy from localized slow photons resulting in the least enhancement of light harvesting.

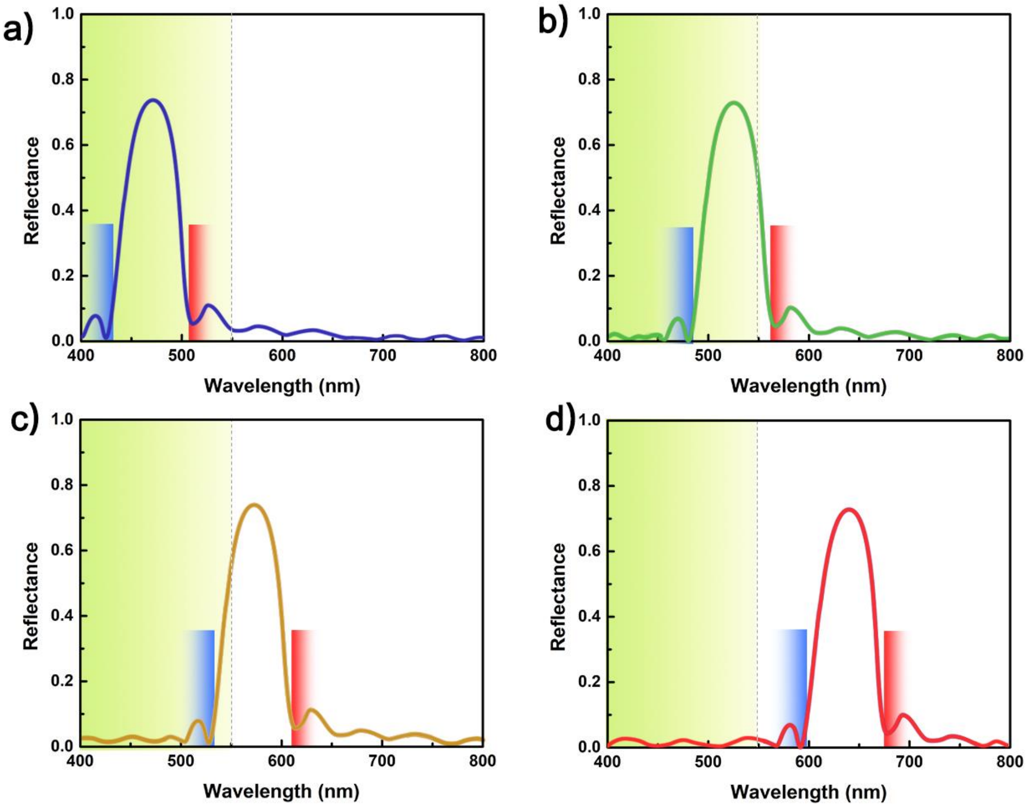

Fig. 1.19: Schematic representation of the various possibilities of tuning the red and blue edge slow photons (red and blue shades) to the electronic absorption of the light harvesting material (green shade). **(a)** Both red and blue edge slow photons, along with the reflection peak, are tuned; **(b)** Blue edge slow photons, and the reflection peak are tuned while red edge slow photons are away; **(c)** Blue edge slow photons are tuned while the reflection peak and the red edge slow photons are tuned; **(d)** Red and blue edge slow photons, along with the reflection peak, are away from the electronic absorption of the photocatalyst.

It is obvious from the above discussion that meticulous tuning of slow photons to the electronic absorption of the photoactive material while simultaneously minimizing reflection losses is essential for optimal enhancement of light harvesting. However, it is not obvious which of the two factors dominates when both are operative, especially under polychromatic irradiation. Based on theoretical studies, it was speculated that the attenuation of light harvesting due to pPBG reflection dominates, since the spectral width of the reflection peak is larger than that of the slow photons[188]. However, experimental evidence does not necessarily seem to agree with this perspective, probably due to the presence of additional contributing factors apart from slow photon assistance in practical applications.

An example of the four different tuning conditions, obtained through lattice parameter variation, can be found in the work involving IO Ti-Si oxide photonic crystal, that was tested for the solid-state photodegradation of RhB under monochromatic irradiation[204]. It was reported that RE tuning showed the highest activity (15.6 enhancement factor compared to nc-TiO_2) followed by BE tuning and then by pPBG peak tuning. The least activity was reported for the condition in which the peak and the edges were far away from both incidence light and TiO_2 absorption.

The competing effects of SPE and PBG reflection losses were experimentally probed by many authors since the earliest discussion reported by Ozin's group[189, 205], as in the case of bilayer IO TiO_2 grown on TiO_2 nanorods and sensitized with Au np's, tested for photoelectrochemical (PEC) water splitting under visible and simulated solar irradiation[206]. SPE was probed by varying the pore diameter to tune slow photons to the localized SPR wavelengths of Au NPs. It was observed that the sample templated from 250 nm colloids showed the highest solar-to-hydrogen conversion efficiency (0.71%) due to RE tuning, while the least activity was reported for that templated from 292 nm colloids due to pPBG reflection tuning condition. Similar discussion about the competing effects can be found in other works, like that involving IO CdS for photocatalytic H_2 generation under monochromatic and UV-Vis irradiation[203] and IO TiO_2-graphene quantum dots for photodegradation of salicylic acid under UV-Vis and Vis irradiation[207].

1.2.3.1.3. Red edge and/or blue edge tuning

As seen from the various tuning possibilities mentioned above, it is possible for either RE slow photons, BE slow photons or both to be tuned to the EA of the photoactive material, with each case having its specific benefits and drawbacks. Red edge tuning has the advantage of slow light at the red edge being preferentially localized in the higher dielectric medium (photoactive IO matrix material), which ensures better light-matter interaction and increased light harvesting. However, in this case, the pPBG peak necessarily falls within the EA range of the photoactive material, resulting in slow photon gains being attenuated by reflection losses. Blue edge tuning, on the other hand, enables tuning such that BE slow photons are tuned to the EA of the material while the pPBG remains away from it, thereby avoiding reflection losses. However, on the negative side, blue edge slow photons are preferentially localized in the lower dielectric medium (IO void), resulting in lesser interaction with the photoactive material with lesser light harvesting potential.

Most of the early works on slow photon assisted photocatalysis provided experimental evidence for higher enhancement under RE tuning conditions[189, 204]. Some works explicitly compared both the tuning conditions and reported the supremacy of RE tuning over BE tuning, as found for example in the effort to trace SPE in IO ZnO for RhB degradation under UV-Vis irradiation[208]. In one of the samples, coded ZnO-IO-260 (the number representing the size of the colloid template), photocatalytic enhancement compared to the non-IO ZnO film was 28% at 20^{o} light incidence angle and 48% at 40^{o} incidence angle, compared to non-IO ZnO film, due to blue edge and red edge tuning respectively. By conducting experiments on IO ZnO samples with two different pore diameters at three different light incident angles, the authors studied different tuning conditions and explicitly concluded that RE tuning resulted in higher photocatalytic activity than BE tuning.

It is worth noting in the above example, that the activity under BE tuning despite being lower compared to that under RE tuning, still resulted in significant activity enhancement, which solicits adequate justification. The need for explanation became imminent as more scientific reports emerged that exclusively discussed BE tuning for photocatalytic enhancement like those involving IO TiO_2-Au for 2,4-dichlorophenol degradation under visible irradiation[209], IO $ZnGa_2O_4$ for MO degradation under UV irradiation[210], IO ZrO_2-CdS for H_2 generation through water splitting under visible light[211], and more recently IO β-Bi_2O_3 for MO and RhB degradation under visible irradiation[212].

Some researchers even reported that BE tuning resulted in greater photoactivity enhancement than RE tuning. The earliest of them was reported for the photoisomerization of trans-azobenzene to its cis isomer under tuneable monochromatic irradiation when the reactant was supported on opal SiO_2 photonic structure[213]. Later, Halaoui's group reported greater blue edge enhancement (4.7 EF relative to nc-TiO_2) compared to RE enhancement (1.4-1.8 EF) in incident photon-to-current conversion efficiency (IPCE) by CdS quantum dot (QD)-sensitized IO TiO_2 under monochromatic irradiation[214]. The higher efficiency of BE tuning was attributed to the inevitable presence of disorder in synthesized PC structures that induces diffuse light scattering, resulting in a greater increase in group velocity of light at the red edge compared to that at the blue edge[215]. A second reason was hypothesized whereby the ultrasmall CdS QD's (2-3 nm) were thought to be partly solvated in the aqueous medium (low RI medium where BE slow photons are localized) that resulted in enhanced light absorption. Similar IPCE results were reported by the same group while working on CdSe-sensitized IO TiO_2[216].

Higher enhancement under BE tuning than RE tuning was also reported in slow photon-assisted photocatalytic applications. For instance, in the photodegradation of RhB and 4-CP on IO ZnO-Au under visible irradiation, BE slow photons tuned to the plasmon resonance absorption of Au NPs in the sample with pPBG at 590 nm showed higher activity than that with pPBG at 510 nm with RE tuning[217]. Similarly, superior BE tuning efficiency was reported in angle-dependency tests on slow photon-assisted photocatalysis by IO TiO_2 for stearic acid degradation using a UV monochromatic LED light source[200]. The comparison between BE and RE tuning was more exclusively studied by Su's group in a ternary IO TiO_2-Au-CdS particulate (powder) photocatalyst system that manifested angle-independent photonic properties[218]. BE tuning to CdS material incorporated in the IO structure helped achieve the highest H_2 production of 3.5 $mmolh^{-1}g^{-1}$ by photocatalytic water splitting, which was much higher than that of RE tuning.

The above-mentioned experimental observations left two questions unanswered: i. how do slow photons at blue edge enhance light absorption despite being localized in the lower dielectric medium (void medium surrounding the photoactive IO matrix material)? ii. Given that some reported RE tuning to be more effective while others reported BE tuning to be more effective, which strategy is to be adopted in photocatalytic applications?

To address the first question, Deparis *et al.*[89] initiated a theoretical study of light absorption and photocurrent enhancement in high dielectric (red) and low dielectric (blue) regions of inverse opal TiO_2 using Rigorous Coupled Wave Analysis (RCWA) simulations. Initially, the study in a 1D Bragg reflector of TiO_2 and air revealed that blue edge tuning also resulted in absorption enhancement despite light being localized in the voids. The study was then extended to both non-connected porous and interconnected porous 3D inverse opal TiO_2 which led to similar observations of absorption and photocurrent increase in blue edge-tuned conditions.

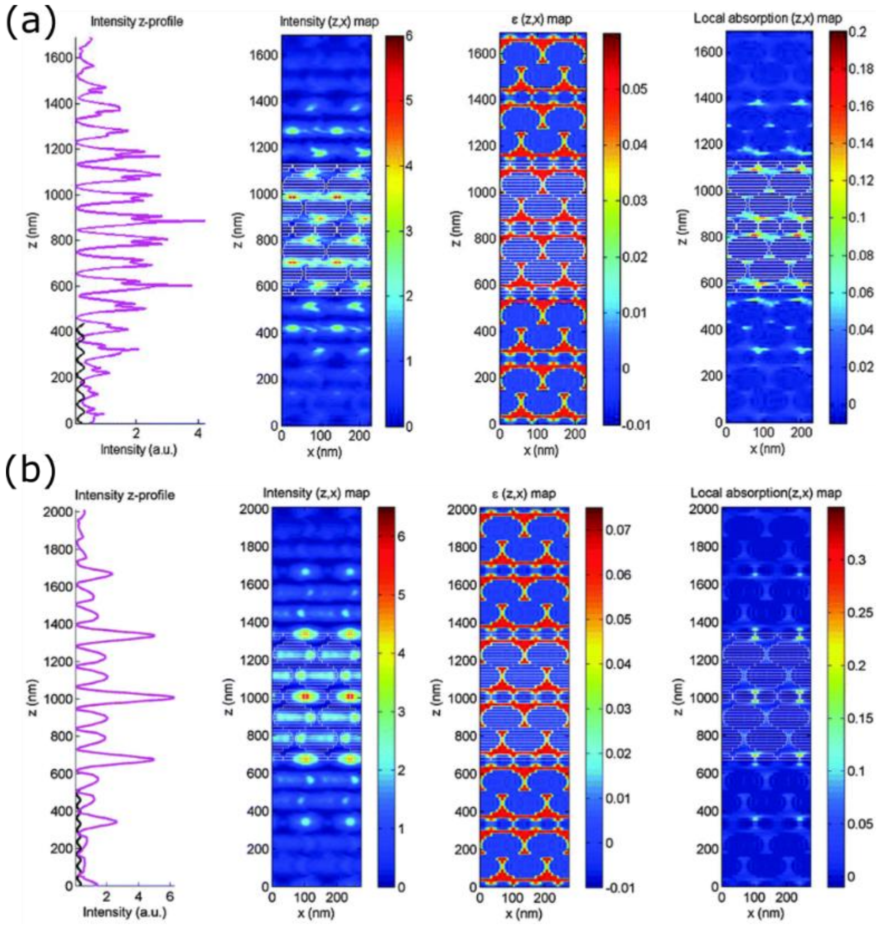

Fig. 1.20: Computed field tomography in inverse opals under **(a)** red edge and **(b)** blue edge tuning conditions showing the intensity z-profiles at the centre of the unit cell (represented by magenta curves) and the *x, z* cross section maps of field intensity, imaginary part of dielectric constant, and local absorption in a close-packed inverse opal slab (represented respectively by the three field maps from left to right in each case) with lattice parameter D = 115 nm in the case of red edge tuning (a) and D = 137 nm in the case of blue edge tuning (b) (ref[89]).

The reasoning was based on computed field tomography in inverse opals **(Fig. 1.20)**. Since TiO_2 and void regions are of subwavelength size, localized electromagnetic fields of both red edge and blue are loosely confined in the respective material and void regions. As a result, there is a significant overlap of the field confined in the voids with the TiO_2 material in the blue edge tuned sample, causing absorption enhancement. The same principle applies to the case of RE tuning wherein the loosely confined field in the IO matrix material overlaps with the void region. This explanation confirmed by analysis of light intensity maps justified absorption and activity enhancement by blue edge slow photons. The second question, however, remains unanswered, as it calls for more systematic and comparative experimental studies.

1.2.3.2. Varying light incidence angle to tune slow photons

As discussed earlier, variation of incidence angle is one of the parameters that can be employed to tune slow photon wavelengths to the electronic absorption of the photoactive material. More importantly, this parameter was used as a strategy to unambiguously attribute the increase in photoactivity to slow photon assistance. The underlying principle is that an increase in light incidence angle (with respect to the normal of the exposed plane of the IO structure) shifts the pPBG and slow photon spectral positions to lower wavelengths, thereby changing the tuning conditions and causing a variation in photoactivity. In contrast, the activities of both disordered porous structures and non-structured counterparts do not vary with light incidence angle, as they do not exhibit photonic properties. The advantage of this strategy is that it involves the comparison of activities of the same sample at varying incidence angles, as opposed to the previous strategy of lattice parameter variation that involves comparison of activities among different samples.

As a strategy, it was employed in very few research works, as it requires a more sophisticated experimental set up[200] for the accurate determination of both angle-resolved reflectance and angle-dependent photoactivity. The first implementation of this strategy can be found in the seminal work described earlier[189]. Later, it was employed in the solid-state photodegradation of crystal violet on IO Fe_2O_3 under monochromatic irradiation[219]. The claim of slow photon assistance was justified by demonstrating the variation in photocatalytic enhancement factors with light incidence angle (1.44, 1.31 and 1.63 EF compared to nc-Fe_2O_3 at 0^o, 34^o and 45^o respectively), caused by the spectral shift of slow photons that changed the tuning conditions. A similar strategy was later employed to justify slow photon assistance in the photodegradation of salicylic acid using IO Bi_2WO_6 under visible irradiation[220]. In both the above examples, pPBG spectral positions were estimated from Bragg's law and not experimentally measured to correlate the photocatalytic activities with the tuning of slow photons to the electronic absorption of the photoactive material.

A more systematic study based on experimental measurements of angle-resolved pPBG spectral positions was later carried out by Su's group on IO TiO_2 for the angle-dependent photodegradation of RhB[169]. Different from the previous work that tested angle-dependent activity for the solid phase photodegradation of MB on IO TiO_2[189], they tested SPE under more real-time industrially relevant conditions, namely in liquid phase photodegradation under UV-Vis irradiation.

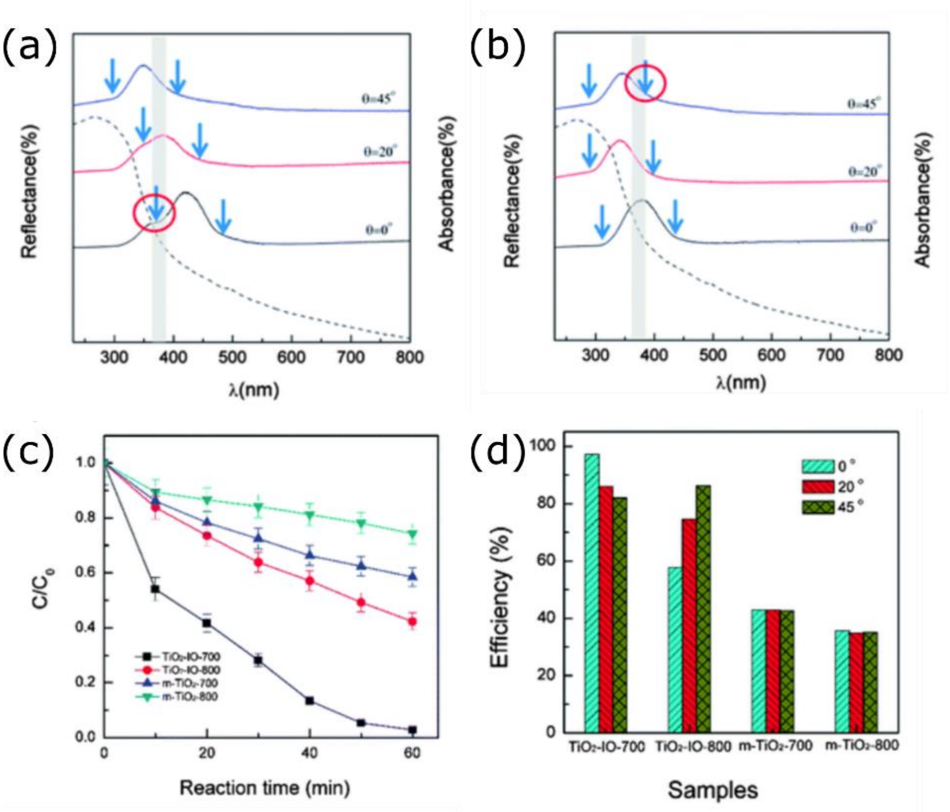

Fig. 1.21: (a-b) Reflectance spectra at $\theta = 0$, 20, 45° light incidence angles of IO TiO_2 with (a) 185 nm pore diameter, and (b) 165 nm pore diameter. The shaded region indicates TiO_2 electronic absorption band, while the arrows indicate the positions of red and blue edge slow photons. The dotted line indicates TiO_2 absorbance spectrum; **(c)** photodegradation of TiO_2-IO-700 (185 nm pore diameter), TiO_2-IO-800 (165 nm pore diameter) and the corresponding mesoporous TiO_2 films at $\theta = 0°$ light incidence angle; **(d)** Variation of photodegradation activity over the same samples at $\theta = 0$, 20, 45° light incidence angle variation[169].

Two samples with 165 and 185 nm pore sizes were tested for photocatalytic activity under 0, 20 and 45° light incidence angles. At 0° incidence angle, the 185 nm sample showed the highest activity due to BE slow photon tuning while the 165 nm sample showed the least activity due to pPBG tuning condition. This order of activity was reversed at 45° incidence angle due to BE slow photon tuning in 165 nm sample and pPBG peak tuning in 185 nm sample (**Fig. 1.21**). These results were justified by theoretical simulations involving the RCWA method. In a subsequent work[221], they extended their testing to include more samples that permitted a more elaborate and detailed study of the competing effects of pPBG reflection losses and slow photon enhancement. The same approach was later extended to IO ZnO for RhB photodegradation under UV-Vis irradiation[208], along with an additional discussion on the impact of slow photon at the edges of the second-order pPBG on angle-dependent photocatalytic activity.

Significant studies were also done by Curti *et al*. on the correlation between angle-dependent photonic properties and photoactivities[200, 222], in an attempt to justify SPE and to experimentally treat the 'underexplored questions' in slow photon-assisted photocatalysis that they discussed in their earlier perspective article[223]. In their initial work[222], they tried to single out SPE from other contributing factors like surface area, rugosity and mass transport, by studying the impact of lattice parameter and incidence angle variations on IO TiO_2 photocatalysis for both aqueous phase MB degradation and gas-phase acetaldehyde degradation under UV and monochromatic visible irradiation. Isolating SPE was facilitated by comparing the activities of structured IO samples with the disordered sample (prepared by templating mixed colloid sizes) that had comparable interconnected porosity and surface area. This was also achieved by testing SPE under gas-phase photodegradation wherein the impact of other contributing factors is relatively minimized. In a later work, they conducted exclusive studies on angle-dependency in slow photon-assisted photocatalytic degradation of stearic acid over IO TiO_2[200]. Light incidence angles were varied accurately using a self-made goniometer to channel light from an LED light source. Angle-dependent activity over a series of angles revealed that the BE tuning condition obtained at 40° light incidence produced the highest activity, 1.8 times higher than the reference IO disordered sample.

Variation of photoactivity with incidence angle was also recently tested in an opal system involving brush-particle polystyrene-SiO_2 opal PC for photothermal conversion under laser irradiation (~532 nm)[224]. The sample with 318 nm core-to-core distance showed a decreasing trend in absorption enhancement with increasing incidence angle (15, 20, 25°) due to BE slow photons tuned away from irradiation wavelength, while the 246 nm sample showed an increasing trend due to RE slow photons tuned towards irradiation wavelength. The impact of increase in the optical path length of light in the material with increase in incidence angle over photoactivity was overruled and considered as negligible as the 163 nm sample did not show any trend with change in incidence angle, which should have been otherwise if optical path length were to be the dominant effect. Although employing incidence angle variation to test angle-dependent photoactivity is technically challenging, especially in aqueous phase conditions, this strategy continues to be an effective and reliable strategy to validate SPE.

1.2.3.3. Varying incident light wavelength to justify slow photon effect

The principle underlying this strategy is that slow photons can be utilized only if the wavelength of light irradiation span the slow photon wavelengths and the electronic absorption of the photoactive material[51]. Thus, the impact of varying irradiation wavelengths is like that of an on/off switch for slow photon assistance in light harvesting applications. Just as in the case of the previous strategy, this strategy serves to justify SPE, as varying irradiation wavelengths (UV, Visible, UV-Vis and single/multiple monochromatic irradiations), varies the photoactivity, thereby confirming slow photon assistance.

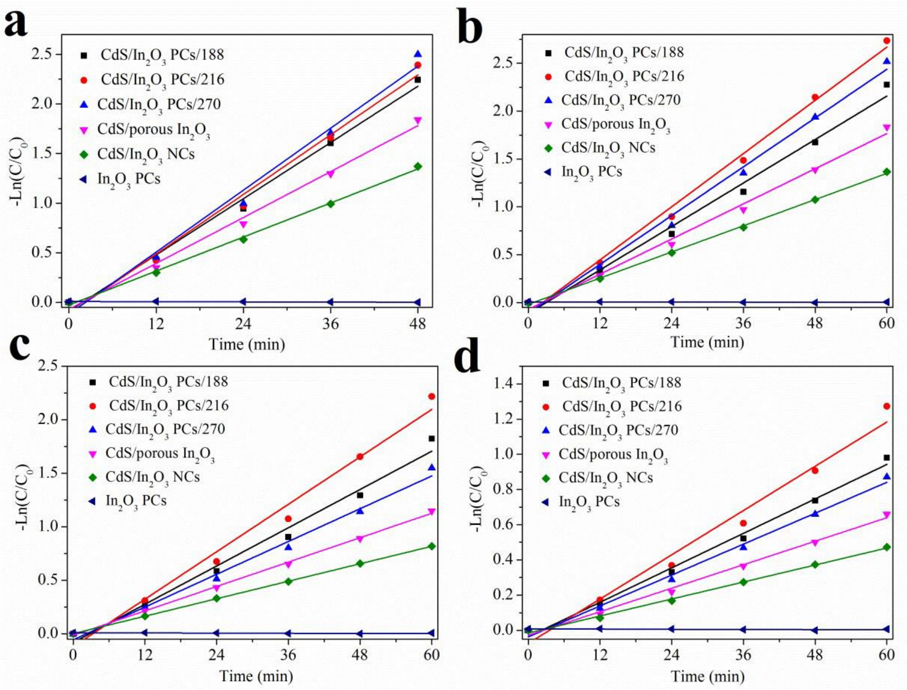

Fig. 1.22: Photocatalytic efficiencies of IO In_2O_3-CdS samples with 188, 216, 270 nm pore diameters compared with porous In_2O_3-CdS, NC In_2O_3-CdS and IO In_2O_3 at monochromatic irradiation of **(a)** 400 nm, **(b)** 420 nm**, (c)** 450 nm, and **(d)** 475 nm.

The most employed approach to categorically prove SPE was to compare photoactivities under multiple monochromatic sources using either a single sample or multiple samples (with varying lattice parameters)[189, 199, 200, 204, 222]. One such example is the work involving the photocatalytic hydrogenation of 4-nitroaniline to *p*-phenylenediamine over IO In_2O_3-CdS under visible and multiple monochromatic irradiations[225] (**Fig. 1.22)**. Three samples with pore sizes 188, 216 and

270 nm were tested under ~400, 420, 450 and 475 nm irradiation wavelengths. Under 400 nm irradiation, the variation in activity was limited, which was attributed to the change in pore size. However, at 420, 450 and 475 nm irradiation, the activity of 216 nm sample exceeded that of 270 nm sample due to irradiation wavelength matching the BE slow photons that overlapped CdS absorption. Similarly, at 450 and 475 nm irradiation, the activity of 188 nm sample also exceeded that of 270 nm sample due to irradiation wavelength matching the RE slow photons. The activity of 270 nm sample, despite having slow photons in the vicinity of CdS absorption region, could not exploit them as the irradiation wavelength was outside the suitable range.

In yet another work, photocatalytic water-splitting activities of three different IO $SrTiO_3$-Au-CdS samples (colloid template sizes 200, 300 and 400 nm) were compared under polychromatic irradiation and multiple monochromatic light sources (435, 475, 550 and 578 nm)[226]. The 300 nm templated sample, which showed the highest activity under polychromatic irradiation, and monochromatic irradiations of 435 nm and 475 nm due to irradiation wavelength-slow photon wavelength overlap, showed a drastic decrease in activity under 550 and 578 nm irradiations, which were beyond the slow photon wavelength range. In addition, under 550 and 578 nm monochromatic sources, the 400 nm templated sample showed slightly higher activity than the other two samples due to the matching of irradiation wavelength with slow photon spectral regions. These results were used to undeniably establish the role of slow photons in photocatalytic enhancement.

A similar deployment of the strategy of varying irradiation wavelengths to prove SPE can be found in other works like those involving opaline ZnO PC film for the photoreduction of CO_2[227], IO TiO_2-nanographene oxide films for surface-enhanced Raman Scattering (SERS)[228], hydrogen-treated IO TiO_2-Au for photocatalytic water splitting[229] and more recently IO CdS for photocatalytic hydrogen generation[203].

It can be deduced from the above works that comparing photoactivities under varying incident light wavelengths can serve as a reliable strategy to prove the assistance of slow photons in light harvesting applications. Its reliability stems from the fact that SPE can be studied independently of other interfering factors like pPBG reflection. It can also be an effective method in real-time applications involving the usage of monochromatic light source, that permits the choice of either the suitable light source or the suitable pore size sample to attain optimal photoactivity.

1.2.3.4. Tuning electronic absorption to incident light wavelength

When an absorbing material is chosen such that, its absorption falls within the spectral range of slow photons, enhanced photocatalytic activity can be expected compared to that of the material whose absorption lies outside the slow photon range. This strategy of testing the activities of various photoactive materials (with varying absorption ranges), under the same irradiation conditions, has been effectively employed in some research works to demonstrate the role of slow photons in enhancing light harvesting.

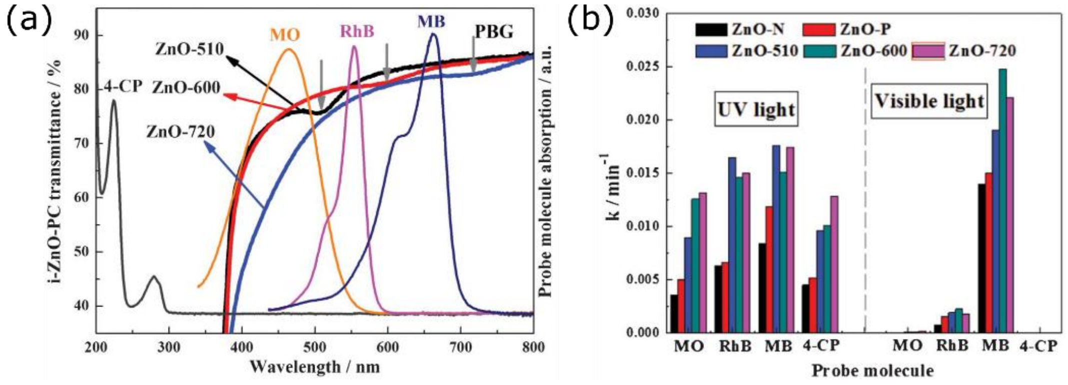

Fig. 1.22: (a) The transmittance peaks of three IO ZnO samples with pPBG peaks at 510, 600, 720 nm superimposed with the absorption peaks of methyl orange (MO), rhodamine B (RhB), methylene blue (MB) and 4-chlorophenol (4-CP) probe molecules, to show correlation between the slow photon spectral positions and the dye absorption; **(b)** the activities of the three IO ZnO samples for the photodegradation of each of the dyes, under UV light and visible light[230].

In a typical work involving dye-sensitized photocatalytic degradation, four common polluting dyes (MO, RhB, MB, 4-CP) having different absorption peaks (~464, 554, 664, and 225/280 nm respectively) were tested for photocatalytic degradation over three IO ZnO samples with varying pore diameters (pPBG peaks at 510, 600, 720nm) (**Fig.1.22)**[230]. Testing was done under both UV irradiation, wherein ZnO was the photoactive component, and under visible irradiation, wherein the reactant dye molecule was the photoactive component. MO and 4-CP, being anionic dye molecules, are poorly adsorbed on IO ZnO, resulting in poor photodegradation. The degradation of MB and RhB dye molecules with high adsorption capacity varied significantly with the sample and irradiation wavelength. IO ZnO-600 sample showed the highest activity under visible irradiation as MB absorption peak and RhB absorption peak overlapped with RE and BE slow photon wavelengths respectively. However, the activity of the same sample under UV irradiation was the least due to the absence of dye sensitization. A similar work involving the same dyes, with the exception of 4-CP being replaced with BA (absorption peak at 225 nm), can be found in the work on IO TiO_2 under simulated solar light and visible light irradiation, which led to similar conclusions[231]. Results from the above works indicate that the strategy of varying the probe molecules and irradiation wavelengths can not only be used to optimize photoactivity but also to justify slow photon assistance.

It is to be noted, from the above examples, that both the IO material and the reactant dye molecule can play an active role in light harvesting. To avoid interfering factors and to study slow photon effect of the IO material independently of the dye sensitization effect, probe molecules that are non-responsive under the chosen irradiation wavelength were selected and tested. For instance, in the photodegradation of RhB over IO ZnO-Au under visible light[217], 4-CP was chosen as an additional probe molecule as it is responsive only in the UV region. In this case the slow photons were tuned to the surface plasmon resonance (SPR) of Au nanoparticles to prove that the enhancement was due to SPE and not due to dye sensitization. With the same objective, salicylic acid which is a non-absorbing pollutant, was also used as a probe molecule in some works such as SPE-assisted photocatalysis over IO TiO_2-CoOx under visible light[232] and that over IO TiO_2-graphene quantum dot under UV-Vis and visible irradiation[207].

This strategy of changing probe molecules was also applied in the slow photon-assisted enhancement of fluorescence of dye molecules complexed with cucurbit[7]uril (CB7), supported on a polystyrene (PS) colloidal photonic crystal[233]. In the case of RhB, the fluorescence enhancement factor was 150-fold as the excitation and emission wavelengths of the dye were within the pPBG edges of the colloidal PC, while in the case of MB, the EF was nearly negligible as the excitation and emission wavelengths of the dye were away from the pPBG edges of the colloidal PC.

1.2.3.5. Using slow photons from non-absorbing photonic material

IO photonic structures that are non-responsive in the desired wavelength range were scarcely used in photoconversion applications, as the use of absorbing materials moulded into IO structures could be more beneficial for light harvesting. However, this strategy was employed to have a better understanding of slow photon assistance by separating the slow photon generating component and the light harvesting component in composite systems. Also, in this case, light harvesting enhancement can be studied independently of other porosity-related benefits like increase in mass transport and surface area[234, 235] or increase in conductivity and charge separation especially in photoelectrochemical (PEC) conversions[236, 237].

The role of a non-absorbing IO structure as a 'photonic support' providing slow photon assistance was suggested and discussed in a few cases like those involving IO SiO_2-CdS Q dots for photodegradation of carbamazepine (CBZ) organic pollutant under visible light[238] and IO SnO_2-WO_3 for PEC conversion under one sun conditions[239]. However, in both these cases, the role of SPE was not adequately justified.

A detailed study was conducted on a photochemically inert IO ZrO_2 photonic structure supporting photoactive CdS NPs for photocatalytic water splitting under visible light irradiation[211]. Four IO ZrO_2 samples were synthesized with different pore sizes (165, 255, 270, 320 nm) to tune the slow photons to CdS absorption (~520 nm). In the case of 255 nm sample the blue edge slow photons were found to overlap with the EA of CdS, which explained the highest H_2 production, 4.7 times higher than CdS NPs deposited on a non-photonic support. Enhancement of H_2 production on other samples was lower, as the slow photons of 165 nm sample were confined to the UV-region while those of 270 and 320 nm samples were away from CdS absorption. To attribute the highest EF in 255 nm sample to slow photon enhancement, additional experiments were conducted by replacing CdS nanoparticles with nc-TiO_2. In this case, there was no significant difference in activity between the samples, as the absorption of TiO_2 (UV-region) was away from both slow photon and irradiation wavelength (visible light).

1.2.3.6. Synergizing slow photon effect with surface plasmon resonance

Localized Surface Plasmon Resonance LSPR is the collective oscillation of electric charges (collective electron oscillations) observed when light interacts with metal NPs whose size is less than or comparable to the wavelength of light[40]. This charge oscillation generates an electric field localized on the metal NP, that enhances broadband visible light absorption reaching a maximum under resonant frequency conditions[41]. This light-manipulating property can be exploited either to assist photochemical transformations on the surface of the metal NP[42] or to increase light absorption of another material coupled to the metal NP. When coupled with a semiconductor photocatalyst, for instance, LSPR-sensitization of metal NPs enhances light absorption of the photocatalyst through amplification of local electric field and excitation of active charge carriers[43, 44]. When plasmonic metal NPs are coupled with a photonic crystal, a synergy between SPE and

LSPR can be created. The reduction in group velocity of light by the PC can amplify the LSPR of the plasmonic metal NPs (under proper tuning conditions), which in turn can enhance the light harvesting potential of the photoactive material[240-243] (**Fig. 1.24**). The key to realizing this synergy lies in tuning the slow photon wavelengths to the LSPR frequency of metal NPs.

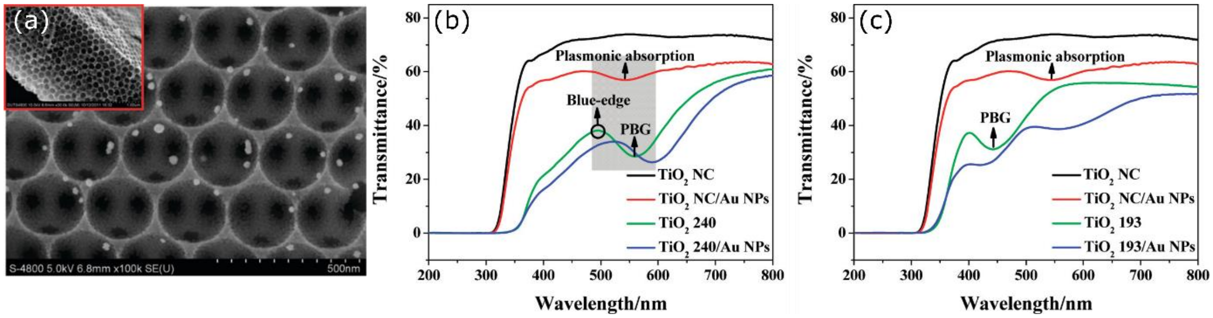

Fig. 1.23: (a) SEM images of IO TiO_2 (prepared from 240 nm PS colloids) loaded with Au nanoparticles; **(b-c)** transmittance spectra of IO TiO_2-Au synthesized using (b) 240 nm PS colloids and (c) 193 nm colloids. The shaded region in (b) represents the plasmonic absorption of Au NPs. In the case of (b), blue edge slow photons overlap with Au plasmonic absorption whereas in (c), slow photons are far away from Au plasmonic absorption[209].

The strategy of integrating plasmonic NPs into IO structures for light harvesting applications was employed initially to realize the synergy between IO porosity-related benefits and LSPR[244-248]. The synergy between SPE and LSPR was claimed in some later works without experimental validation of synergistic effects[249]. One of the first works that demonstrated this synergistic strategy was that on IO TiO_2-Au for the photodegradation of 2,4-dichlorophenol under visible light, which resulted in 2.3 times increase in activity compared to that of NC-TiO_2-Au[209]. Among the two samples prepared with different pore sizes and distinct pPBG spectral positions, the one whose BE of pPBG (~ 493 nm) was within the absorption range of Au NPs showed the highest activity, thereby confirming the synergy between SPE and LSPR (**Fig. 1.23**). Similar results were reported for PEC water splitting over IO TiO_2-Au under simulated sunlight illumination that resulted in the highest photoconversion efficiency under RE tuning conditions[206], and over IO SnO_2-Au-$BiVO_4$ under simulated solar irradiation that resulted in a 3-fold higher IPCE than that of planar $BiVO_4$ under BE tuning conditions[250]. In a subsequent work, both RE and BE tuning conditions were tested on IO ZnO-Au by lattice parameter variation for the photodegradation of RhB and 4-CP under visible light[217], with BE tuning condition yielding better enhancement than RE tuning condition, which was 24.8 times higher than that of ZnO NPs.

In all the above cases, slow photons were tuned to the LSPR absorption range of Au NPs, but in some cases, tuning was realized relative to the semiconductor photocatalyst absorption, as in the case of IO TiO_2-Au-CdS where slow photons were tuned to TiO_2 absorption to achieve maximum efficiency for photocatalytic reduction of CO_2 under UV-Vis irradiation[251]. Tuning of slow photons to both the semiconductor absorption and LSPR frequencies was also probed for photocatalytic H_2 production over N,F doped-IO TiO_2-Au-Pt[252] and a higher H_2 production was observed for slow photon tuning with Au LSPR (134 $mmolh^{-1}g^{-1}$) compared to the tuning with TiO_2 absorption (97 $mmolh^{-1}g^{-1}$).

More recently, a synergy between SPE and LSPR was realized for the first time in a perovskite solar cell (PSC) of IO $CsPbBr_3$ coupled with Au nanoparticles[253]. Careful tuning of RE slow photons of the PC to the SPR region of Au NPs enhanced light harvesting efficiency, resulting in a high photoelectric conversion efficiency of 8.08%, an increased short-circuit current density (J_{sc}) of 8.40 $mAcm^{-2}$ and a circuit voltage (V_{oc}) of 1.30V. Besides providing the synergistic enhancement of light harvesting, Au NPs also provided a Schottky barrier and reduced the exciton binding energy from 53.5 to 32.9 meV, which promoted charge generation and separation.

1.2.3.7. Generating slow photons at multiple spectral ranges

The Achilles heel in slow photon-assisted light harvesting, as discussed earlier, is the narrow spectral range that delimits light harvesting enhancement. According to a theoretical study based on Scalar Wave Approximation (SWA)[189], a maximum of 2.1 light enhancement factor can be attained, which is calculated as the ratio between the group velocity of light in nc-TiO_2 to that in IO TiO_2 of the same thickness. A strategy to overcome this spectral limitation is to generate pPBG peaks and slow photons at multiple spectral regions, by fabricating stacked/layered photonic structures with each layer having a different lattice parameter.

Fabricating such structures involves the usage of templating colloids of different sizes, periodically assembled and stacked one over the other, as seen in the premier work involving SiO_2 colloids of different sizes stacked into layers, with each layer retaining its distinctive pPBG[254]. Subsequently, different methods were developed to synthesize multiple band gap structures by repeating either the two-step colloidal assembly-infiltration process[255] or the one-step coassembly process[256], followed by template removal to obtain stacked IO structures. The same methods were also employed to create stacked structures either with each layer having a different material[257] or with each layer of the same material having a different filling fraction [258]. The resulting difference in effective RI of each layer resulted in either the broadening of pPBG due to the additive effect of individual pPBGs or the manifestation of multiple pPBGs.

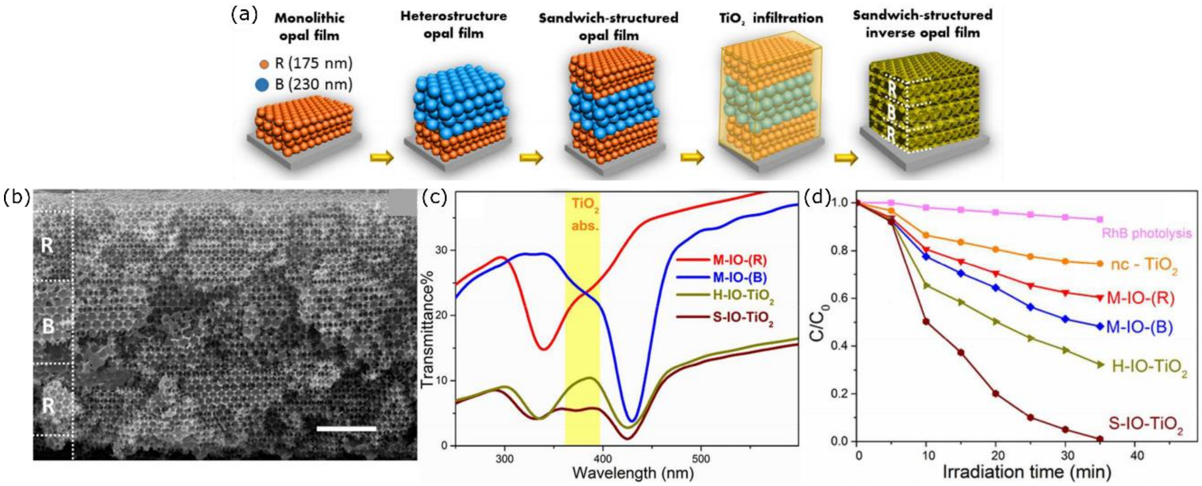

Fig. 1.24: (a) Schematic representation of sandwich structured multi-layer IO TiO2 structure with top and bottom layer having 175 nm pore size (R) and the middle layer having 230 nm pore size (B); **(b)** cross-section SEM image of the sandwich structure (scale bar is 1 µm); **(c)** UV-Visible transmission spectra of single layer structures R and B, bilayer structure R-B, and sandwich structure R-B-R; **(d)** photocatalytic RhB degradation of monolayer, bilayer and trilayer IO TiO_2 structures[259].

Although considerable progress was made regarding synthesis methods, it was not until recently that such structures were tested for various applications such as information encryption[260, 261], anticounterfeiting in both layered opal[262] and layered inverse opal structures[263] and for electrochromic applications[264]. Regarding energy conversion applications, it was initiated in the work on IO TiO_2 multimodal layered structure for RhB degradation under UV-Vis irradiation[259]. A three-layered sandwich IO TiO_2 structure was prepared using colloids of two different sizes arranged in the configuration PS 175 nm-PS 230 nm-PS 175 nm (**Fig. 1.24**). The base layer was prepared by horizontal deposition of colloids on a substrate followed by backfilling with TiO_2 precursor, while the successive layers were stacked by doctor blading method. The top and bottom layers manifested a pPBG at 346 nm with RE slow photons overlapping TiO_2 absorption region while the middle layer manifested a pPBG at 432 nm with BE slow photons overlapping TiO_2 absorption. In addition, the middle layer of the sandwich structure trapped both light transmitted by the top layer and light reflected by the bottom layer. As a result of the utilization of both blue and red edge slow photons and the added advantage of light trapping, the structure exhibited a 4-

fold increase in RhB degradation and a 5-fold increase in photocurrent density. This strategy was also employed in non-IO structures as in dual band gap opal SiO_2 composited with nc-TiO_2 and sensitized with CdS Q-dots for gas-phase photodegradation of acetaldehyde under white light irradiation[265] and in dual band gap anodic aluminium oxide nanoarray photonic structure towards SERS activity for RhB detection[266].

Practical application of the strategy of using multi-spectral slow photons in layered/stacked photonic structures is easier said than done. Two major challenges are encountered while employing this strategy. The first concerns the synthesis of highly ordered structures that manifest distinct pPBGs and slow photons at multiple spectral regions. Stacking of an ordered second layer on the first becomes complicated either due to the disorder of the first layer that is transmitted and accentuated in the second or due to the high hydrophobicity of the first colloid-material assembly, that prevents the adhesion of the second to the first. The latter difficulty was addressed in one of the works by treating the first layer with UV light[255] before depositing the second layer, to improve the hydrophilicity. Also, employing the coassembly method to fabricate layered photonic structures was found to yield more ordered structures with distinct pPBGs, as it reduced the number of steps involved, thereby reducing the degree of disorder[256]. The second challenge concerns the control of the positions of multi-spectral slow photons relative to the material absorption, particularly in aqueous phase, that is necessary to achieve optimal light harvesting. Although practically challenging, this strategy offers promising potential to further increase slow photon assistance in light harvesting applications.

1.2.3.8. Engineering photonic structure designs

Besides layered structures manifesting multiple pPBGs, other layered structures were also designed and tested for light harvesting enhancement, the most common among which is that of a photonic structure coupled with a NC layer. One of the earliest examples can be found in the work on IO TiO_2 coupled with nc-TiO_2 film to improve light harvesting efficiency in dye-sensitized electrodes[185]. As a result, a 26% enhancement in short circuit photocurrent efficiency across the visible spectrum was observed in this layered structure compared to that of dye-sensitized NC-TiO_2. This was attributed to the dual role of IO TiO_2 that not only slowed the group velocity of light at pPBG edges but also acted as a dielectric mirror to trap light. The same strategy was explored in other related works with a more profound discussion on the impact of photon resonant modes[188, 267], light scattering effects[186] and slow photon effect[268] in increasing light localization in the absorbing layer. Coupling the light absorbing layer with a photonic film was found to yield higher photocurrent efficiency than in the case of coupling with a perfect mirror[269], which confirmed the dual SPE and dielectric mirror effects operating in the layered structure. Besides being coupled with a NC-film, IO TiO_2 was also coupled with a mesoporous TiO_2 film in a DSSC to benefit not only from slow photon assistance but also from interconnected porosity between the two layers that facilitated electrolyte infiltration and charge mobility[270].

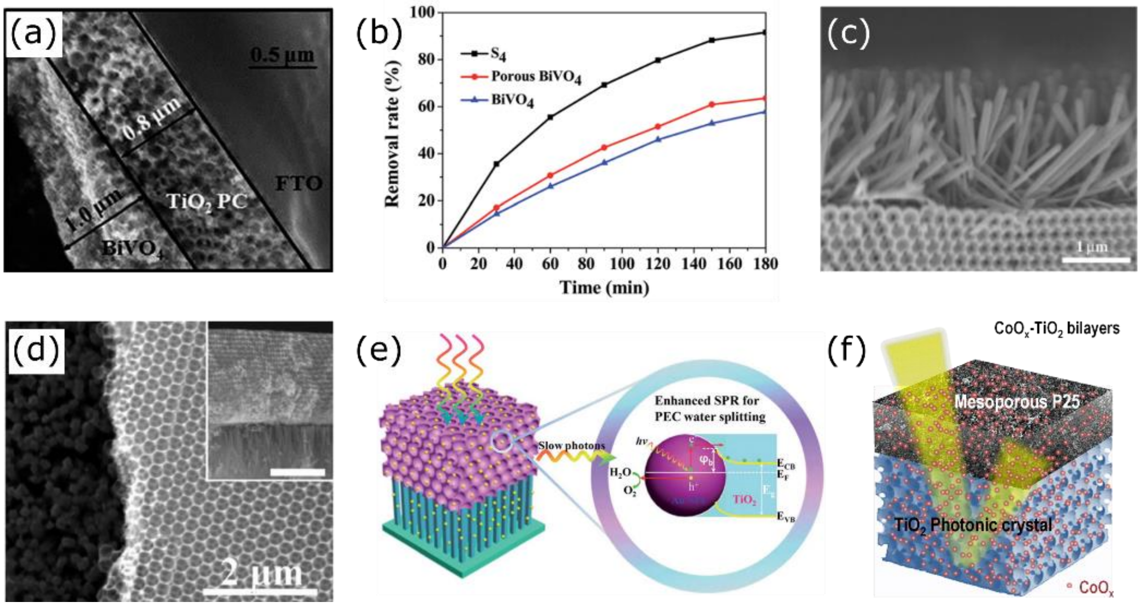

Fig. 1.25: **(a)** Cross-section SEM image of IO TiO_2 layer with NC $BiVO_4$ layer on the top, and **(b)** photocatalytic MB degradation of the above sample in comparison with the activities of porous $BiVO_4$ and $BiVO_4$ films[271]; **(c)** Cross-section SEM image of ZnO nanowire arrays grown over IO TiO_2 structure, that resulted in enhanced PEC response[272]; **(d)** IO TiO_2 grown over TiO_2 nanorods and sensitized with Au NPs, and **(e)** schematic representation of the synergy between SPE and SPR in the above system for enhanced PEC water splitting[206]; **(f)** schematic representation of light harvesting in P25 (commercial TiO_2) deposited over IO TiO_2 and sensitized with CoO_x NPs[273].

The strategy of coupling a photonic layer with a light absorbing layer, which was initially applied in DSSC, was also applied in photocatalysis with great success. One of the early works was on nc-TiO_2/IO SnO_2 composite (the first being the top layer and the second being the bottom layer), where the photoactive TiO_2 layer harvested both the pPBG reflected light and the slow photons generated from IO SnO_2 for enhanced photodegradation of MO under UV light[274], and that of RhB under white light[275]. In these works of the same research group, which was later tested by them over opal SiO_2 photonic layer for acetaldehyde degradation[276], the pPBG reflection of the PC layer was designed to overlap with TiO_2 absorption, such that light reflected by the bottom PC layer was absorbed by the top NC-TiO_2 layer, while the localized slow photons were harvested at the interface between the two layers. The efficacity of this bilayer design was also tested under visible light irradiation over porous $BiVO_4$/IO TiO_2 composite for MB degradation, and the enhanced activity was attributed to the IO photonic layer acting as a back reflector[271] (**Fig. 1.25 (a-b)**).

With the principles of light harvesting enhancement in NC (porous)/IO PC layered designs clearly laid out, other structures involving the coupling with IO PCs were engineered and tested. For instance, a composite structure of ZnO nanowire arrays (NA) grown on IO TiO_2, and later sensitized with CdS Q-dots, was tested as photoanode for photoelectrochemical conversion[272] (**Fig. 1.25 (c)**). The photocurrent enhancement observed was attributed to simultaneous 'electrical and optical coupling' between the two layers. In this case, SPE was investigated by studying the variation in photocurrent and incident photon to electron conversion efficiency (IPCE) by varying pore size of the IO PC to tune slow photon wavelengths to CdS absorption.

Another rational design, exactly opposite to the above, was designed with the growth of IO TiO_2 over TiO_2 nanorod arrays, and later sensitized with Au NPs before testing for slow photon-assisted photoelectrochemical water splitting efficiency[206] ((**Fig. 1.25 (d-e)**). By varying the pore size to tune red edge slow photons to SPR spectral region of Au NPs, a significantly high 0.71% photoconversion efficiency was obtained. A similar study of SPE in this type of layered design was conducted over mesoporous P25/IO TiO_2 sensitized with CoO_x clusters for the photodegradation of salicylic acid under visible and UV-Vis irradiation[273] (**Fig. 1.25 (f)**). Slow photon wavelengths were tuned to CoO_x absorption range by lattice parameter variation to obtain optimal enhancement of photoactivity. More recently, this strategy was successfully adopted, albeit with the reversal of the position of IO layer, over IO TiO_2/NC-Mo-doped $BiVO_4$ for PEC water splitting efficiency[277]. A twofold increase in photon-to-electron conversion efficiency compared to the non-photonic counterpart was observed in the samples whose slow photons at pPBG edges were tuned to the electronic absorption of $BiVO_4$, which justified the role of slow photons in enhancing light harvesting.

As a strategy to improve light harvesting, the rational design of coupling an absorbing material layer to a light-manipulating PC was demonstrated to be highly rewarding. However, a decisive factor that needs to be considered while applying this strategy is the thickness of each layer. If the thickness of the top layer exceeds a critical light penetration depth, then the intended impact of the bottom layer would be minimized or completely absent[271, 273]. Additionally, increase in thickness could amplify the diametrically opposing effect of reduced charge carrier transport[206, 277], besides inducing greater disorder in the IO photonic structure that is detrimental to the photonic properties. Hence, employing this strategy requires a calculated control of thickness of each layer for optimal light harvesting enhancement.

1.2.3.9. Exploiting slow light in particulate form inverse opals

Slow photon assistance in light harvesting applications was more often demonstrated in photonic structures rendered as films rather than in those rendered as particulate/powder photoactive materials. The reason for this is that, in the case of IO films, the pPBG manifested is usually distinct and unique, as the [111] crystallographic plane of the PC parallel to the surface of the substrate (in the entropically favoured *fcc* arrangement) is usually the only plane exposed to incident light[278]. As a result, slow photons are located at precise and desired wavelengths, that permits their tuning and exploitation for light harvesting and enables the adequate justification of SPE.

By contrast, in IO powders, owing to the random orientation of crystals planes relative to incident light, multiple pPBG's emanating from odd or even h, k, l value *fcc* planes like [111], [200], [220], [311], could be manifested, as demonstrated by Schroeden *et al*. over IO TiO_2, SiO_2 and ZrO_2 powders[279] (**Fig. 1.26 (a-d)**). Eliciting photonic properties in IO powders is not evident, as the limited size of ordered domains and the increased disorder could either result in an averaged manifestation of pPBG that is angle-independent[279] or the elimination of pPBG altogether[280, 281].

Despite this intrinsic difficulty, attempts were made to employ and elucidate SPE in IO powders. One of the earliest among them was the work on IO TiO_2 particulate form photocatalyst employed for the photodegradation of phenol under varying monochromatic irradiations[282]. Slow photon wavelengths at the edges of the manifested pPBG were tuned by lattice parameter variation and the justification of SPE was provided by the strategy of varying irradiation wavelengths. Further justification was provided by comparing the activity of the ordered sample with that of the crushed sample having similar porosity and specific surface area. Similar strategies were employed by the same group in yet another work involving IO TiO_2-Pt particulate photocatalyst for H_2 production under the same monochromatic irradiation conditions[283].

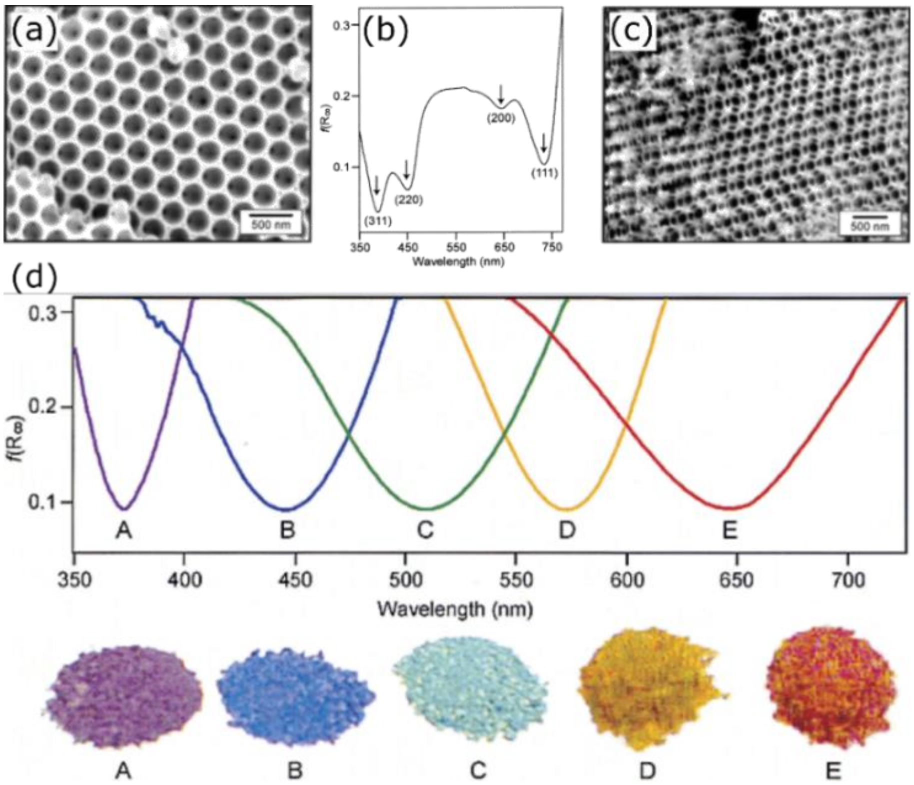

Fig. 1.26: Photonic properties of IO powders (particulate form): **(a-b)** SEM image of IO mercaptopropyl silica and the diffuse reflectance spectrum of the powder form showing peaks corresponding to the diffraction from [111], [200], [220], and [311] planes; **(c-d)** SEM image of IO zirconia and the diffuse reflectance of the powder form of samples A, B, C with 200, 250, and 285 nm pore sizes and those of D, E when B, C were filled with methanol.

Attempts to employ SPE in the particulate form of photonic structures were made in other subsequent works[93, 284], although the justification of SPE was not always adequate in some cases. In other cases, the precise spectral positions of pPBG and slow photons were determined on IO films but the photocatalytic tests were conducted on powders scraped from the substrate[285, 286]. Although relevant, this approach undermines the accuracy of interpretation as the spectral positions in film and particulate photonic structures are not necessarily the same.

Both films and powders were prepared and tested for slow assistance in a few cases, as in that of self-doped IO TiO_2 for Acid Orange 7 degradation under UV light[287] and in that of IO TiO_2 for gas-phase photooxidation of ethanol under UV light[202]. In the latter work, a two-fold increase in photocatalytic efficiency was reported on powders when the RE of the pPBG overlapped with TiO_2 absorption. Although photonic properties were determined on IO powders in this case, the authors added that slow photon assistance in an IO particulate system is to be moderately considered, as only a small fraction of the [111] planes will be exposed to incident light at normal angles, while other fractions will be irradiated at different angles.

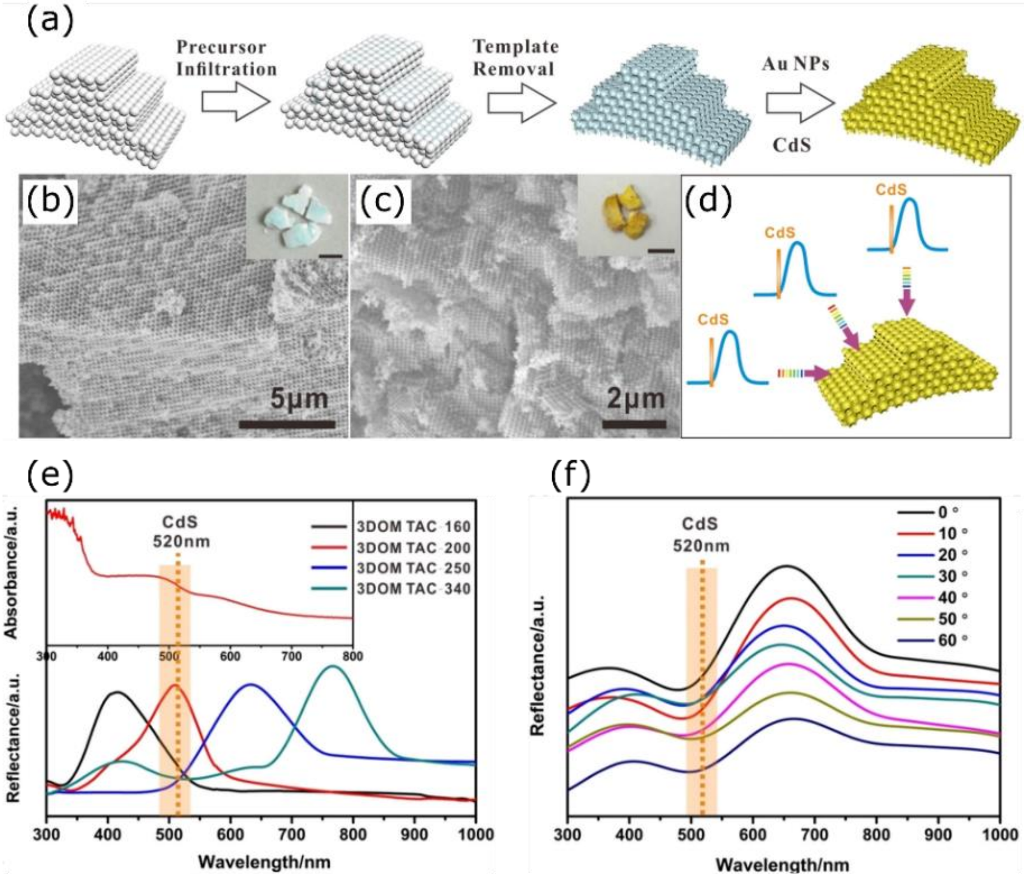

Fig. 1.27: (a) Schematic representation of the synthesis of cascading structure of the particulate form of IO TiO_2 and its sensitization with Au and CdS; **(b-c)** SEM images of IO TiO_2 (b) before modification with CdS and (c) after modification with CdS, showing bright structural colours (inset); **(d)** schematic representation of angle-independent photonic properties; **(e)** reflectance spectra of IO TiO_2-Au-CdS samples of different pore sizes, indicating distinct photonic properties; **(f)** reflectance spectra of 3DOM TAC 250 at different angles, indicating that SBG position does not change with light incidence angle[218].

To address this challenge, a carefully controlled gradient cascading structure of IO TiO_2 powder was synthesized in a more recent work, wherein the photonic structure possessed large domain size and exhibited angle-independent pPBG[218] (**Fig. 1.27**). After sensitizing with Au NPs and CdS, the system was tested for water splitting H_2 production under visible light over samples of varying diameter, with a maximum yield of 3.50 $mmolh^{-1}g^{-1}$ of H_2 over the sample with BE slow photons tuned to CdS absorption (3 DOM TAC 250 in **Fig. 1.27 (e)**). This work revealed that SPE can not only be efficiently employed in particulate form photonic systems but also be adequately justified.

Recently, SPE has also been demonstrated for water splitting O_2 production over particulate IO WO_3, where both RE slow photons tuned to the absorption edge of WO_3 and lattice defect engineering contributed to enhanced activity[288].

SPE in IO powders is more challenging to realize. However, it is more relevant given that industrial processes tend to rely more on particulate (powder) catalysis than film catalysis, although each approach has its specific advantages and disadvantages[289]. Also, IO powders offer other light manipulating properties like multiple scattering, the extent of which depends on the size of the powder grain. This multiple scattering leads to further interaction between propagating electromagnetic wave and the materials, increasing light absorption[290, 291].

1.2.3.10. Using spherical photonic structures

The most striking advantage of spherical inverse opals is the manifestation of angle-independent photonic properties[292, 293] that permits enhanced light harvesting from slow photons at the desired wavelength range, independent of light incidence angle. Spherical PCs are periodic structures rendered in the form of beads, in which the curvature of the bead with respect to incident light results in the display of angle-independent pPBG[294]. Spherical IO structures are derived from spherical opal templates that are formed from droplets usually generated by a microfluidic device[295]. The unique optical properties of spherical IOs were exploited in very few applications like biosensing[296, 297], although their opal counterparts were more extensively studied[298] and tested in wider range of applications like barcodes and displays[293].

In light harvesting applications, spherical IOs were employed for slow photon-assistance in very few cases, with the most recent being spherical IO TiO_2 for visible light MB degradation[299]. However, in this case, SPE was not demonstrated. The only work, to the best of my knowledge, that exclusively demonstrated SPE, was the work on spherical IO TiO_2, prepared by spray drying-assisted coassembly templating technique, and tested for MB photodegradation under UV light[300]. A maximum of 1.66 times higher activity relative to P25 under optimal conditions was reported, which was attributed to the synergistic effects of slow photons at pPBG edges and Mie scattering from the spherical particles. SPE was validated through experiments on five different samples with varying pore diameters and pPBG spectral positions. The results pointed out that the sample with RE slow photons tuned to TiO_2 absorption showed the highest activity, despite possessing comparatively lesser surface area.

Spherical IOs can be highly promising for slow photon assistance, especially in the form of particulate (powder) suspensions in aqueous phase photocatalysis. However, they remain underexplored mostly due to the challenges involved in synthesizing these structures.

1.2.3.11. Engineering defects to improve slow photon assistance

Defects in PCs are inevitable. In colloid-templated IO PCs, they could arise from any of the synthesis steps involving either materials or methods: colloidal size distribution, assembly methods and conditions, precursor properties and proportions, infiltration conditions, template removal and post-modification. This results in various types of imperfections that include point defects like vacancies, line defects like dislocations, planar defects like stacking faults and grain boundaries[301], and macro-defects like cracks[302]. Most of them are inherited from the templating opal structures[303, 304].

When defects occur in photonic structures, their optical properties are affected[290, 291]. This usually leads to the enlargement of the reflectance peak, the desaturation of the displayed colour, the decrease in the peak intensity, and possibly diffuse reflection. In addition, it could also provoke various types of light scattering effects[214], and an eventual deterioration of pPBG[280]. Numerical studies have revealed that the magnitude of disorder as low as 2% of the lattice constant in IO PCs can completely close the photonic band gap formation[280, 281] due to localized photonic states[305]. Various methods have been proposed not only to minimize disorder in IO structures[144], but also to engineer and introduce controlled disorder for achieving the desired functionality[306].

The presence of defects and disorders adversely affects not only the photonic properties but also the slow photon-assisted photoactivity. Although many studies were undertaken to study the impact of disorder on optical properties, very few qualified and quantified its impact on slow photon-assisted light harvesting. Among the few, the work by Chen *et. al.* on IO TiO_2 for MB degradation under visible light[307] stands out. Disorder in the IO PC was progressively increased by substituting monodisperse templating colloids with colloids of a different size. The resulting inverse opals, when tested for MB degradation, showed a retention of 50% of the EF relative to nc-TiO_2, even up to a threshold substitution fraction as high as 0.4 by guest spheres that were even 1.2 times the size of host spheres. It was thus concluded that although disorder impacts photonic properties and decreases photocatalytic activity, a certain limited disorder can be tolerated that still results in increased photocatalytic activity compared to non-IO structure that does not benefit from slow photon effect. Many later studies have reported a reduced activity among disordered structures compared to ordered structures, but without further deliberation.

A few important strategies for inverse opal photocatalysis can be deduced from the above studies. Firstly, to make optimal utilization of SPE for light harvesting enhancement, a high degree of order in the PC is highly desirable. This calls for an optimization of synthesis strategies, endorsed by theoretical studies on disorder formation and minimization. Secondly, given that disorder is a crucial factor in slow photon-assistance for light harvesting applications, more experimental and theoretical studies on the impact of disorder on SPE need to be undertaken. Thirdly, engineering of disorder, as in the case of ordering the formation of cracks in inverse opal PCs[302], can be further investigated to attain optimum optical gains.

1.2.3.12. Employing theoretical and simulation studies

The prediction of optical properties in photonic structures used for slow photon-enhanced photocatalytic applications is critical to their development. Although numerical simulations have been used to compute the optical behaviour of slow light in photonic structures for decades[90, 91, 308, 309], the scientific community seemed to have overlooked these possibilities, for a long time, and has only recently recognized the potential of these simulations[89, 169]. In many cases, enhanced photocatalytic activity was attributed to slow light without proper demonstration of this cause. However, numerical predictions have been used in a few cases to pinpoint the origin of such enhancement. Besides confirming the cause of enhanced photocatalytic activity, numerical studies can also throw light on the understanding of the underlying fundamental mechanisms[89], and may help to optimise the design of the photocatalyst structures[310, 311]. This optimisation by numerical tools saves time and resources in the design of efficient devices compared to the development by trial-and-error method in the laboratory. Moreover, it opens new avenues for exploration[311].

The typical optical quantities simulated for slow-photon enhanced photocatalysis are reflectance, transmittance and absorptance spectra[89, 169, 200] (the latter allows the calculation of maximum achievable photocurrent density and various enhancement factors), photonic band structures[89, 310, 311], Poynting vectors[310-312], as well as energy and field intensity maps[89, 310, 311].

The RCWA method[313-315] was used widely for numerical simulations in photonics and is probably the most popular method for slow-photon enhanced photocatalysis[89, 169, 200]. It is usually employed to compute reflectance, transmittance, and absorptance spectra, Poynting vectors as well as energy and field intensity maps. It solves Maxwell’s equations without any approximation. RCWA is based on Fourier series expansions of laterally periodic permittivity and the electromagnetic fields following the Bloch-Floquet theorem. Photonic band structures are typically computed using the Plane Wave Expansion (PWE) methods[316], which also solves Maxwell's equations exactly by formulating them as an eigenvalue problem. The Finite-Difference Time-Domain (FDTD) method is prevalent in the scientific literature for simulating field propagation, allowing the generation of field maps and spectra[317-320]. This method solves the space and time partial derivatives in Maxwell’s equations by discretising them through a finite-difference approximation. The Finite Element Method (FEM) is another useful tool for predicting electromagnetic field maps and spectra[321-324]. In this approximation method, the partial differential equations are solved by discretising the medium into small finite elements, imposing boundary conditions on a mesh.

A few experimental works on slow photon assistance in light harvesting applications made use of simulations to justify SPE. For instance, the slow photon assisted enhancement in the photodegradation of RhB in aqueous phase over IO TiO_2 PC fabricated on ~ 5 mm quartz substrate was demonstrated, thanks to RCWA simulations of reflectance spectra of the samples under different incidence angles[169]. Similarly, RCWA was also used to predict absorptance spectra in order to assess the origin of the enhancement of photocatalytic degradation of stearic acid in titania inverse opals[200]. In addition, the usefulness of optical simulations in this context was shown, to a further extent, when the light harvesting enhancement at the blue edge of photonic structures, including TiO_2 inverse opal, was explained by the overlap of the electromagnetic field of the slow light with the backbone/matrix of the photonic structure[89]. Furthermore, numerical methods were recently used to predict the conditions required for optimising photocatalytic activity in titania photonic structures nm[310]. These simulations revealed that higher-order 5th to 15th photonic bands increase efficiency. To have these bands active in the visible range, the studies predicted that the inverse-opal pore diameters should be increased to approximately 380 nm. Similarly, such simulations were also used to predict the optimal type of photonic structure that would yield the highest light harvesting potential for photocatalysis[311]. Four different TiO_2 photonic structures were studied, and it was concluded that the square lattice slanted conical-pore structure on a highly reflective substrate was the optimal configuration for high photocatalytic efficiency, compared to the inverse opal photonic structure on the same substrate.

References

1. Global energy perspective: Power outlook **2023**, McKinsey & Company, https://www.mckinsey.com/industries/oil-and-gas/our-insights/global-energy-perspective-2023-power-outlook
2. Statistical review of world energy, **2023**, 72nd edition, Energy Institute. https://www.energyinst.org/statistical-review
3. Breeze, P., *Power generation technologies*. Newnes: 2019.
4. Takanabe, K., Photocatalytic water splitting: fundamentals and current concepts. *Heterogeneous Photocatalysis: From Fundamentals to Applications in Energy Conversion and Depollution*, Wiley **2021**, 269-286.
5. Detz, R.; Reek, J.; Van Der Zwaan, B., The future of solar fuels: when could they become competitive? *Energy & Environmental Science* **2018,** *11* (7), 1653-1669.
6. Yang, X.; Wang, D., Photocatalysis: from fundamental principles to materials and applications. *ACS Applied Energy Materials* **2018,** *1* (12), 6657-6693.
7. Zhu, S.; Wang, D., Photocatalysis: basic principles, diverse forms of implementations and emerging scientific opportunities. *Advanced Energy Materials* **2017,** *7* (23), 1700841.
8. Braslavsky, S. E.; Braun, A. M.; Cassano, A. E.; Emeline, A. V.; Litter, M. I.; Palmisano, L.; Parmon, V. N.; Serpone, N., Glossary of terms used in photocatalysis and radiation catalysis (IUPAC Recommendations 2011). *Pure and Applied Chemistry* **2011,** *83* (4), 931-1014.
9. Osterloh, F. E., Photocatalysis versus photosynthesis: A sensitivity analysis of devices for solar energy conversion and chemical transformations. *ACS Energy Letters* **2017,** *2* (2), 445-453.
10. Wang, Q.; Domen, K., Particulate photocatalysts for light-driven water splitting: mechanisms, challenges, and design strategies. *Chemical Reviews* **2019,** *120* (2), 919-985.
11. Albini, A.; Fagnoni, M., 1908: Giacomo Ciamician and the concept of green chemistry. *ChemSusChem: Chemistry & Sustainability Energy & Materials* **2008,** *1* (1-2), 63-66.
12. Eibner, A., Action of light on pigments I. *Chem.-Ztg* **1911,** *35*, 753-755.
13. Fujishima, A.; Honda, K., Electrochemical photolysis of water at a semiconductor electrode. *Nature* **1972,** *238* (5358), 37-38.
14. Ma, Y.; Lin, L.; Takata, T.; Hisatomi, T.; Domen, K., A perspective on two pathways of photocatalytic water splitting and their practical application systems. *Physical Chemistry Chemical Physics* **2023,** *25* (9), 6586-6601.
15. Mazloomi, K.; Gomes, C., Hydrogen as an energy carrier: Prospects and challenges. *Renewable and Sustainable Energy Reviews* **2012,** *16* (5), 3024-3033.
16. Kim, J. H.; Hansora, D.; Sharma, P.; Jang, J.-W.; Lee, J. S., Toward practical solar hydrogen production–an artificial photosynthetic leaf-to-farm challenge. *Chemical Society Reviews* **2019,** *48* (7), 1908-1971.
17. Zheng, Y.; Ma, M.; Shao, H., Recent advances in efficient and scalable solar hydrogen production through water splitting. *Carbon Neutrality* **2023,** *2* (1), 23.
18. Chen, X.; Shen, S.; Guo, L.; Mao, S. S., Semiconductor-based photocatalytic hydrogen generation. *Chemical Reviews* **2010,** *110* (11), 6503-6570.
19. Li, X.; Yu, J.; Low, J.; Fang, Y.; Xiao, J.; Chen, X., Engineering heterogeneous semiconductors for solar water splitting. *Journal of Materials Chemistry A* **2015,** *3* (6), 2485-2534.
20. Hisatomi, T.; Kubota, J.; Domen, K., Recent advances in semiconductors for photocatalytic and photoelectrochemical water splitting. *Chemical Society Reviews* **2014,** *43* (22), 7520-7535.

21. Ong, W.-J.; Tan, L.-L.; Ng, Y. H.; Yong, S.-T.; Chai, S.-P., Graphitic carbon nitride (g-C_3N_4)-based photocatalysts for artificial photosynthesis and environmental remediation: are we a step closer to achieving sustainability? *Chemical Reviews* **2016,** *116* (12), 7159-7329.

22. Li, X.; Wang, Z.; Zhang, Z.; Chen, L.; Cheng, J.; Ni, W.; Wang, B.; Xie, E., Light illuminated α− Fe_2O_3/Pt nanoparticles as water activation agent for photoelectrochemical water splitting. *Scientific Reports* **2015,** *5* (1), 9130.

23. Meng, A.; Zhu, B.; Zhong, B.; Zhang, L.; Cheng, B., Direct Z-scheme TiO_2/CdS hierarchical photocatalyst for enhanced photocatalytic H_2-production activity. *Applied Surface Science* **2017,** *422*, 518-527.

24. Kormann, C.; Bahnemann, D. W.; Hoffmann, M. R., Photocatalytic production of hydrogen peroxides and organic peroxides in aqueous suspensions of titanium dioxide, zinc oxide, and desert sand. *Environmental Science & Technology* **1988,** *22* (7), 798-806.

25. Wu, T.; Liu, G.; Zhao, J.; Hidaka, H.; Serpone, N., Photoassisted degradation of dye pollutants. V. Self-photosensitized oxidative transformation of rhodamine B under visible light irradiation in aqueous TiO_2 dispersions. *The Journal of Physical Chemistry B* **1998,** *102* (30), 5845-5851.

26. Bard, A., *Standard potentials in aqueous solution*. Routledge: 2017.

27. Chen, S.; Takata, T.; Domen, K., Particulate photocatalysts for overall water splitting. *Nature Reviews Materials* **2017,** *2* (10), 1-17.

28. Wang, Z.; Li, C.; Domen, K., Recent developments in heterogeneous photocatalysts for solar-driven overall water splitting. *Chemical Society Reviews* **2019,** *48* (7), 2109-2125.

29. Qureshi, M.; Takanabe, K., Insights on measuring and reporting heterogeneous photocatalysis: efficiency definitions and setup examples. *Chemistry of Materials* **2017,** *29* (1), 158-167.

30. Zhou, P.; Navid, I. A.; Ma, Y.; Xiao, Y.; Wang, P.; Ye, Z.; Zhou, B.; Sun, K.; Mi, Z., Solar-to-hydrogen efficiency of more than 9% in photocatalytic water splitting. *Nature* **2023,** *613* (7942), 66-70.

31. Turro, N. J.; Ramamurthy, V.; Scaiano, J. C., *Modern molecular photochemistry of organic molecules*. University Science Books Sausalito, CA: 2010; Vol. 188.

32. Takanabe, K., Photocatalytic water splitting: quantitative approaches toward photocatalyst by design. *ACS Catalysis* **2017,** *7* (11), 8006-8022.

33. Maeda, K.; Domen, K., New non-oxide photocatalysts designed for overall water splitting under visible light. *The Journal of Physical Chemistry C* **2007,** *111* (22), 7851-7861.

34. Li, X.-B.; Tung, C.-H.; Wu, L.-Z., Semiconducting quantum dots for artificial photosynthesis. *Nature Reviews Chemistry* **2018,** *2* (8), 160-173.

35. Maeda, K.; Domen, K., Photocatalytic water splitting: recent progress and future challenges. *The Journal of Physical Chemistry Letters* **2010,** *1* (18), 2655-2661.

36. Nishiyama, H.; Yamada, T.; Nakabayashi, M.; Maehara, Y.; Yamaguchi, M.; Kuromiya, Y.; Nagatsuma, Y.; Tokudome, H.; Akiyama, S.; Watanabe, T., Photocatalytic solar hydrogen production from water on a 100-m2 scale. *Nature* **2021,** *598* (7880), 304-307.

37. Pinaud, B. A.; Benck, J. D.; Seitz, L. C.; Forman, A. J.; Chen, Z.; Deutsch, T. G.; James, B. D.; Baum, K. N.; Baum, G. N.; Ardo, S., Technical and economic feasibility of centralized facilities for solar hydrogen production via photocatalysis and photoelectrochemistry. *Energy & Environmental Science* **2013,** *6* (7), 1983-2002.

38. Shaner, M. R.; Atwater, H. A.; Lewis, N. S.; McFarland, E. W., A comparative technoeconomic analysis of renewable hydrogen production using solar energy. *Energy & Environmental Science* **2016,** *9* (7), 2354-2371.

39. Abe, R., Recent progress on photocatalytic and photoelectrochemical water splitting under visible light irradiation. *Journal of Photochemistry and Photobiology C: Photochemistry Reviews* **2010,** *11* (4), 179-209.

40. Boriskina, S. V.; Ghasemi, H.; Chen, G., Plasmonic materials for energy: From physics to applications. *Materials Today* **2013,** *16* (10), 375-386.

41. Kale, M. J.; Avanesian, T.; Christopher, P., Direct photocatalysis by plasmonic nanostructures. *ACS Catalysis* **2014,** *4* (1), 116-128.

42. Linic, S.; Aslam, U.; Boerigter, C.; Morabito, M., Photochemical transformations on plasmonic metal nanoparticles. *Nature Materials* **2015,** *14* (6), 567-576.

43. Li, S.; Miao, P.; Zhang, Y.; Wu, J.; Zhang, B.; Du, Y.; Han, X.; Sun, J.; Xu, P., Recent advances in plasmonic nanostructures for enhanced photocatalysis and electrocatalysis. *Advanced Materials* **2021,** *33* (6), 2000086.

44. Zhang, X.; Chen, Y. L.; Liu, R.-S.; Tsai, D. P., Plasmonic photocatalysis. *Reports on Progress in Physics* **2013,** *76* (4), 046401.

45. Wang, Y.; Suzuki, H.; Xie, J.; Tomita, O.; Martin, D. J.; Higashi, M.; Kong, D.; Abe, R.; Tang, J., Mimicking natural photosynthesis: solar to renewable H_2 fuel synthesis by Z-scheme water splitting systems. *Chemical Reviews* **2018,** *118* (10), 5201-5241.

46. Le Bahers, T.; Rerat, M.; Sautet, P., Semiconductors used in photovoltaic and photocatalytic devices: assessing fundamental properties from DFT. *The Journal of Physical Chemistry C* **2014,** *118* (12), 5997-6008.

47. Takanabe, K., Solar water splitting using semiconductor photocatalyst powders. *Solar Energy for Fuels* **2016**, 73-103.

48. Garcia-Esparza, A. T.; Takanabe, K., A simplified theoretical guideline for overall water splitting using photocatalyst particles. *Journal of Materials Chemistry A* **2016,** *4* (8), 2894-2908.

49. Tang, J.; Durrant, J. R.; Klug, D. R., Mechanism of photocatalytic water splitting in TiO_2. Reaction of water with photoholes, importance of charge carrier dynamics, and evidence for four-hole chemistry. *Journal of the American Chemical Society* **2008,** *130* (42), 13885-13891.

50. Ran, J.; Zhang, J.; Yu, J.; Jaroniec, M.; Qiao, S. Z., Earth-abundant cocatalysts for semiconductor-based photocatalytic water splitting. *Chemical Society Reviews* **2014,** *43* (22), 7787-7812.

51. Liu, J.; Zhao, H.; Wu, M.; Van der Schueren, B.; Li, Y.; Deparis, O.; Ye, J.; Ozin, G. A.; Hasan, T.; Su, B. L., Slow photons for photocatalysis and photovoltaics. *Advanced Materials* **2017,** *29* (17), 1605349.

52. Kim, K.-H.; Park, Q.-H., Perfect anti-reflection from first principles. *Scientific Reports* **2013,** *3* (1), 1-5.

53. Mozumder, M. S.; Mourad, A.-H. I.; Pervez, H.; Surkatti, R., Recent developments in multifunctional coatings for solar panel applications: A review. *Solar Energy Materials and Solar Cells* **2019,** *189*, 75-102.

54. Wang, W.; Qi, L., Light management with patterned micro-and nanostructure arrays for photocatalysis, photovoltaics, and optoelectronic and optical devices. *Advanced Functional Materials* **2019,** *29* (25), 1807275.

55. Saive, R., Light trapping in thin silicon solar cells: A review on fundamentals and technologies. *Progress in Photovoltaics: Research and Applications* **2021,** *29* (10), 1125-1137.

56. Massiot, I.; Cattoni, A.; Collin, S., Progress and prospects for ultrathin solar cells. *Nature Energy* **2020,** *5* (12), 959-972.

57. Wen, S.; Zhou, J.; Schuck, P. J.; Suh, Y. D.; Schmidt, T. W.; Jin, D., Future and challenges for hybrid upconversion nanosystems. *Nature Photonics* **2019,** *13* (12), 828-838.

58. Yu, D.; Yu, T.; Lin, H.; Zhuang, S.; Zhang, D., Recent Advances in Luminescent Downconversion: New Materials, Techniques, and Applications in Solar Cells. *Advanced Optical Materials* **2022**, 2200014.

59. Wang, Y.; Liu, H.; Zhu, J., Solar thermophotovoltaics: Progress, challenges, and opportunities. *APL Materials* **2019,** *7* (8), 080906.

60. Schuller, J. A.; Barnard, E. S.; Cai, W.; Jun, Y. C.; White, J. S.; Brongersma, M. L., Plasmonics for extreme light concentration and manipulation. *Nature Materials* **2010,** *9* (3), 193-204.

61. Zhou, N.; López-Puente, V.; Wang, Q.; Polavarapu, L.; Pastoriza-Santos, I.; Xu, Q.-H., Plasmon-enhanced light harvesting: applications in enhanced photocatalysis, photodynamic therapy and photovoltaics. *RSC Advances* **2015,** *5* (37), 29076-29097.

62. Zada, A.; Muhammad, P.; Ahmad, W.; Hussain, Z.; Ali, S.; Khan, M.; Khan, Q.; Maqbool, M., Surface plasmonic-assisted photocatalysis and optoelectronic devices with noble metal nanocrystals: design, synthesis, and applications. *Advanced Functional Materials* **2020,** *30* (7), 1906744.

63. Hore, S.; Nitz, P.; Vetter, C.; Prahl, C.; Niggemann, M.; Kern, R., Scattering spherical voids in nanocrystalline TiO 2–enhancement of efficiency in dye-sensitized solar cells. *Chemical Communications* **2005,** (15), 2011-2013.

64. Li, Y.; Kunitake, T.; Fujikawa, S., Efficient fabrication and enhanced photocatalytic activities of 3D-ordered films of titania hollow spheres. *The Journal of Physical Chemistry B* **2006,** *110* (26), 13000-13004.

65. Mokkapati, S.; Catchpole, K., Nanophotonic light trapping in solar cells. *Journal of Applied Physics* **2012,** *112* (10), 101101.

66. Zheng, X.; Zhang, L., Photonic nanostructures for solar energy conversion. *Energy & Environmental Science* **2016,** *9* (8), 2511-2532.

67. Burresi, M.; Pratesi, F.; Riboli, F.; Wiersma, D. S., Complex photonic structures for light harvesting. *Advanced Optical Materials* **2015,** *3* (6), 722-743.

68. Boyd, R. W., Slow and fast light: fundamentals and applications. *Journal of Modern Optics* **2009,** *56* (18-19), 1908-1915.

69. Khurgin, J. B.; Tucker, R. S., *Slow light: Science and applications*. CRC press: 2018.

70. Herráez, M. G.; Song, K. Y.; Thévenaz, L., Arbitrary-bandwidth Brillouin slow light in optical fibers. *Optics Express* **2006,** *14* (4), 1395-1400.

71. Zhu, Z.; Dawes, A. M.; Gauthier, D. J.; Zhang, L.; Willner, A. E., Broadband SBS slow light in an optical fiber. *Journal of Lightwave Technology* **2007,** *25* (1), 201-206.

72. Cabrera-Granado, E.; Calderón, O. G.; Melle, S.; Gauthier, D. J., Observation of large 10-Gb/s SBS slow light delay with low distortion using an optimized gain profile. *Optics Express* **2008,** *16* (20), 16032-16042.

73. Piredda, G.; Boyd, R. W., Slow light by means of coherent population oscillations: laser linewidth effects. *Journal of the European Optical Society-Rapid Publications* **2007,** *2*.

74. Yelleswarapu, C. S.; Philip, R.; Aranda, F. J.; Kimball, B. R.; Rao, D., Slow light in bacteriorhodopsin solution using coherent population oscillations. *Optics Letters* **2007,** *32* (13), 1788-1790.

75. Liu, C.; Dutton, Z.; Behroozi, C. H.; Hau, L. V., Observation of coherent optical information storage in an atomic medium using halted light pulses. *Nature* **2001,** *409* (6819), 490-493.

76. Solli, D.; McCormick, C.; Chiao, R.; Popescu, S.; Hickmann, J., Fast light, slow light, and phase singularities: a connection to generalized weak values. *Physical Review Letters* **2004,** *92* (4), 043601.

77. Asano, M.; Bliokh, K. Y.; Bliokh, Y. P.; Kofman, A. G.; Ikuta, R.; Yamamoto, T.; Kivshar, Y.; Yang, L.; Imoto, N.; Özdemir, Ş., Anomalous time delays and quantum weak measurements in optical micro-resonators. *Nature Communications* **2016,** *7* (1), 13488.

78. Zacharias, T.; Hareli, L.; Bahabad, A., Slow and Fast Light through Weak Measurements of Spectral Superoscillations. *Laser & Photonics Reviews* **2021,** *15* (10), 2100151.

79. Bouchard, F.; Harris, J.; Mand, H.; Boyd, R. W.; Karimi, E., Observation of subluminal twisted light in vacuum. *Optica* **2016,** *3* (4), 351-354.

80. Notomi, M.; Kuramochi, E.; Tanabe, T., Large-scale arrays of ultrahigh-Q coupled nanocavities. *Nature Photonics* **2008,** *2* (12), 741-747.

81. Lee, M.; Gehm, M. E.; Neifeld, M. A., Systematic design study of an all-optical delay line based on Brillouin scattering enhanced cascade coupled ring resonators. *Journal of Optics* **2010,** *12* (10), 104012.

82. Lu, W. T.; Savo, S.; Casse, B. D. F.; Sridhar, S., Slow microwave waveguide made of negative permeability metamaterials. *Microwave and Optical Technology Letters* **2009,** *51* (11), 2705-2709.

83. Savo, S.; Casse, B.; Lu, W.; Sridhar, S., Observation of slow-light in a metamaterials waveguide at microwave frequencies. *Applied Physics Letters* **2011,** *98* (17), 171907.

84. Tsakmakidis, K. L.; Boardman, A. D.; Hess, O., 'Trapped rainbow'storage of light in metamaterials. *Nature* **2007,** *450* (7168), 397-401.

85. Tang, H.; Du, F.; Carr, S.; DeVault, C.; Mello, O.; Mazur, E., Modeling the optical properties of twisted bilayer photonic crystals. *Light: Science & Applications* **2021,** *10* (1), 157.

86. Krauss, T. F., Slow light in photonic crystal waveguides. *Journal of Physics D: Applied Physics* **2007,** *40* (9), 2666.

87. Baba, T., Slow light in photonic crystals. *Nature Photonics* **2008,** *2* (8), 465-473.

88. Üstün, K.; Kurt, H., Ultra slow light achievement in photonic crystals by merging coupled cavities with waveguides. *Optics Express* **2010,** *18* (20), 21155-21161.

89. Deparis, O.; Mouchet, S.; Su, B.-L., Light harvesting in photonic crystals revisited: why do slow photons at the blue edge enhance absorption? *Physical Chemistry Chemical Physics* **2015,** *17* (45), 30525-30532.

90. Jacobs, M.; Lopez-Garcia, M.; Phrathep, O.; Lawson, T.; Oulton, R.; Whitney, H. M., Photonic multilayer structure of Begonia chloroplasts enhances photosynthetic efficiency. *Nature Plants* **2016,** *2* (11), 1-6.

91. Castillo, M. A.; Wardley, W. P.; Lopez-Garcia, M., Light-dependent morphological changes can tune light absorption in iridescent plant chloroplasts: a numerical study using biologically realistic data. *ACS Photonics* **2021,** *8* (4), 1058-1068.

92. Collins, G.; Armstrong, E.; McNulty, D.; O'Hanlon, S.; Geaney, H.; O'Dwyer, C., 2D and 3D photonic crystal materials for photocatalysis and electrochemical energy storage and conversion. *Science and Technology of Advanced Materials* **2016,** *17* (1), 563-582.

93. Wu, M.; Li, Y.; Deng, Z.; Su, B. L., Three-Dimensionally Ordered Macroporous Titania with Structural and Photonic Effects for Enhanced Photocatalytic Efficiency. *ChemSusChem* **2011,** *4* (10), 1481-1488.
94. Zalfani, M.; van der Schueren, B.; Mahdouani, M.; Bourguiga, R.; Yu, W.-B.; Wu, M.; Deparis, O.; Li, Y.; Su, B.-L., ZnO quantum dots decorated 3DOM TiO2 nanocomposites: Symbiose of quantum size effects and photonic structure for highly enhanced photocatalytic degradation of organic pollutants. *Applied Catalysis B: Environmental* **2016,** *199*, 187-198.
95. Joannopoulos, J. D.; Villeneuve, P. R.; Fan, S., Photonic crystals: putting a new twist on light. *Nature* **1997,** *386* (6621), 143-149.
96. Villeneuve, P. R.; Piche, M., Photonic bandgaps in periodic dielectric structures. *Progress in Quantum Electronics* **1994,** *18* (2), 153-200.
97. Yablonovitch, E., Photonic crystals. *Journal of Modern Optics* **1994,** *41* (2), 173-194.
98. Zhao, Y.; Xie, Z.; Gu, H.; Zhu, C.; Gu, Z., Bio-inspired variable structural color materials. *Chemical Society Reviews* **2012,** *41* (8), 3297-3317.
99. Deparis, O.; Mouchet, S. R., *Natural Photonics and Bioinspiration*. Artech House: 2021.
100. Gaillou, E.; Fritsch, E.; Aguilar-Reyes, B.; Rondeau, B.; Post, J.; Barreau, A.; Ostroumov, M., Common gem opal: An investigation of micro-to nano-structure. *American Mineralogist* **2008,** *93* (11-12), 1865-1873.
101. Joannopoulos, J. D.; Johnson, S. G.; Winn, J. N.; Meade, R. D., *Molding the flow of light*. Princeton Univ. Press: 2008.
102. Bykov, V. P., Spontaneous emission from a medium with a band spectrum. *Soviet Journal of Quantum Electronics* **1975,** *4* (7), 861.
103. Ohtaka, K., Energy band of photons and low-energy photon diffraction. *Physical Review B* **1979,** *19* (10), 5057.
104. Yablonovitch, E., Inhibited spontaneous emission in solid-state physics and electronics. *Physical Review Letters* **1987,** *58* (20), 2059.
105. John, S., Strong localization of photons in certain disordered dielectric superlattices. *Physical Review Letters* **1987,** *58* (23), 2486.
106. Lopez, C., Materials aspects of photonic crystals. *Advanced Materials* **2003,** *15* (20), 1679-1704.
107. Armstrong, E.; O'Dwyer, C., Artificial opal photonic crystals and inverse opal structures – fundamentals and applications from optics to energy storage. *Journal of Materials Chemistry C* **2015,** *3* (24), 6109-6143.
108. Busch, K.; John, S., Photonic band gap formation in certain self-organizing systems. *Physical Review E* **1998,** *58* (3), 3896.
109. Sakoda, K.; Sakoda, K., *Optical properties of photonic crystals*. Springer: 2005; Vol. 2.
110. Johnson, S. G.; Joannopoulos, J. D., *Photonic crystals: the road from theory to practice*. Springer Science & Business Media: 2001.
111. Cersonsky, R. K.; Antonaglia, J.; Dice, B. D.; Glotzer, S. C., The diversity of three-dimensional photonic crystals. *Nature Communications* **2021,** *12* (1), 1-7.
112. Ho, K.; Chan, C. T.; Soukoulis, C. M., Existence of a photonic gap in periodic dielectric structures. *Physical Review Letters* **1990,** *65* (25), 3152.
113. Maldovan, M.; Thomas, E. L., Diamond-structured photonic crystals. *Nature Materials* **2004,** *3* (9), 593-600.
114. Yablonovitch, E.; Gmitter, T.; Leung, K.-M., Photonic band structure: The face-centered-cubic case employing nonspherical atoms. *Physical Review Letters* **1991,** *67* (17), 2295.

115. Lin, S.-y.; Fleming, J.; Hetherington, D.; Smith, B.; Biswas, R.; Ho, K.; Sigalas, M.; Zubrzycki, W.; Kurtz, S.; Bur, J., A three-dimensional photonic crystal operating at infrared wavelengths. *Nature* **1998,** *394* (6690), 251-253.

116. Moon, J. H.; Yang, S., Chemical aspects of three-dimensional photonic crystals. *Chemical Reviews* **2010,** *110* (1), 547-574.

117. Carlson, R. J.; Asher, S. A., Characterization of optical diffraction and crystal structure in monodisperse polystyrene colloids. *Applied Spectroscopy* **1984,** *38* (3), 297-304.

118. Flaugh, P. L.; O'Donnell, S. E.; Asher, S. A., Development of a new optical wavelength rejection filter: demonstration of its utility in Raman spectroscopy. *Applied Spectroscopy* **1984,** *38* (6), 847-850.

119. Stein, A.; Wilson, B. E.; Rudisill, S. G., Design and functionality of colloidal-crystal-templated materials—chemical applications of inverse opals. *Chemical Society Reviews* **2013,** *42* (7), 2763-2803.

120. Bolhuis, P. G.; Frenkel, D.; Mau, S.-C.; Huse, D. A., Entropy difference between crystal phases. *Nature* **1997,** *388* (6639), 235-236.

121. Woodcock, L., Entropy difference between the face-centred cubic and hexagonal close-packed crystal structures. *Nature* **1997,** *385* (6612), 141-143.

122. Likodimos, V., Photonic crystal-assisted visible light activated TiO_2 photocatalysis. *Applied Catalysis B* **2018,** *230*, 269-303.

123. van der Hoeven, J. E.; Shneidman, A. V.; Nicolas, N. J.; Aizenberg, J., Evaporation-induced self-assembly of metal oxide inverse opals: from synthesis to applications. *Accounts of Chemical Research* **2022,** *55* (13), 1809-1820.

124. Velev, O.; Jede, T.; Lobo, R.; Lenhoff, A., Porous silica via colloidal crystallization. *Nature* **1997,** *389* (6650), 447-448.

125. Holland, B. T.; Blanford, C. F.; Stein, A., Synthesis of macroporous minerals with highly ordered three-dimensional arrays of spheroidal voids. *Science* **1998,** *281* (5376), 538-540.

126. Wijnhoven, J. E.; Vos, W. L., Preparation of photonic crystals made of air spheres in titania. *Science* **1998,** *281* (5378), 802-804.

127. Stein, A.; Li, F.; Denny, N. R., Morphological control in colloidal crystal templating of inverse opals, hierarchical structures, and shaped particles. *Chemistry of Materials* **2008,** *20* (3), 649-666.

128. Li, F.; Josephson, D. P.; Stein, A., Colloidal assembly: the road from particles to colloidal molecules and crystals. *Angewandte Chemie International Edition* **2011,** *50* (2), 360-388.

129. Sacanna, S.; Pine, D. J., Shape-anisotropic colloids: Building blocks for complex assemblies. *Current Opinion in Colloid & Interface Science* **2011,** *16* (2), 96-105.

130. Stöber, W.; Fink, A.; Bohn, E., Controlled growth of monodisperse silica spheres in the micron size range. *Journal of Colloid and Interface Science* **1968,** *26* (1), 62-69.

131. von Freymann, G.; Kitaev, V.; Lotsch, B. V.; Ozin, G. A., Bottom-up assembly of photonic crystals. *Chemical Society Reviews* **2013,** *42* (7), 2528-2554.

132. Stein, A., Achieving Functionality and Multifunctionality through Bulk and Interfacial Structuring of Colloidal-Crystal-Templated Materials. *Langmuir* **2023,** *39* (8), 2890-2910.

133. Allard, M.; Sargent, E. H., Impact of polydispersity on light propagation in colloidal photonic crystals. *Applied Physics Letters* **2004,** *85* (24), 5887-5889.

134. Du, X.; He, J., Facile size-controllable syntheses of highly monodisperse polystyrene nano- and microspheres by polyvinylpyrrolidone-mediated emulsifier-free emulsion polymerization. *Journal of Applied Polymer Science* **2008,** *108* (3), 1755-1760.

135. Vogel, N.; Retsch, M.; Fustin, C.-A.; Del Campo, A.; Jonas, U., Advances in colloidal assembly: the design of structure and hierarchy in two and three dimensions. *Chemical Reviews* **2015,** *115* (13), 6265-6311.

136. Mishchenko, L.; Hatton, B.; Kolle, M.; Aizenberg, J., Patterning hierarchy in direct and inverse opal crystals. *Small* **2012,** *8* (12), 1904-1911.

137. Norris, D. J.; Arlinghaus, E. G.; Meng, L.; Heiny, R.; Scriven, L., Opaline photonic crystals: How does self-assembly work? *Advanced Materials* **2004,** *16* (16), 1393-1399.

138. Phillips, K. R.; England, G. T.; Sunny, S.; Shirman, E.; Shirman, T.; Vogel, N.; Aizenberg, J., A colloidoscope of colloid-based porous materials and their uses. *Chemical Society Reviews* **2016,** *45* (2), 281-322.

139. Li, L.; Goodrich, C.; Yang, H.; Phillips, K. R.; Jia, Z.; Chen, H.; Wang, L.; Zhong, J.; Liu, A.; Lu, J., Microscopic origins of the crystallographically preferred growth in evaporation-induced colloidal crystals. *Proceedings of the National Academy of Sciences* **2021,** *118* (32), e2107588118.

140. Dimitrov, A. S.; Nagayama, K., Continuous convective assembling of fine particles into two-dimensional arrays on solid surfaces. *Langmuir* **1996,** *12* (5), 1303-1311.

141. Jiang, P.; Bertone, J.; Hwang, K. S.; Colvin, V., Single-crystal colloidal multilayers of controlled thickness. *Chemistry of Materials* **1999,** *11* (8), 2132-2140.

142. Vlasov, Y. A.; Bo, X.-Z.; Sturm, J. C.; Norris, D. J., On-chip natural assembly of silicon photonic bandgap crystals. *Nature* **2001,** *414* (6861), 289-293.

143. Kuai, S.-L.; Hu, X.-F.; Hache, A.; Truong, V.-V., High-quality colloidal photonic crystals obtained by optimizing growth parameters in a vertical deposition technique. *Journal of Crystal Growth* **2004,** *267* (1-2), 317-324.

144. Cai, Z.; Li, Z.; Ravaine, S.; He, M.; Song, Y.; Yin, Y.; Zheng, H.; Teng, J.; Zhang, A., From colloidal particles to photonic crystals: advances in self-assembly and their emerging applications. *Chemical Society Reviews* **2021,** *50* (10), 5898-5951.

145. Xu, P.; Mujumdar, A.; Yu, B., Drying-induced cracks in thin film fabricated from colloidal dispersions. *Drying Technology* **2009,** *27* (5), 636-652.

146. Xu, Y.; German, G. K.; Mertz, A. F.; Dufresne, E. R., Imaging stress and strain in the fracture of drying colloidal films. *Soft Matter* **2013,** *9* (14), 3735-3740.

147. Zeng, F.; Sun, Z.; Wang, C.; Ren, B.; Liu, X.; Tong, Z., Fabrication of inverse opal via ordered highly charged colloidal spheres. *Langmuir* **2002,** *18* (24), 9116-9120.

148. Zhang, Y.; Wang, J.; Huang, Y.; Song, Y.; Jiang, L., Fabrication of functional colloidal photonic crystals based on well-designed latex particles. *Journal of Materials Chemistry* **2011,** *21* (37), 14113-14126.

149. Rengarajan, R.; Mittleman, D.; Rich, C.; Colvin, V., Effect of disorder on the optical properties of colloidal crystals. *Physical Review E* **2005,** *71* (1), 016615.

150. Marlow, F.; Muldarisnur; Sharifi, P.; Brinkmann, R.; Mendive, C., Opals: status and prospects. *Angewandte Chemie International Edition* **2009,** *48* (34), 6212-6233.

151. Li, H.-L.; Marlow, F., Solvent effects in colloidal crystal deposition. *Chemistry of Materials* **2006,** *18* (7), 1803-1810.

152. Cai, Z.; Teng, J.; Yan, Q.; Zhao, X., Solvent effect on the self-assembly of colloidal microspheres via a horizontal deposition method. *Colloids and Surfaces A: Physicochemical and Engineering Aspects* **2012,** *402*, 37-44.

153. Wong, S.; Kitaev, V.; Ozin, G. A., Colloidal crystal films: advances in universality and perfection. *Journal of the American Chemical Society* **2003,** *125* (50), 15589-15598.

154. Smith, M.; Sharp, J., Effects of substrate constraint on crack pattern formation in thin films of colloidal polystyrene particles. *Langmuir* **2011,** *27* (13), 8009-8017.

155. Zhou, J.; Wang, J.; Huang, Y.; Liu, G.; Wang, L.; Chen, S.; Li, X.; Wang, D.; Song, Y.; Jiang, L., Large-area crack-free single-crystal photonic crystals via combined effects of polymerization-assisted assembly and flexible substrate. *NPG Asia Materials* **2012,** *4* (8), e21-e21.

156. Kim, M. R.; Im, S. H.; Kim, Y. S.; Cho, K. Y., Transferable Crack-Free Colloidal Crystals on an Elastomeric Matrix with Surface Relief. *Advanced Functional Materials* **2013,** *23* (46), 5700-5705.

157. Pham, K.; Temerov, F.; Saarinen, J. J., Multicompound inverse opal structures with gold nanoparticles for visible light photocatalytic activity. *Materials & Design* **2020,** *194*, 108886.

158. Cai, Z.; Teng, J.; Xiong, Z.; Li, Y.; Li, Q.; Lu, X.; Zhao, X., Fabrication of TiO2 binary inverse opals without overlayers via the sandwich-vacuum infiltration of precursor. *Langmuir* **2011,** *27* (8), 5157-5164.

159. Galusha, J. W.; Tsung, C.-K.; Stucky, G. D.; Bartl, M. H., Optimizing sol− gel infiltration and processing methods for the fabrication of high-quality planar titania inverse opals. *Chemistry of Materials* **2008,** *20* (15), 4925-4930.

160. Li, H.-L.; Dong, W.; Bongard, H.-J.; Marlow, F., Improved controllability of opal film growth using capillaries for the deposition process. *The Journal of Physical Chemistry B* **2005,** *109* (20), 9939-9945.

161. Velev, O.; Jede, T.; Lobo, R.; Lenhoff, A., Porous silica via colloidal crystallization. *Nature* **1997,** *389* (6650), 447-448.

162. Holland, B. T.; Blanford, C. F.; Stein, A., Synthesis of macroporous minerals with highly ordered three-dimensional arrays of spheroidal voids. *Science* **1998,** *281* (5376), 538-540.

163. Wijnhoven, J. E.; Vos, W. L., Preparation of photonic crystals made of air spheres in titania. *Science* **1998,** *281* (5378), 802-804.

164. Yan, H.; Blanford, C. F.; Holland, B. T.; Smyrl, W. H.; Stein, A., General synthesis of periodic macroporous solids by templated salt precipitation and chemical conversion. *Chemistry of Materials* **2000,** *12* (4), 1134-1141.

165. Norris, D. J.; Vlasov, Y. A., Chemical approaches to three-dimensional semiconductor photonic crystals. *Advanced Materials* **2001,** *13* (6), 371-376.

166. Hatton, B.; Mishchenko, L.; Davis, S.; Sandhage, K. H.; Aizenberg, J., Assembly of large-area, highly ordered, crack-free inverse opal films. *Proceedings of the National Academy of Sciences* **2010,** *107* (23), 10354-10359.

167. Gao, J.; Tian, W.; Zhang, H.; Wang, S., Engineered inverse opal structured semiconductors for solar light-driven environmental catalysis. *Nanoscale* **2022,** *14* (39), 14341-14367.

168. Li, Y.; Piret, F.; Léonard, T.; Su, B.-L., Rutile TiO2 inverse opal with photonic bandgap in the UV–visible range. *Journal of Colloid and Interface science* **2010,** *348* (1), 43-48.

169. Wu, M.; Jin, J.; Liu, J.; Deng, Z.; Li, Y.; Deparis, O.; Su, B.-L., High photocatalytic activity enhancement of titania inverse opal films by slow photon effect induced strong light absorption. *Journal of Materials Chemistry A* **2013,** *1* (48), 15491-15500.

170. Wang, L.; Zhao, X., Fabrication of crack-free colloidal crystals using a modified vertical deposition method. *The Journal of Physical Chemistry C* **2007,** *111* (24), 8538-8542.

171. Hatton, B.; Mishchenko, L.; Davis, S.; Sandhage, K. H.; Aizenberg, J., Assembly of large-area, highly ordered, crack-free inverse opal films. *Proceedings of the National Academy of Sciences* **2010,** *107* (23), 10354-9.

172. Han, J. H.; Shneidman, A. V.; Kim, D. Y.; Nicolas, N. J.; van der Hoeven, J. E.; Aizenberg, M.; Aizenberg, J., Highly Ordered Inverse Opal Structures Synthesized from Shape-Controlled Nanocrystal Building Blocks. *Angewandte Chemie International Edition* **2022,** *61* (3), e202111048.

173. Zheng, Z.; Gao, K.; Luo, Y.; Li, D.; Meng, Q.; Wang, Y.; Zhang, D., Rapidly infrared-assisted cooperatively self-assembled highly ordered multiscale porous materials. *Journal of the American Chemical Society* **2008,** *130* (30), 9785-9789.

174. Phillips, K. R.; Shirman, T.; Shirman, E.; Shneidman, A. V.; Kay, T. M.; Aizenberg, J., Nanocrystalline Precursors for the Co-Assembly of Crack-Free Metal Oxide Inverse Opals. *Advanced Materials* **2018,** *30* (19), 1706329.

175. Cai, Z.; Liu, Y. J.; Lu, X.; Teng, J., In situ "doping" inverse silica opals with size-controllable gold nanoparticles for refractive index sensing. *The Journal of Physical Chemistry C* **2013,** *117* (18), 9440-9445.

176. Shirman, E.; Shirman, T.; Shneidman, A. V.; Grinthal, A.; Phillips, K. R.; Whelan, H.; Bulger, E.; Abramovitch, M.; Patil, J.; Nevarez, R., Modular design of advanced catalytic materials using hybrid organic–inorganic raspberry particles. *Advanced Functional Materials* **2018,** *28* (27), 1704559.

177. Apostolaki, M.-A.; Sakellis, E.; Tsipas, P.; Giannouri, M.; Gardelis, S.; Boukos, N.; Dimoulas, A.; Likodimos, V., Three-phase co-assembly of compositionally tunable WO_3/TiO_2 inverse opal photoelectrodes. *Applied Surface Science* **2023,** *613*, 155919.

178. Phillips, K. R.; Shirman, T.; Aizenberg, M.; England, G. T.; Vogel, N.; Aizenberg, J., Silica–titania hybrids for structurally robust inverse opals with controllable refractive index. *Journal of Materials Chemistry C* **2020,** *8* (1), 109-116.

179. Erola, M. O.; Philip, A.; Ahmed, T.; Suvanto, S.; Pakkanen, T. T., Fabrication of Au-and Ag–SiO_2 inverse opals having both localized surface plasmon resonance and Bragg diffraction. *Journal of Solid State Chemistry* **2015,** *230*, 209-217.

180. Yablonovitch, E., Inhibited spontaneous emission in solid-state physics and electronics. *Physical Review Letters* **1987,** *58* (20), 2059-2062.

181. Krauss, T. F., Why do we need slow light? *Nature Photonics* **2008,** *2* (8), 448-450.

182. Baba, T., Slow light in photonic crystals. *Nature Photonics* **2008,** *2* (8), 465-473.

183. Dowling, J. P.; Scalora, M.; Bloemer, M. J.; Bowden, C. M., The photonic band edge laser: A new approach to gain enhancement. *Journal of Applied Physics* **1994,** *75* (4), 1896-1899.

184. Vlasov, Y. A.; Luterova, K.; Pelant, I.; Hönerlage, B.; Astratov, V., Enhancement of optical gain of semiconductors embedded in three-dimensional photonic crystals. *Applied Physics Letters* **1997,** *71* (12), 1616-1618.

185. Nishimura, S.; Abrams, N.; Lewis, B. A.; Halaoui, L. I.; Mallouk, T. E.; Benkstein, K. D.; Van de Lagemaat, J.; Frank, A. J., Standing wave enhancement of red absorbance and photocurrent in dye-sensitized titanium dioxide photoelectrodes coupled to photonic crystals. *Journal of the American Chemical Society* **2003,** *125* (20), 6306-6310.

186. Halaoui, L. I.; Abrams, N. M.; Mallouk, T. E., Increasing the conversion efficiency of dye-sensitized TiO2 photoelectrochemical cells by coupling to photonic crystals. *The Journal of Physical Chemistry B* **2005,** *109* (13), 6334-6342.

187. Zeng, L.; Yi, Y.; Hong, C.; Liu, J.; Feng, N.; Duan, X.; Kimerling, L.; Alamariu, B., Efficiency enhancement in Si solar cells by textured photonic crystal back reflector. *Applied Physics Letters* **2006,** *89* (11), 111111.

188. Mihi, A.; Míguez, H., Origin of light-harvesting enhancement in colloidal-photonic-crystal-based dye-sensitized solar cells. *The Journal of Physical Chemistry B* **2005,** *109* (33), 15968-15976.
189. Chen, J. I.; von Freymann, G.; Choi, S. Y.; Kitaev, V.; Ozin, G. A., Amplified photochemistry with slow photons. *Advanced Materials* **2006,** *18* (14), 1915-1919.
190. Aguirre, C. I.; Reguera, E.; Stein, A., Tunable colors in opals and inverse opal photonic crystals. *Advanced Functional Materials* **2010,** *20* (16), 2565-2578.
191. Richel, A.; Johnson, N.; McComb, D., Observation of Bragg reflection in photonic crystals synthesized from air spheres in a titania matrix. *Applied Physics Letters* **2000,** *76* (14), 1816-1818.
192. Blanford, C. F.; Schroden, R. C.; Al-Daous, M.; Stein, A., Tuning solvent-dependent color changes of three-dimensionally ordered macroporous (3DOM) materials through compositional and geometric modifications. *Advanced Materials* **2001,** *13* (1), 26-29.
193. Schroden, R. C.; Al-Daous, M.; Blanford, C. F.; Stein, A., Optical properties of inverse opal photonic crystals. *Chemistry of Materials* **2002,** *14* (8), 3305-3315.
194. Yu, X.; Lee, Y. J.; Furstenberg, R.; White, J. O.; Braun, P. V., Filling fraction dependent properties of inverse opal metallic photonic crystals. *Advanced Materials* **2007,** *19* (13), 1689-1692.
195. Teyssier, J.; Saenko, S. V.; Van Der Marel, D.; Milinkovitch, M. C., Photonic crystals cause active colour change in chameleons. *Nature Communications* **2015,** *6* (1), 6368.
196. Seo, H.-b.; Lee, S.-Y., Bio-inspired colorimetric film based on hygroscopic coloration of longhorn beetles (Tmesisternus isabellae). *Scientific Reports* **2017,** *7* (1), 44927.
197. Rashid, I.; Hassan, M. U.; Khandwalla, A.; Ameen, R. M.; Yetisen, A. K.; Dai, Q.; Butt, H., Structural coloration in Caloenas nicobarica pigeons and refractive index modulated sensing. *Advanced Optical Materials* **2018,** *6* (9), 1701218.
198. Schroden, R. C.; Al-Daous, M.; Stein, A., Self-modification of spontaneous emission by inverse opal silica photonic crystals. *Chemistry of Materials* **2001,** *13* (9), 2945-2950.
199. Toumazatou, A.; Arfanis, M. K.; Pantazopoulos, P.-A.; Kontos, A. G.; Falaras, P.; Stefanou, N.; Likodimos, V., Slow-photon enhancement of dye sensitized TiO2 photocatalysis. *Materials Letters* **2017,** *197*, 123-126.
200. Curti, M.; Zvitco, G.; Grela, M. A.; Mendive, C. B., Angle dependence in slow photon photocatalysis using TiO2 inverse opals. *Chemical Physics* **2018,** *502*, 33-38.
201. Diamantopoulou, A.; Sakellis, E.; Romanos, G. E.; Gardelis, S.; Ioannidis, N.; Boukos, N.; Falaras, P.; Likodimos, V., Titania photonic crystal photocatalysts functionalized by graphene oxide nanocolloids. *Applied Catalysis B: Environmental* **2019,** *240*, 277-290.
202. Jovic, V.; Idriss, H.; Waterhouse, G. I., Slow photon amplification of gas-phase ethanol photo-oxidation in titania inverse opal photonic crystals. *Chemical Physics* **2016,** *479*, 109-121.
203. Lin, Q.; Liang, S.; Wang, J.; Zhang, R.; Wang, X., Cadmium sulfide 3D photonic crystal with hierarchically ordered macropores for highly efficient photocatalytic hydrogen generation. *Inorganic Chemistry* **2022,** *61* (6), 2920-2928.
204. Liu, J.; Li, M.; Wang, J.; Song, Y.; Jiang, L.; Murakami, T.; Fujishima, A., Hierarchically macro-/mesoporous Ti− Si oxides photonic crystal with highly efficient photocatalytic capability. *Environmental Science & Technology* **2009,** *43* (24), 9425-9431.
205. Chen, J. I.; Loso, E.; Ebrahim, N.; Ozin, G. A., Synergy of slow photon and chemically amplified photochemistry in platinum nanocluster-loaded inverse titania opals. *Journal of the American Chemical Society* **2008,** *130* (16), 5420-5421.

206. Zhang, X.; Liu, Y.; Lee, S.-T.; Yang, S.; Kang, Z., Coupling surface plasmon resonance of gold nanoparticles with slow-photon-effect of TiO_2 photonic crystals for synergistically enhanced photoelectrochemical water splitting. *Energy & Environmental Science* **2014,** *7* (4), 1409-1419.

207. Apostolaki, M.-A.; Toumazatou, A.; Antoniadou, M.; Sakellis, E.; Xenogiannopoulou, E.; Gardelis, S.; Boukos, N.; Falaras, P.; Dimoulas, A.; Likodimos, V., Graphene quantum dot-TiO2 photonic crystal films for photocatalytic applications. *Nanomaterials* **2020,** *10* (12), 2566.

208. Liu, J.; Jin, J.; Li, Y.; Huang, H.-W.; Wang, C.; Wu, M.; Chen, L.-H.; Su, B.-L., Tracing the slow photon effect in a ZnO inverse opal film for photocatalytic activity enhancement. *Journal of Materials Chemistry A* **2014,** *2* (14), 5051-5059.

209. Lu, Y.; Yu, H.; Chen, S.; Quan, X.; Zhao, H., Integrating plasmonic nanoparticles with TiO_2 photonic crystal for enhancement of visible-light-driven photocatalysis. *Environmental Science & Technology* **2012,** *46* (3), 1724-1730.

210. Li, X.; Zhang, X.; Zheng, X.; Shao, Y.; He, M.; Wang, P.; Fu, X.; Li, D., A facile preparation of ZnGa 2 O 4 photonic crystals with enhanced light absorption and photocatalytic activity. *Journal of Materials Chemistry A* **2014,** *2* (38), 15796-15802.

211. Mitchell, R.; Brydson, R.; Douthwaite, R. E., Enhancement of hydrogen production using photoactive nanoparticles on a photochemically inert photonic macroporous support. *Physical Chemistry Chemical Physics* **2015,** *17* (1), 493-499.

212. Li, X.; Chen, Z.; Quan, H.; Shao, Y.; Li, D., Constructing photocatalyst from β-Bi_2O_3 photonic crystals for enhanced photocatalytic performance. *Journal of Porous Materials* **2018,** *25*, 677-685.

213. Chen, J. I.; Ozin, G. A., Tracing the effect of slow photons in photoisomerization of azobenzene. *Advanced Materials* **2008,** *20* (24), 4784-4788.

214. El Harakeh, M.; Halaoui, L., Enhanced conversion of light at TiO_2 photonic crystals to the blue of a stop band and at TiO2 random films sensitized with Q-CdS: Order and disorder. *The Journal of Physical Chemistry C* **2010,** *114* (6), 2806-2813.

215. Galisteo-López, J.; Galli, M.; Patrini, M.; Balestreri, A.; Andreani, L.; López, C., Effective refractive index and group velocity determination of three-dimensional photonic crystals by means of white light interferometry. *Physical Review B* **2006,** *73* (12), 125103.

216. Bayram, S.; Halaoui, L., Amplification of Solar Energy Conversion in Quantum-Confined CdSe-Sensitized TiO2 Photonic Crystals by Trapping Light. *Particle & Particle Systems Characterization* **2013,** *30* (8), 706-714.

217. Meng, S.; Li, D.; Fu, X.; Fu, X., Integrating photonic bandgaps with surface plasmon resonance for the enhancement of visible-light photocatalytic performance. *Journal of Materials Chemistry A* **2015,** *3* (46), 23501-23511.

218. Zhao, H.; Hu, Z.; Liu, J.; Li, Y.; Wu, M.; Van Tendeloo, G.; Su, B.-L., Blue-edge slow photons promoting visible-light hydrogen production on gradient ternary 3DOM TiO_2-Au-CdS photonic crystals. *Nano Energy* **2018,** *47*, 266-274.

219. Xie, H.; Li, Y.; Jin, S.; Han, J.; Zhao, X., Facile fabrication of 3D-ordered macroporous nanocrystalline iron oxide films with highly efficient visible light induced photocatalytic activity. *The Journal of Physical Chemistry C* **2010,** *114* (21), 9706-9712.

220. Zhang, L.; Baumanis, C.; Robben, L.; Kandiel, T.; Bahnemann, D., Bi_2WO_6 inverse opals: facile fabrication and efficient visible-light-driven photocatalytic and photoelectrochemical water-splitting activity. *Small* **2011,** *7* (19), 2714-2720.

221. Wu, M.; Liu, J.; Jin, J.; Wang, C.; Huang, S.; Deng, Z.; Li, Y.; Su, B.-L., Probing significant light absorption enhancement of titania inverse opal films for highly exalted photocatalytic degradation of dye pollutants. *Applied Catalysis B: Environmental* **2014,** *150*, 411-420.
222. Curti, M.; Mendive, C. B.; Grela, M. A.; Bahnemann, D. W., Stopband tuning of TiO_2 inverse opals for slow photon absorption. *Materials Research Bulletin* **2017,** *91*, 155-165.
223. Curti, M.; Schneider, J.; Bahnemann, D. W.; Mendive, C. B., Inverse opal photonic crystals as a strategy to improve photocatalysis: Underexplored questions. *The Journal of Physical Chemistry Letters* **2015,** *6* (19), 3903-3910.
224. Cang, Y.; Lee, J.; Wang, Z.; Yan, J.; Matyjaszewski, K.; Bockstaller, M. R.; Fytas, G., Transparent Hybrid Opals with Unexpected Strong Resonance-Enhanced Photothermal Energy Conversion. *Advanced Materials* **2021,** *33* (2), 2004732.
225. Li, X.; Wang, C.; Li, B.; Shao, Y.; Li, D., Efficient light harvesting over a CdS/In_2O_3 photonic crystal photocatalyst for hydrogenation of 4-nitroaniline to p-phenylenediamine. *Physical Chemistry Chemical Physics* **2016,** *18* (40), 27848-27857.
226. Chang, Y.; Yu, K.; Zhang, C.; Yang, Z.; Feng, Y.; Hao, H.; Jiang, Y.; Lou, L.-L.; Zhou, W.; Liu, S., Ternary CdS/Au/3DOM-SrTiO3 composites with synergistic enhancement for hydrogen production from visible-light photocatalytic water splitting. *Applied Catalysis B: Environmental* **2017,** *215*, 74-84.
227. Wu, X.; Lan, D.; Zhang, R.; Pang, F.; Ge, J., Fabrication of opaline ZnO photonic crystal film and its slow-photon effect on photoreduction of carbon dioxide. *Langmuir* **2018,** *35* (1), 194-202.
228. Papadakis, D.; Diamantopoulou, A.; Pantazopoulos, P. A.; Palles, D.; Sakellis, E.; Boukos, N.; Stefanou, N.; Likodimos, V., Nanographene oxide–TiO_2 photonic films as plasmon-free substrates for surface-enhanced Raman scattering. *Nanoscale* **2019,** *11* (44), 21542-21553.
229. Chang, Y.; Xuan, Y.; Quan, H.; Zhang, H.; Liu, S.; Li, Z.; Yu, K.; Cao, J., Hydrogen treated Au/3DOM-TiO2 with promoted photocatalytic efficiency for hydrogen evolution from water splitting. *Chemical Engineering Journal* **2020,** *382*, 122869.
230. Meng, S.; Li, D.; Wang, P.; Zheng, X.; Wang, J.; Chen, J.; Fang, J.; Fu, X., Probing photonic effect on photocatalytic degradation of dyes based on 3D inverse opal ZnO photonic crystal. *RSC Advances* **2013,** *3* (38), 17021-17028.
231. Zheng, X.; Meng, S.; Chen, J.; Wang, J.; Xian, J.; Shao, Y.; Fu, X.; Li, D., Titanium dioxide photonic crystals with enhanced photocatalytic activity: matching photonic band gaps of TiO2 to the absorption peaks of dyes. *The Journal of Physical Chemistry C* **2013,** *117* (41), 21263-21273.
232. Toumazatou, A.; Antoniadou, M.; Sakellis, E.; Tsoutsou, D.; Gardelis, S.; Romanos, G. E.; Ioannidis, N.; Boukos, N.; Dimoulas, A.; Falaras, P., Boosting visible light harvesting and charge separation in surface modified TiO 2 photonic crystal catalysts with CoO_x nanoclusters. *Materials Advances* **2020,** *1* (7), 2310-2322.
233. Vipin, V.; Chandran, P. R.; Ramachandran, A. M.; Mohamed, A.; Pillai, S., Photonic band gap effect and dye-encapsulated cucurbituril-triggered enhanced fluorescence using monolithic colloidal photonic crystals. *New Journal of Chemistry* **2019,** *43* (41), 16264-16272.
234. Lu, L.; Teng, F.; Qi, D.; Wang, L.; Zhang, J., Synthesis of visible-light driven CrxOy–TiO2 binary photocatalyst based on hierarchical macro–mesoporous silica. *Applied Catalysis B: Environmental* **2015,** *163*, 9-15.

235. Li, W.; Cheng, B.; Xiao, P.; Chen, T.; Zhang, J.; Yu, J., Low-Temperature-Processed Monolayer Inverse Opal SnO_2 Scaffold for Efficient Perovskite Solar Cells. *Small* **2022,** *18* (49), 2205097.
236. Gun, Y.; Song, G. Y.; Quy, V. H. V.; Heo, J.; Lee, H.; Ahn, K.-S.; Kang, S. H., Joint effects of photoactive TiO2 and fluoride-doping on SnO2 inverse opal nanoarchitecture for solar water splitting. *ACS Applied Materials & Interfaces* **2015,** *7* (36), 20292-20303.
237. Norman, M. A.; Perez, W. L.; Kline, C. C.; Coridan, R. H., Enhanced Photoelectrochemical Energy Conversion in Ultrathin Film Photoanodes with Hierarchically Tailorable Mesoscale Structure. *Advanced Functional Materials* **2018,** *28* (29), 1800481.
238. Guo, S.; Li, D.; Zhang, Y.; Zhang, Y.; Zhou, X., Fabrication of a novel SnO_2 photonic crystal sensitized by CdS quantum dots and its enhanced photocatalysis under visible light irradiation. *Electrochimica Acta* **2014,** *121*, 352-360.
239. Yun, G.; Balamurugan, M.; Kim, H.-S.; Ahn, K.-S.; Kang, S. H., Role of WO_3 layers electrodeposited on SnO2 inverse opal skeletons in photoelectrochemical water splitting. *The Journal of Physical Chemistry C* **2016,** *120* (11), 5906-5915.
240. Raja-Mogan, T.; Ohtani, B.; Kowalska, E., Photonic crystals for plasmonic photocatalysis. *Catalysts* **2020,** *10* (8), 827.
241. Yadav, A.; Gerislioglu, B.; Ahmadivand, A.; Kaushik, A.; Cheng, G. J.; Ouyang, Z.; Wang, Q.; Yadav, V. S.; Mishra, Y. K.; Wu, Y., Controlled self-assembly of plasmon-based photonic nanocrystals for high performance photonic technologies. *Nano Today* **2021,** *37*, 101072.
242. Tran, V. T.; Nguyen, H.-Q.; Kim, Y.-M.; Ok, G.; Lee, J., Photonic–Plasmonic Nanostructures for Solar Energy Utilization and Emerging Biosensors. *Nanomaterials* **2020,** *10* (11), 2248.
243. Klimonsky, S.; Baranchikov, A.; Lad, V.; Eremina, E.; Garshev, A.; Kuznetsov, A.; Jalolov, F.; Demidovich, P., Photonic and plasmonic effects in inverse opal films with Au nanoparticles. *Photonics and Nanostructures-Fundamentals and Applications* **2021,** *43*, 100899.
244. Boppella, R.; Marques Mota, F.; Lim, J. W.; Kochuveedu, S. T.; Ahn, S.; Lee, J.; Kawaguchi, D.; Tanaka, K.; Kim, D. H., Plasmon and upconversion mediated broadband spectral response in TiO_2 inverse opal photocatalysts for enhanced photoelectrochemical water splitting. *ACS Applied Energy Materials* **2019,** *2* (5), 3780-3790.
245. Temerov, F.; Pham, K.; Juuti, P.; Mäkelä, J. M.; Grachova, E. V.; Kumar, S.; Eslava, S.; Saarinen, J. J., Silver-decorated TiO2 inverse opal structure for visible light-induced photocatalytic degradation of organic pollutants and hydrogen evolution. *ACS Applied Materials & Interfaces* **2020,** *12* (37), 41200-41210.
246. Zheng, X.; Zhang, Z.; Meng, S.; Wang, Y.; Li, D., Regulating charge transfer over 3D Au/ZnO hybrid inverse opal toward efficiently photocatalytic degradation of bisphenol A and photoelectrochemical water splitting. *Chemical Engineering Journal* **2020,** *393*, 124676.
247. Liu, Y.; Xu, G.; Ma, D.; Li, Z.; Yan, Z.; Xu, A.; Zhong, W.; Fang, B., Synergistic effects of g-C3N4 three-dimensional inverse opals and Ag modification toward high-efficiency photocatalytic H2 evolution. *Journal of Cleaner Production* **2021,** *328*, 129745.
248. Birnal, P.; de Lucas, M. M.; Pochard, I.; Herbst, F.; Heintz, O.; Saviot, L.; Domenichini, B.; Imhoff, L., Visible-light photocatalytic degradation of dyes by TiO_2–Au inverse opal films synthesized by Atomic Layer Deposition. *Applied Surface Science* **2023,** *609*, 155213.
249. Zhang, L.; Lin, C. Y.; Valev, V. K.; Reisner, E.; Steiner, U.; Baumberg, J. J., Plasmonic enhancement in $BiVO_4$ photonic crystals for efficient water splitting. *Small* **2014,** *10* (19), 3970-3978.

250. Zhou, S.; Tang, R.; Zhang, L.; Yin, L., Au nanoparticles coupled three-dimensional macroporous BiVO4/SnO2 inverse opal heterostructure for efficient photoelectrochemical water splitting. *Electrochimica Acta* **2017,** *248*, 593-602.

251. Wei, Y.; Jiao, J.; Zhao, Z.; Liu, J.; Li, J.; Jiang, G.; Wang, Y.; Duan, A., Fabrication of inverse opal TiO2-supported Au@ CdS core–shell nanoparticles for efficient photocatalytic CO_2 conversion. *Applied Catalysis B: Environmental* **2015,** *179*, 422-432.

252. Rahul, T. K.; Sandhyarani, N., Plasmonic and photonic effects on hydrogen evolution over chemically modified titania inverse opals. *ChemNanoMat* **2018,** *4* (7), 642-648.

253. Li, H.; Zhou, S.; Yin, L., Surface Plasmon Resonance Effect Enhanced $CsPbBr_3$ Inverse Opals for High-Performance Inorganic Perovskite Solar Cells. *Advanced Materials Interfaces* **2020,** *7* (12), 1901885.

254. Jiang, P.; Ostojic, G. N.; Narat, R.; Mittleman, D. M.; Colvin, V. L., The fabrication and bandgap engineering of photonic multilayers. *Advanced Materials* **2001,** *13* (6), 389-393.

255. Kubrin, R.; Lee, H. S.; Zierold, R.; Yu. Petrov, A.; Janssen, R.; Nielsch, K.; Eich, M.; Schneider, G. A., Stacking of ceramic inverse opals with different lattice constants. *Journal of the American Ceramic Society* **2012,** *95* (7), 2226-2235.

256. Cai, Z.; Liu, Y. J.; Teng, J.; Lu, X., Fabrication of large domain crack-free colloidal crystal heterostructures with superposition bandgaps using hydrophobic polystyrene spheres. *ACS Applied Materials & Interfaces* **2012,** *4* (10), 5562-5569.

257. Hwang, D.-K.; Noh, H.; Cao, H.; Chang, R. P., Photonic bandgap engineering with inverse opal multistacks of different refractive index contrasts. *Applied Physics Letters* **2009,** *95* (9), 091101.

258. Wang, A.; Chen, S.-L.; Dong, P.; Zhou, Z., Preparation of photonic crystal heterostructures composed of two TiO_2 inverse opal films with different filling factors. *Synthetic Metals* **2011,** *161* (5-6), 504-507.

259. Eftekhari, E.; Broisson, P.; Aravindakshan, N.; Wu, Z.; Cole, I. S.; Li, X.; Zhao, D.; Li, Q., Sandwich-structured TiO 2 inverse opal circulates slow photons for tremendous improvement in solar energy conversion efficiency. *Journal of Materials Chemistry A* **2017,** *5* (25), 12803-12810.

260. Qi, Y.; Chu, L.; Niu, W.; Tang, B.; Wu, S.; Ma, W.; Zhang, S., New encryption strategy of photonic crystals with bilayer inverse heterostructure guided from transparency response. *Advanced Functional Materials* **2019,** *29* (40), 1903743.

261. Zhou, C.; Qi, Y.; Zhang, S.; Niu, W.; Wu, S.; Ma, W.; Tang, B., Bilayer heterostructure photonic crystal composed of hollow silica and silica sphere arrays for information encryption. *Langmuir* **2020,** *36* (5), 1379-1385.

262. Wu, S.; Liu, T.; Tang, B.; Li, L.; Zhang, S., Structural color circulation in a bilayer photonic crystal by increasing the incident angle. *ACS Applied Materials & Interfaces* **2019,** *11* (10), 10171-10177.

263. Meng, Z.; Wu, Y.; Ren, J.; Li, X.; Zhang, S.; Wu, S., Upconversion Nanoparticle-Integrated Bilayer Inverse Opal Photonic Crystal Film for the Triple Anticounterfeiting. *ACS Applied Materials & Interfaces* **2022,** *14* (10), 12562-12570.

264. Li, H.; Wang, J.-f.; Robichaud, J.; Djaoued, Y., New one step self-assembly strategy of large-area highly ordered, crack-free 2D inverse opal films of transition metal oxides and its application to fabrication of bilayer inverse opal films. *Macromolecular Research* **2019,** *27* (12), 1229-1238.

265. Wang, Y.; Li, P.; Chen, S.-L.; Wang, A.-J., Dual-bandgap effect of photonic crystals on TiO 2 photocatalytic activity in ultraviolet and visible light regions. *Catalysis Surveys from Asia* **2019,** *23*, 23-32.

266. Wang, X.-G.; Wang, J.; Jiang, Z.-J.; Tao, D.-W.; Zhang, X.-Q.; Wang, C.-W., Silver loaded anodic aluminum oxide dual-bandgap heterostructure photonic crystals and their application for surface enhanced Raman scattering. *Applied Surface Science* **2021,** *544*, 148881.

267. Mihi, A.; Míguez, H.; Rodríguez, I.; Rubio, S.; Meseguer, F., Surface resonant modes in colloidal photonic crystals. *Physical Review B* **2005,** *71* (12), 125131.

268. Lee, S.-H. A.; Abrams, N. M.; Hoertz, P. G.; Barber, G. D.; Halaoui, L. I.; Mallouk, T. E., Coupling of titania inverse opals to nanocrystalline titania layers in dye-sensitized solar cells. *The Journal of Physical Chemistry B* **2008,** *112* (46), 14415-14421.

269. O'Brien, P. G.; Kherani, N. P.; Zukotynski, S.; Ozin, G. A.; Vekris, E.; Tetreault, N.; Chutinan, A.; John, S.; Mihi, A.; Miguez, H., Enhanced Photoconductivity in Thin-Film Semiconductors Optically Coupled to Photonic Crystals. *Advanced Materials* **2007,** *19* (23), 4177-4182.

270. Guldin, S.; Huttner, S.; Kolle, M.; Welland, M. E.; Muller-Buschbaum, P.; Friend, R. H.; Steiner, U.; Tétreault, N., Dye-sensitized solar cell based on a three-dimensional photonic crystal. *Nano Letters* **2010,** *10* (7), 2303-2309.

271. Huo, T.; Zhang, X.; Dong, X.; Zhang, X.; Ma, C.; Wang, G.; Ma, H.; Xue, M., Photonic crystal coupled porous BiVO 4 hybrid for efficient photocatalysis under visible light irradiation. *Journal of Materials Chemistry A* **2014,** *2* (41), 17366-17370.

272. Karuturi, S. K.; Cheng, C.; Liu, L.; Su, L. T.; Fan, H. J.; Tok, A. I. Y., Inverse opals coupled with nanowires as photoelectrochemical anode. *Nano Energy* **2012,** *1* (2), 322-327.

273. Loukopoulos, S.; Toumazatou, A.; Sakellis, E.; Xenogiannopoulou, E.; Boukos, N.; Dimoulas, A.; Likodimos, V., Heterostructured CoOx–TiO_2 mesoporous/photonic crystal bilayer films for enhanced visible-light harvesting and photocatalysis. *Materials* **2020,** *13* (19), 4305.

274. Chen, S. L.; Wang, A. J.; Hu, C. T.; Dai, C.; Benziger, J. B., Enhanced photocatalytic performance of nanocrystalline TiO2 membrane by both slow photons and stop-band reflection of photonic crystals. *AIChE Journal* **2012,** *58* (2), 568-572.

275. Chen, S.-L.; Wang, A.-J.; Dai, C.; Benziger, J. B.; Liu, X.-C., The effect of photonic band gap on the photo-catalytic activity of nc-TiO_2/SnO_2 photonic crystal composite membranes. *Chemical Engineering Journal* **2014,** *249*, 48-53.

276. Li, P.; Wang, Y.; Chen, S.-L.; Wang, A.-J., Enhancement of gas–solid photocatalytic activity of nanocrystalline TiO_2 by SiO_2 opal photonic crystal. *Journal of materials science* **2016,** *51*, 2079-2089.

277. Al Rammal, M.; Akkaoui, K.; Halaoui, L. I., Multijunction Photoanode of Mo: $BiVO_4$ Layered with TiO2 Inverse Opal and NiBi Oxygen Evolution Catalyst to Trap Light and Enhance Water Splitting. *The Journal of Physical Chemistry C* **2022,** *126* (16), 6960-6972.

278. Xia, Y.; Gates, B.; Yin, Y.; Lu, Y., Monodispersed colloidal spheres: old materials with new applications. *Advanced Materials* **2000,** *12* (10), 693-713.

279. Schroden, R. C.; Al-Daous, M.; Blanford, C. F.; Stein, A., Optical properties of inverse opal photonic crystals. *Chemistry of Materials* **2002,** *14* (8), 3305-3315.

280. Li, Z.-Y.; Zhang, Z.-Q., Fragility of photonic band gaps in inverse-opal photonic crystals. *Physical Review B* **2000,** *62* (3), 1516.

281. Li, Z. Y.; Zhang, Z. Q., Photonic Bandgaps in Disordered Inverse-Opal Photonic Crystals. *Advanced Materials* **2001,** *13* (6), 433-436.

282. Sordello, F.; Duca, C.; Maurino, V.; Minero, C., Photocatalytic metamaterials: TiO_2 inverse opals. *Chemical Communications* **2011,** *47* (21), 6147-6149.

283. Sordello, F.; Minero, C., Photocatalytic hydrogen production on Pt-loaded TiO_2 inverse opals. *Applied Catalysis B: Environmental* **2015,** *163*, 452-458.

284. Cai, J.; Wu, M.; Wang, Y.; Zhang, H.; Meng, M.; Tian, Y.; Li, X.; Zhang, J.; Zheng, L.; Gong, J., Synergetic enhancement of light harvesting and charge separation over surface-disorder-engineered TiO_2 photonic crystals. *Chem* **2017,** *2* (6), 877-892.

285. Liu, J.; Liu, G.; Li, M.; Shen, W.; Liu, Z.; Wang, J.; Zhao, J.; Jiang, L.; Song, Y., Enhancement of photochemical hydrogen evolution over Pt-loaded hierarchical titania photonic crystal. *Energy & Environmental Science* **2010,** *3* (10), 1503-1506.

286. Rahul, T. K.; Sandhyarani, N., In Situ Gold-Loaded Fluorinated Titania Inverse Opal Photocatalysts for Enhanced Solar-Light-Driven Hydrogen Production. *ChemNanoMat* **2017,** *3* (7), 503-510.

287. Qi, D.; Lu, L.; Xi, Z.; Wang, L.; Zhang, J., Enhanced photocatalytic performance of TiO_2 based on synergistic effect of Ti^{3+} self-doping and slow light effect. *Applied Catalysis B: Environmental* **2014,** *160*, 621-628.

288. Wang, Y.; Peng, C.; Jiang, T.; Zhang, J.; Jiang, Z.; Li, X., Construction of defect-engineered three-dimensionally ordered macroporous WO_3 for efficient photocatalytic water oxidation reaction. *Journal of Materials Chemistry A* **2021,** *9* (5), 3036-3043.

289. Gopinath, C. S.; Nalajala, N., A scalable and thin film approach for solar hydrogen generation: a review on enhanced photocatalytic water splitting. *Journal of Materials Chemistry A* **2021,** *9* (3), 1353-1371.

290. Lagendijk, A., Gomez Rivas, J., Imhof, A., Schuurmans, F.J.P., Sprik, R. (2001). Propagation of Light in Disordered Semiconductor Materials. In: Soukoulis, C.M. (eds) *Photonic Crystals and Light Localization in the 21st Century*. NATO Science Series, vol 563. Springer.

291. Mouchet, S. R.; Luke, S.; McDonald, L. T.; Vukusic, P., Optical costs and benefits of disorder in biological photonic crystals. *Faraday Discussions* **2020,** *223*, 9-48.

292. Moon, J. H.; Yi, G. R.; Yang, S. M.; Pine, D. J.; Park, S. B., Electrospray-Assisted Fabrication of Uniform Photonic Balls. *Advanced Materials* **2004,** *16* (7), 605-609.

293. Zhao, Y.; Shang, L.; Cheng, Y.; Gu, Z., Spherical colloidal photonic crystals. *Accounts of Chemical Research* **2014,** *47* (12), 3632-3642.

294. Vogel, N.; Utech, S.; England, G. T.; Shirman, T.; Phillips, K. R.; Koay, N.; Burgess, I. B.; Kolle, M.; Weitz, D. A.; Aizenberg, J., Color from hierarchy: Diverse optical properties of micron-sized spherical colloidal assemblies. *Proceedings of the National Academy of Sciences* **2015,** *112* (35), 10845-10850.

295. Zhao, Y.; Shang, L.; Cheng, Y.; Gu, Z., Spherical colloidal photonic crystals. *Accounts of Chemical Research* **2014,** *47* (12), 3632-3642.

296. Zhao, Y.; Zhao, X.; Hu, J.; Xu, M.; Zhao, W.; Sun, L.; Zhu, C.; Xu, H.; Gu, Z., Encoded porous beads for label-free multiplex detection of tumor markers. *Advanced Materials* **2009,** *21* (5), 569-572.

297. Cui, J.; Zhu, W.; Gao, N.; Li, J.; Yang, H.; Jiang, Y.; Seidel, P.; Ravoo, B. J.; Li, G., Inverse opal spheres based on polyionic liquids as functional microspheres with tunable optical properties and molecular recognition capabilities. *Angewandte Chemie International Edition* **2014,** *53* (15), 3844-3848.

298. Ohnuki, R.; Sakai, M.; Takeoka, Y.; Yoshioka, S., Optical characterization of the photonic ball as a structurally colored pigment. *Langmuir* **2020,** *36* (20), 5579-5587.

299. Liu, X.-M.; Zhong, W.-L.; Huang, Y.-C.; Zhang, G.-S.; Bai, X.-K.; Wei, X.-C.; Lei, C.-X., Facile preparation of spherical TiO 2 inverse opals with enhanced visible-light photodegradation of methylene blue. *Journal of Materials Science: Materials in Electronics* **2021,** *32*, 21742-21755.

300. Yang, Q.; Li, M.; Liu, J.; Shen, W.; Ye, C.; Shi, X.; Jiang, L.; Song, Y., Hierarchical TiO 2 photonic crystal spheres prepared by spray drying for highly efficient photocatalysis. *Journal of Materials Chemistry A* **2013,** *1* (3), 541-547.

301. von Freymann, G.; Kitaev, V.; Lotsch, B. V.; Ozin, G. A., Bottom-up assembly of photonic crystals. *Chemical Society Reviews* **2013,** *42* (7), 2528-54.

302. Phillips, K. R.; Zhang, C. T.; Yang, T.; Kay, T.; Gao, C.; Brandt, S.; Liu, L.; Yang, H.; Li, Y.; Aizenberg, J., Fabrication of photonic microbricks via crack engineering of colloidal crystals. *Advanced Functional Materials* **2020,** *30* (26), 1908242.

303. Palacios-Lidón, E.; Juárez, B. H.; Castillo-Martinez, E.; López, C., Optical and morphological study of disorder in opals. *Journal of Applied Physics* **2005,** *97* (6), 063502.

304. Rengarajan, R.; Mittleman, D.; Rich, C.; Colvin, V., Effect of disorder on the optical properties of colloidal crystals. *Physical Review E* **2005,** *71* (1), 016615.

305. Vlasov, Y. A.; Astratov, V.; Baryshev, A.; Kaplyanskii, A.; Karimov, O.; Limonov, M., Manifestation of intrinsic defects in optical properties of self-organized opal photonic crystals. *Physical Review E* **2000,** *61* (5), 5784.

306. Phillips, K. R.; England, G. T.; Sunny, S.; Shirman, E.; Shirman, T.; Vogel, N.; Aizenberg, J., A colloidoscope of colloid-based porous materials and their uses. *Chemical Society Reviews* **2016,** *45* (2), 281-322.

307. Chen, J. I.; von Freymann, G.; Kitaev, V.; Ozin, G. A., Effect of disorder on the optically amplified photocatalytic efficiency of titania inverse opals. *Journal of the American Chemical Society* **2007,** *129* (5), 1196-1202.

308. Mortensen, N. A.; Xiao, S., Slow-light enhancement of Beer-Lambert-Bouguer absorption. *Applied Physics Letters* **2007,** *90* (14), 141108.

309. Grgić, J.; Pedersen, J. G.; Xiao, S.; Mortensen, N., Group index limitations in slow-light photonic crystals. *Photonics and Nanostructures-Fundamentals and Applications* **2010,** *8* (2), 56-61.

310. Zhang, X.; John, S., Enhanced photocatalysis by light-trapping optimization in inverse opals. *Journal of Materials Chemistry A* **2020,** *8* (36), 18974-18986.

311. Zhang, X.; John, S., Photonic crystal light trapping for photocatalysis. *Optics Express* **2021,** *29* (14), 22376-22402.

312. Deparis, O., Poynting vector in transfer-matrix formalism for the calculation of light absorption profile in stratified isotropic optical media. *Optics Letters* **2011,** *36* (20), 3960-3962.

313. Moharam, M.; Gaylord, T., Rigorous coupled-wave analysis of planar-grating diffraction. *JOSA* **1981,** *71* (7), 811-818.

314. Pendry, J., Photonic band structures. *Journal of Modern Optics* **1994,** *41* (2), 209-229.

315. Vigneron, J.-P.; Forati, F.; André, D.; Castiaux, A.; Derycke, I.; Dereux, A., Theory of electromagnetic energy transfer in three-dimensional structures. *Ultramicroscopy* **1995,** *61* (1-4), 21-27.

316. Johnson, S. G.; Joannopoulos, J. D., Block-iterative frequency-domain methods for Maxwell's equations in a planewave basis. *Optics Express* **2001,** *8* (3), 173-190.

317. Yee, K., Numerical solution of initial boundary value problems involving Maxwell's equations in isotropic media. *IEEE Transactions on Antennas and Propagation* **1966,** *14* (3), 302-307.
318. Taflove, A., Application of the finite-difference time-domain method to sinusoidal steady-state electromagnetic-penetration problems. *IEEE Transactions on Electromagnetic Compatibility* **1980,** (3), 191-202.
319. Taflove, A.; Hagness, S. C.; Piket-May, M., Computational electromagnetics: the finite-difference time-domain method. *The Electrical Engineering Handbook* **2005,** *3*, 629-670.
320. Taflove, A.; Oskooi, A.; Johnson, S. G., *Advances in FDTD computational electrodynamics: photonics and nanotechnology*. Artech house: 2013.
321. Hrennikoff, A., Solution of problems of elasticity by the framework method. *Journal of Applied* Mechanics **1941**, 8(4), A169-A175.
322. Courant, R., Variational methods for the solution of problems of equilibrium and vibrations. **1943**.
323. Zienkiewicz, O. C.; Taylor, R. L.; Zhu, J. Z., *The finite element method: its basis and fundamentals*. Elsevier: 2005.
324. Reddy, J. N., *Introduction to the finite element method*. McGraw-Hill Education: 2019.

CHAPTER II

Research objectives and strategies

Overview

This chapter deals with the research objectives and the strategies employed to attain them. Firstly, the overall objective of this thesis work is presented. This broad objective serves as the thread that binds all the independent works that constitute different sections of this thesis. The broad objective is then broken down into smaller objectives that are enumerated and presented in detail. Secondly, the strategies pertaining to the overall objective and each of the smaller objectives are presented in detail. Strategies were designed based on challenges encountered by other researchers in this field, as obtained from the literature survey.

2. Research objectives and strategies

2.1. Objectives

The ultimate objective of my research was to improve visible light harvesting efficiency in photocatalytic hydrogen evolution from water by using the ‘slow photon effect’ in inverse opal photonic structures. Photonic structures have the unique property of reducing the group velocity of light at specific frequencies and localizing it within the structure thereby increasing light-matter interaction and improving light harvesting efficiency, which can be potentially used in many light harvesting applications. The objective of my research was to use this light-manipulating photonic property to enhance photocatalytic water splitting efficiency. This overall objective was addressed by breaking it down into smaller and more specific objectives.

The first specific objective was to establish a proof of concept concerning the ability to generate and tune slow photons in IO photonic structures for photocatalytic enhancement. Previous researchers who had attempted to establish the concept were limited to single component IO photocatalysts, mostly IO TiO_2, responsive in the UV-range. Further, they were mostly limited to solid and gas phase photocatalysis, whereas most industrial applications including water splitting are conducted in aqueous phase. Hence, my objective was to validate the concept in aqueous phase photocatalysis using a composite photocatalyst system that absorbs light in the visible range. This objective was further sub-divided into the following smaller goals: (i) synthesizing quality IO structures that can generate slow photons, and (ii) attaining control over the wavelengths of slow photons to tune them to the electronic absorption of the photocatalyst.

The second specific objective was to generate slow photons over multiple spectral ranges, to further improve light harvesting efficiency. This objective was based on the fact that slow photons in photonic structures are limited to narrow spectral ranges, which limits light absorption enhancement. Prior research towards attaining this objective is highly limited. The few research works that attempted to slow down light at multiple spectral ranges resulted in sub-optimal structures, lacking precise control over the frequencies of slow photons. Hence, the objective was to synthesize structures that are capable of slowing down light at multiple spectral ranges and to accurately tune their frequencies for enhancing light absorption and photocatalytic efficiency.

The third specific objective was to utilize slow photons in the photocatalytic evolution of hydrogen from water under UV-Visible light. Most of the research works on ‘slow photon effect’ in IO structures were limited to photocatalytic dye degradation. The primary reason for this is that photocatalytic water splitting is a thermodynamically ‘uphill reaction’, which is more challenging, requiring the deployment of additional strategies to realize it. Hence, the third specific objective was conceived to tackle this challenge, and make slow photon effect relevant for practical applications, particularly in the field of renewable and sustainable energy.

2.2. Scientific strategies

The strategy used to achieve the overall objective was to first ratify the concept of slow photon assistance in improving visible light photocatalytic dye degradation and then to extend it to photocatalytic water splitting.

The basic requisites to implement these strategies are firstly to generate slow photons by synthesizing high quality inverse opal photonic structures and secondly to tune their frequencies to the absorption of the photo-responsive material. Although other photonic structures like opal structures, nanoarrays and nanorods were tested in slow photon-assisted photocatalysis, IO structures were preferred in this work due to the versatility of the colloid-templated method that facilitates the synthesis of high-quality photonic structures. Various semiconductor photocatalysts can be moulded into IO structures like TiO_2, ZnO, WO_3, Fe_2O_3, Ga_2O_3, $InVO_4$, $BiVO_4$, $SrTiO_3$, Fe_2TiO_5, $ZnGa_2O_4$, $CuCrO_2$ and CdS. Among them, TiO_2 was chosen in this work, firstly since it is a low-cost, non-toxic semiconductor, and secondly since it is relatively easier to synthesize highly ordered IO photonic structures of this semiconductor.

Contrary to most prior research works that focussed on particulate form of IO TiO_2 in a suspended photocatalyst system, this work preferred IO TiO_2 as film on a substrate in a fixed photocatalyst system. The rationale behind this strategy is that in IO particulate form, different planes of the IO structure are exposed to the incident light causing the averaging of the SBG in all directions, that results either in the broadening of SBG or the complete disappearance of SBG. Precise control over slow photon frequencies in this case becomes extremely challenging. Contrarily, in IO film, a single plane is exposed to incident light, resulting in a distinct SBG with slow photons at its edges, whose frequencies can be precisely tuned.

The two-step coassembly approach was adopted in this work to synthesize IO TiO_2 on a substrate. This synthesis strategy was intended to reduce disorder, as it reduces the number of steps in the synthesis and avoids the challenges of overlayer formation and crack formation in the three-step process. Precursors in the coassembly approach can be either 'soft', as in the case of TiBALDH and Ti(OPr)$_4$, or hard as in the case of crystalline TiO_2 nanoparticles. In the first case, shrinkage of the 'soft' precursor in the process of phase transformation during calcination leads to structural deterioration while in the second case, the 'hard' precursor fails to accommodate the stresses resulting from the natural shrinkage of the films during the process of drying. To address these issues, prefabricated crystalline-amorphous bi-phase TiO_2 nanoparticles were used, that served as a dynamic 'soft-hard' precursor, to mitigate stresses during drying and calcination.

The disadvantage of TiO_2 is that it absorbs light only in the UV range (3.2 eV and 3.1 eV band gap for anatase and rutile TiO_2 phases respectively), which limits its efficiency under sunlight, as most of the sunlight is concentrated in the visible range. Since the objective of this research was to use slow photons in the visible range, the strategy adopted to extend the absorption of IO TiO_2 to the visible range was to embed visible light responsive $BiVO_4$ nanoparticles in IO TiO_2 structure. Successive Ionic Layer Adsorption and Reaction (SILAR) method was opted for this purpose as this method permits a precise control of the $BiVO_4$ deposition by controlling the concentration of the respective cationic and anionic salts and by controlling the number of SILAR cycles.

The next challenge was to tune the wavelength of SBG and hence those of the slow photons. Tuning of slow photon wavelengths was mostly realized in prior research works by changing the lattice parameter (pore size) of the IO structure, which in turn was controlled by varying the size of the templating colloids. However, this single approach does not unambiguously justify the impact of slow photons in photocatalysis. To firmly establish the proof of concept, we adopted the strategy of employing both lattice parameter and light incidence angle variations to tune slow photons. To ensure a precise change in light incidence angle, we set up a device involving an optical fibre connected to a light source, mounted on an optical fiber holder, with the IO film photocatalyst fixed to the bottom of the fibre holder. The optical fibre holder permitted the precise change in light incidence angle with an increment of 15°. Determination of both angle-dependent photonic properties and angle-dependent photocatalysis were undertaken using this set-up.

The strategy employed to realize the second sub-objective of using slow photons at multiple spectral ranges was to synthesize bilayer IO structures, with each layer having a different lattice parameter (pore size), that manifests two distinct stop band gaps with slow photons at either edge of each of them. Bilayer IO structures can be synthesized by either of these approaches: (i) synthesizing the IO structure and using it as a substrate for the coassembly of the second PS+TiO_2 layer, (ii) coassembly of the first PS+TiO_2 layer and using it as a substrate for the coassembly of the second PS+TiO_2 layer. The second approach was adopted after trying both methods, as it yielded structures with better structural order and more consistent photonic properties.

Multiple strategies were employed to attain the third sub-objective of using slow photons for improving light harvesting in the photocatalytic evolution of hydrogen from water under UV-Visible light. Besides the strategies pertaining to slow photon effect mentioned above, additional strategies of localized surface plasmon resonance effect using Au NPs and cocatalyst assistance using Pt NPs were envisaged. Since $BiVO_4$ does not satisfy the thermodynamic requirements for water splitting, CdS was used as a visible light absorbing semiconductor photocatalyst in this case. Slow photons were envisaged to be tuned such that both CdS electronic absorption and Au plasmonic absorption could be enhanced.

CHAPTER III

Materials and characterization methods

Overview

This chapter provides a list of the materials and characterization methods used in the experimental part of this thesis. Firstly, the materials used, the vendors from which they were ordered, and their purity as indicated by the vendor, are enlisted. Secondly, the characterization methods employed in this thesis, along with the details of the instruments used are provided.

3. Materials and characterization methods

3.1. Materials

The chemicals used in this research work were ordered from the following vendors: styrene (99%), and titanium (IV) isopropoxide (TIP) (98+%), sodium sulfide (Na_2S) (98+%), and ammonia (NH_3) (25% in water) from Acros Organics, polyvinylpyrrolidone (PVP) from TCI Chemicals, potassium persulfate ($K_2S_2O_8$) (≥ 99%), tetramethylammonium hydroxide (TMAH) (25% in water) and 2-propanol (≥ 99.5%) from Sigma Aldrich; bismuth (III) nitrate pentahydrate ($Bi(NO_3)_3.5H_2O$) (≥ 98%), ammonium monovanadate (NH_4VO_3) (≥ 99.8%), sulfuric acid (H_2SO_4) (≥ 98%), nitric acid (HNO_3) (≥ 65%) and hydrogen peroxide (H_2O_2) (≥ 98%) from Carl Roth; Rhodamine B (RhB), sodium tetrachloroaurate(III) dihydrate ($NaAuCl_4.2H_2O$) (99%) and hexachloroplatinic(IV) acid hexahydrate ($H_2PtCl_6.6H_2O$) (99%) from Alfa Aesar, and hydrochloric acid (HCl) (37% in water) from Thermoscientific; sodium sulfide (Na_2S) and sodium sulfite (Na_2SO_3) from Alladin chemicals.

Polystyrene (PS) colloids were procured from the following vendors: PS 300 nm diameter (10% w/v) from Sigma Aldrich, PS 418 nm, PS 425 nm and PS 460 nm diameter (5% w/v) from gMBH, and PS 397 nm diameter (10% w/v) from Bangs Laboratories.

Microscope glass slides (7.5×2.5 cm^2) were ordered from VWR, while Fluorine-doped Tin Oxide (FTO) substrates (20×15 mm^2) were ordered from Ossila. Deionized milli-Q water (12 mΩ) was used in all experiments. All glassware was cleaned with aqua regia (3:1 HNO_3:HCl) (caution: highly corrosive) and rinsed thoroughly with distilled water before use.

3.2. Characterization methods

Dynamic Light Scattering (DLS) technique was employed to estimate the size distribution of PS colloids and Au NPs, using NanoPlus HD zeta/nanoparticle analyser.

Zeta potential of PS colloids and TiO_2 nanoparticles was measured by Electrophoretic Light Scattering using Zetasizer Ultra, with M3-PALS under constant current zeta mode, and the data was analyzed using ZS XPLORER Software.

Scanning Electron Microscope (SEM) images to study the morphology of the synthesized structures, were taken with a JEOL JSM-7500F SEM equipped with an X-ray analysis probe operating at 20-kV accelerating voltage.

Energy Dispersive X-ray Spectroscopy (EDX) for elemental mapping and quantitative analysis was performed using the same instrument.

Transmission Electron Microscope (TEM) and **High-Angle Annular Dark-Field Scanning Transmission Electron Microscope (HAADF-STEM)** along with **Selected Area Electron Diffraction (SAED)** patterns and **Energy Dispersive X-ray spectroscopy (EDX)** elemental mapping and analysis were obtained from Tecnai G^2 20LaB6 TEM equipped with Bruker X-flash 6Ti30 detector operated at 200 kV, and from a field emission gun (FEG) Talos microscope (Thermofischer Scientific) operated at 200 kV.

Atomic force microscopy (AFM) images to study the surface morphology were recorded in tapping-mode using Nanoscope III, BrukerTM, with Si cantilevers (Nanosensors PPP-NCHR) having a resonance frequency of 290 kHz, a nominal spring constant of 42 N/m, and an integrated Si tip with a nominal apex radius of curvature lower than 10 nm.

Optical microscopic images (OM) to study the morphology of the structures under low resolution were obtained using an Olympus BX 61 microscope fitted with an Olympus XC50 camera and a halogen Osram HLX 64625 visible light source.

Micro-spectrophotometric reflectance measurement to determine the position of the stop band gap of the photonic structures were taken using the same instrument, with an Ocean optics QE65 Pro spectrophotometer connected to the microscope, after normalizing with respect to the intensity reflected by an Avantes WS-2 white diffusor.

Angle-dependent specular reflectance measurements to study the variation of reflectance with light incidence angle were taken with Avantes AvaSpec-2048-2 spectrophotometer (after calibrating with an Avantes WS-2 white diffusor), equipped with AvaLight-DH-S-BAL deuterium-halogen light source. For reflectance measurements at normal light incidence, an Avantes FCR UV200 bifurcated optical fibre reflection probe (with one part connected to the light source and the other to the spectrophotometer) was used to guide the incident and reflected light. For reflectance measurements at other angles, two Avantes FC-UV-200 optical fibres in specular configuration (one connected to the light source and the other to the spectrophotometer) were used. To mount the probes, an Avantes AFH-15 fibre holder that permitted the variation of angle of incidence and detection from 0° to 75° in steps of 15° was used.

UV-Visible spectroscopy to determine the absorptance of the solid samples was performed using Perkin Elmer 750S UV/Vis/NIR spectrophotometer after calibration with a Labsphere SRS-99-020 white reference. Absorbance of RhB solutions during photodegradation experiments was determined using Varian Cary 5000 UV-Vis-NIR (UV 1001M187) and Bio-Tek Instruments UVIKON XS UV-Visible spectrophotometers in the spectral range of 400-700 nm.

Thermogravimetric analysis (TGA) and Differential Scanning Calorimetry (DSC) measurements were performed on a Mettler Toledo TGA/DSC 3+ apparatus. Solid samples (6-7 mg) were placed in open alumina pans (100µL). Nitrogen (60 mL/min) was used as purge gas. Temperature range was from 0 to 700°C with a heating rate of 2°C/min. Results were analysed using the STARe software, version 16.20.

X-ray diffraction (XRD) patterns to study the crystalline structure of the materials were obtained from PANalytical X'PERT PRO Bragg-Brentano diffractometer using Cu Kα radiation (λ = 1.54184 Å) measured in 2θ angle range 20° - 60°.

Grazing-incident powder X-ray diffraction patterns to study the crystalline structure of inverse opal films were collected using Stoe STADI MP diffractometer (2θ-θ geometry, Cu Kα*1* radiation, focusing Ge(111) monochromator in parallel beam position, silicon strip detector MYTHEN 1K). The height of each sample was aligned using micrometre stage. Grazing angle was optimized for each sample and was typically less than 1°. The powder patterns were obtained from 20 to 80° in 2θ, and the data collection time was adjusted from 2 to 50 h to ensure sufficient quality.

X-ray photoelectron spectroscopy (XPS) measurements to study the valence states and the chemical environment of the elements were obtained from a K-alpha spectrometer (Thermofisher), using a monochromatic Al Kα source (1,486.6 eV) with a spot size of 300 µm. Survey and high-resolution spectra were recorded by calibrating with C_{1s} with an energy step of 1.0 and 0.1 eV, and a pass energy of 200 eV and 25 eV respectively. Data processing was done using Thermo Avantage software. To prevent surface charging during measurements, a flood gun with combined electron and low energy ions was used.

Contact angle (CA) measurements to study the hydrophilicity of the films were taken with an OCA 35 contact angle instrument using 2 µL droplets of water. used.

Photoelectrochemical (PEC) measurements to determine the photocurrent of the samples were obtained from CH1660D electrochemical workstation using PLS-SXE-300D light source ($320<\lambda<780$ nm, 158 mW cm^{-2}). Measurements were taken in a 100-mL quartz cell containing 0.5-M Na_2SO_4 electrolyte under a three-electrode configuration with the sample as working electrode, calomel electrode as reference electrode and Pt foil as counter electrode. The sample deposited over 1.875 cm^2 on the FTO substrate was placed at 10 cm from the light source and was illuminated at zero bias voltage with respect to the reference electrode. used.

Photoluminescence (PL) excitation spectra to study the charge separation/recombination were taken using Hitachi FL 4700 Spectrophotometer under emission scan mode with the excitation wavelength at 320 nm.

N_2-adsorption/desorption isotherms were obtained from ASAP 2420, Micrometrics, porosimeter. The isotherms were recorded at -196°C, after degassing the samples at 150°C for 8h. From the data, the specific surface area was calculated using Brunauer-Emmett-Teller (BET) equation[1], with relative pressures ranging from 0.05 to 0.21. The total pore volume was estimated based on the amount adsorbed at a relative pressure of 0.98[2]. The pore size distribution and average pore size were plotted based on calculations usin Barrett-Joyner-Halenda (BJH) method[3].

References

1. Brunauer, S.; Emmett, P. H.; Teller, E., Adsorption of gases in multimolecular layers. *Journal of the American Chemical Society* **1938,** *60* (2), 309-319.
2. Zepeda, T.; Fierro, J.; Pawelec, B.; Nava, R.; Klimova, T.; Fuentes, G. A.; Halachev, T., Synthesis and characterization of Ti-HMS and CoMo/Ti-HMS oxide materials with varying Ti content. *Chemistry of Materials* **2005,** *17* (16), 4062-4073.
3. Barrett, E. P.; Joyner, L. G.; Halenda, P. P., The determination of pore volume and area distributions in porous substances. I. Computations from nitrogen isotherms. *Journal of the American Chemical Society* **1951,** *73* (1), 373-380.

CHAPTER IV

Tuning and transferring slow photons from TiO_2 photonic crystals to $BiVO_4$ nanoparticles for highly enhanced visible light photocatalysis*

Abstract

Periodic structures with alternating refractive indices such as inverse opal photonic crystals are capable of reducing the group velocity of light such that this slowed light can be more efficiently harvested for highly enhanced solar energy conversion. However, the generation, the manipulation and, in particular, the practical applications of these slow photons remain highly challenging. Here, we report the first proof of concept on the ability to control, in an inverse opal TiO_2-$BiVO_4$ hetero-composite, the transfer of slow photons generated from the inverse opal photonic structure to the visible light-responsive $BiVO_4$ nanoparticles for highly enhanced visible light photocatalysis. Tuning the slow photon frequencies, in order to accommodate the electronic band gap of $BiVO_4$ for slow photon transfer and for significantly improved light harvesting, was successfully achieved by varying the structural periodicity (pore size) of inverse opal and the light incidence angle. The photocatalytic activity of $BiVO_4$ in all inverse opal structures, promoted by slow photon effect, reached up to 7 times higher than those in the non-structured compact films. This work opens new avenues for the practical utilization of slow photon effect under visible light in photocatalytic energy-related applications like water splitting and carbon dioxide reduction and in photovoltaics.

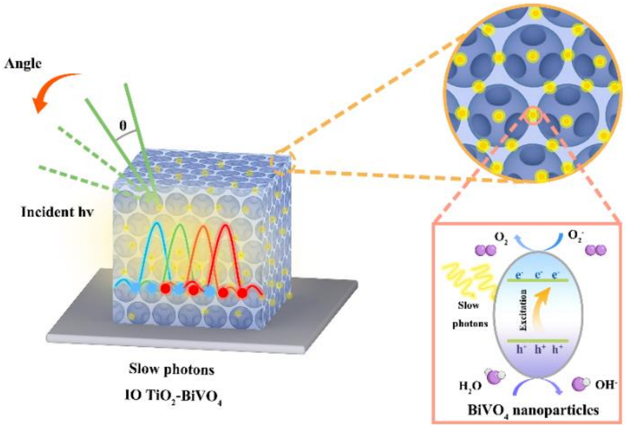

---

*This part of the work has been published in *Journal of Colloids and Interface Science*, 2023, 634, 290-299.

4. Tuning and transferring slow photons from TiO_2 photonic crystals to $BiVO_4$ nanoparticles for highly enhanced visible light photocatalysis

4.1. Introduction

Harnessing solar energy for photocatalytic energy conversion is a pressing global challenge. In the recent past, significant advances have been made in choosing and modifying materials to improve photocatalytic performance[1-3]. However, modifying light for improved light-matter interaction in photocatalysis remains largely underexplored. Inverse opal (IO) photonic structures are among the most promising light-manipulating materials for photocatalytic applications, thanks to their fascinating and exclusive property of slow photon effect (SPE)[4, 5]. Having periodic structures with alternating refractive indices, they are capable of influencing the propagation of photons such that light at a certain wavelength is reflected, creating a photonic stop band gap (SBG), while the group velocity of light at lower and higher frequency edges (blue and red) of the SBG is reduced nearly to zero[6-9]. Such photons, called "slow photons" form a standing wave within the material[10]. When the spectral regions of these slow photons are accurately tuned to overlap with the electronic absorption of the semiconductor, these "confined photons" could be efficiently harvested to improve light energy conversion in photocatalytic, photovoltaic and photoelectrochemical devices[11-14]. To maximize slow photon utilization, tuning strategies including the variation of lattice constant (related to pore diameter), effective refractive index (RI), filling fraction and angle of incidence can be employed to modulate slow photon frequencies.

In the past two decades, various attempts have been made to test IO structures for photocatalysis. Many of them claimed the contribution of slow photons in photocatalytic enhancement, but very few unambiguously established it[15]. The first attempt to demonstrate SPE in photocatalysis was realized in IO TiO_2 for the solid phase photodegradation of methylene blue (MB) by measuring activity at different angles using IO samples with different pore sizes[16]. Later on, researchers probed SPE on IO TiO_2 for RhB degradation in aqueous phase[17, 18]. This was a significant improvement since most industrial photocatalytic reactions are carried out in aqueous phase wherein the change in slow photon frequencies with change in medium needs to be considered. Similarly, SPE was also studied in other materials such as IO Fe_2O_3[19], IO Bi_2WO_6[20] and IO ZnO[21]. Recently, it was explored again in IO TiO_2 for aqueous-phase MB degradation[22] and solid-state stearic acid degradation[23] with supportive evidence from simulation studies. The above works, which reported photocatalytic enhancement factors ranging from 2 to 4, between IO structured photocatalysts and their non-structured counterparts were, however, limited to single component photocatalysts, most of them responsive only in the UV region. Exploiting slow photons for visible light photocatalysis becomes an urgent and compelling research subject of current interest.

Although IO structures of visible light responsive semiconducting materials such as simple oxides (e.g. WO_3, Fe_2O_3, Cu_2O etc.), complex oxides (e.g. $BiVO_4$, Fe_2TiO_5), nitrides (e.g. C_3N_4, Ta_3N_5) and sulphides (e.g. CdS, SnS, SnS_2) can be used, the difficulty involved in preparing IO structures of these compounds with tuneable photonic properties along with the lack of satisfactory experimental protocols for preparing long-range ordered structures, renders them less effective for the maximum utilization of slow photon effect. Also, the toxicity of some materials like sulphides impede the implementation of practical research. In addition, forming heterocomposite systems of IO photocatalysts with noble precious metals, which has often been employed to improve visible light harvesting, increases the cost involved in photocatalyst synthesis. The best and realistic scenario is to combine the relatively easy-to-fabricate IO photonic structure of TiO_2, with a low cost, non-toxic and highly visible light-responsive semiconducting material.

We report here, for the first time, the utilization of slow photons in a visible-light active, bi-component IO TiO_2-$BiVO_4$ (ITBV) hetero-composite photocatalyst system, chosen in this work to serve as a proof of concept, for highly enhanced photocatalytic performance. Such a concept involving the generation of slow photons by the IO structure, tuning their frequencies through lattice constant and light incidence angle variations, and transferring them to the composited visible light semiconductor for photocatalytic enhancement, particularly in aqueous phase, was never proved either theoretically or experimentally. The photocatalytic reaction was realized using a series of IO TiO_2-$BiVO_4$ samples having varying lattice constants (pore sizes) at increasing light incidence angles in aqueous solutions. The four to seven-fold increase in efficiency of all IO TiO_2-$BiVO_4$ samples under slow photon-assisted tuning conditions compared to their non-IO counterparts, firmly established, and confirmed the ability to tune and transfer slow photons in visible light-responsive IO photonic composite materials for photocatalytic enhancement. This experimentally proved concept was further theoretically justified by RCWA simulation. Through this work, we envisage that more efficient pathways using slow photon effect can be successfully explored and implemented to solve the current problem of low light harvesting efficiency in all solar energy conversion technologies.

4.2. Experimental section - synthesis and photocatalytic tests

4.2.1. Synthesis of inverse opal TiO_2-$BiVO_4$ composites

Inverse opal TiO_2-$BiVO_4$ composites were prepared by first synthesizing IO TiO_2 structures using colloid-templated method followed by the deposition of $BiVO_4$ nanoparticles using Successive Ionic Layer Adsorption (SILAR) method. The colloid-templated method to synthesize IO TiO_2 structures involved the evaporation-induced simultaneous self-assembly (EISSA) of polystyrene (PS) colloids and TiO_2 NPs into an opal structure, followed by the removal of templating colloids by calcination to obtain the inverse opal structure[24]. The synthesis process is schematically shown in **Fig. 4.1.** Polystyrene (PS) colloids were chosen as templating colloids in this work, primarily due to the ready availability of optimized protocols in our research group. In addition, poly (methyl methacrylate) (PMMA) colloids, commonly used in other research works, were not preferred in our work, as the colloids when self-assembled tend to form a necking contact instead of the closely touching colloids in the case of PS colloids[25, 26], which could impact the photonic properties. Also, SiO_2 colloids, used less frequently, were not preferred as they require the use of highly toxic solvents like HF to remove them.

The pore size of the IO structure was controlled by the diameter of the templating colloid. IO TiO_2 structures of various pore sizes were prepared for the purpose of this research work using PS colloids of 300 nm, 370 nm, 400 nm, 420 nm, 460 nm, and 500 nm. The details of each of the steps involved in IO synthesis are presented below.

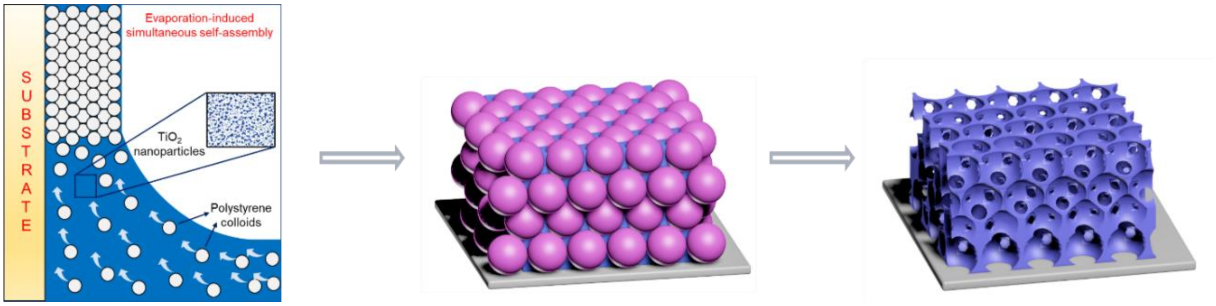

Fig. 4.1: Schematic representation of the synthesis of inverse opal TiO_2 structures. The first step shows the simultaneous self-assembly of polystyrene colloids and TiO_2 nanoparticles on a glass substrate that resulted in an opal structure with the interstices filled with the TiO_2 matrix material. The second step shows the removal of the templating PS colloids by calcination to give the inverse opal structure.

4.2.1.1. Synthesis of polystyrene colloids

Monodisperse polystyrene (PS) colloids/latex microspheres were synthesized by an emulsifier-free emulsion polymerization method[27]. Styrene monomer was washed three times with 10 wt% NaOH solution to ensure complete removal of self-polymerization inhibitor, followed by three times washing with distilled water. Washed styrene was added to 500 mL water in a double neck round bottom 1L flask in which polyvinylpyrrolidone (PVP), which acts as stabilizer, was previously dissolved. The emulsion was bubbled for 15 minutes with N_2 gas to remove dissolved air and then refluxed at a specific temperature for 30 minutes, following which potassium persulfate ($K_2S_2O_8$) initiator dissolved in 50 mL water was added. The solution was left stirring at 475 rpm in an oil bath for 24 hours of polymerization under reflux. At the end of the polymerization, the reaction was stopped by rapidly cooling the suspension in an ice bath. The specific quantities of monomer, stabilizer, and initiator, along with the reaction temperature required for the synthesis of different sizes of PS colloids are presented in **Table 4.1**.

The monodispersity of colloids in the milky-white suspension was improved by gradient centrifugation method. Typically, 10 mL of the obtained colloid suspension was centrifuged successively for three minutes at increasing speeds in the range of 5000 to 9000 rpm, each time collecting the bigger spheres precipitated and separating the residual suspension with the smaller spheres. The sedimented beads were later re-dispersed in water to give 5% wt. dispersion.

Table 4.1: Proportion of chemicals used and experimental parameters for the synthesis of polystyrene (PS) colloids of different sizes.

Sample code	Styrene (mL)	PVP (g)	$K_2S_2O_8$ (g)	Temperature (°C)	Mean diameter (nm)
PS 370	68	2.5	1	60	370
PS 420	56	0.6	0.2	75	420
PS 460	59	0	0.2	87	460

4.2.1.2. Synthesis of TiO_2 nanoparticles

Phase controlled TiO_2 NPs were prepared based on a peptization method involving the hydrolysis and condensation of titanium isopropoxide (TIP) in the presence of tetramethyl ammonium hydroxide (TMAH)[28]. Typically, 0.81 mL of TMAH (2.25 mmol) was added to 90 ml of water taken in a 250 ml double neck round bottom flask and previously cooled in an ice bath. To this solution, 1.1 mL of TIP (3.6 mmol) previously dispersed in 15 mL of 2-propanol was added drop-by-drop. A molar ratio of TIP/TMAH = 1.6 was optimized for the synthesis. On addition of TIP, the solution turned milky white. This suspension was left to stir for 15 min. and later transferred to a silicone oil bath where it was refluxed at 105°C for 6 hrs. The colourless nanoparticle suspension obtained was cooled and used within an ageing period of 3 to 10 days.

4.2.1.3. Synthesis of inverse opal TiO_2

The templating PS colloids and TiO_2 NPs were simultaneously assembled on the substrate by a self-assembly approach using the method of evaporation of the suspension containing both the species. Simultaneous self-assembly of both PS colloids and TiO_2 NPs was preferred in this work, compared to the conventional method of assembling the colloids and back-filling of the interstices with precursor. The reason behind the choice is the relatively higher degree of order that results from the single step co-assembly process compared to the two-step process, as previously reported[29]. Firstly, glass substrates cut to the dimensions 1.85×1.25 cm^2 were treated with acid piranha to render them hydrophilic (caution: piranha solution is highly corrosive). The slides were initially washed with soap water, ethanol, and acetone before treating them with acid/base piranha. For acid piranha treatment, the microscope glass slides were immersed in a 3:1 H_2SO_4/H_2O_2 solution previously heated to 70°C in an oil bath and left for an hour. The slides were then rinsed thoroughly with water and stored in water for further use. For the coassembly, 7mL of the PS colloid suspension diluted to 0.1 w/v% was taken in a 10 mL vial and 40 µL/mL of the suspension of TiO_2 NPs was added to it. The substrate was dried under N_2 gas just before use and suspended vertically in the vial using clips. The vial was then placed in an oven at 40°C for 48h for simultaneous self-assembly. The substrates with PS colloid-TiO_2 NPs coassembly were then calcined for two hours at 500°C at a ramp rate of 1°C/min to obtain IO TiO_2 film.

4.2.1.4. Sensitizing inverse opal TiO_2 with $BiVO_4$ nanoparticles

$BiVO_4$ nanoparticles were embedded in IO TiO_2 films using Successive Ionic Layer Adsorption and Reaction (SILAR) method, also termed Chemical Bath Deposition (CBD) method[30]. Four solutions were initially prepared: a) 0.742×10^{-3} moles of $Bi(NO_3)_3.5H_2O$ dissolved in a solution of 30 ml water containing 3 mL acetic acid b) 30 ml water containing 3 mL acetic acid c) 1.453×10^{-3} moles of NH_4VO_3 dissolved in 30 mL water at 60°C and d) 30 mL water. The substrate with IO TiO_2 film was sequentially dipped in solution (a) for 20s to adsorb Bi^{3+} ions, rinsed in solution (b) for 5 s to remove loosely adsorbed cations, dipped in solution (c) for 20s to adsorb VO_4^{3-} ions and finally rinsed in solution (d) to remove loosely adsorbed anions. This entire cycle was repeated 20 times to obtain optimum deposition of reacted cationic and anionic parts. The substrate was then dried and calcined at 500ºC to obtain the crystalline phase of $BiVO_4$ nanoparticles.

4.2.2. Synthesis of TiO_2, $BiVO_4$ and TiO_2-$BiVO_4$ compact films

Compact films of TiO_2 (T), $BiVO_4$ (BV) and TiO_2-$BiVO_4$ (TBV) were prepared as reference samples to compare the photocatalytic activity of the inverse opal structures with those of the non-structured counterparts. TiO_2 compact film was prepared by a sol-gel dip coating method[31] wherein the substrate was dipped in a sol, containing TIP precursor, 0.7N HCl catalyst and isopropanol, in the ratio 1:26:1.5 at a pH of 5.0. After each cycle of dipping, the substrate was dried in an oven for 30 min. at 100ºC. This was repeated for 5 cycles to get the desired thickness, following which the film was calcined at 500ºC for one hour at a ramp rate of 1ºC/min.

$BiVO_4$ compact film was prepared by a dip coating method[32] wherein the substrate was dipped in a solution of 50 mL 1M HNO_3 containing 2.5×10^{-3} moles of $Bi(NO_3)_3.5H_2O$ and 2.5×10^{-3} moles of NH_4VO_3. After each cycle of dipping, the substrate was calcined in a furnace for 30 min. at 500ºC. This was repeated for 5 cycles to get the desired thickness. TiO_2-$BiVO_4$ film was prepared by SILAR method using the substrate containing TiO_2 compact film for sequential dipping in bismuth and vanadium-containing precursors.

4.2.3. Photocatalytic dye degradation – experimental set up and parameters

Photocatalytic degradation was carried out at different light incidence angles using a purpose-designed experimental set-up **(Fig. 4.2)**, that was equipped with a 300 W ELDIM-RFLX-ET101-01 EZ Reflex light source with a spectral range of 390-770 nm. Light from the light source was channelled through an Avantes FC-UV-200 optical fibre mounted on Avantes AFH-15 fibre holder. The fibre holder permitted the change in light incidence angle (0°, 15°, 30° and 45°) (**Fig. 4.2 (b)**). The sample was attached to the bottom of the fibre holder and immersed in RhB solution. The distance between the end of the optical fibre and the sample was adjusted such that the spot size of illumination of the catalyst was ca. 1 cm in diameter (**Fig. 4.2 (c)**).

For photocatalytic degradation, the sample was attached to the bottom of the fibre holder and immersed in 4 ml of 2.5 μM RhB solution and left in the dark for 30 minutes to reach equilibrium. The distance between the end of the optical fibre and the sample was adjusted such that the spot size of illumination of the catalyst was ca. 1 cm in diameter. The experiments were conducted at 0°, 15°, 30° and 45°, each for six hours, during which 1 ml of the solution was taken out every 30 minutes for absorptance measurement and returned to the solution immediately. Comparison between the photocatalytic activities of all samples was done after normalization with respect to the weight of the photocatalyst deposited on the substrate, and from the weight fractions of TiO_2 and $BiVO_4$ deposited, estimated from EDS elemental mass composition data.

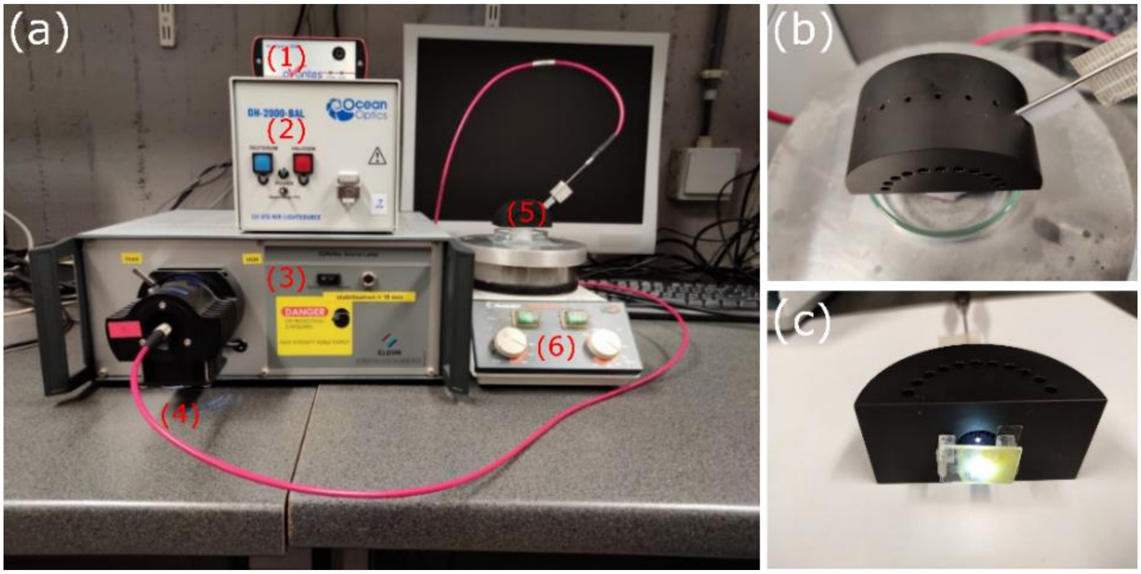

Fig. 4.2: Experimental set up for angle-resolved reflectance measurement and angle-resolved photocatalytic activity: (1) Spectrophotometer for reflectance measurement (2) Light source for angle-resolved reflectance measurement (3) Light source for photodegradation (4) Optical fibre for photodegradation (bifurcated optical fibre for reflectance measurement is not shown here) (5) Optical fibre holder (6) Magnetic stirrer (b) Top-view of optical fibre holder (c) Side-view of optical fibre holder with the photocatalyst fixed at the bottom.

4.3. Results and discussion

4.3.1. Generating and tuning slow photons in inverse opal IO TiO_2-$BiVO_4$

Slow photons were generated by synthesizing IO photonic structures that manifested a distinct SBG, at whose edges the group velocity of light was potentially reduced to zero. To synthesize SBG-manifesting photonic structures, a high degree of structural order is required, which was ensured in this work by adopting a colloid-templated method, that involved the simultaneous self-assembly of PS colloids and phase-controlled TiO_2 NPs.

The preliminary requirement to obtain high-quality photonic structures is to use highly monodisperse polystyrene templating colloids[33, 34]. Studies correlating size distribution of colloid spheres and the photonic properties of colloid PC's obtained by convective self-assembly, revealed that the manifestation of SBG typical of a photonic structure requires a critical size distribution lower than 6%, beyond which the SBG deteriorates rapidly[35]. In this work, PS colloids of high monodispersity were obtained by an emulsifier-free emulsion polymerization method using styrene as monomer, $K_2S_2O_8$ as initiator and PVP as stabilizer, followed by gradient centrifugation to improve their monodispersity.

PS colloids of three different sizes were prepared, since varying the size of the templating colloids varies the IO pore size (lattice parameter) which helps manipulate the photonic properties. It was previously reported that the size of PS colloids increases with increase in monomer concentration, decreases with increase in the amounts of stabilizer and initiator, and decreases with increase in reaction temperature[33]. Based on these parameters, the synthesis was optimized to obtain the desired sizes of PS colloids. The details of the proportion of chemicals and reaction parameters are indicated in **Table 4.1**. The sizes of the PS colloids were determined both from DLS measurements **(Fig. 4.3 (a-c))** and from the analysis of 25 particles in SEM images using image J software **(Fig. 4.3(d-f))**. The sizes of three different sizes of colloids that were synthesized were measured to be 372 nm, 416 nm, and 458 nm, and were coded as PS 370, PS 420, and PS 460 respectively.

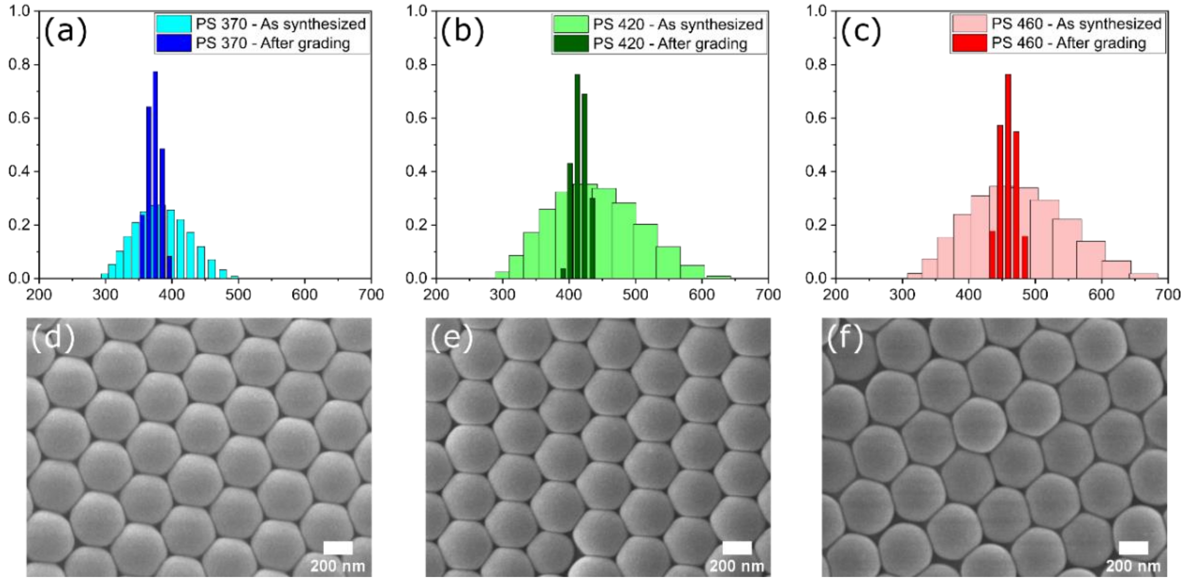

Fig. 4.3: (a-c) Size distribution plots of colloidal diameter in nm (X-axis) vs intensity (Y-axis) obtained from DLS measurements of (a) PS 370 (b) PS 420 and (c) PS 460 colloid suspensions before and after gradient centrifugation; **(d-f)** SEM images of coassembly of the corresponding PS colloids and TiO_2 NPs on a glass substrate.

To determine the monodispersity, the coefficient of variation (CV) of the PS colloids was calculated from DLS data using the following formula:

$$C_v = \frac{\sqrt{1/N\,\Sigma(fx^2) - (1/N\,\Sigma fx)^2}}{1/N \sum fx} \times 100$$

→ **Eq. 4.1**

where C_v = Coefficient of variation (%), x = Colloidal particle diameter (nm), f = Cumulative intensity, N = ∑ f. The CV of PS colloids (before washing) was between 10-15% **(Table 4.2)**. This indicated that the polydispersity was too high for the synthesis of high-quality photonic structures. Hence, to improve the monodispersity, the colloids were subjected to gradient centrifugation. The colloid suspension was centrifuged at increasing speeds in the range of 5000 to 9000 rpm, during which the bigger spheres sedimented were discarded and the suspension with the smaller spheres was collected. The plots of particle diameter size (nm) vs cumulative intensity before and after grading **(Fig. 4.3 (a-c))**, indicated a significant improvement in monodispersity after gradient centrifugation. Also, the CV calculated after washing was observed to reduce from 10.5 % to 2.8 % for PS 370, from 14.8 % to 2.7 % for PS 420, and from 14.8 % to 2.8 % for PS 460 **(Table 4.2).**

Table 4.2: CV of PS 370, PS 420, and PS 460, before and after gradient centrifugation.

PS 370				**PS 420**				**PS 460**			
Before grading		**After grading**		**Before grading**		**After grading**		**Before grading**		**After grading**	
x	**f**	**x**	**f**	**x**	**f**	**x**	**f**	**x**	**f**	**x**	**f**
298.86	0.81	309.69	0.00	287.01	0.00	341.85	0.00	287.01	0.00	341.85	0.00
309.79	2.39	318.28	0.00	307.11	1.12	350.78	0.00	329.61	0.88	381.48	0.00
321.12	4.61	327.11	0.00	327.61	3.88	360.33	0.00	351.23	3.33	391.72	0.00
332.86	7.09	336.18	0.00	349.48	7.74	370.14	0.00	374.28	6.96	402.22	0.00
345.03	9.44	345.50	0.00	372.80	11.66	380.22	0.00	398.84	10.82	435.47	8.01
357.65	11.27	355.09	10.70	397.69	14.62	390.57	1.69	425.01	13.93	447.16	25.78
370.73	12.30	364.93	28.91	424.23	15.89	401.21	19.41	452.89	15.53	459.15	34.36
384.28	12.40	375.05	34.82	452.55	15.19	412.13	34.33	482.61	15.27	471.47	24.73
398.33	11.56	385.45	21.84	482.76	12.73	423.35	31.09	514.28	13.25	484.12	7.12
412.90	9.93	396.14	3.73	514.98	9.16	434.87	13.48	548.02	9.98	497.11	0.00
427.99	7.76	407.13	0.00	549.35	5.35	446.71	0.00	583.98	6.27	510.45	0.00
443.64	5.40	418.42	0.00	586.02	2.23	458.88	0.00	622.29	2.98	524.14	0.00
459.87	3.20	430.02	0.00	625.14	0.43	471.37	0.00	663.13	0.81	538.20	0.00
476.68	1.46	441.95	0.00	664.19	0.00	485.92	0.00	702.04	0.00	553.87	0.00
494.11	0.39	454.20	0.00	703.12	0.00	500.04	0.00	748.19	0.00	569.04	0.00
CV=10.5%		**CV=2.8%**		**CV=14.8%**		**CV=2.7%**		**CV=15.1%**		**CV=2.8%**	

The secondary requirement to obtain highly ordered photonic structures is the optimization of the ordered assembly of templating colloids and the choice of precursor to fill their interstitial voids. Evaporation-induced self-assembly (EISA) of colloids followed by back-filling of the voids with precursor had been the most employed approach to prepare IO structures. However, this often results in higher disorder, as cracks are formed both during drying of the assembled films due to stresses from capillary forces[36, 37], and during calcination due to volume shrinkage caused by the amorphous-to-crystalline phase transformation[38-40]. To address the first issue, a coassembly technique that involves the simultaneous self-assembly of templating colloids and precursor was previously proposed, as it reduces the drying-related crack formation[29]. To address the second, the usage of bi-phase NPs, with careful control of the proportion of amorphous and crystalline phases, was reported to minimize crack formation, as the amorphous phase reduces capillary stresses during colloidal assembly, while the crystalline phase reduces volume shrinkage related to phase transition during calcination[24]. In this work, the coassembly of PS colloids and phase controlled TiO_2 NPs was adopted to prepare ordered IO photonic structures with minimized crack formation.

Phase controlled TiO_2 NPs were synthesized by a peptization process involving the hydrolysis and condensation of $Ti(OPr)_4$ (TIP) in the presence of Me_4NOH (TMAH), wherein the control of TIP/TMAH ratio permitted the control of particle size, shape, and crystallinity[28]. Bi-phase (amorphous-crystalline) TiO_2 NPs were preferred based on a previous report on the comparison of IO structures prepared by using TiO_2 NPs of varying crystallinity[24]. The use of bi-phase TiO_2 NPs was shown to yield highly ordered IO structures as the amorphous component mitigated stresses arising during the colloid assembly process while the crystalline component minimized volume shrinkage caused by calcination-induced phase transition of TiO_2 to anatase phase. The degree of crystallinity of TiO_2 NPs was controlled by varying TMAH proportion in the peptization process. TMAH provides a basic medium and plays a dual role in the peptization process. Firstly, it catalyzes the hydrolysis and condensation reactions **(Eqs. 4.2, 4.3)** by favouring the formation of highly nucleophilic TiO^- **(Eq. 4.4)**, which reacts with positively charged titanium to form poly-condensates. Secondly, Me_4N^+ cations in TMAH help stabilize the condensed species through electrostatic interactions, preventing further condensation and thereby forming titania clusters and poly-titanate anions **(Eq. 4.5)**. As seen in the hydrolysis-condensation reactions in the presence of a base in dilute alcoholic solutions, the Me_4NOH (TMAH) concentration determines the x and y values, which in turn determine the crystallinity of the nanoparticles[28].

$Ti(OR)_4 + 4H_2O \rightarrow Ti(OH)_4 + 4ROH$ **(Eq. 4.2)**

$Ti\text{-}OH + XO\text{-}Ti \rightarrow Ti\text{-}O\text{-}Ti + XOH\ (X = H, R)$ **(Eq. 4.3)**

$Ti\text{-}OH + Me_4NOH \rightarrow Ti\text{-}O^- + Me_4N^+ + H_2O$ **(Eq. 4.4)**

$Ti_xO_yH_z + Me_4NOH \rightarrow (Ti_xO_yH_{z-1})Me_4N + H_2O$ **(Eq. 4.5)**

The degree of crystallinity decreases with increase in TMAH concentration, as demonstrated in previous research through XRD and Raman analysis[24]. In other words, the degree of crystallinity increased with an increase in TIP/TMAH ratio. Hence, by keeping the amount of TIP constant, the amount of TMAH was varied in this work to obtain the desired crystallinity of TiO_2 NPs. Also, the size of the NPs varied with TIP/TMAH ratio. A lower TIP/TMAH ratio, which implies a greater proportion of TMAH, was reported to result in smaller nanocrystal size, as the large sized $[(CH_3)_4N]^+$ cations prevent the growing anatase nuclei from agglomerating, reducing the effective collision between them and hindering TiO_2 particle growth. However, this lower ratio was shown to produce disordered structures, as excess TMAH ions interfere with colloidal electrostatic forces, disrupting ordered self-assembly. On the other hand, a very high ratio was also reported to produce disordered structures, as this implies the presence of a greater proportion of TIP resulting in larger particle size, that interferes with the forces of colloidal self-assembly[24]. Based on this reasoning, in this work, the concentration of TMAH was chosen such that the TIP/TMAH molar ratio was 1.6, which provided the optimum crystallinity and size required for the formation of ordered IO structures manifesting a distinct, sharp SBG.

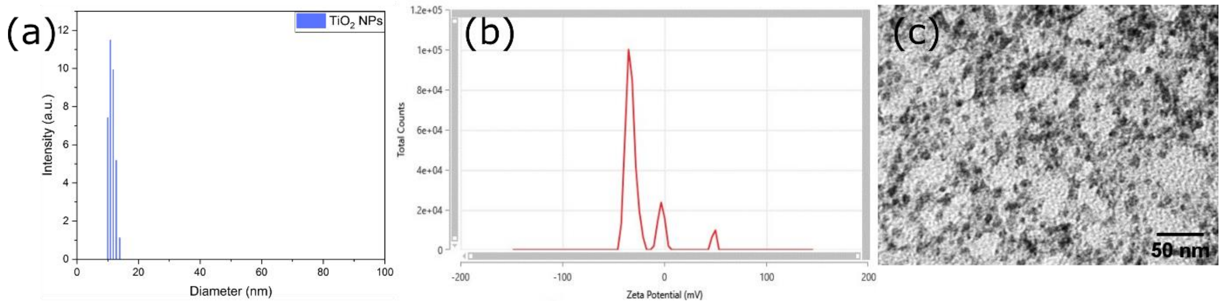

Fig. 4.4: (a) Plot of TiO_2 nanoparticle diameter in nm (X-axis) vs Cumulative intensity (Y-axis) as obtained from DLS measurement; **(b)** Zeta potential of the prepared TiO_2 NP suspension; **(c)** TEM image of the as-prepared TiO_2 NPs.

TiO_2 NPs synthesized with the optimized TIP/TMAH ratio were found to possess a narrow size distribution, having an average size of 11.8 nm with an average polydispersity index (PDI) of 0.128

(Fig. 4.4 (a)), obtained from DLS measurement of TiO_2 NPs suspended in basic and dilute alcoholic solution. The zeta potential of the particles in the suspension, which was measured to be an average of -25.5mV **(Fig. 4.4 (b))**, confirmed the high stability of the particles in the suspension[41]. In addition, the TEM image **(Fig. 4.4(b))** revealed that the NPs were stable without significant agglomeration and possessed a relatively uniform spherical shape.

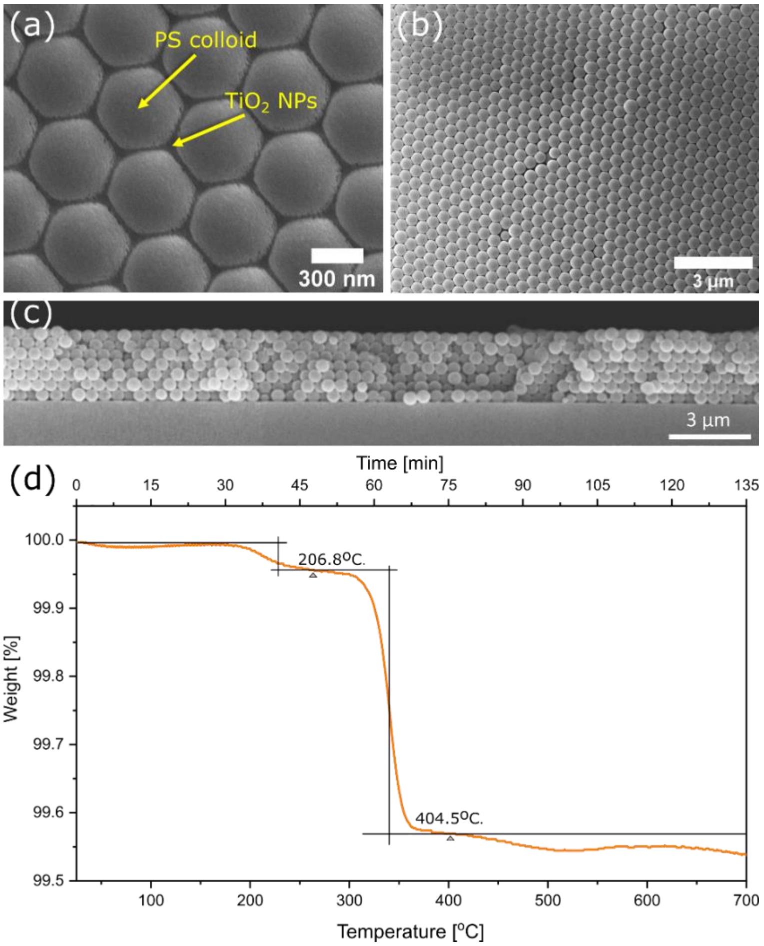

Fig. 4.5: (a) High magnification SEM image of the simultaneous self-assembly of PS 420 colloids and TiO_2 NPs; **(b)** Low magnification SEM image of the coassembly indicating long-range order; **(c)** Thermogravimetric analysis (TGA) curve of the coassembly of PS 420 colloids and TiO_2 NPs on a glass substrate.

The SEM images of the coassembly **(Fig. 4.5(a-c))** revealed that the coassembly of PS colloids and phase controlled TiO_2 NPs resulted in an ordered *fcc* arrangement. The high magnification SEM image clearly showed that the interstitial voids between the colloids were uniformly filled with the phase controlled TiO_2 NPs **(Fig. 4.5(a))**. Also, it was noted from the low magnification top-view SEM image **(Fig. 4.5(b))** and the cross-section image **(Fig. 4.5(c))** that the coassembly was homogeneous over a long range with uniform thickness**.** The coassembly was subjected to thermogravimetric analysis to see the effects of calcination that is required to obtain the inverse opal structure. As seen in **Fig. 4.5 (d)**, three phases of weight loss were observed with increasing temperature. The weight loss below 266.82°C can be attributed to the loss of moisture in the sample. The weight loss between 266.82°C and 404.52°C corresponds to the elimination of polystyrene, while the weight loss above this temperature can be attributed to the phase transformation of TiO_2 NPs.

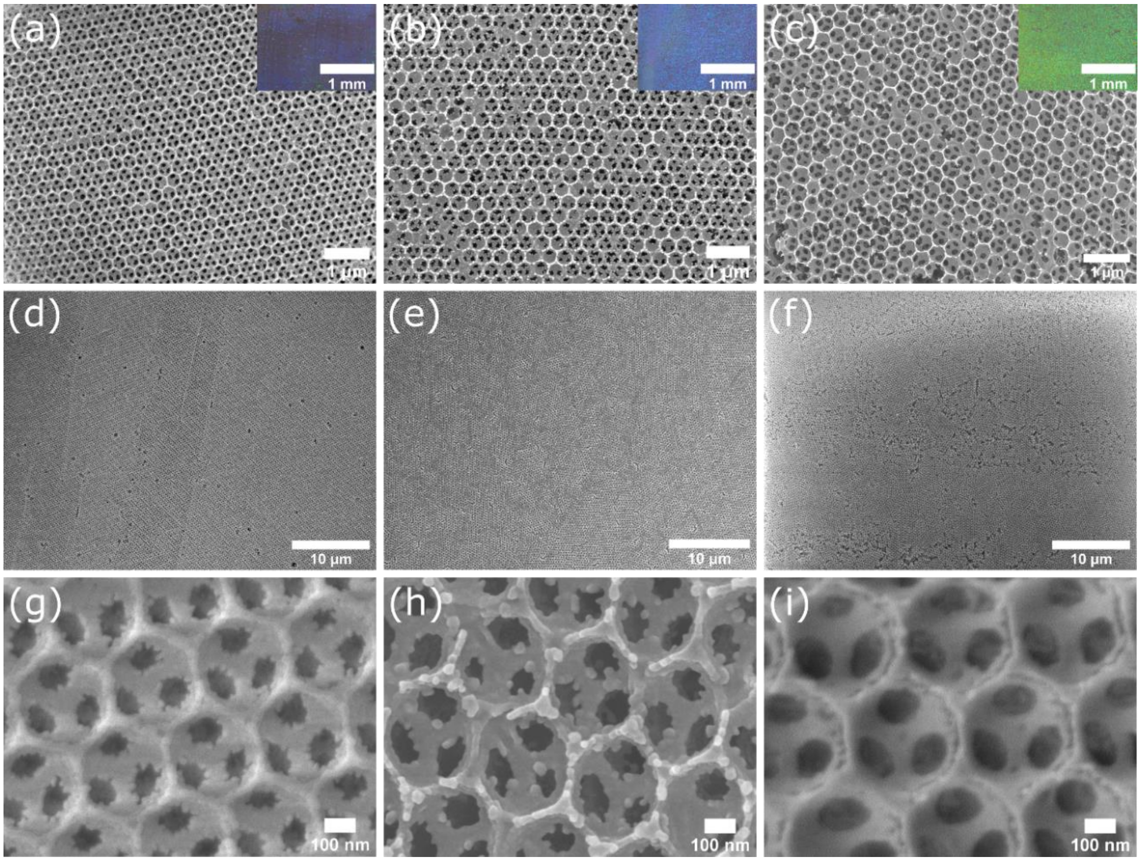

Fig. 4.6: Top view SEM images in low and high magnification of inverse opal TiO_2 samples: **(a, d, g)** IT 370, **(b, e, h)** IT 420 and **(c, f, i)** IT 460. Optical microscope images are shown in inset.

SEM images of the IO structures obtained after calcination, as seen in **Fig. 4.6 (a-f)**, indicate that the structures possessed a high degree of structural order over a long range. Diameters of the air spheres were measured from SEM images to be 258, 286 and 323 nm (±10 nm), for IO structures prepared from PS colloids of 370, 420 and 460 nm respectively (**Fig. 4.6 (g-i)**). The average 30% shrinkage of pore size compared to original colloid size can be attributed to the formation of much condensed crystalline phase of TiO_2[42, 43]. The optical microscope images in **Fig. 4.6 (a-c)** show the distinctive colours of the inverse opal photonic structures (dark blue, blue, and green, respectively) resulting from the stop band gap reflection, whose wavelength red shifts with increase in lattice constant (pore size).

The thickness of the IO film, which varies with colloid concentration, is of considerable significance since it impacts the photonic properties by broadening the SBG reflection peak with increasing thickness[44, 45]. Cross-section images of the IO films **(Fig. 4.7(a-c))** revealed that the average thickness of the film was 1.5 μm. Thickness can be increased by increasing the concentration of colloids in the coassembly. The concentration of colloids used in this work was diluted to 0.1 wt%, which was found to result in excellent photonic properties of the IOs. The number of layers (rows) in the IO structures varied from 6 to10 **(Fig. 4.7(a-c))**, generally decreasing with increase in colloid size. TEM images of IT 370 at different magnifications **(Fig. 4.7(d-f))** not only confirmed the high degree of order in the IO structure but also revealed the size of the nanocrystal blocks that compose the TiO_2 framework, which was measured to be 20-30 nm **(Fig. 4.7(f))**. The nanocrystal blocks introduced additional inter-particular mesopores of around 2-5 nm, which rendered the filling fraction of TiO_2 lower than the close-packed value of 0.26 in a hexagonal close packed system, which could be as low as 0.12 based on previous reports[17]. Consequently, the position of the SBG blue-shifted compared to that of the expected ideal structure, since the effective refractive index of the photocatalyst was reduced.

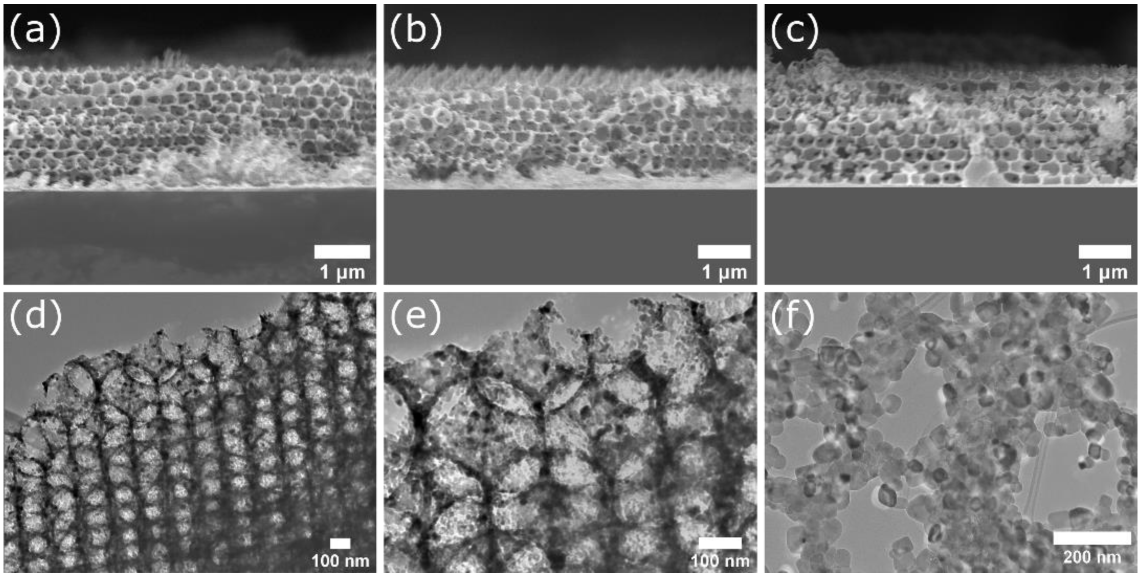

Fig. 4.7: (a-c) Cross section SEM images of inverse opal TiO_2 samples: (a) IT 370, (b) IT 420, (c) IT 460; **(d-f)** TEM images of IT 370 at different magnifications.

The ageing time of the TiO_2 NP suspension was reported to influence the size and shape of the TiO_2 NPs[24]. To optimize the ageing period of the suspension, a series of inverse opals were prepared using suspensions aged from 1 to 30 days. As shown in **Fig. 4.8**, the particle size gradually increased with ageing time from around 10 nm for 3-day aged suspension to 40 nm for 30-day aged suspension (TIP/TMAH=1.6). Apart from the growth in particle size owing to agglomeration of TiO_2 anatase nuclei over time, it was observed that the shape of the particles gradually changed from being spherical to being slightly elongated. Again, longer ageing time implies that the particle size grows to an extent where they disrupt the ordered assembly of the colloids. Hence, the suspension was aged between 5-10 days to obtain high-quality inverse opal structures.

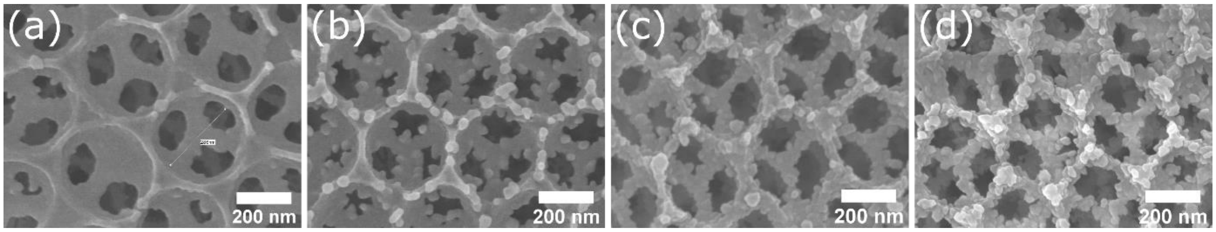

Fig. 4.8: SEM images of IT 420 samples prepared different ageing periods of the phase controlled TiO_2 suspension: IT 420 from **(a)** 1 day, **(b)** 5 days, **(c)** 15 days and **(d)** 30 days suspension.

Tunability of the stop band gap with incidence angle was verified by measuring angle-resolved reflectance spectra of IT 370, IT 420, and IT 460 in air medium **(Fig. 4.9 (a-c))**. In each case, the SBG reflection peak red-shifted with increase in pore size and blue-shifted with increase in incidence angle, which is characteristic of photonic structures. This confirmed not only that the IO TiO_2 samples exhibited excellent photonic properties but also that the highly ordered structures permitted exceptional controllability of the slow photon wavelengths at the edges of the SBG.

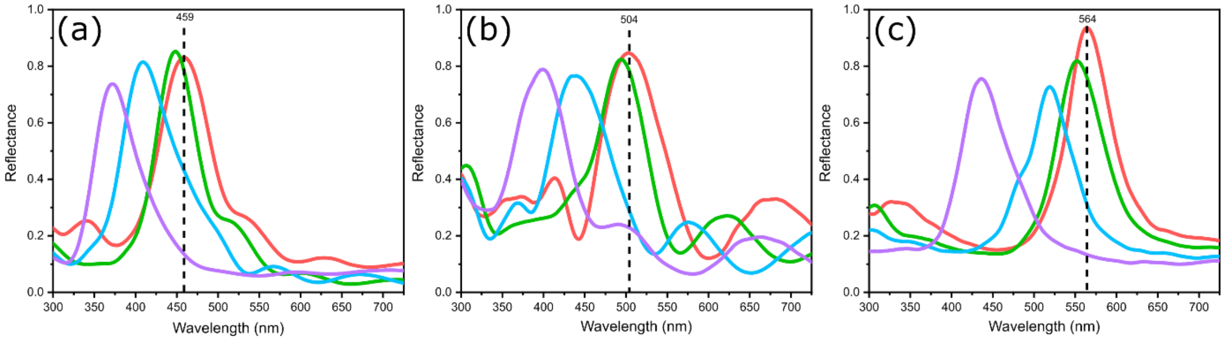

Fig. 4.9: Angle-resolved specular reflectance spectra in air of: **(a)** IT 370, **(b)** IT 420, **(c)** IT 460 at 0° (red), 15° (green), 30° (blue) and 45° (violet).

For comparison, a TiO_2 compact film was synthesized with ~1 µm thickness and nanocrystal size of 20-40 nm (Fig. 3.10 (a-b)). Contrary to the structured film, the TiO_2 compact film did not show any photonic properties, as evidenced from the lack of any structural colour **(Fig. 4.10 (a, inset))** and the absence of a distinct SBG peak in the reflectance spectra.

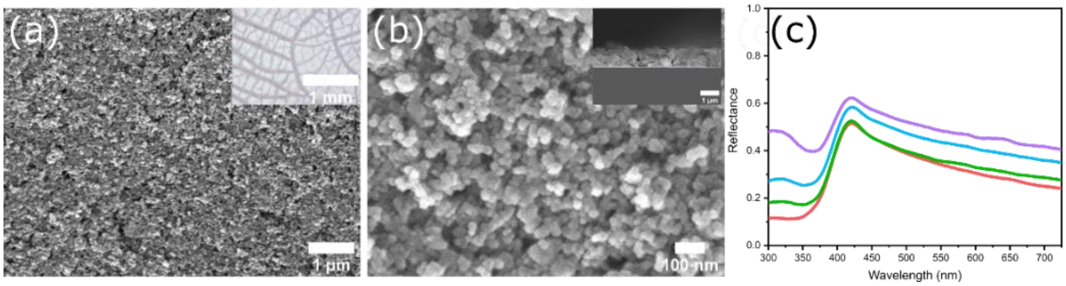

Fig. 4.10: (a) Low magnification SEM image of TiO_2 compact film with the optical microscope image in the inset; **(b)** High magnification SEM image with the cross-section image in the inset; **(c)** Angle-resolved spectra in air at 0° (red), 15° (green), 30° (blue) and 45° (violet**).**

Creating a heterocomposite of IO TiO_2 with visible light responsive $BiVO_4$, was carried out by Successive Ionic Layer Adsorption and Reaction (SILAR) method[30].

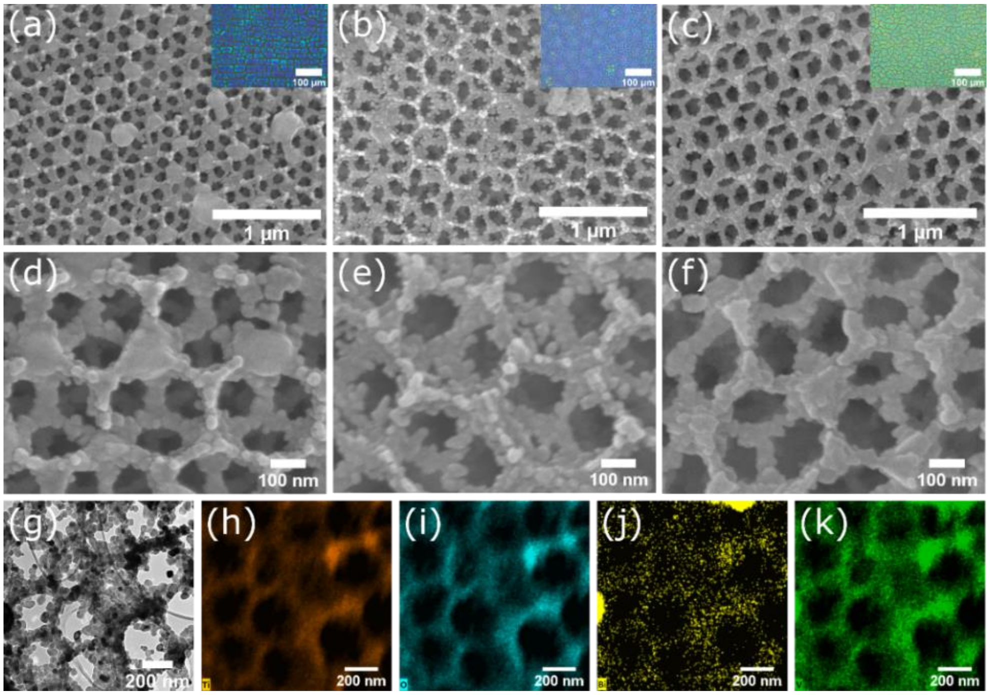

Fig. 4.11: (a-c) Low magnification SEM images of (a) ITBV 370, (b) ITBV 420, (c) ITBV 460 along with their corresponding optical microscope images (inset); **(d-f)** High magnification SEM images of (d) ITBV 370, (e) ITBV 420, (f) ITBV 460. **(g-k)** HAADF-STEM image of ITBV 370 (g), and the corresponding EDS elemental mapping of Ti (h), O (i), Bi (j) and V (k).

SEM images revealed that the IO composite structures retained their highly ordered structures after $BiVO_4$ deposition **(Fig. 4.11 (a-c))**, albeit the presence of randomly agglomerated crystals of $BiVO_4$. The optical microscope images of ITBV 370, ITBV 420 and ITBV 460, shown in the inset of **Fig. 4.11 (a-c)**, displayed similar colours to that of the IO TiO_2 samples (**Fig. 4.11 (a-c))**, indicating that the photonic properties were retained after $BiVO_4$ deposition. It was also noted that the pore sizes did not change significantly after $BiVO_4$ deposition, which were measured from the SEM images in **Fig. 4.11 (a-c)** to be 255, 286 and 322 nm (±10 nm) for ITBV 370, ITBV 420, and ITBV 460 respectively**.** The HAADF-STEM image and the corresponding elemental mapping shown in **Fig. 4.11 (g-k)** revealed that $BiVO_4$ was homogeneously deposited in the IO TiO_2 structure.

Angle-resolved reflectance was measured in air after deposition of IO TiO_2 with $BiVO_4$. It was observed that the position of the SBG reflectance peaks **(Fig. 4.12 (a-c))** were similar to those of their respective IO TiO_2 counterparts **(Fig. 4.9 (a-c))**, confirming that no significant change in photonic properties occurred after the deposition process.

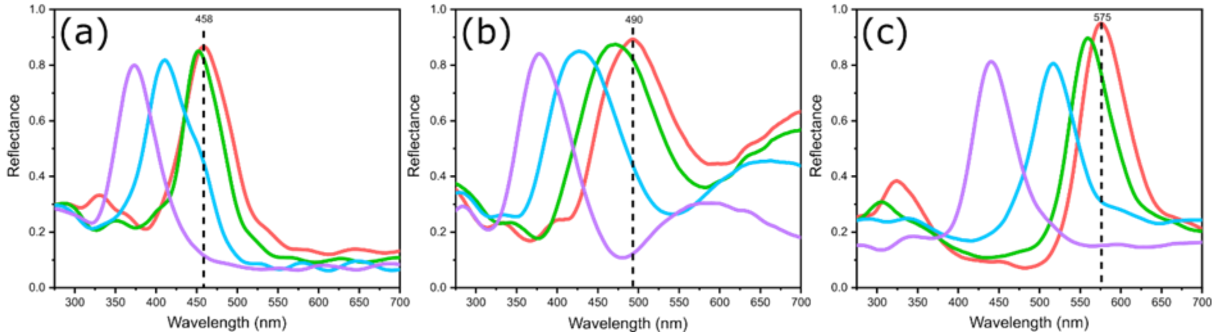

Fig. 4.12: (a-c) Angle-resolved reflectance spectra in air of: **(a)** ITBV 370, **(b)** ITBV 420, **(c)** ITBV 460 at 0° (red), 15° (green), 30° (blue) and 45° (violet**).**

Similar to the case of TiO_2 compact film, the reference TiO_2-$BiVO_4$ compact film **(Fig. 4.13 (a-c))** synthesized by the SILAR deposition of $BiVO_4$ on TiO_2 compact film did not exhibit any photonic properties but showed only the characteristic reflectance spectra corresponding to that of TiO_2-$BiVO_4$ composite.

The deposition of $BiVO_4$ had to be carefully controlled to avoid the formation of overlayer of $BiVO_4$ over IO TiO_2, such that an optimum balance between improved light absorption in the visible range and simultaneous retention of photonic properties was achieved. The SILAR method, which is a wet chemical method that used alternating baths of cationic and anionic precursors (with additional baths of pure solvent in between to remove excessively adsorbed precursors) for successive adsorption and reaction[46], permitted the layer-by-layer controlled deposition of $BiVO_4$.

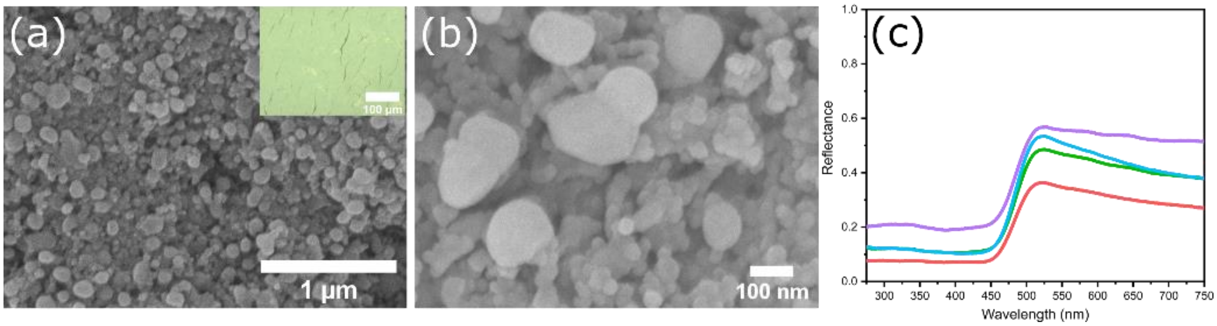

Fig. 4.13: (a) Low magnification SEM image of TiO_2-$BiVO_4$ (ITBV) compact film with the optical microscope image in the inset; **(b)** High magnification SEM image of ITBV compact film; **(c)** Angle-resolved spectra in air at 0° (red), 15° (green), 30° (blue) and 45° (violet**)**.

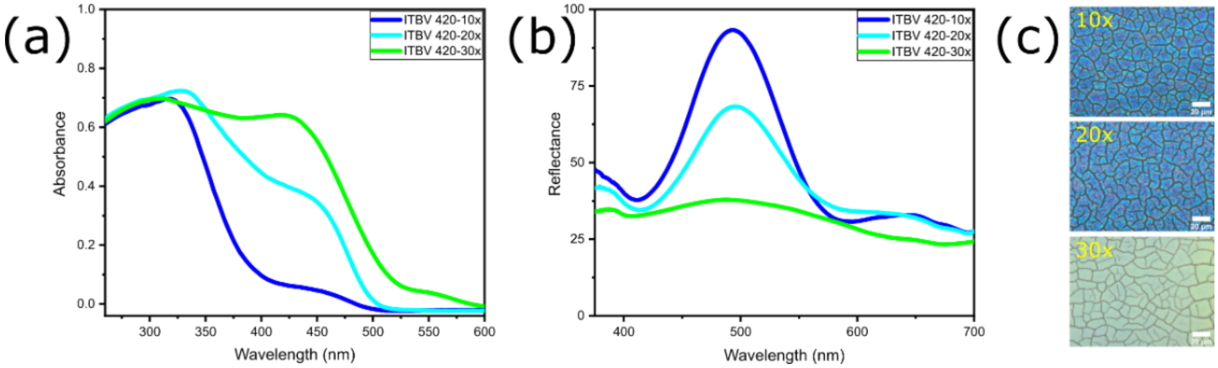

Fig. 4.14: (a) UV-Visible absorptance spectra of ITBV 420 samples prepared with different amounts of $BiVO_4$ deposition – 10, 20 and 30 SILAR cycles (blue, cyan, green). **(b)** Optical micro-spectrophotometric reflectance spectra of the three samples, showing the variation of reflectance peak intensity with variation of $BiVO_4$ deposition. **(c)** The corresponding optical microscope images of the same samples.

The amount of $BiVO_4$ deposition through SILAR was controlled by the number of SILAR cycles. The optimization of the number of cycles was done by preparing samples with 10, 20 and 30 SILAR cycles, followed by the measurement of absorptance and SBG reflection of each of them. As seen in **Fig. 4.14**, the increase in the number of SILAR cycles increasingly shifted the absorption to the visible range **(Fig. 4.14 (a))**, however it resulted in a deterioration of photonic properties as indicated by the diminishing reflectance peak **(Fig. 4.14 (b))**, due to the formation of overlayer of $BiVO_4$ on IO TiO_2 **(Fig. 4.14 (c)).** Having determined the balance between improving light absorption and the retention of photonic properties, 20 SILAR cycles was determined to be the optimum deposition.

To quantify the amount of $BiVO_4$ deposited in each sample, EDS elemental mapping and quantitative analysis were performed. As seen in **Fig. 4.15 (a-c)**, the elemental mapping confirmed the homogeneous deposition of $BiVO_4$ in the entire IO TiO_2 structure. EDS spectra recorded for each sample **(Fig. 4.15 (d-f)** showed the characteristic peaks of Ti, Bi, V and O elements. Elemental quantification obtained from the EDS analysis **(Table 4.3)**, enabled the calculation of the proportion by molecular weight of $BiVO_4$ loaded on each sample, which was calculated to be 26.8%, 25.3% and 24.9% for ITBV 370, ITBV 420 and ITBV 460 respectively.

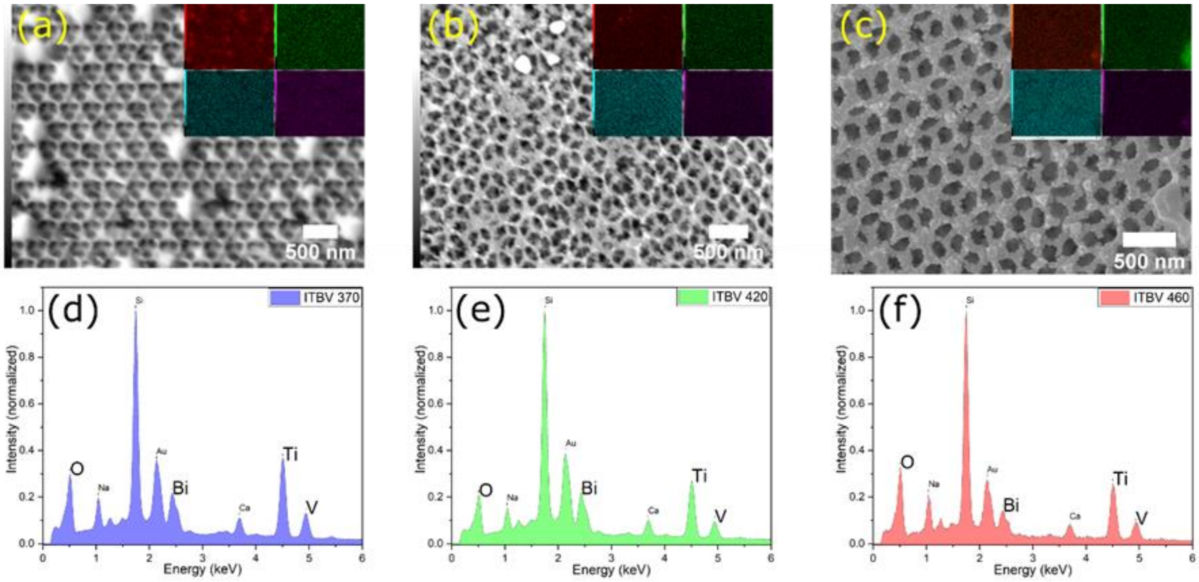

Fig. 4.15: (a-c) SEM images of the elemental mapping domains and the corresponding elemental mapping (inset) of Bi (red), V (green), Ti (cyan) and O (purple) in **(a)** ITBV 370, **(b)** ITBV 420 and **(c)** ITBV 460; **(d-f)** EDX spectra of **(d)** ITBV 370, **(e)** ITBV 420 and **(f)** ITBV 460.

Table 4.3: Estimation of the elemental mass and atom percentages as obtained from Energy Dispersive X-ray Spectroscopy (EDX) quantitative analysis.

Sample	**Ti**		**Bi**		**V**		**O**	
	Mass %	**Atom %**	**Mass %**	**Atom %**	**Mass %**	**Atom %**	**Mass %**	**Atom %**
ITBV 370	36.1	27.6	29.3	5.1	7.5	5.4	27	61.9
ITBV 420	32.46	21.1	24.22	3.61	6.73	4.11	36.59	71.18
ITBV 460	32	20.5	23.4	3.4	7.1	4.3	37.5	71.8

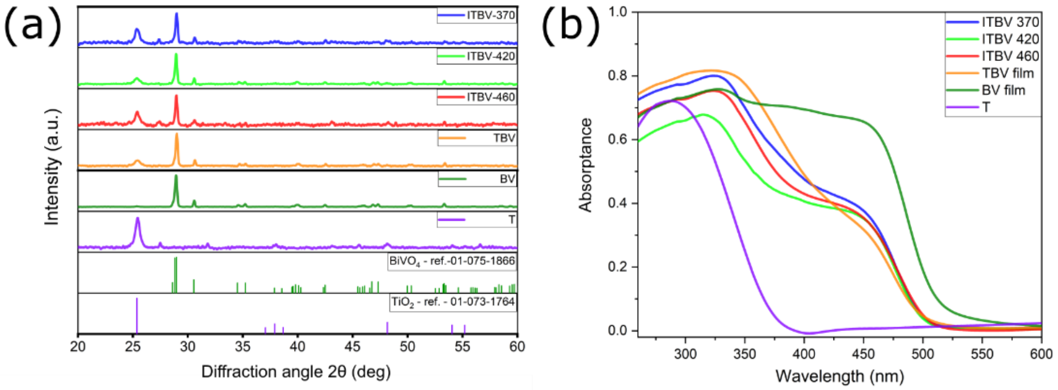

Fig. 4.16: (a) XRD patterns of IO TiO_2 deposited with $BiVO_4$ (from top to bottom): ITBV 370, ITBV 420, ITBV 460, TiO_2-$BiVO_4$ (TBV), $BiVO_4$ (BV), and TiO_2 (T) compact films; monoclinic $BiVO_4$ and anatase TiO_2 as references; **(b)** The corresponding UV-Visible absorptance spectra of the same samples mentioned above indicated with the same colour.

XRD patterns **(Fig. 4.16 (a))** confirmed that TiO_2 was present predominantly in the anatase phase (with traces of rutile phase) while $BiVO_4$ was present in the monoclinic phase. Based on XRD data, calculation of the approximative crystallite sizes was done using the Scherrer equation. The crystallite sizes of TiO_2 and $BiVO_4$ in ITBV films were calculated to be 14 nm and 23 nm while those in TBV, BV and T compact films were 28 nm and 35 nm respectively. UV-Visible absorptance measurements of the three IO TiO_2-$BiVO_4$ films and their comparison with TiO_2, $BiVO_4$ and TiO_2-$BiVO_4$ compact films **(Fig. 4.16 (b))** indicated that the absorptance of all ITBV composites as well as that of TBV compact film shifted to the visible range owing to the narrow electronic band gap (EBG) of $BiVO_4$, rendering them efficient for visible light photocatalysis.

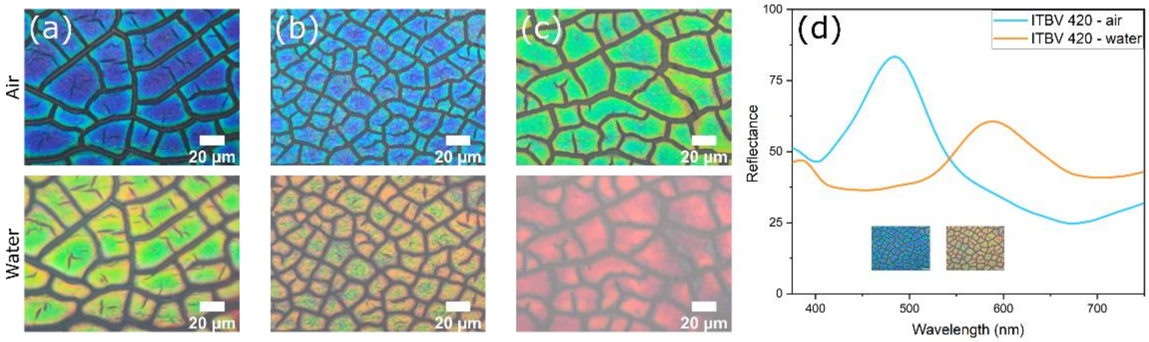

Fig. 4.17: Optical microscope images of the same area of ITBV samples in air and in water of **(a)** ITBV 370, **(b)** ITBV 420, and **(c)** ITBV 460; micro-spectrophotometric reflectance spectra of ITBV 420 in air and in water of the domain shown in the optical microscope images.

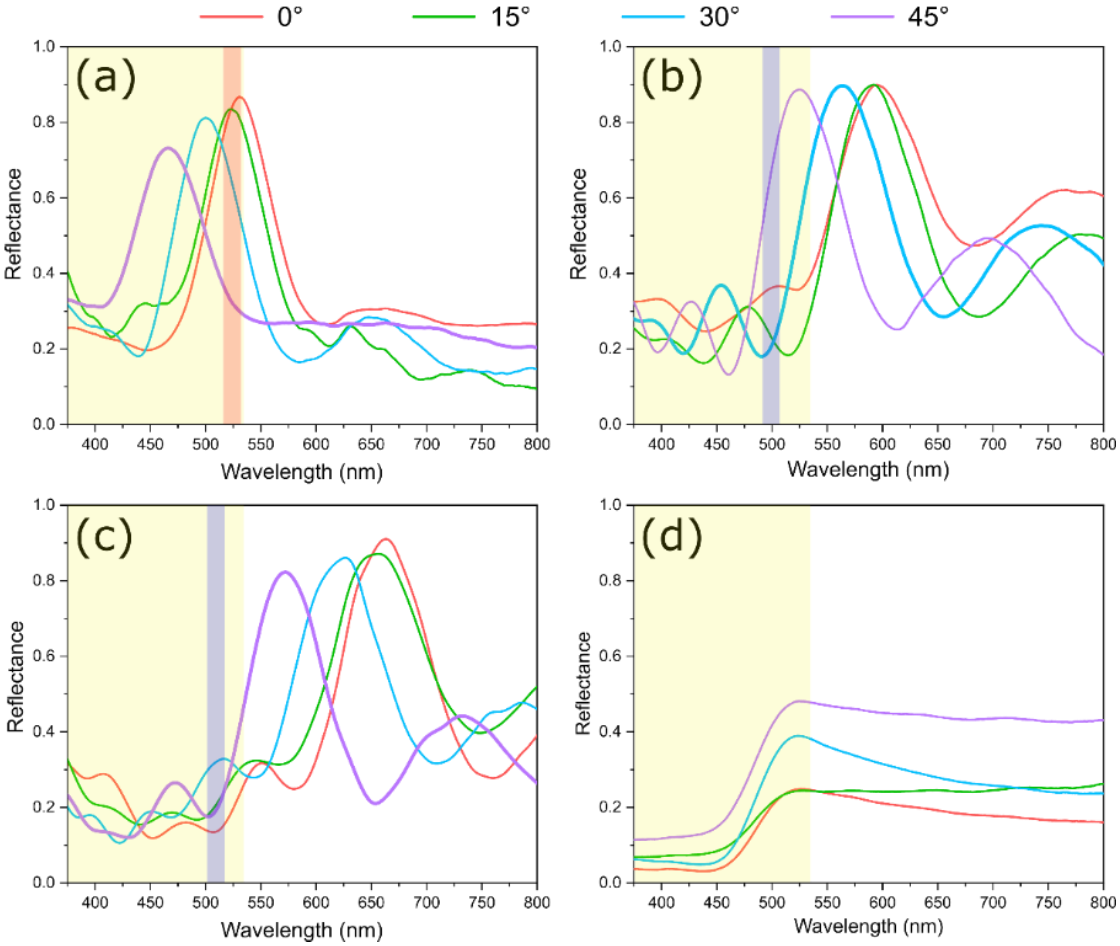

Fig. 4.18: Angle-resolved reflectance measurements in water of **(a)** ITBV 370, **(b)** ITBV 420, **(c)** ITBV 460 and **(d)** TiO_2-$BiVO_4$ film; yellow shade indicates the electronic absorption region of $BiVO_4$; red shade in (a) refers to red edge slow photons of ITBV 370 at 45° while blue shades in (b, c) refer to blue edge slow photons of ITBV 420 at 30° and ITBV 460 at 45° respectively.

As photocatalytic activities were to be conducted in aqueous medium, the investigation of photonic properties in water in comparison with those in air was essential. Optical images taken on the same IO domains in air and under water clearly showed a red shift in colour with change in medium **(Fig. 4.17 (a-c))**. Compared to the reflectance spectra in air **(Fig. 4.12)**, all the SBG peaks red-shifted under water **(Fig. 4.17)**, due to the increase in effective RI of the system caused by the increase in RI of the pore-filling medium (from $n_{\text{air}} = 1$ to $n_{\text{water}} = 1.33$). The effect of the medium on the position of SBG and hence on that of the slow photons became evident. As in the case of air medium, reflectance measurements in water showed that the SBG peak red-shifted with increase in pore size and blue-shifted with increase in incidence angle for all the three ITBV samples **(Fig. 4.18).** The intensity of the SBG reflection peak in water, however, was found to be relatively reduced compared to that in air, as indicated in micro-spectrophotometric reflectance measurements **(Fig. 4.17 (d))**. This attenuation in intensity in aqueous medium can be explained by the reduction in RI contrast between the pore-filling medium i.e. water and the IO material. Reflectance measurements of TiO_2-$BiVO_4$ compact film under water did not show any significant change in spectra with change in medium from air to water **(Figs. 4.13 (c), 4.18 (d))**.

4.3.2. Stop band gap peak estimation using modified Braggs law

The observations of shift in SBG peak position with pore size, incidence angle and pore-filling medium were found to be consistent with theoretical predictions, simulations, and previously reported experiments on optical properties of photonic crystals[47]. A modified Bragg equation[48, 49] was used to estimate the effective refractive index (n_{eff}) of IO TiO_2-$BiVO_4$ by simultaneously fitting SBG peak positions (λ_B) of all the IO samples having different pore diameters (D), i.e., IO periodicities, measured at different incidence angles (θ), both in air and in water (incidence medium refractive index: n_{inc}).

$$\lambda = 2 \cdot \sqrt{2/3} \cdot D \cdot \sqrt{n_{eff}^2 - n_{inc}^2 \sin^2\theta} \qquad \textbf{(Eq. 4.6)}$$

where λ is the wavelength of pPBG reflection, D is the IO pore diameter, n_{eff} is the effective RI of the IO structure and θ is the light incidence angle with respect to the normal of the exposed (111) plane of the IO structure. The effective RI n_{eff} was calculated using Bruggeman's formula[50, 51] (assuming spherical pores) from the volume filling fraction (f) of material in the inverse opal, the RI of the composite material (n_{mat}) and the RI of the pore filling medium (n_{med}) as follows:

$$n_{eff}^2 = \frac{1}{4} \cdot \left(\beta + \sqrt{\beta^2 + 8n_{mat}^2 n_{void}^2}\right) \qquad \textbf{(Eq. 4.7)}$$

Here, β was calculated as:

$$\beta = [(3f_{mat} - 1)n_{mat}^2 + (3f_{void} - 1)n_{void}^2] \qquad \textbf{(Eq. 4.8)}$$

where n_{mat} and n_{void} represent the RIs of IO matrix material and void-filling material respectively while f_{mat} and f_{void} represent their filling fractions respectively.

A value of f=0.12, lower than the perfect IO close packing value (f=0.26), was inferred from the analysis of microscope images, which was found to be consistent with previous reports[17, 23]. The composite material RI was calculated as $n_{mat} = xn_1 + (1 - x)n_2$, where n_1 and n_2 are the RI of porous TiO_2 and $BiVO_4$, while (x) and (1-x) are the volume fractions of TiO_2 and $BiVO_4$. Based on the above consideration and the calculation of wavelength-dependent complex RI using data reported for dense TiO_2[52] and dense $BiVO_4$[53], the RI (real part) of the porous TiO_2 and porous $BiVO_4$ materials (at λ=500 nm) were estimated to be 1.836 and 2.764 respectively **(Fig. 4.19 (a))**.

The decrease in the estimated RI of the porous, thin films compared to that of bulk TiO_2 and bulk $BiVO_4$ can be attributed to the decrease in density of the material, a fact established in previous reports through the correlation between density and RI in thin films[54, 55]. As a result, for the composite material, $n_{mat} = 1.95$ was obtained; this real and constant value was used in the modified Bragg formula. For data fitting related to optical measurements in water, Fresnel correction ($n_{inc} \neq n_{med}$) was applied in order to account for the refraction at the interface between air and water in the present experimental configuration. In addition, incomplete infiltration of the pores in water medium had to be considered and a RI value of $n_{med} = 1.20$ (60% water and 40% air) was tuned to give the best fit to the optical measurements in water. With the above factors taken into consideration, a nearly perfect fit was obtained between experimentally observed SBG peak positions shown by the dots in **Fig. 4.19 (b)** and theoretically calculated ones shown by the solid lines in **Fig. 4.19 (b)**, for all samples (ITBV 370-blue, ITBV 420-green, ITBV 460-red), at all angles, both in air (open dots and dotted lines) and in water (closed dots and solid lines). This accurate prediction of the SBG peak positions validated the procedure used for RI calculation.

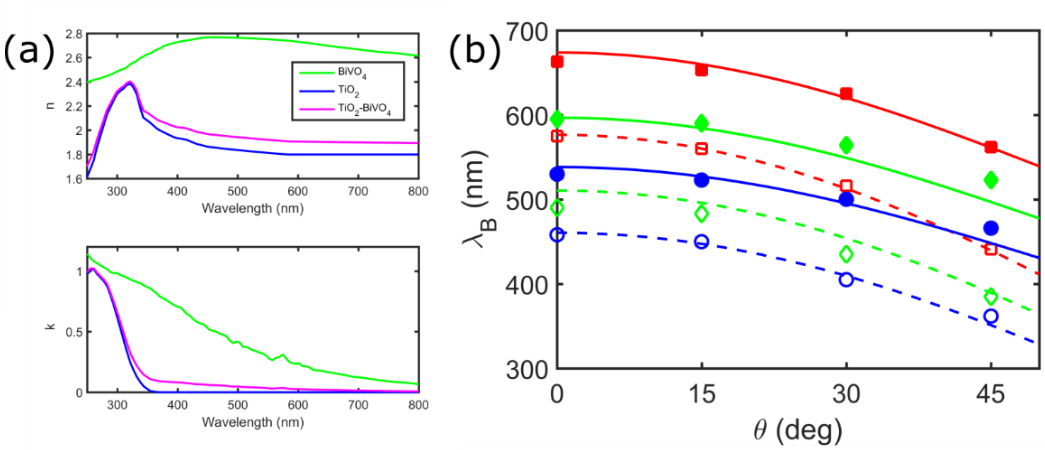

Fig. 4.19: (a) Simulated refractive index (n) and extinction coefficient (k) as a function of wavelength for $BiVO_4$ nanoparticle film, IO TiO_2 film and IO TiO_2-$BiVO_4$ film. **(b)** Bragg law approximation of SBG reflectance peak position (λ_B) in air (dotted lines) and in water (solid lines) of ITBV 370 (blue), ITBV 420 (green) and ITBV 460 (red); experimental measurement of reflectance of the same samples are indicated by open dots (air) and closed dots (water).

4.3.3. Simulation and theoretical studies to justify slow photon effect

The angular dependence of reflectance and absorptance spectra in IO slabs **(Fig. 4.20 (a, c))** were predicted using RCWA simulations.

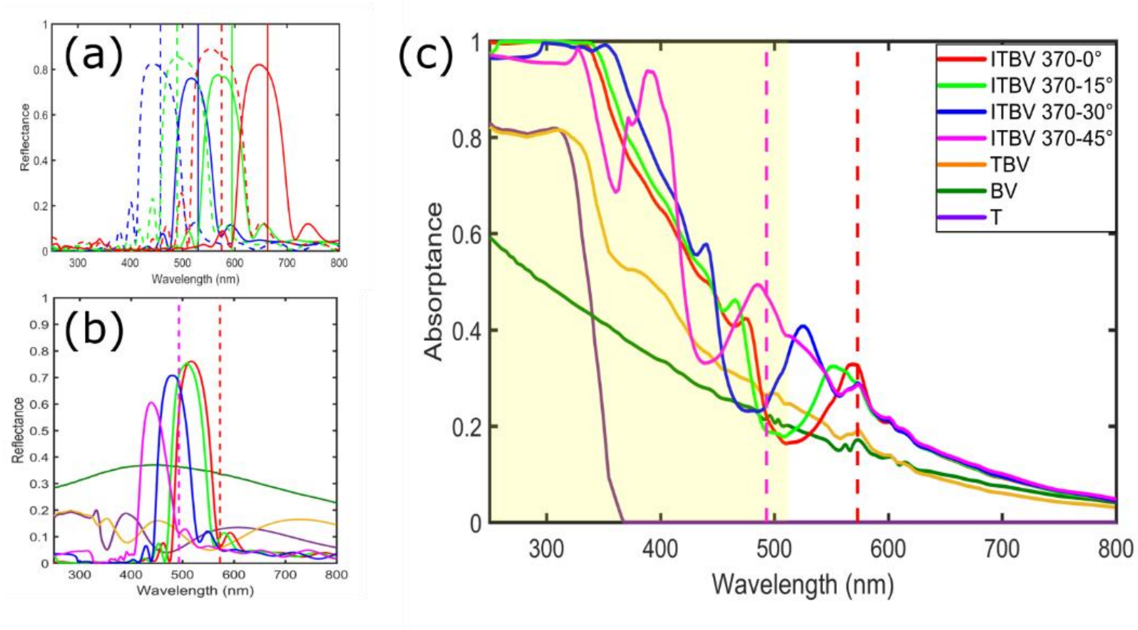

Fig. 4.20: (a) RCWA simulation of reflectance at normal incidence in air (dotted lines) and in water (thick lines) of ITBV 370 (blue), ITBV 420 (green) and ITBV 460 (red) at normal incidence (0°); the lines corresponding to the peaks of the simulated plots represent the experimental peaks. **(b)** RCWA simulation of reflectance and absorptance of TiO_2 film (violet), $BiVO_4$ film (dark green), TiO_2-$BiVO_4$ film (orange) and ITBV 370 in water at 0° (red), 15° (green), 30° (blue) and 45° (magenta); corresponding dotted lines indicate red edge slow photon regions at 0° (red) and 45° (magenta). **(c)** RCWA simulation of absorptance of ITBV 370 in water at 0° (red), 15° (green), 30° (blue) and 45° (magenta), TiO_2-$BiVO_4$ thin film (orange), $BiVO_4$ thin film (green), and TiO_2 thin film (violet); corresponding dotted lines indicate red edge slow photon regions at 0° (red) and 45° (magenta).

RCWA is a full vector, three-dimensional, electromagnetic computational method that is well suited to simulations of the optical response of inverse opals[23, 56]. Spectra were calculated, at different incident polar angles (θ), assuming fixed incident azimuth angle and non-polarized light. Calculations considered contributions of all diffraction orders and evanescent waves[56]. RCWA, being based on Fourier series expansion of the permittivity in lateral directions, numerical convergence was checked with respect to the number of Fourier components (n_g), which is also equal to the number of plane waves in electric (magnetic) field expansions. It was found that $n_g = 5 \times 5$ plane waves were sufficient to reach good accuracy. Simulated IO slabs ([111] crystal facet exposed to the surface) consisted of 4-unit cells that were stacked one over the other such that the slab thickness was close to the sample thickness in experiments. The parameter D of simulated IO slabs was taken equal to the pore diameters determined from SEM images.

The same values of f and n_{med} used for Bragg fitting were used for RCWA. However, unlike for Bragg's equation predictions, the wavelength-dependent complex RI data were used in order to account for material's absorption and its spectral dependence. Estimation of n_{mat}, to be used for RCWA simulation, was carried out after considering the porosity of the IO skeleton. The volume fractions of TiO_2 (x) and $BiVO_4$ (1-x) were calculated from the volumes of each constituent obtained by measuring mass and density of IO TiO_2 and IO TiO_2-$BiVO_4$ samples; a value of x=0.885 was thus obtained. Then, the porosity of each constituent was estimated from the ratio of measured sample density and bulk material density of individual components. The RI values of each constituent were estimated by weighting the RI values of the corresponding bulk material and air, based on the corresponding porosity values determined above.

RCWA reflectance simulations were found to be in excellent agreement with experimentally observed values of SBG peak wavelengths, both in air and in water, at all angles **(Fig. 4.20 (a, b))**. From reflectance simulations, the wavelengths of slow photons, at both blue and red edges of the SBG, were determined **(Fig. 4.20 (a, b))**. Absorptance spectra were also simulated at different angles for ITBV 370 in water, taken as an example, and compared with absorptance spectra of thin films of TiO_2, $BiVO_4$ and TiO_2-$BiVO_4$, whose thicknesses were calculated to lead to identical volume fractions of the corresponding materials in the ITBV samples **(Fig. 4.20 (c))**. RCWA reflectance and absorptance simulations permitted not only the theoretical prediction of the exact position of slow photons but also the justification of photocatalytic activity based on the correlation between tuning of slow photon wavelengths and enhancement of light absorption.

4.3.4. Tuning and transfer of slow photons for enhanced photocatalysis

The ability to tune the wavelengths of slow photons for obtaining maximum photocatalytic activity was demonstrated through the photodegradation of RhB using a lab set-up device **(Fig. 4.2)** using three IO TiO_2-$BiVO_4$ samples - ITBV 370, ITBV 420 and ITBV 460 - each at incidence angles 0°, 15°, 30° and 45°, and comparing them with the non-IO compact films - TiO_2-$BiVO_4$, $BiVO_4$, TiO_2 - and with the inverse opal TiO_2 (IT 420). The comparison of normalized photocatalytic activities of all the samples is presented in terms of degradation efficiency $((C_0 - C) \times 100 / C_0)$ in **Fig.**

4.21, in tabular form in **Table 4.4**, normalized RhB concentration (C_0/C) in **Fig. 4.22** and in variation in RhB absorptance with time in **Fig. 4.23**.

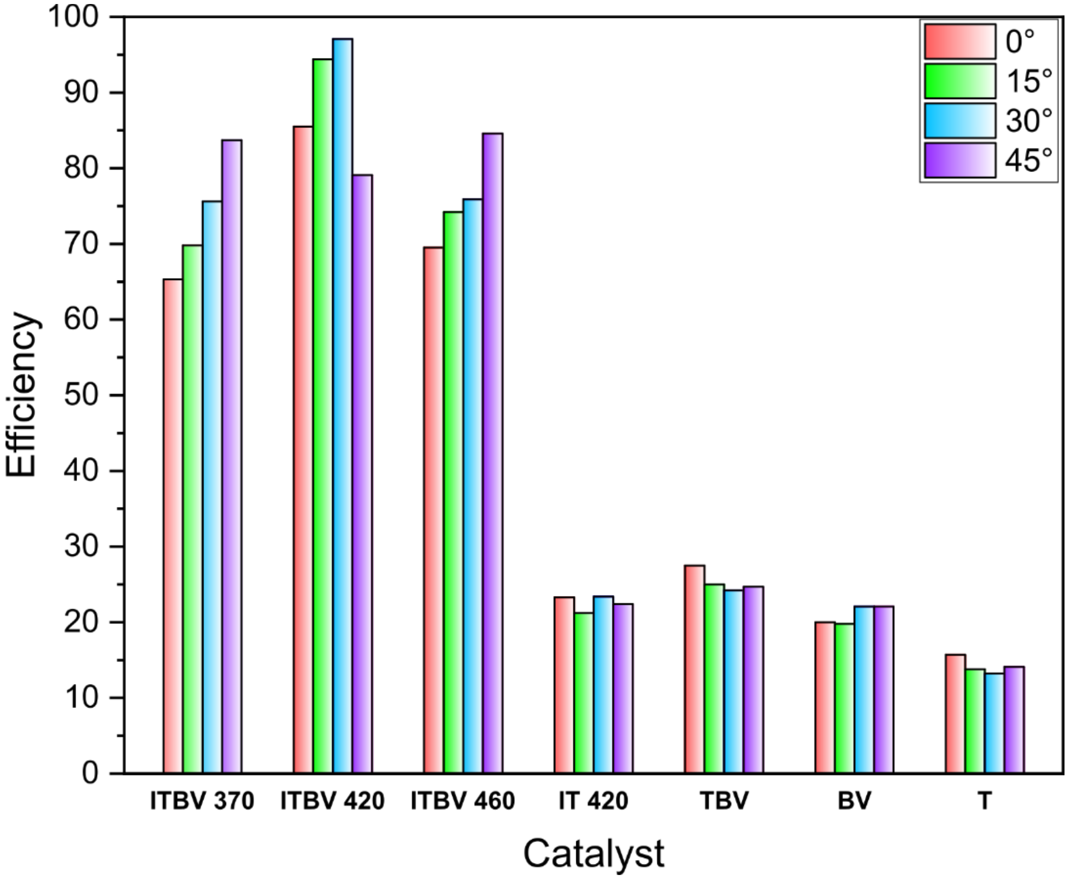

Fig. 4.21: Comparison of the photocatalytic RhB degradation efficiency of: ITBV 370, ITBV 420, ITBV 460, IO TiO_2 (IT 420), TiO_2-$BiVO_4$ thin film (TBV), $BiVO_4$ thin film (BV) and TiO_2 thin film (T) at 0°, 15°, 30° and 45°.

ITBV 370 exhibited a degradation efficiency of 65% at 0° incidence angle. However, with increase in incidence angle to 15°, 30° and 45°, the activity increased to 69%, 75% and 84% respectively **(Fig. 4.21)**. This can be explained by the shift of SBG reflection peak and the wavelengths of red edge slow photons with incidence angle **(Fig. 4.18 (a))**. At 0°, the red edge slow photons at ≈ 590 nm, generated by ITBV 370, were far away from the electronic absorption edge of $BiVO_4$. With increasing incidence angles in aqueous conditions, they underwent a gradual blue shift, closer to the electronic absorption of $BiVO_4$. At 45°, the wavelengths of red edge slow photons overlapped completely with the absorption region of $BiVO_4$. In this case, the photons at the red edge whose group velocity was drastically reduced and localized preferentially in the higher RI medium (IO material skeleton), were able to be more efficiently harvested by $BiVO_4$ nanoparticles resulting in significant improvement in photocatalytic activity. When compared to the degradation efficiency of non-IO compact films, this highest activity achieved by the accurate tuning and transfer of slow photons at 45° incidence angle was 3.5, 3.5 and 6 times higher than those of TiO_2-$BiVO_4$, $BiVO_4$ and TiO_2 compact films that did not manifest any distinct SBG with tuneable slow photon regions at the edges **(Figs. 4.10 (c), 4.13 (c), 4.18 (d))**.

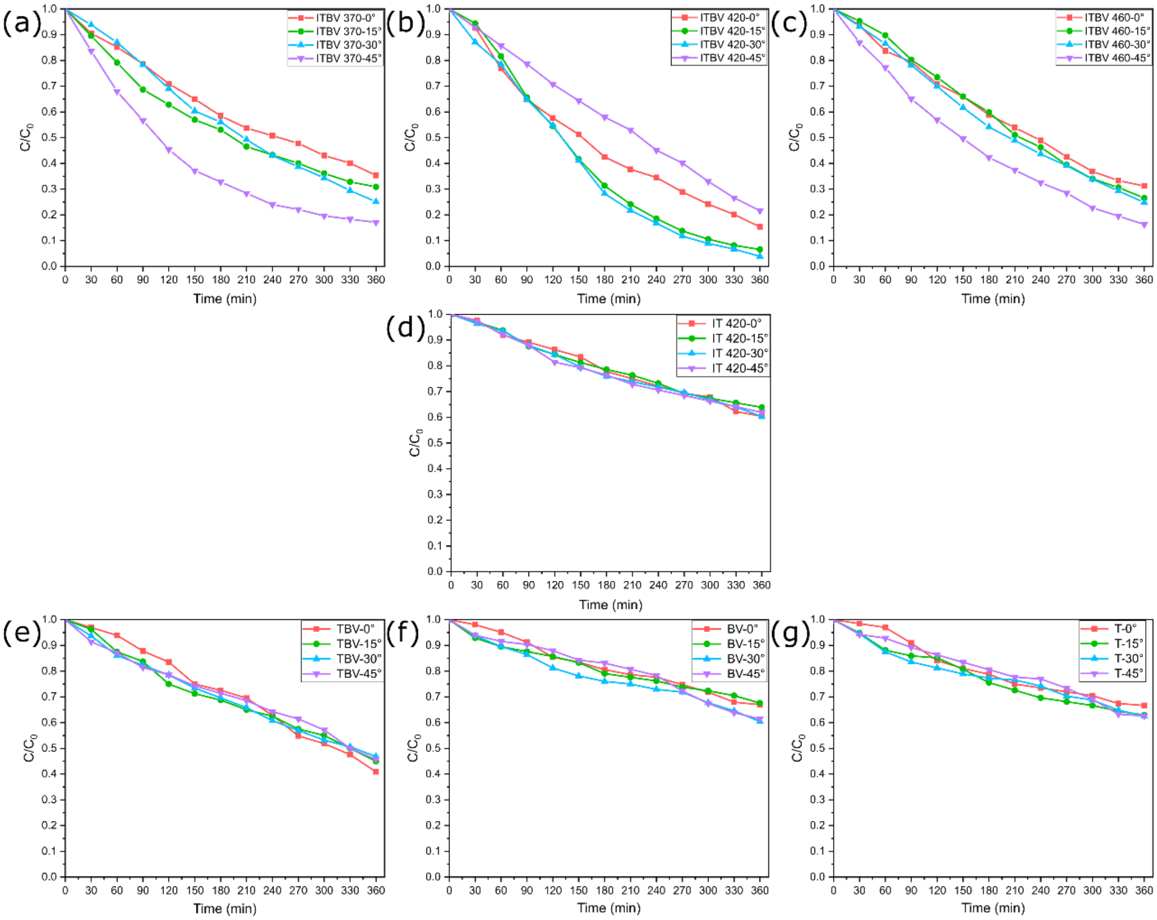

Fig. 4.22: Plots of normalized concentration (C/C_0) as a function of time indicating the RhB degradation activity of: (a) ITBV 370; (b) ITBV 420; (c) ITBV 460; (d) IT 420; (e) TiO_2-$BiVO_4$ thin film (TBV), $BiVO_4$ thin film (BV) and TiO_2 thin film (T) at 0°, 15°, 30° and 45°.

Additional conclusive evidence of the slow photon effect was drawn from the observation that the change in activity with incidence angle variation found in IO TiO_2-$BiVO_4$ samples was not present in the non-IO compact films **(Fig. 4.21)**. Further comparison was made with the IO TiO_2 sample (IT 420) without the $BiVO_4$ component. In this case, the activity of ITBV 370 at 45° incidence angle was 4.5 times higher than that of IT 420. This confirmed that, in the experimental conditions, $BiVO_4$ was the predominant contributor for light absorption and photodegradation, as the slow photons of the ITBV samples in aqueous medium were in the visible range around the electronic absorption edge of $BiVO_4$ (ca. 516 nm = 2.4 eV) and far away from the electronic absorption edge of TiO_2 (ca. 387 nm = 3.2 eV).

Table 4.4: Variation of SBG peak position of the IO samples as a function of the pore diameter, pore filling medium and incidence angle, along with their photocatalytic activities compared with those of compact films.

Sample	**Pore diameter (nm)**	**SBG in air λ - (nm)**				**SBG in water - λ (nm)**				**Photocatalytic efficiency (%)**			
		0°	**15°**	**30°**	**45°**	**0°**	**15°**	**30°**	**45°**	**0°**	**15°**	**30°**	**45°**
ITBV 370	258	458	450	405	362	530	523	500	466	65.3	69.8	75.2	83.7
ITBV 420	286	490	483	435	385	595	590	564	523	85.5	94.4	97.1	79.1
ITBV 460	323	575	560	516	441	663	653	625	562	69.5	74.2	75.9	84.6
IT 420	286	499	493	439	395	593	582	561	520	23.3	21.2	23.4	22.4
TiO_2-$BiVO_4$ film	-	-	-	-	-	-	-	-	-	27.5	25	24.2	24.7
$BiVO_4$ film	-	-	-	-	-	-	-	-	-	22	21.8	24.1	23.1
TiO_2 film	-	-	-	-	-	-	-	-	-	15.7	13.8	13.2	14.1

Similarly, for ITBV 420, with increase in incidence angle, the degradation efficiency gradually increased to reach the highest activity of 97% at 30° incidence angle and then decreased at 45° incidence angle. In this case, the blue edge slow photons were tuned to the electronic absorption of $BiVO_4$ **(Fig. 4.18 (b))**. Photons at the blue edge with their reduced group velocity are localized preferentially in the lower RI medium (water). Although counter-intuitive to understand, these blue-edge slow photons, despite their preferential localization in water, were able to effectively enhance absorption by $BiVO_4$ nanoparticles. This blue edge SPE was previously established and explained through both theoretical explanations based on optical simulations[56] and experimental results[57]. In fact, it was noted in these experiments that, among the three ITBV photocatalysts where tuning was actualized, ITBV 420 demonstrated the highest performance of 97% at 30° incidence angle. This can be explained by the interplay between two opposing factors in IO photocatalysis - increased light absorption due to slow photons and decreased light harvesting due to stop band gap reflection. In the case of ITBV 420 at 30° incidence angle, the blue edge slow photons were tuned to overlap with the electronic absorption of $BiVO_4$ while at the same time the SBG reflection peak remained outside the absorption region of the photocatalyst, thereby maximizing absorption and simultaneously avoiding reflection. This reasoning was further substantiated by the observation of a drop in degradation efficiency to 79% with further increase in incidence angle to 45°. At this angle, the SBG reflection peak further blue shifted to overlap with $BiVO_4$ absorption region causing light to be reflected, thereby attenuating the absorption of light by $BiVO_4$, and reducing the activity of the photocatalyst. The highest activity obtained under accurate tuning conditions in ITBV 420 was 4, 4, and 7 times higher than those of TiO_2-$BiVO_4$, $BiVO_4$ and TiO_2 compact films respectively.

ITBV 460 showed similar trends with the highest activity (85%) at 45° incidence where the blue edge slow photons overlapped with the electronic absorption of $BiVO_4$ **(Fig. 4.18 (c))**. At lower incidence angles, it exhibited lower photocatalytic activities as the slow photons were located at longer wavelengths, far away from the absorption region of $BiVO_4$. The manipulation of slow photons, in this sample, resulted in an increase in photocatalytic activity that was 3.5, 3.5 and 6 times higher than those of TiO_2-$BiVO_4$, $BiVO_4$ and TiO_2 compact films.

RCWA reflectance and absorptance simulations further validated the above interpretation of experimental results. In the case of ITBV 370, taken as an example, the red edge slow photons at 0° and 45° incidence angles, are highlighted by vertical dashed lines in the simulated absorptance spectra **(Fig. 4.20 (c))**. It is observed that the red edge at normal incidence ($\theta=0°$) lies beyond the electronic absorption edge of $BiVO_4$ (yellow shaded region in **(Fig. 4.20 (c))**. On the other hand, the red edge at incidence angle equal to $\theta=45°$ lies well within the absorption of bismuth vanadate. This justifies the difference in the experimentally measured photocatalytic activity, which was the highest at 45°, with slow photon assistance, and the least at 0°, without slow photon assistance. Furthermore, due to slow photons, ITBV 370 exhibited significantly higher absorptance than the compact films at all angles, despite slight attenuation of the absorptance in the spectral region of SBG angle-dependent reflection. This validates the experimental observation wherein the photocatalytic activities of all IO samples were 4-7 times higher than their corresponding equivalent compact films **(Fig. 4.21)**. RCWA simulations, by quantitatively predicting the total absorption of the samples, enabled us to rationalize the accurate correspondence between theoretical and experimental results in terms of the activities of all the samples. In addition, the reflectance and absorptance spectra predicted by RCWA permitted us to justify the correspondence between the slow photon tuning conditions, their transfer from the IO TiO_2 structure to the photoactive $BiVO_4$ composite and the enhancement of absorption that led to highly increased photocatalytic activity.

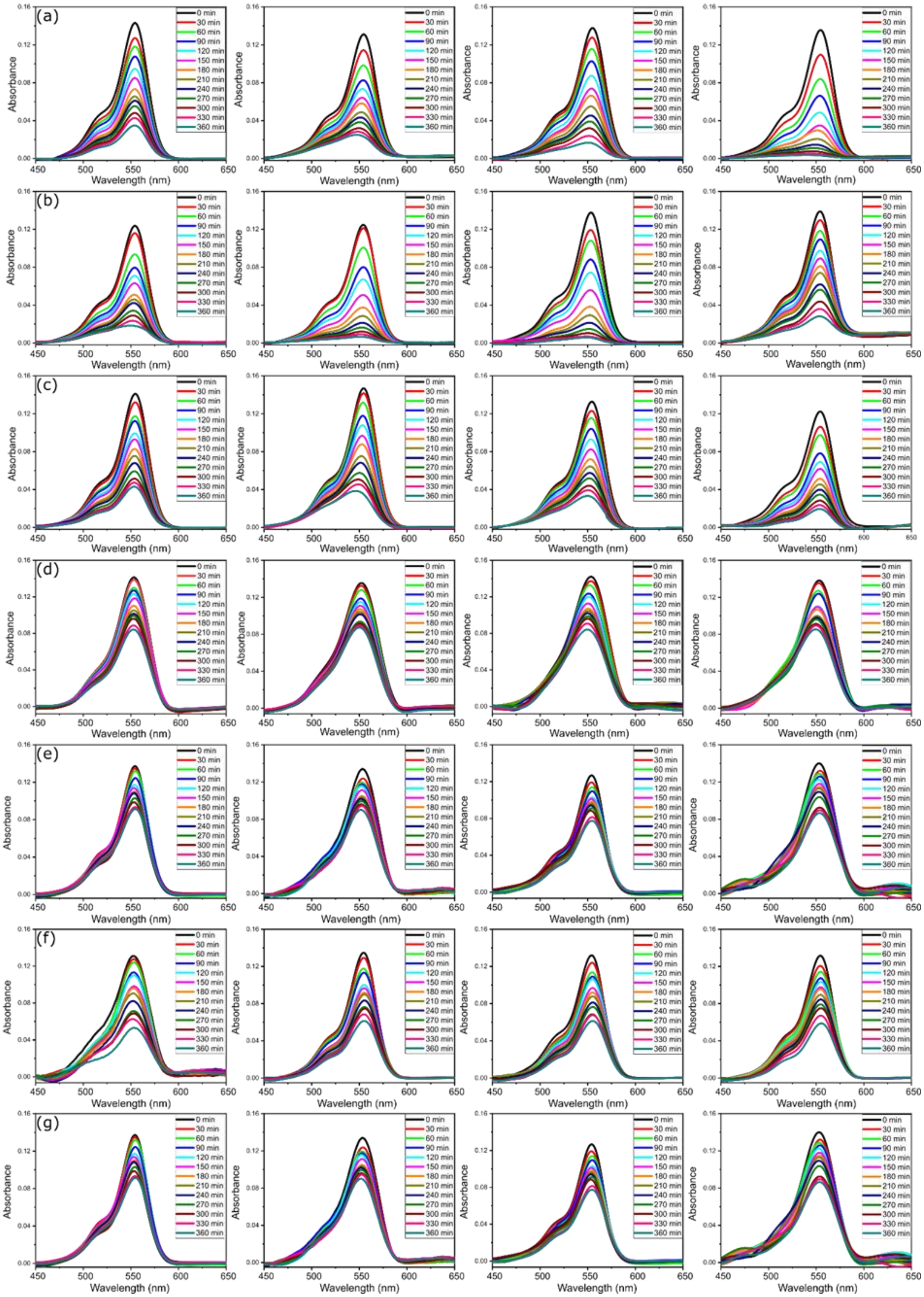

Fig. 4.23: Decrease of RhB absorptance with time of photocatalysis of: (a) ITBV 370; (b) ITBV 420; (c) ITBV 460; (d) IT 420; (e) TiO_2-$BiVO_4$ thin film (TBV), $BiVO_4$ thin film (BV) and TiO_2 thin film (T) at 0°, 15°, 30° and 45°.

4.3.5. Normalization of photocatalytic efficiencies

The change in optical path length with increase in light incidence angle was considered in order to better compare the photocatalytic activities at different incidence angles. Normalization of photocatalytic efficiency was done based on the following principles. Firstly, Snell's law of refraction was used to determine the actual angle of light incidence as it passes from air through water and then through the inverse opal sample having the pores filled with water. The optical path of light from air to the sample is schematically represented in **Fig. 4.24** with the red lines indicating the optical path lengths in the sample at normal incidence and at increased incidence angle.

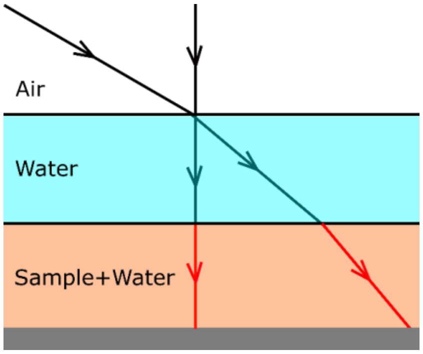

Fig. 4.24: Schematic representation of the optical path of light from air medium to the sample. The lines marked in red represent the optical path lengths inside the sample at normal incidence and increased incidence angle.

The effective RI of the sample in water was calculated based on Bruggemann approximation as discussed earlier. The change in optical path length with light incidence angle was then calculated as presented in **Table 4.5**.

Table 4.5: Calculation of normalization factors for different light incidence angles based on the change in optical path length with increase in incidence angle.

Incidence angle (θ_1) (degrees)	RI of air (n_1)	RI of water (n_2)	RI of IO sample with water (n_3)	Effective incidence angle (θ_3)	Optical path (µm)	Optical path normalization factor
0	1.00	1.33	1.60	0.00	1.50	1.00
15	1.00	1.33	1.60	9.31	1.52	0.99
30	1.00	1.33	1.60	18.22	1.58	0.95
45	1.00	1.33	1.60	26.24	1.67	0.90

In addition to the above, Fresnel reflection at the interface between two different media, which changes with light incidence angle, was also considered. Fresnel reflection coefficients (spolarized: r_s and p-polarized: r_p) were calculated for both air-water and water-sample interfaces. Based on the above, the normalization factor for each angle was calculated as 1, 0.98, 0.95, 0.90 for 0°, 15°, 30°, and 45° respectively **(Tables 4.6)**.

Table 4.6: Calculation of normalization factors for different light incidence angles based on the change in Fresnel reflection with increase in incidence angle (R-Reflectance, T-Transmittance)

	Air-Water interface				**Water-Sample interface**					
Incidence angle (θ_1) (degrees)	**Rs**	**Rp**	**R= (Rs+Rp)/2**	**T1= 1-R**	**Rs**	**Rp**	**R= (Rs+Rp)/ 2**	**T2= 1-R**	**Light reflection normalization**	**Resulting normalization**
0	0.02	0.02	0.02	0.98	0.01	0.01	0.01	0.99	1.00	1.00
15	0.02	0.02	0.02	0.98	0.01	0.01	0.01	0.99	1.00	0.99
30	0.03	0.01	0.02	0.98	0.01	0.00	0.01	0.99	1.00	0.95
45	0.05	0.00	0.03	0.97	0.02	0.00	0.01	0.99	1.01	0.91

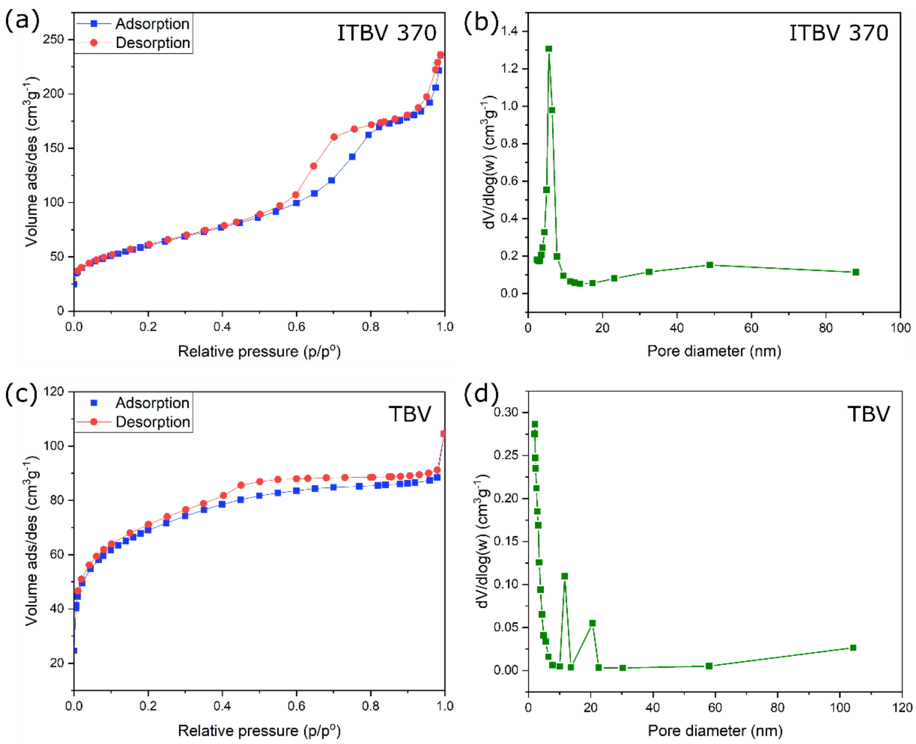

Fig. 4.25: (a-b) Nitrogen physisorption isotherms and pore size distribution of ITBV 370; **(c-d)** nitrogen physisorption isotherms and pore size distribution of TBV.

Comparison between the photocatalytic activities of macroporous IO films with those of compact films was better rendered by normalization based on the specific surface area. Using N_2 physisorption method, the specific surface area of IO TiO_2-$BiVO_4$ and bulk TiO_2-$BiVO_4$ were determined as 218.35 m^2g^{-1} and 197.56 m^2g^{-1} respectively **(Fig. 4.25)**. The specific surface area of

IO samples was significantly higher than the theoretically predicted specific surface area for IO structures[58], as the walls of the IO matrix were composed of nanoparticles that induces additional porosity in the sample, as evidenced from the pore size distribution in **Fig. 4.25 (b)**. Also, the high specific surface area of the bulk sample is attributed to the small size of NPs that compose the bulk structure. The resulting normalized values of photocatalytic efficiencies are shown in **Table 4.7** and depicted in **Fig. 4.26**.

Table 4.7: Photocatalytic efficiencies at various light incidence angles after normalization with optical path length and specific surface area

Photocatalyst	Photocatalytic efficiency				Normalized with path length				Normalized with surface area			
	0°	15°	30°	45°	0°	15°	30°	45°	0°	15°	30°	45°
ITBV-370	65.3	69.8	75.6	83.7	65.3	68.9	72.0	76.0	65.3	68.9	72.0	76.0
ITBV-420	85.5	94.4	97.1	79.1	85.5	93.2	92.4	71.8	85.5	93.2	92.4	71.8
ITBV-460	69.5	74.2	75.9	84.6	69.5	73.2	72.2	76.8	69.5	73.2	72.2	76.8
IT 420	23.3	21.2	23.4	22.4	23.3	20.9	22.3	20.3	23.3	20.9	22.3	20.3
TBV	27.5	25.0	24.2	24.7	27.5	24.7	23.0	22.4	30.4	27.3	25.4	24.8
BV	19.0	18.8	22.1	22.1	19.0	18.6	21.0	20.1	21.0	20.5	23.2	22.2
T	15.7	12.8	13.2	14.1	15.7	12.6	12.6	12.8	17.4	14.0	13.9	14.1

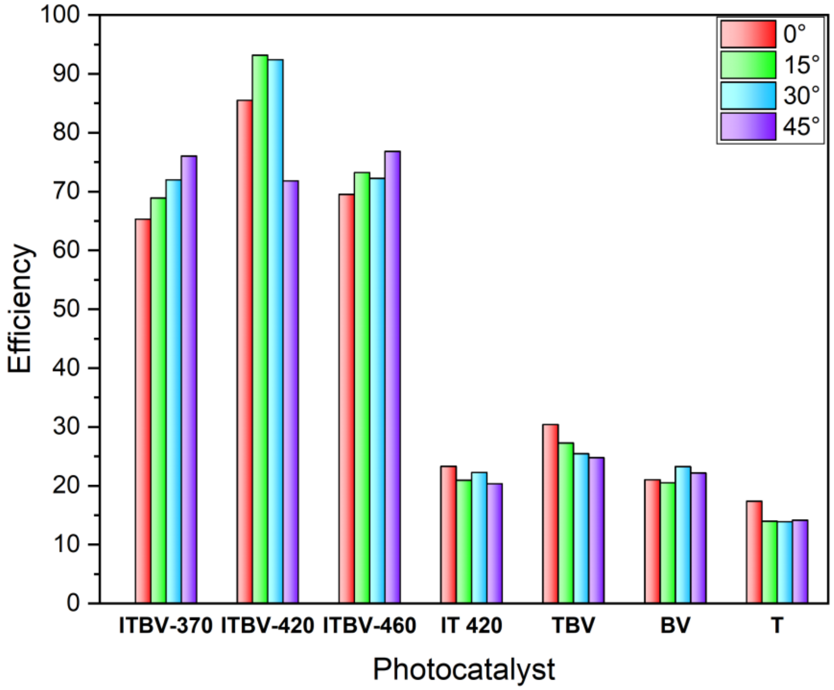

Fig. 4.26: Photocatalytic efficiencies at various light incidence angles after normalization with optical path length and specific surface area

Comparison between the results was analyzed after normalization. It was observed that there was no difference in the overall trends of photocatalytic activities. However, the photocatalytic enhancement factors were relatively decreased. For instance, in the case of ITBV 370, the enhancement factor when light incidence angle changed from 0° to 45° which was 1.28, was reduced to 1.26 after normalization. Similarly, the highest activity obtained under optimal tuning conditions in ITBV 420 was 4, 4, and 7 times higher than those of TiO_2-$BiVO_4$, $BiVO_4$ and TiO_2 compact films, while after normalization it was 3.4, 3.5, and 6.7 times higher after normalization.

4.3.6. Mechanism of RhB degradation by $BiVO_4$

The mechanism of RhB degradation by $BiVO_4$ under visible light is shown schematically in **Fig. 4.27** and can be explained based on the following steps[59, 60]:

1. Photoexcitation: Light having energy (*hv*) greater than or equal to the band gap of $BiVO_4$ (~2.3 eV) is absorbed by it causing photoexcitation. Electrons in the valence band are excited to the conduction band (e^-_{CB}) leaving behind holes in the valence band (h^+_{VB}) as shown in the following equation:

$$BiVO_4 + hv \rightarrow BiVO_4\ (e^-_{CB} + h^+_{VB})$$

2. Ionization of water: Photogenerated holes in VB react with adsorbed water molecule or OH^- ion to form $OH^\cdot$ radical, which is an extremely powerful oxidizing agent.

$$H_2O\ (ads) + h^+_{VB} \rightarrow OH^\bullet\ (ads) + H^+(ads)$$

$$OH^-\ (ads) + h^+_{VB} \rightarrow OH^\bullet\ (ads)$$

3. Oxygen ionosorption and protonation of superoxide: Meanwhile electrons in CB react with dissolved oxygen to generate superoxide radical ($O_2^{-\cdot}$).

$$O_2 + e^-_{CB} \rightarrow O_2^{-\bullet}$$

This superoxide gets protonated producing hydroperoxyl radical and subsequently H_2O_2. The H_2O_2 formed further dissociates into highly reactive hydroxyl radicals.

$$O_2^{-\bullet}\ (ads) + H^+ \rightarrow HOO^\bullet\ (ads)$$

$$2HOO^\bullet\ (ads) \rightarrow H_2O_2\ (ads) + O_2$$

$$H_2O_2\ (ads) \rightarrow 2OH^\bullet\ (ads)$$

4. Dye degradation: The hydroxyl radicals thus formed react with RhB to form degradation products via various intermediates.

$$RhB + 2OH^\bullet \rightarrow \text{Intermediate degradation products} \rightarrow CO_2 + H_2O$$

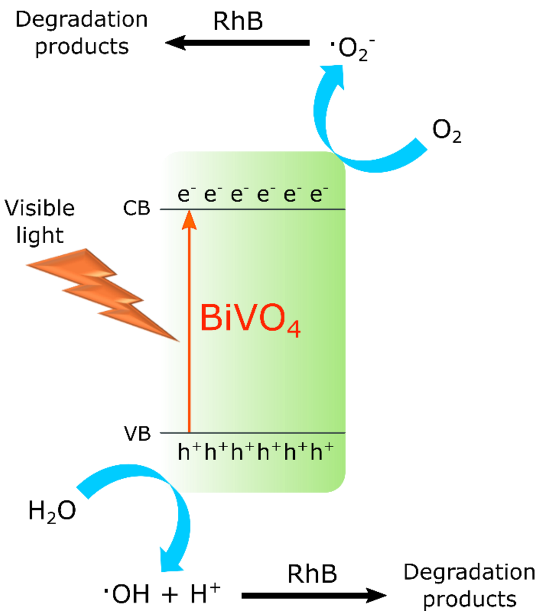

Fig. 4.27: Schematic representation of the mechanism of Rhodamine B over $BiVO_4$.

Rhodamine B is a type of xanthene dye with a xanthene core that consists of three benzene rings fused together in a specific arrangement. Attached to the xanthene core are two diethyl amino groups ($-N(C_2H_5)_2$) that are basic. In addition, there is a phenyl group($-C_6H_5$) with an attached carboxylic group (-COOH). The main RhB absorption peak at 554 nm is due to the presence of ethylated groups on the dye molecule.

Degradation of RhB under visible light over $BiVO_4$ could occur through two possible mechanisms **(Fig. 4.28)**. Firstly, it could occur through successive de-ethylation of the diethyl amino groups that leads to a blue wavelength shift of RhB absorption peak (pathway 1). However, this mechanism is not applicable in this work as the blue shift of absorption peak was not observed during photocatalytic degradation. Alternatively, the highly oxidizing $OH^{\cdot}$ radicals could attack the aromatic chromophore ring, leading to the degradation of RhB, which reduces the intensity of RhB absorption peak during photocatalytic degradation (pathway 2). This is the plausible mechanism in this work as the intensity of RhB absorption peak decreased with photocatalytic degradation. Hence, it can be assumed that, in this work, photocatalytic degradation of RhB over BiVO4 under visible light occurred through the cleavage of the aromatic chromophore ring. Various intermediate products like *o*-xylene, *m*-xylene, ethyl benzene and phthalic anhydride could be formed, as reported in previous research on RhB degradation by $BiVO_4$ under visible light. The final degradation products resulting from the mineralization of dye are CO_2 and H_2O. The two pathways for RhB degradation and the possible intermediates formed are shown in **Fig. 4.28**.

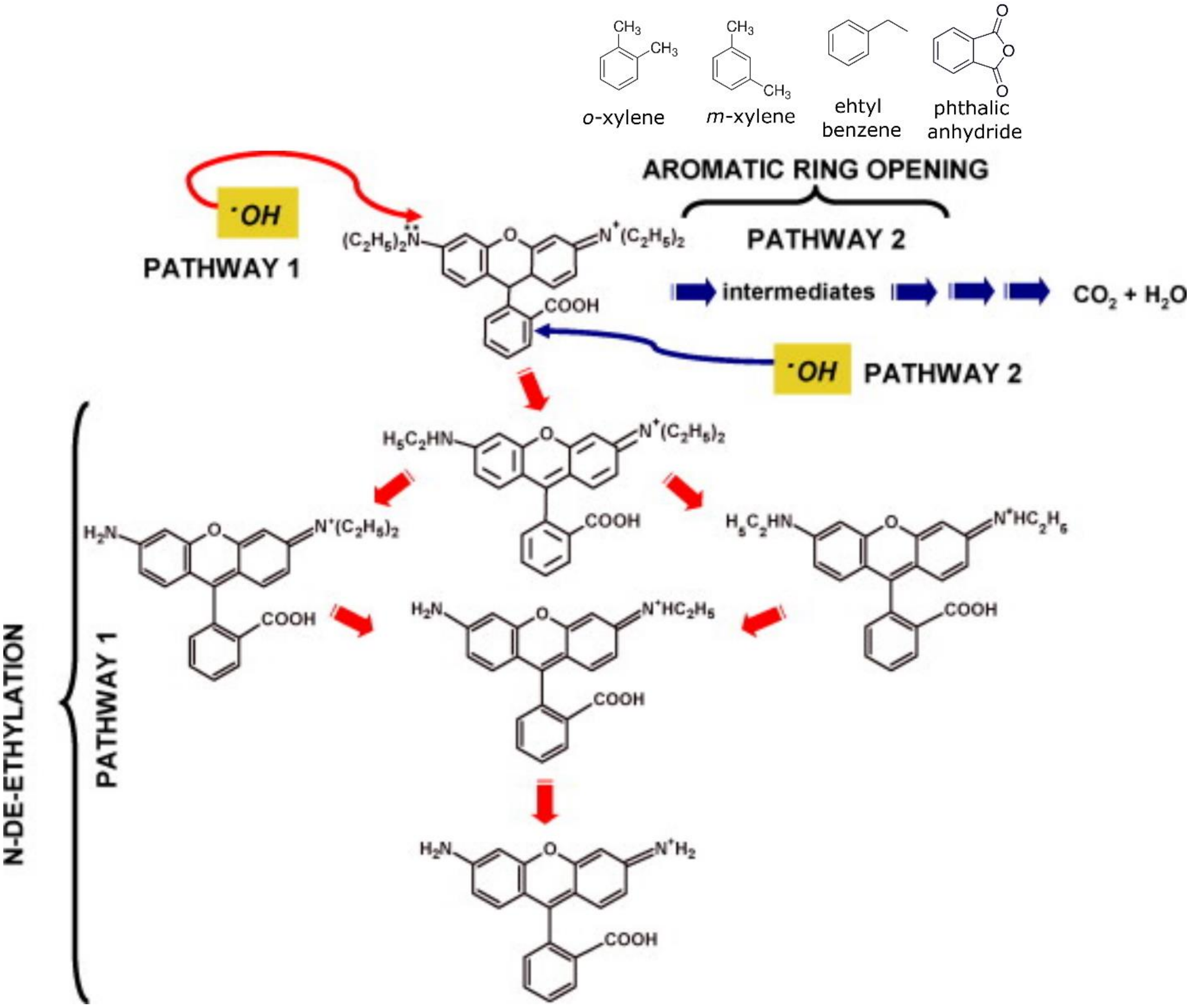

Fig. 4.28: Two different pathways for the photocatalytic degradation of Rhodamine B, along with the possible intermediates.

4.3.7. Stability and recyclability of the photocatalyst

The IO TiO_2-$BiVO_4$ photocatalyst was verified for morphological stability by analysing the images in SEM after photocatalysis. The IO structure of one of the samples, ITBV 370, shown in **Fig. 4.29 (a)**, revealed that the structure remained relatively stable after four cycles of photocatalysis, each for six hours. Photocatalytic consistency was verified by additional photocatalytic tests using the same sample, ITBV 370, for four further cycles at the same light incidence angle of 0°. The results, as shown in **Fig. 4.29 (b-c)**, indicated that was no significant difference in photocatalytic activity.

The above experimental results, firmly supported by simulations studies, establish the feasibility to generate, control, tune and transfer slow photons from IO TiO_2 structures to the composited $BiVO_4$ nanoparticles for highly enhanced visible light photocatalysis. Further, from the above data, it can be generalized that photocatalytic efficiency can be drastically improved by using inverse opal semiconductor photocatalysts, particularly by accurately tuning the wavelengths of slow photons to the electronic absorption of the photocatalyst while simultaneously avoiding the overlap of SBG reflection peak with the electronic absorption region.

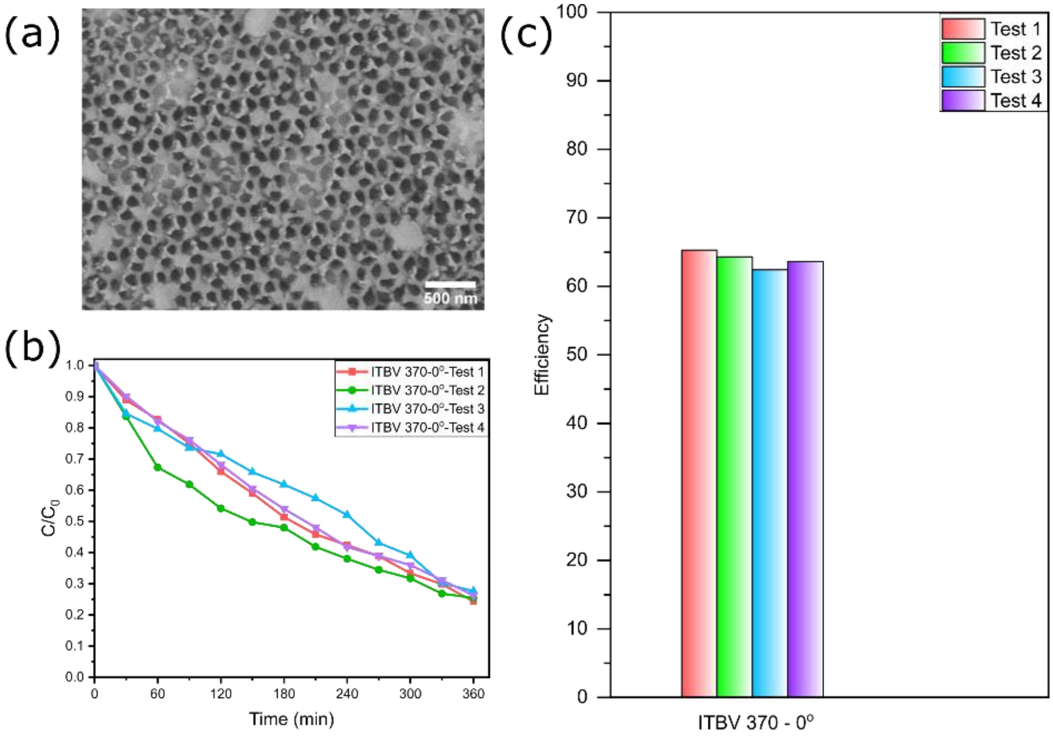

Fig. 4.29: (a) SEM image of ITBV 370 after photocatalysis. **(b-c)** Plots of normalized concentration (C/C_0) as a function of time (b) and of photocatalytic efficiency (c) of ITBV 370 at the same light incidence angle of 0° for four repeated tests.

4.4. Summary

In summary, this work presents the ability to control and tune the frequencies of slow photons generated from inverse opal TiO_2 photonic structures, in aqueous media, such that they can be efficiently harvested by the visible light responsive $BiVO_4$ component of the heterocomposite for enhanced photocatalysis. Tuning of slow photons was realized by regulating the lattice parameter of the photonic structures (pore size) using different template sizes and by variation of light incidence angle from 0° to 45° in steps of 15° using an optical fibre mounted on an angled fibre holder. The photocatalytic efficiencies of the IO photonic structures, under accurate tuning of slow photon frequencies to the electronic absorption of $BiVO_4$, reached up to 7 times higher than those of the non-IO compact films. These experimental results were further substantiated by RCWA reflectance and absorptance simulations, which revealed not only a close match between experimental and theoretical positions of SBG's and slow photons but also a strong correlation between tuning of slow photon frequencies and increased absorptance that justified the enhanced photocatalytic activity. Through this work, I demonstrated the first proof of concept of tuning slow photon frequencies in aqueous medium and transferring them from IO photonic structures (TiO_2) to visible light-active photocatalyst ($BiVO_4$), for achieving exceptional photocatalytic activity. I believe that this work would instigate further research to improve light manipulation and harvesting in IO photonic structures for visible light photocatalysis, thereby opening innovative pathways for sustainable energy applications.

References

1. Kubacka, A.; Fernandez-Garcia, M.; Colon, G., Advanced nanoarchitectures for solar photocatalytic applications. *Chemical Reviews* **2012,** *112* (3), 1555-1614.
2. Meng, X.; Liu, L.; Ouyang, S.; Xu, H.; Wang, D.; Zhao, N.; Ye, J., Nanometals for solar-to-chemical energy conversion: from semiconductor-based photocatalysis to plasmon-mediated photocatalysis and photo-thermocatalysis. *Advanced Materials* **2016,** *28* (32), 6781-6803.
3. Xu, C.; Anusuyadevi, P. R.; Aymonier, C.; Luque, R.; Marre, S., Nanostructured materials for photocatalysis. *Chemical Society Reviews* **2019,** *48* (14), 3868-3902.
4. Armstrong, E.; O'Dwyer, C., Artificial opal photonic crystals and inverse opal structures – fundamentals and applications from optics to energy storage. *Journal of Material Chemistry C* **2015,** *3* (24), 6109-6143.
5. Likodimos, V., Photonic crystal-assisted visible light activated TiO_2 photocatalysis. *Applied Catalysis B* **2018,** *230*, 269-303.
6. Joannopoulos, J. D.; Johnson, S. G.; Winn, J. N.; Meade, R. D., *Photonic crystals*. Princeton Univ. Press: 2011.
7. John, S., Strong localization of photons in certain disordered dielectric superlattices. *Physical Review Letters* **1987,** *58* (23), 2486-2489.
8. Soukoulis, C. M., *Photonic crystals and light localization in the 21st century*. Springer Science & Business Media: 2012; Vol. 563.
9. Yablonovitch, E., Inhibited spontaneous emission in solid-state physics and electronics. *Physical Review Letters* **1987,** *58* (20), 2059-2062.
10. Baba, T., Slow light in photonic crystals. *Nature Photonics* **2008,** *2* (8), 465-473.
11. Collins, G.; Armstrong, E.; McNulty, D.; O'Hanlon, S.; Geaney, H.; O'Dwyer, C., 2D and 3D photonic crystal materials for photocatalysis and electrochemical energy storage and conversion. *Science and Technology of Advanced Materials* **2016,** *17* (1), 563-582.
12. Curti, M.; Schneider, J.; Bahnemann, D. W.; Mendive, C. B., Inverse opal photonic crystals as a strategy to improve photocatalysis: underexplored questions. *Journal of Physical Chemistry Letters* **2015,** *6* (19), 3903-10.
13. Pietron, J. J.; DeSario, P. A., Review of roles for photonic crystals in solar fuels photocatalysis. *Journal of Photonics Energy* **2016,** *7,* (1).
14. Zheng, X.; Zhang, L., Photonic nanostructures for solar energy conversion. *Energy Environmental Science* **2016,** *9* (8), 2511-2532.
15. Liu, J.; Zhao, H.; Wu, M.; Van der Schueren, B.; Li, Y.; Deparis, O.; Ye, J.; Ozin, G. A.; Hasan, T.; Su, B. L., Slow photons for photocatalysis and photovoltaics. *Advanced Materials* **2017,** *29* (17), 1605349.
16. Chen, J. I. L.; von Freymann, G.; Choi, S. Y.; Kitaev, V.; Ozin, G. A., Amplified photochemistry with slow photons. *Advanced Materials* **2006,** *18* (14), 1915-1919.
17. Wu, M.; Jin, J.; Liu, J.; Deng, Z.; Li, Y.; Deparis, O.; Su, B.-L., High photocatalytic activity enhancement of titania inverse opal films by slow photon effect induced strong light absorption. *Journal of Material Chemistry A* **2013,** *1* (48), 15491-15500.
18. Wu, M.; Liu, J.; Jin, J.; Wang, C.; Huang, S.; Deng, Z.; Li, Y.; Su, B.-L., Probing significant light absorption enhancement of titania inverse opal films for highly exalted photocatalytic degradation of dye pollutants. *Applied Catalysis B* **2014,** *150-151*, 411-420.
19. Xie, H.; Li, Y.; Jin, S.; Han, J.; Zhao, X., Facile fabrication of 3D-ordered macroporous nanocrystalline iron oxide films with highly efficient visible light induced photocatalytic activity. *Journal of Physical Chemistry C* **2010,** *114* (21), 9706-9712.

20. Zhang, L.; Baumanis, C.; Robben, L.; Kandiel, T.; Bahnemann, D., Bi_2WO_6 inverse opals: facile fabrication and efficient visible-light-driven photocatalytic and photoelectrochemical water-splitting activity. *Small* **2011,** *7* (19), 2714-20.

21. Liu, J.; Jin, J.; Li, Y.; Huang, H.-W.; Wang, C.; Wu, M.; Chen, L.-H.; Su, B.-L., Tracing the slow photon effect in a ZnO inverse opal film for photocatalytic activity enhancement. *Journal of Material Chemistry A* **2014,** *2* (14).

22. Curti, M.; Mendive, C. B.; Grela, M. A.; Bahnemann, D. W., Stopband tuning of TiO_2 inverse opals for slow photon absorption. *Materials Research Bulletin* **2017,** *91*, 155-165.

23. Curti, M.; Zvitco, G.; Grela, M. A.; Mendive, C. B., Angle dependence in slow photon photocatalysis using TiO_2 inverse opals. *Chemical Physics* **2018,** *502*, 33-38.

24. Phillips, K. R.; Shirman, T.; Shirman, E.; Shneidman, A. V.; Kay, T. M.; Aizenberg, J., Nanocrystalline precursors for the co-assembly of crack-free metal oxide inverse opals. *Advanced Materials* **2018,** *30* (19), 1706329.

25. Hyun Jeong, J.; Myoung Soo, G.; Seuk Beum, K.; Byoung Joon, A.; Wong Hil, C., *Journal of Industrial and Engineering Chemistry* **2006,** *12* (5), 689-693.

26. Waterhouse, G. I.; Waterland, M. R., Opal and inverse opal photonic crystals: Fabrication and characterization. *Polyhedron* **2007,** *26* (2), 356-368.

27. Shen, K.; Zhang, L.; Chen, X.; Liu, L.; Zhang, D.; Han, Y.; Chen, J.; Long, J.; Luque, R.; Li, Y., Ordered macro-microporous metal-organic framework single crystals. *Science* **2018,** *359* (6372), 206-210.

28. Chemseddine, A.; Moritz, T., Nanostructuring titania: control over nanocrystal structure, size, shape, and organization. *European Journal of Inorganic Chemistry* **1999,** *1999* (2), 235-245.

29. Hatton, B.; Mishchenko, L.; Davis, S.; Sandhage, K. H.; Aizenberg, J., Assembly of large-area, highly ordered, crack-free inverse opal films. *Proceedings of the National Academy of Sciences* **2010,** *107* (23), 10354-9.

30. Kumbhar, V. S.; Lee, H.; Lee, J.; Lee, K., Interfacial growth of the optimal $BiVO_4$ nanoparticles onto self-assembled WO_3 nanoplates for efficient photoelectrochemical water splitting. *Journal of Colloid and Interface Science* **2019,** *557*, 478-487.

31. Kim, D. J.; Hahn, S. H.; Oh, S. H.; Kim, E. J., Influence of calcination temperature on structural and optical properties of TiO_2 thin films prepared by sol–gel dip coating. *Materials Letters* **2002,** *57* (2), 355-360.

32. Hernández, S.; Thalluri, S. M.; Sacco, A.; Bensaid, S.; Saracco, G.; Russo, N., Photo-catalytic activity of $BiVO_4$ thin-film electrodes for solar-driven water splitting. *Applied Catalysis A-Gen.* **2015,** *504*, 266-271.

33. Du, X.; He, J., Facile size-controllable syntheses of highly monodisperse polystyrene nano- and microspheres by polyvinylpyrrolidone-mediated emulsifier-free emulsion polymerization. *Journal of Applied Polymer Science* **2008,** *108* (3), 1755-1760.

34. Gonzalez-Urbina, L.; Baert, K.; Kolaric, B.; Perez-Moreno, J.; Clays, K., Linear and nonlinear optical properties of colloidal photonic crystals. *Chemical Reviews* **2012,** *112* (4), 2268-85.

35. Rengarajan, R.; Mittleman, D.; Rich, C.; Colvin, V., Effect of disorder on the optical properties of colloidal crystals. *Physical Review E* **2005,** *71* (1), 016615.

36. Vogel, N.; Retsch, M.; Fustin, C.-A.; Del Campo, A.; Jonas, U. J., Advances in colloidal assembly: the design of structure and hierarchy in two and three dimensions. *Chemical Reviews* **2015,** *115* (13), 6265-6311.

37. Xu, Y.; German, G. K.; Mertz, A. F.; Dufresne, E. R., Imaging stress and strain in the fracture of drying colloidal films. *Soft Matter* **2013,** *9* (14), 3735-3740.

38. Moon, J. H.; Yang, S., Chemical aspects of three-dimensional photonic crystals. *Chemical Reviews* **2010,** *110* (1), 547-574.

39. Stein, A.; Wilson, B. E.; Rudisill, S. G., Design and functionality of colloidal-crystal-templated materials—chemical applications of inverse opals. *Chemical Society Reviews* **2013,** *42* (7), 2763-2803.

40. von Freymann, G.; Kitaev, V.; Lotsch, B. V.; Ozin, G. A., Bottom-up assembly of photonic crystals. *Chemical Society Reviews* **2013,** *42* (7), 2528-2554.

41. Bhattacharjee, S., DLS and zeta potential–what they are and what they are not? *Journal of Controlled Release* **2016,** *235*, 337-351.

42. Fattakhova-Rohlfing, D.; Zaleska, A.; Bein, T., Three-dimensional titanium dioxide nanomaterials. *Chemical Reviews* **2014,** *114* (19), 9487-558.

43. Wei, Y.; Jiao, J.; Zhao, Z.; Liu, J.; Li, J.; Jiang, G.; Wang, Y.; Duan, A., Fabrication of inverse opal TiO_2-supported Au@ CdS core–shell nanoparticles for efficient photocatalytic CO_2 conversion. *Applied Catalysis B* **2015,** *179*, 422-432.

44. Galisteo-López, J.; Palacios-Lidón, E.; Castillo-Martínez, E.; López, C., Optical study of the pseudogap in thickness and orientation controlled artificial opals. *Physical Reviews B* **2003,** *68* (11), 115109.

45. Jiang, P.; Bertone, J.; Hwang, K. S.; Colvin, V., Single-crystal colloidal multilayers of controlled thickness. *Chemistry of Materials* **1999,** *11* (8), 2132-2140.

46. Ratnayake, S. P.; Ren, J.; Colusso, E.; Guglielmi, M.; Martucci, A.; Della Gaspera, E., SILAR deposition of metal oxide nanostructured films. *Small* **2021,** *17* (49), 2101666.

47. Schroden, R. C.; Al-Daous, M.; Blanford, C. F.; Stein, A., Optical properties of inverse opal photonic crystals. *Chemistry of Materials* **2002,** *14* (8), 3305-3315.

48. Blanford, C. F.; Schroden, R. C.; Al-Daous, M.; Stein, A., Tuning solvent-dependent color changes of three-dimensionally ordered macroporous (3DOM) materials through compositional and geometric modifications. *Advanced Materials* **2001,** *13* (1), 26-29.

49. Lonergan, A.; O'Dwyer, C., Many Facets of Photonic Crystals: From Optics and Sensors to Energy Storage and Photocatalysis. *Advanced Materials Technologies* **2023,** *8* (6), 2201410.

50. Choy, T. C., *Effective medium theory: principles and applications*. Oxford Univ. Press: 2015; Vol. 165.

51. Deparis, O.; Ghazzal, M.; Simonis, P.; Mouchet, S.; Kebaili, H.; De Coninck, J.; Gaigneaux, E. M.; Vigneron, J.-P., Theoretical condition for transparency in mesoporous layered optical media: application to switching of hygrochromic coatings. *Applied Physics Letters* **2014,** *104* (2), 023704.

52. Park, Y. R.; Kim, K. J., Structural and optical properties of rutile and anatase TiO_2 thin films: effects of Co doping. *Thin Solid Films* **2005,** *484* (1-2), 34-38.

53. Yuan, Y.; Huang, Y.; Ma, F.; Zhang, Z.; Wei, X., Effects of oxygen vacancy on the mechanical, electronic and optical properties of monoclinic $BiVO_4$. *Journal of Materials Science* **2017,** *52* (14), 8546-8555.

54. Ottermann, C.; Bange, K., Correlation between the density of TiO_2 films and their properties. *Thin Solid Films* **1996,** *286* (1-2), 32-34.

55. Sarkar, S.; Das, N.; Chattopadhyay, K., Optical constants, dispersion energy parameters and dielectric properties of ultra-smooth nanocrystalline $BiVO_4$ thin films prepared by rf-magnetron sputtering. *Solid State Science* **2014,** *33*, 58-66.

56. Deparis, O.; Mouchet, S.; Su, B.-L., Light harvesting in photonic crystals revisited: why do slow photons at the blue edge enhance absorption? *Physical Chemistry Chemical Physics* **2015,** *17* (45), 30525-30532.

57. Zhao, H.; Hu, Z.; Liu, J.; Li, Y.; Wu, M.; Van Tendeloo, G.; Su, B.-L., Blue-edge slow photons promoting visible-light hydrogen production on gradient ternary 3DOM TiO_2-Au-CdS photonic crystals. *Nano Energy* **2018,** *47*, 266-274.

58. Stein, A., Achieving Functionality and Multifunctionality through Bulk and Interfacial Structuring of Colloidal-Crystal-Templated Materials. *Langmuir* **2023,** *39* (8), 2890-2910.

59. Ajmal, A.; Majeed, I.; Malik, R. N.; Idriss, H.; Nadeem, M. A., Principles and mechanisms of photocatalytic dye degradation on TiO_2 based photocatalysts: a comparative overview. *RSC Advances* **2014,** *4* (70), 37003-37026.

60. Martinez-de La Cruz, A.; Perez, U. G., Photocatalytic properties of $BiVO_4$ prepared by the co-precipitation method: degradation of rhodamine B and possible reaction mechanisms under visible irradiation. *Materials Research Bulletin* **2010,** *45* (2), 135-141.

CHAPTER V

Manipulating multi-spectral slow photons in bilayer inverse opal TiO_2-$BiVO_4$ composites for highly enhanced visible light photocatalysis[*]

Abstract

Manipulation of light has been proved to be a promising strategy to increase light harvesting in solar-to-chemical energy conversion, especially in photocatalysis. Inverse opal (IO) photonic structures are highly promising for light manipulation as their periodic dielectric structures enable them to slow down light and localize it within the structure, thereby improving light harvesting and photocatalytic efficiency. However, slow photons are confined to narrow wavelength ranges and hence limit the amount of energy that can be captured through light manipulation. To address this challenge, we synthesized bilayer IO TiO_2-$BiVO_4$ structures that manifested two distinct stop band gap (SBG) peaks, arising from different pore sizes in each layer, with slow photons available at either edge of each SBG. In addition, we achieved precise control over the frequencies of these multi-spectral slow photons through pore size and incidence angle variations, that enabled us to tune their wavelengths to the electronic absorption of the photocatalyst for optimal light utilization in aqueous phase visible light photocatalysis. This first proof of concept involving multi-spectral slow photon utilization enabled us to achieve up to 8.5 times and 2.2 times higher photocatalytic efficiencies than the corresponding non-structured and monolayer IO photocatalysts respectively. Through this work, we have successfully and significantly improved light harvesting efficiency in slow photon-assisted photocatalysis, the principles of which can be extended to other light harvesting applications.

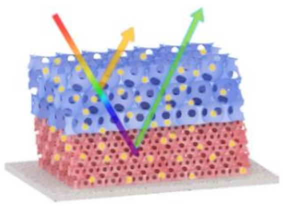

Bilayer inverse opal

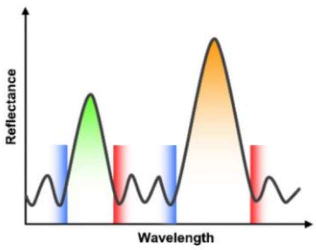

Multi-spectral slow photons

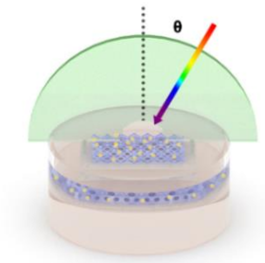

Angle-dependent photocatalysis

---

[*] This part of the work has been published in *Journal of Colloids and Interface Science*, 2023, 647, 233-245.

5. Manipulating multi-spectral slow photons in bilayer inverse opal TiO_2-$BiVO_4$ composites for highly enhanced visible light photocatalysis

5.1. Introduction

The quest for improving light harvesting in photocatalytic applications has led researchers to explore the strategy of light manipulation[1, 2], in synergy with conventional strategies of material modification[3-6]. Ever since the early theoretical propositions on the spontaneous inhibition of light emission and localization of light in periodic dielectric structures[7, 8], photonic crystals (PCs) have been extensively investigated for light manipulation. Among the vast diversity of photonic crystals[9], inverse opal (IO) photonic structures possess numerous advantages due to their promising optical and structural properties in addition to their relative ease of design and synthesis[10-12].

When the periodicity of these structures is in the order of the wavelength of light and the refractive index contrast of the dielectric media is sufficiently high, photons of certain wavelengths are reflected due to Bragg's scattering, leading to a photonic stop band gap (SBG)[13-16]. At either edge of the SBG, the group velocity of light is reduced nearly to zero. These localized photons, also called slow photons, offer huge potential for amplified light harvesting as their increased optical pathlength and lifetime within the material favour strong light-matter interaction[17, 18].

The optical properties of these IO photonic structures have enabled them to be explored in applications like optics[10], sensors[19], photocatalysis[20], photoelectrocatalysis[21], and photovoltaics[22] besides other structure-based applications like catalysis[23], fuel cells[24], energy storage[25], drug delivery and tissue engineering[26]. Given the immense potential of IO structures, rapid progress has been made over the past two decades to address the primary challenge of developing such structures over a large area and with high quality[27]. In particular, the relatively cost-effective bottom-up colloid-template approach, which involves the assembly of opal template colloids, filling the interstices with the desired material and inversion of the structure by the removal of colloids[28-32], was frequently employed.

The key to use slow photon effect in IO structures for photocatalysis lies in the accurate tuning of the slow photon wavelengths to the electronic absorption edge of the photocatalyst, while simultaneously avoiding the detrimental effect of SBG reflection[33, 34]. By tuning various parameters[35, 36] like lattice spacing, index contrast, filling fraction of each dielectric medium and angle of incidence, successful photocatalytic enhancement in IO structures has been reported in the past two decades, since the first report in 2006[37]. Most of the works ever since were limited to the variation of lattice parameter for tuning slow photon frequencies and lacked an unambiguous justification of slow photon assistance for photocatalytic enhancement. A few works went a step ahead to enhance and justify slow photon effect by variation of light incidence angle[38-44]. Despite their success, they were limited either to single component UV-responsive photocatalysts or involved precious noble metals, mostly in non-aqueous photocatalysis. In chapter IV, I demonstrated the utilization of slow photon effect in composite structures having a photonic structure component to generate slow photons and another photoactive component to harvest the slow photons for enhanced visible light aqueous phase photocatalysis.

In all the above works, the major challenge that persists is the narrow spectral range of slow photons, which limits the slow photon effect. A plausible solution would be to generate slow photons at multiple spectral regions by fabricating layered photonic structures with different structural periodicities, that can manifest multiple SBG peaks and hence slow down light at a wider range of wavelengths. Very few efforts have been made so far to fabricate, and use layered inverse opals for photocatalysis[45, 46]. Even the few attempts that exist are characterized by poor structural quality, the lack of distinct SBG peaks and the lack of control over the slow photons generated.

In this work, I demonstrate the ability to generate slow photons at multiple wavelengths by fabricating bilayer (BL) IO TiO_2 structures over a large area and of high quality, which enables the controlled slowing and trapping of light. Tuning of these slow photons by lattice parameter and incidence angle variations in aqueous medium permitted the $BiVO_4$ nanoparticles (NPs) deposited over these structures to harvest the slow light efficiently in the visible region for an unprecedented increase in photocatalytic activity. To establish this first proof of concept, I have chosen three different pore sizes to form bilayer structures in four different arrangements and compared their activities with single layer IO samples and with non-structured photocatalysts at 0°, 15°, 30° and 45° incidence angles. I demonstrated that slow photons can be successfully generated and tuned at multiple spectral regions using layered IO structures to radically enhance light harvesting and increase photocatalytic activity. To the best of my knowledge, this is the first work that reports the generation and tuning of slow photons at multiple spectral regions, especially in a heterocomposite photocatalyst, for aqueous phase visible light photocatalysis.

5.2. Experimental section – synthesis and photocatalytic tests

5.2.1. Synthesis of bilayer inverse opal TiO_2-$BiVO_4$ structures

Bilayer IO structures with each layer having a different pore size were synthesized by two successive steps of coassembly of the first size of PS colloids and TiO_2 NPs in the first step followed by the second size of PS colloids and TiO_2 NPs. Calcination of the bilayer coassembly gave the bilayer IO structure generated.

5.2.1.1. Synthesis of first layer of inverse opal TiO_2

The assembly of PS colloids and TiO_2 NPs was carried out by evaporation-induced simultaneous self-assembly (EISSA) method. Commercial PS colloid suspensions were diluted to 0.1 w/v% using Milli-Q water. Phase controlled TiO_2 NPs were prepared by a peptization method[49] in which 3.6 mmol of TIP dispersed in 15 mL of 2-propanol was added drop-by-drop to 90 mL water containing 2.6 mmol of TMAH (25% w/w in water) cooled previously for 15 min. in an ice bath (TIP/TMAH molar ratio was 1.4). The milky white suspension formed was left to stir for 15 min. and later transferred to a silicone oil bath to be refluxed at 105°C for 6 hrs. This solution was used within an ageing period of 10 days. For coassembly, 40 µL/mL of the above solution was added to 7 mL of the diluted colloid suspension in a vial. The treated glass substrate was suspended vertically in the above mixture and left in an oven at 40°C for 48 h generated. PS colloids of 300 nm, 420 nm and 460 nm diameters were used to prepare different samples. The monolayer samples obtained after calcination were coded as ITB-220, ITB-310, ITB-340, where the numbers represent the IO pore diameters.

5.2.1.2. Synthesis of bilayer layer inverse opal TiO_2 structures

To prepare bilayer IO structures, the coassembled PS colloids-TiO_2 NPs layer (before calcination) was subjected to air plasma treatment for 60 s. using a Q150T ES sputter coater/turbo evaporator under 6W power and 1×10^{-1} mbar pressure, to improve its hydrophilicity. It was then suspended vertically in the second PS colloids-TiO_2 NPs suspension, using the above-mentioned protocol, for coassembly of the second layer. Subsequent calcination of the coassembly resulted in bilayer IO structures. Four inverse opal TiO_2 (IT) samples with different orders of stacking, namely IT-310/220, IT-220/310, IT-340/220, IT-220/340, with the first number denoting the pore diameter of the top layer and the second denoting the pore diameter of the bottom layer, were prepared.

5.2.1.3. Sensitizing inverse opal TiO_2 with $BiVO_4$ nanoparticles

The IO structures were deposited with $BiVO_4$ NPs using Sequential Ionic Layer Adsorption and Reaction (SILAR) method. The IOs were sequentially dipped for 10 cycles in: (a) 0.742 mmol of $Bi(NO_3)_3.5H_2O$ dissolved in water-acetic acid solution (9:1 v/v), for 20s; (b) water-acetic acid solution (9:1 v/v), for 5s; (c) 1.453 mmol of NH_4VO_3 dissolved at 60°C in water and cooled, for 20s; (d) water for 5s. The samples were dried and then calcined for 2h at 500°C. The prepared inverse opal TiO_2-$BiVO_4$ (ITB) samples were coded as ITB-310/220, ITB-220/310, ITB-340/220, ITB-220/340 for bilayer samples.

5.2.2. Photocatalytic dye degradation – experimental set-up and parameters

Photocatalytic degradation experiments of 5 mL of 1.5 μM RhB solution at 0°, 15°, 30° and 45° light incidence angles were carried out using the same set up of the Avantes FC-UV-200 optical fibre mounted on Avantes AFH-15 fibre holder with a 300 W ELDIM-RFLX-ET101-01 EZ Reflex light source emitting in the spectral range of 390-770 nm. Degradation efficiency was calculated by measuring the absorptance of RhB at regular time intervals using UVIKON XS UV-Visible spectrophotometer in the spectral range of 400-700 nm.

5.3. Results and discussion

5.3.1. Synthesis strategies

The synthesis of bilayer IO TiO_2-$BiVO_4$, as depicted by the schematic representation in **Fig. 5.1**, involved the following steps: i. evaporation-induced coassembly of first layer of PS colloids and TiO_2 NPs **(Fig. 5.1 (a))**, ii. plasma treatment of the first layer **(Fig. 5.1 (b))**, iii. coassembly of second layer of PS colloids and TiO_2 NPs **(Fig. 5.1 (c))**, iv. calcination to obtain bilayer IO structure **(Fig. 5.1 (g))** and v. sequential dipping of the IO structure in $Bi(NO_3)_3.5H_2O$ and NH_4VO_3 followed by annealing **(Fig. 5.1 (h))**.

The second layer of PS colloids and TiO_2 NPs was coassembled on the first layer after treating the latter with atmospheric plasma. Plasma treatment of PS colloids is known to increase the surface energy of the polymer, introduce polar hydroxyl groups onto the surface of PS colloids and thereby reduce contact angle with water[47, 48]. Contact angle measurements before and after plasma treatment revealed a steep drop in contact angle from 74° in PS colloids- TiO_2 NPs coassembly before plasma treatment **(Fig. 5.1 (e))** to 14° after atmospheric plasma treatment **(Fig. 5.1 (f))**. The reference pristine colloids without TiO_2 NPs exhibited a much higher contact angle of 118° **(Fig.**

1 (d)). This improved hydrophilicity facilitated the homogeneous coassembly of the second layer over the first as is evidenced from the analysis of the structural properties.

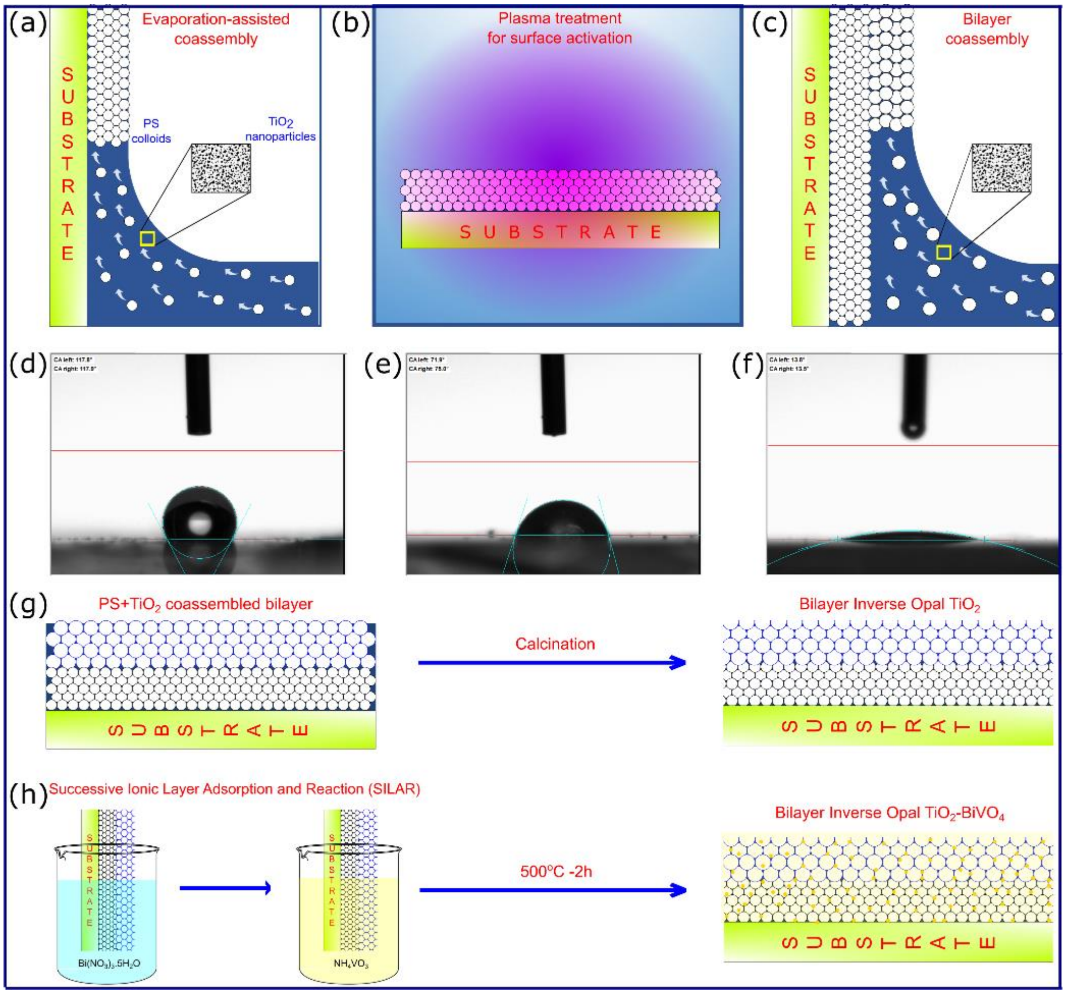

Fig. 5.1: Schematic representation of the synthesis of inverse opal bilayer TiO_2-$BiVO_4$: **(a)** Evaporation-assisted coassembly of PS colloids and TiO_2 NPs; **(b)** Air plasma treatment of assembled first layer; **(c)** coassembly of second layer of PS colloids and TiO_2 NPs; **(d)** contact angle between assembled PS colloids and water (118°); **(e)** contact angle between co-assembled PS colloids+TiO_2 NPs and water before plasma treatment (74°); **(f)** contact angle between co-assembled PS colloids+TiO_2 NPs and water after plasma treatment (14°); **(g)** calcination of assembled bilayer to get IO bilayer structure; **(h)** Deposition of $BiVO_4$ on bilayer IO TiO_2 structure by Successive Ionic Layer Adsorption and Reaction (SILAR) method followed by annealing.

5.3.2. Structural properties and composite formation with $BiVO_4$

Structural properties were first studied from SEM images (top-view and cross-section) and optical microscope images. Cross section SEM images of the bilayer IO structures **(Fig. 5.2 (a-d))** revealed a continuous interface between the two layers confirming that the second layer was homogeneously formed on the first layer. Average thickness of the structures was measured to be 3.5 µm, almost twice the thickness of the monolayer structures **(Fig. 5.2 (e-g))**, which was measured to be around 1.8 µm. The number of layers (relating to the stacking of colloids in each IO monolayer sample) varied from ~8 in IT-220 to ~6 in IT-340, generally decreasing with increase in pore size. The IO thickness was controlled by controlling the PS colloid concentration during coassembly, which was maintained at 0.1 % w/v for all samples.

Four samples with a combination of two different pore sizes (220-310 and 220-340) in both configurations, with the bigger on the smaller and the inverse, were synthesized. A reversal of the order of the pore sizes in the synthesis of bilayer structures did not significantly impact structural homogeneity **(Fig. 5.2 (a,b and c,d))**.

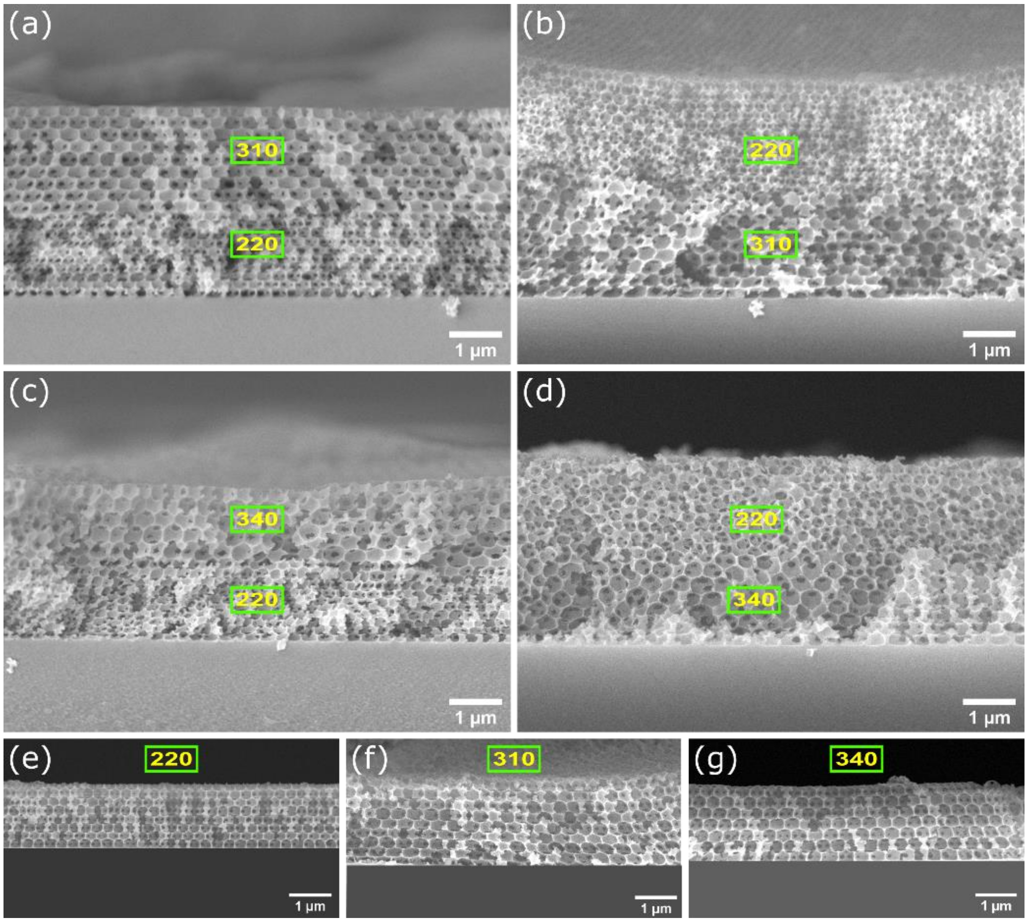

Fig. 5.2: Cross section SEM images of (a-d) bilayer IO TiO_2 structures: **(a)** IT-310/220, **(b)** IT-220/310, **(c)** IT 340/220, **(d)** IT 220/340, and (e-g) monolayer IO TiO_2 structures: **(e)** IT-220, **(f)** IT-310, **(g)** IT-340.

Pore sizes, indicating the lattice parameters of the photonic structures, were determined from top-view SEM images **(Fig. 5.3 (a-c))**. Structures prepared from PS 300, PS 418, and PS 460 (nm) resulted in pore diameters of 220, 310 and 340 nm respectively, indicating a 26% shrinkage from the colloid size to the pore size, which is attributed to the formation of condensed crystalline phase of TiO_2 after calcination. The wall thickness of the IO skeleton was ~20 nm as measured from SEM images and was similar in all the samples. The average dimensions of interconnecting pores (window pores) caused by the touching PS colloids of the *fcc* assembly were measured to be, on an average, 65 nm, 110 nm, and 140 nm, for IT-220, IT-310 and IT-340 respectively.

Optical microscope images as shown in **Fig. 5.3 (d-g)** further confirmed both the domain size and the homogeneous assembly of the second layer over the first. It was observed that the synthesized bilayer IO structures possessed a long-range order in the millimetre scale, which can be attributed to the efficiency of coassembly method adopted in this work. The total area on which the bilayer IO structures were formed on glass slides (1.85×1.25 cm^2) was 1.25×1.25 cm^2. This was controlled by the volume of coassembly suspension used during synthesis. The respective colours caused by the SBG reflection of each IO layer, namely violet (IT-220), blue (IT-310) and green (IT-340), can be observed in the bilayer structures as an intense colour in the forefront pertaining to the top layer and a faded colour in the background pertaining to the bottom layer **(Fig. 5.3 (d-g))**.

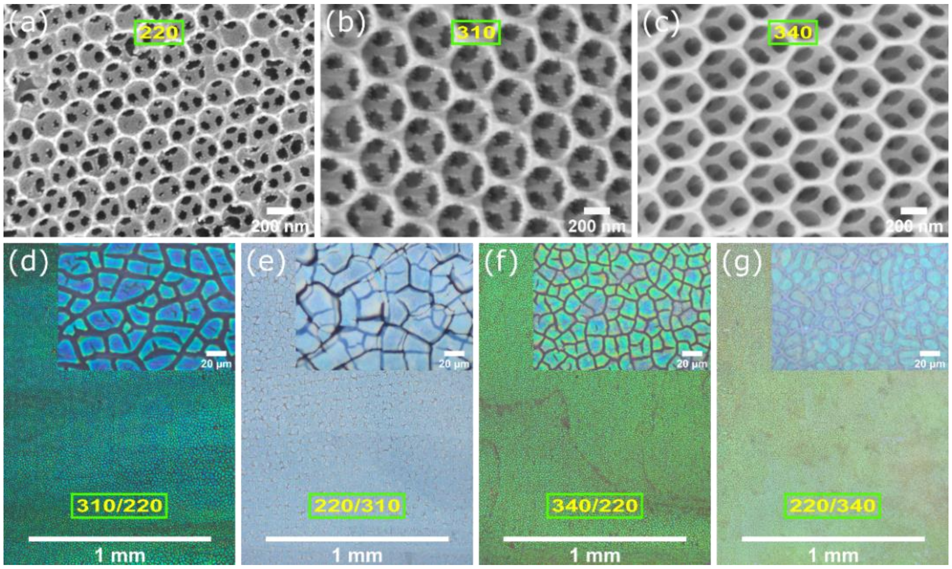

Fig. 5.3: (a-c) SEM images of monolayer and bilayer inverse opal TiO_2 (IT) samples with different pore sizes: Top view of **(a)** IT-220 **(b)** IT-310 **(c)** IT-340; **(d-g)** optical microscope images of bilayer inverse opal TiO_2: **(d)** IT-310/220 **(e)** IT-220/310 **(f)** IT-340/220 **(g)** IT-220/340.

The effect of plasma treatment on the coassembly of the second layer over the first layer was further studied by comparing the optical images of the bilayer inverse opals prepared with and without plasma treatment. As seen in **Fig. 5.3 (a-b)**, synthesized without plasma treatment manifested intermittent formation of the second layer over the first **(Fig. 5.3 (a))**, while those prepared after plasma treatment resulted in homogeneous bilayer formation over a long range **(Fig. 5.3 (b))**. This can be attributed to the improved hydrophilicity of the first coassembly layer, as evidenced from the decrease in contact angle shown in **Fig. 5.1 (e-f)**, that facilitated the homogeneous coassembly of the second layer over the first. The interface of the formation of the second layer over the first was studied by leaving out one-third of the first layer above the second coassembly solution during synthesis. The optical microscope images in **Fig. 5.3 (c-e)** revealed that the initial 20-30 µm at the interface was randomly oriented, as indicated by the non-uniform colours, following which a more uniform bilayer developed, as indicated by the uniform colour pertaining to the SBG reflection.

The pattern of the formation of the second layer over the first was revealed from low magnification cross section SEM image **(Fig. 5.3 (f))**. It was observed that cracks of the first layer were not filled by the second layer, but the second layer developed over the cracks of the first layer. It was also noted the that despite the presence of cracks caused by shrinkage during drying and calcination of the coassembly, large crack-free IO domains of around 20 µm with long-range order were formed.

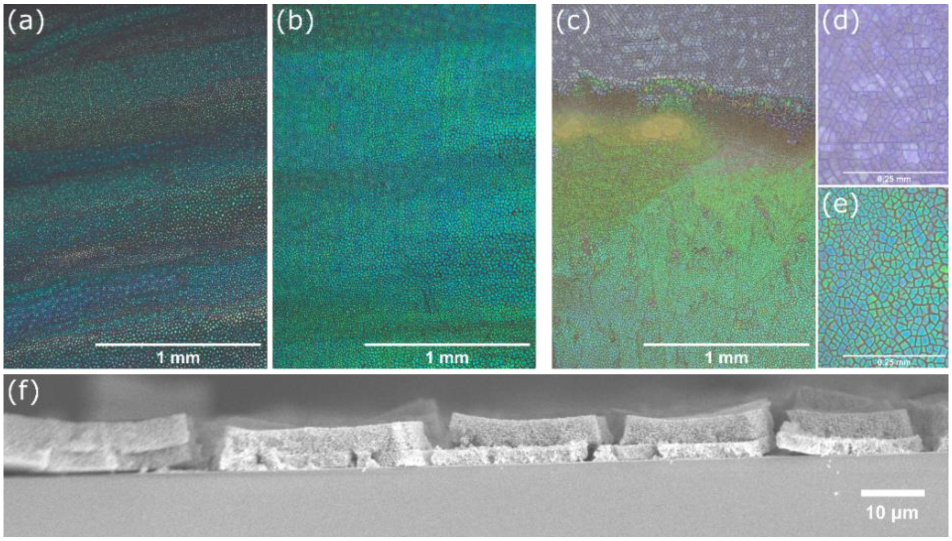

Fig. 5.3: (a-c) SEM images of monolayer and bilayer inverse opal TiO_2 (IT) samples with different pore sizes: Top view of **(a)** IT-220 **(b)** IT-310 **(c)** IT-340; **(d-g)** optical microscope images of bilayer inverse opal TiO_2: **(d)** IT-310/220 **(e)** IT-220/310 **(f)** IT-340/220 **(g)** IT-220/340.

SILAR method was adopted in this work for $BiVO_4$ deposition to permit a homogeneous deposition of $BiVO_4$ and to attain better control over the amount of $BiVO_4$ deposited. The deposition was restricted to 10 SILAR cycles to avoid creating an overlayer of $BiVO_4$ on the IO structures and thus to retain the photonic properties. SEM images taken after $BiVO_4$ deposition on the bilayer IO structures **(Fig. 5.4 (a-c))** reveal that there was very minimum difference between the pore sizes before and after deposition (± 5 nm), although the structure appeared slightly disturbed due to the second calcination process. HAADF-STEM imaging and EDS elemental mapping **(Fig. 5.4 (d-h))** confirmed the homogeneous distribution of Bi and V elements in the IO structure, albeit the presence of random agglomerated $BiVO_4$ NPs.

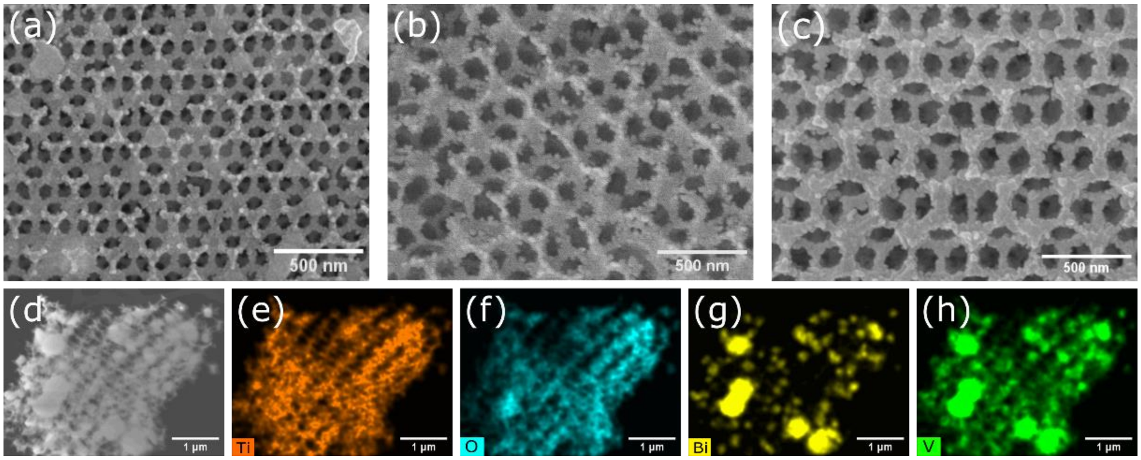

Fig. 5.4: (a-c) Top view SEM images of bilayer IO TiO_2 samples after $BiVO_4$ deposition (ITB): (a) ITB-220/310, (b) ITB-310/220, (c) ITB-340/220; **(d-h)** HR-TEM image of the domain of elemental mapping (d) and the corresponding EDS mapping of Ti (e), O (f), Bi (g) and V (h).

$BiVO_4$ deposition on the bilayer IO structures was further studied by measuring the lattice fringes in high resolution TEM images (HR-TEM), by XRD, EDS elemental analysis and from UV-Visible spectroscopy **(Fig. 5.5 (a-f))**. HR-TEM images **(Fig. 5.5 (a-c))** revealed that $BiVO_4$ was deposited as individual nanoparticles over the TiO_2 NPs that compose the skeletal walls of the IO structures. They also revealed lattice fringes of both TiO_2 **(Fig. 5.5 (b))** and $BiVO_4$ **((Fig. 5.5 (c))** with an interplanar distance of 0.352 nm corresponding to the (101) lattice plane of anatase TiO_2 and an interplanar distance of 0.252 nm corresponding to the (002) plane of monoclinic $BiVO_4$.

XRD patterns **(Fig. 5.5 (d))** confirmed the phases of TiO_2 and $BiVO_4$ in the heterocomposite. The patterns indicated that $BiVO_4$ was present predominantly in the monoclinic phase while TiO_2 was in the anatase phase, as compared to established standards (PDF refs. 01-075-1866 and 01-073-

1764 respectively). XRD patterns of the reference compact films also indicated the same crystalline phases of $BiVO_4$ and TiO_2. The crystallite sizes of $BiVO_4$, as calculated from XRD data using Scherrer equation, were ~32 nm in structured ITB and non-structured TB-NS samples, ~37 nm in $BiVO_4$ compact film and ~18 nm in both IO TiO_2 structured sample and TiO_2 compact film.

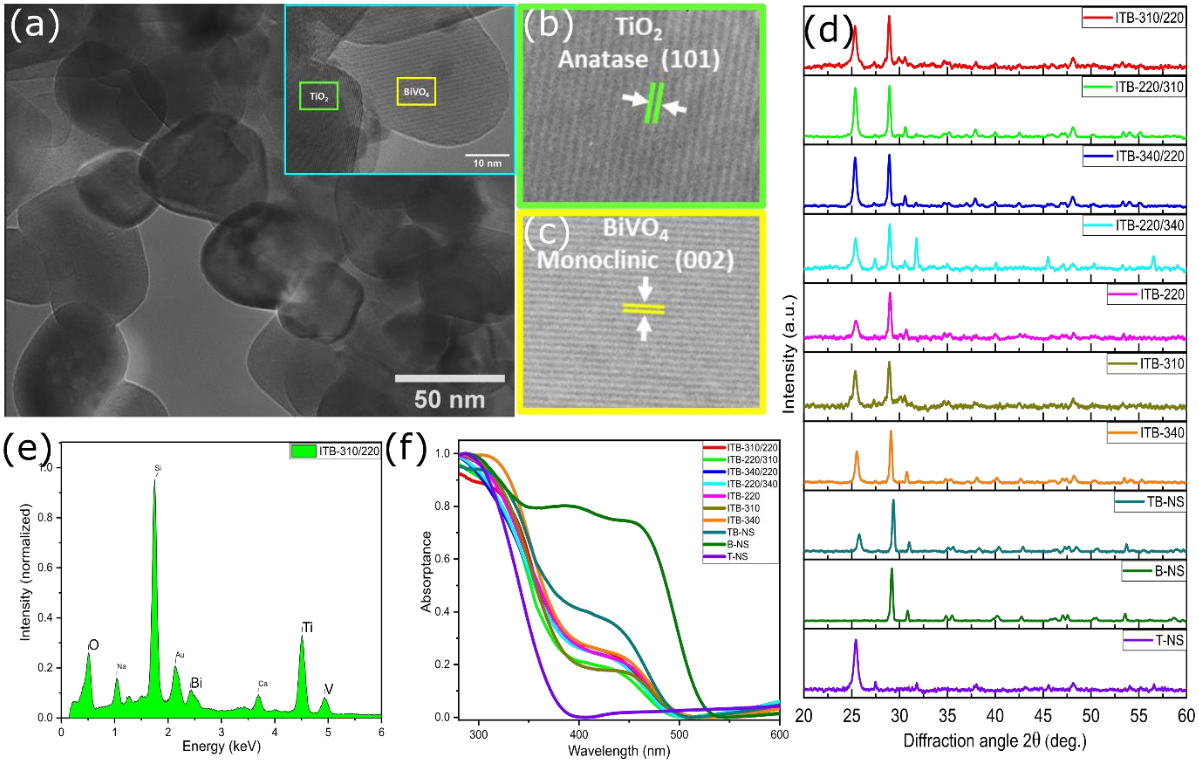

Fig. 5.5: (a-c) HRTEM images of **(a)** TiO_2 NPs and $BiVO_4$ NPs of the IO skeletal walls, **(b)** TiO_2 NP (green) and **(c)** $BiVO_4$ NP (yellow) along with their respective lattice spacings; **(d)** XRD patterns of bilayer ITB-310/220, ITB-220/310, ITB-340/220, ITB-220/340 and monolayer ITB-220, ITB-310, ITB-340 and non-structured TiO_2-$BiVO_4$ (TB-NS), $BiVO_4$ (B-NS), TiO_2 (T-NS) samples; **(e)** EDS elemental analysis spectrum of ITB-310/220; **(f)** UV-Visible absorptance spectra of all the samples.

EDS elemental analysis shown in **Fig. 5.5 (e)** and tabulated in **Table 5.1** permitted the calculation of the amount of $BiVO_4$ deposited with respect to TiO_2, which was, on an average, 20 % by molar ratio on bilayer ITB samples, 16 % on monolayer samples and 25 % on TB-NS compact film. UV-Vis absorptance measurements **(Fig. 5.5 (f))** showed a shift in absorptance towards the visible range in all TiO_2-$BiVO_4$ films due to the presence of $BiVO_4$ which absorbs in the visible range. All ITB structures showed similar absorptance curves while that of the TiO_2-$BiVO_4$ compact film (TB-NS) was higher due to the presence of a higher amount of $BiVO_4$. Compact films of TiO_2 (T-NS) and $BiVO_4$ (B-NS) manifested their characteristic absorptance curves.

Table 5.1: EDX elemental analysis of bilayer and monolayer samples

Sample	Mass percentage (rounded to the nearest whole number)			
	Ti	Bi	V	O
ITB-310/220	36	23	6	35
ITB-220/310	46	21	6	27
ITB-340/220	31	24	7	38
ITB-220/340	36	21	7	36
ITB-220	50	21	5	24
ITB-310	42	18	4	36
ITB-340	47	20	5	28

5.3.3. Optical properties

Angle-resolved specular reflectance of IO structures was measured using the set up shown schematically in **Fig. 5.6**. The reflectance measurements of the structured samples in air **(Fig. 5.7))** showed distinct reflectance peaks corresponding to the pseudo-photonic band gaps (p-PBG) or stop band gaps (SBG), resulting from the coherent diffraction by the (111) planes of the IO *fcc* lattices[49], thereby confirming the high quality of the photonic structures. SBG peaks underwent a spectral shift towards longer wavelengths with increase in lattice parameter (pore size) and a shift towards shorter wavelengths with increase in incidence angle, which is consistent with the optical behaviour of IO photonic crystals[50].

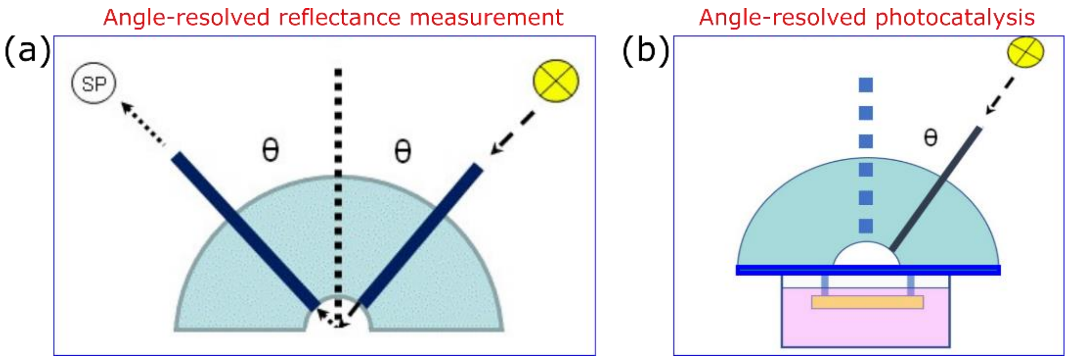

Fig. 5.6: (a) Schematic representation of the set-up used for angle-resolved reflectance measurements; **(b)** Schematic representation of the set-up used for angle-resolved photocatalysis. Yellow colour circle represents light source, SP represents spectrophotometer, dark blue lines represent optical fibres, and the half sphere represents the optical fibre holder that enables the positioning of the optical fibre at increasing angles from 0° to 75° with an increment of 15°.

Bilayer samples ITB-310/220 and ITB-340/220 exhibited two distinct reflectance peaks that blue-shifted with increase in incidence angle **(Fig. 5.7 (a, c))**, with the SBG reflection intensity of the top layer greater than that of the bottom layer. Inversion of layers caused an inversion in the intensity of SBG peaks without giving rise to any significant change in the SBG positions **(Fig. 5.7 (b, d))**. Monolayer ITB samples displayed similar behaviour to that of the corresponding individual layers in the bilayer structures **(Fig. 5.7 (e-g))**. The non-structured TiO_2-$BiVO_4$ compact film did not manifest any photonic properties, which is evidenced by the absence of a distinct SBG reflectance peak **(Fig. 5.7 (h))**.

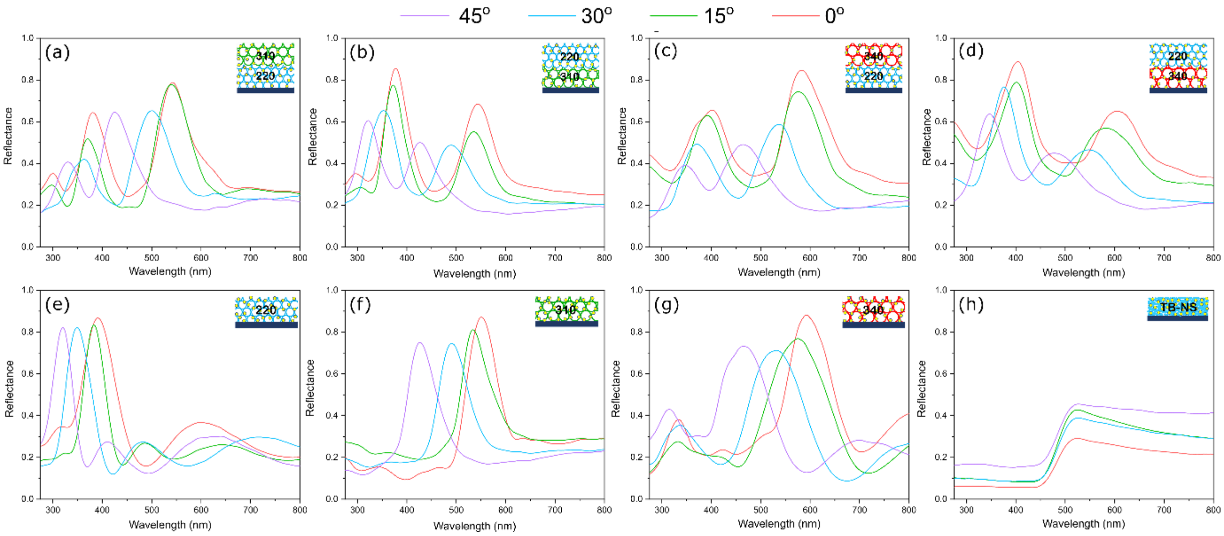

Fig. 5.7: Reflectance measurements in air at incidence angles of 0° (red), 15° (green), 30° (blue), and 45° (violet) of **(a)** ITB-310/220, **(b)** ITB-220/310, **(c)** ITB-340/220, **(d)** ITB-220/340 **(e)** ITB-220 **(f)** ITB-310 **(g)** ITB-340 **(h)** TB-NS non-structured sample.

To study the influence of slow photon effect in aqueous phase photocatalysis, SBG reflectance measurements were taken after filling the pores of the IO structure with water using a micropipette. When air in the pores was replaced with water, SBG peaks of bilayer and monolayer samples red-shifted towards higher wavelengths due to the increase in effective refractive index (n_{eff}) of the structure ($n_{\text{air}} = 1$ and $n_{\text{water}} = 1.33$) **(Fig. 5.8)**.

However, compared to the reflectance peaks in air, the intensity of the peaks under water was attenuated due to the decrease in refractive index contrast between the material and the filling medium. As in the case of air medium, reflectance measurements in water revealed bilayer samples showing two distinct SBG peaks **(Fig. 5.8 (a-d))** and the monolayer samples showing a single SBG peak **(Fig. 5.8 (e-g)** that red-shifted with increase in pore size and blue-shifted with increase in incidence angle.

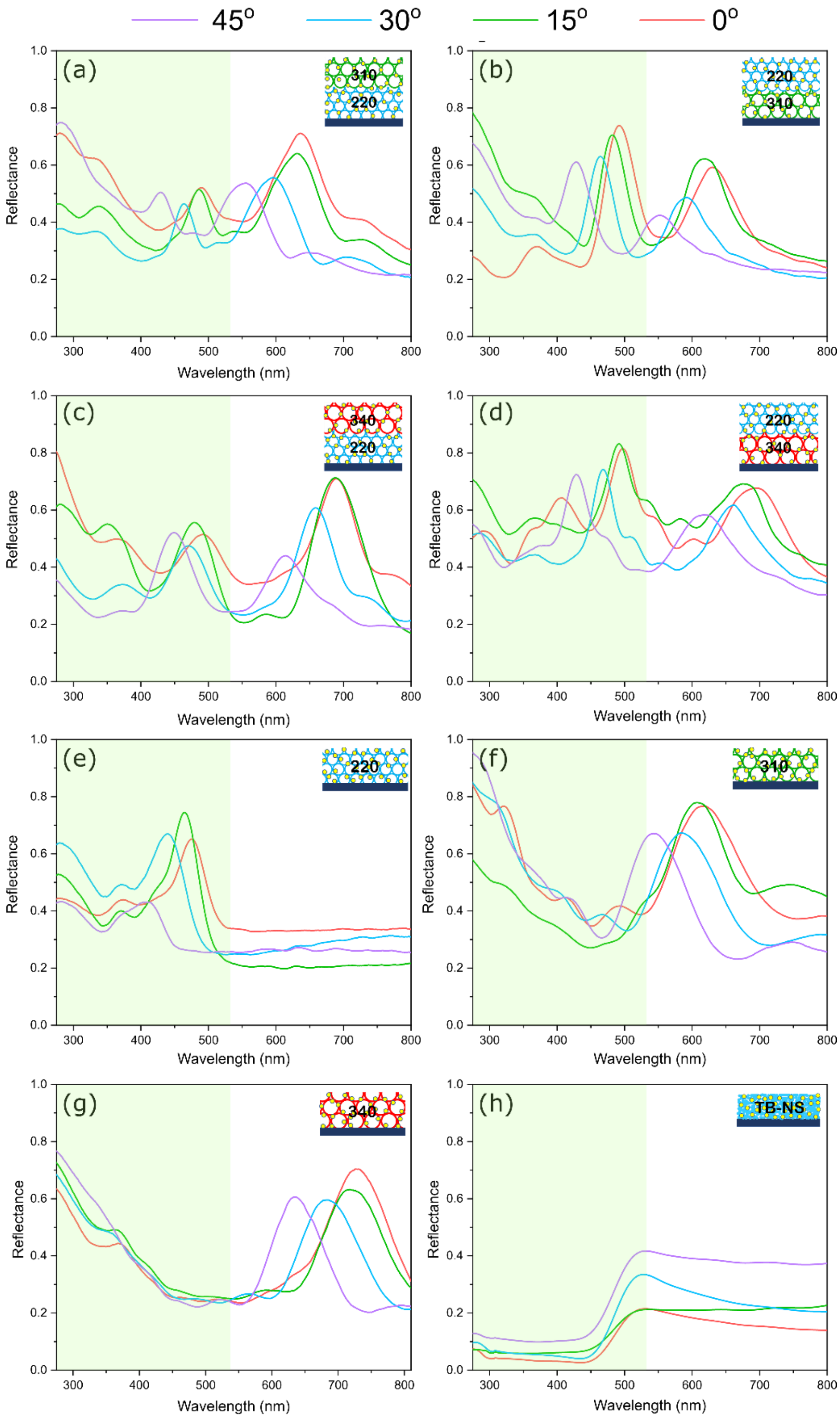

Fig. 5.8: Reflectance measurements in water at incidence angles of 0° (red), 15° (green), 30° (cyan), and 45° (blue) of **(a)** ITB-310/220, **(b)** ITB-220/310, **(c)** ITB-340/220, **(d)** ITB-220/340 **(e)** ITB-220 **(f)** ITB-310 **(g)** ITB-340 **(h)** TB-NS non-structured sample. Green shaded region represents the electronic absorption of $BiVO_4$.

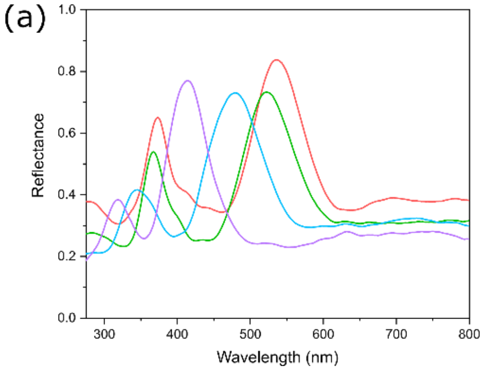

Fig. 5.9: Angle-resolved reflectance measurements of IT-310/220 in air at 0° (red), 15° (green), 30° (blue) and 45° (violet): **(a)** before deposition of $BiVO_4$ (IT-310/220) and **(b)** after deposition of $BiVO_4$ (ITB-310/220).

The influence of $BiVO_4$ deposition on the SBG peak positions was studied by reflectance measurements before and after $BiVO_4$ deposition on bilayer IT-310/220 **(Fig. 5.9 (a-b))**. Although there was a slight decrease in intensity of the peaks, the shift in SBG peak positions was found to be very small (±15 nm).

To determine if the formation of the top layer influenced the SBG peak position of the bottom layer, a bilayer IO structure, IT-310/310, with both the layers having the same pore size **(Fig. 5.10 (a))**, was synthesized and the optical properties were determined. Reflectance measurements **(Fig. 5.10 (b))** revealed that there was no significant difference in the SBG peak positions when compared to the peak positions in both the monolayer sample **(Fig. 5.7 (f))** and that of the same layer in the bilayer samples **(Fig. 5.7 (a-b))**.

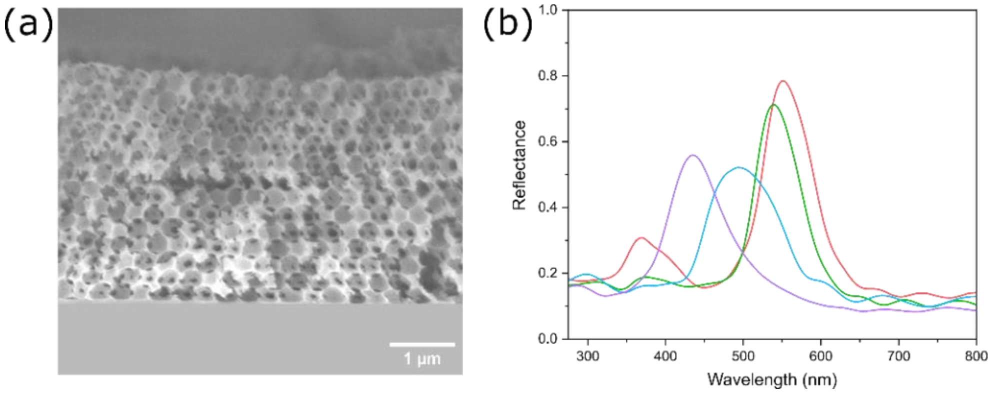

Fig. 5.10: Bilayer IO sample with two layers of the same pore size prepared to probe the mutual influence of the two layers on the optical properties of the individual layer: **(a)** SEM image of IO 310-layer assembled over IO 310-layer (IT-310/310); **(b)** Angle-resolved reflectance measurements of IT-310/310 in air at 0° (red), 15° (green), 30° (blue) and 45° (violet).

5.3.4. Stop band gap peak approximation using modified Braggs law

To compare the experimental SBG peaks positions and their shift with change in pore size, incidence angle and filling medium, a modified Bragg's law that incorporated Fresnel correction to account for refraction of light moving from air to water, was employed:

$$\lambda_{\mathrm{B}} = 2 \cdot \sqrt{2/3} \cdot D \cdot \sqrt{n_{\mathrm{eff}}^2 - n_{\mathrm{inc}}^2 \sin^2\theta} \qquad \textbf{(Eq. 4.1)}$$

where λ_{B} is the wavelength of the SBG peak, D is the diameter of the IO pore, n_{eff} is the effective refractive index of the system, n_{inc} is the incidence-medium refractive index and θ is the incidence angle. Bruggeman's formula[51, 52] was used to calculate n_{eff}, using RIs of composite TiO_2-$BiVO_4$ material (n_{mat}) and filling medium (n_{med}) and their respective filling fractions (f_{mat}, f_{med}). RI of the composite was calculated as $n_{\mathrm{mat}} = x n_{\mathrm{TiO_2}} + (1-x) n_{\mathrm{BiVO_4}}$. Volume fractions of TiO_2 (x) and $BiVO_4$ $(1-x)$ were estimated by deriving weight-volume data from EDS elemental analysis, based on the same approach employed in chapter IV. A value of $x = 0.88$ was thus obtained.

RI (real part) of individual components at $\lambda = 500$ nm, were derived as $n_{\mathrm{TiO_2}} = 1.836$, $n_{\mathrm{BiVO_4}} = 2.764$ from the calculation of wavelength-dependent complex RI based on data reported for dense films of TiO_2[53] and $BiVO_4$[54], as shown in the previous section **(Fig. 3.18 (a)).** For the filling fraction, a value of $f_{\mathrm{mat}} = 0.12$, lower than that in an ideal close-packed *fcc* ($f_{\mathrm{mat}} = 0.26$), was inferred from microscope images and weight-volume data of IO film, which was consistent with previous reports[39, 41]. Based on the above approximations, RI of the TiO_2-$BiVO_4$ composite (n_{mat}) was estimated to be 1.95.

Calculations in aqueous phase considered Fresnel correction for refraction of light and the incomplete infiltration of pores with medium, estimated as resulting from the presence of interparticle micropores. This resulted in a reduced RI estimation of filling medium $n_{\mathrm{med}} = 1.20$, considering 60% filling with water. When SBG reflectance predictions were made based on the above considerations, it was observed that there was a close fit between experimental peaks and predicted peaks, with the fit being more accurate in air than in water **(Fig. 5.11, Table 5.2)**.

Comparison of the SBG peak positions in air and in water of each bilayer sample is shown in **Fig. 5.12 (a-d)** while comparison between SBG peaks corresponding to the same pore size in samples with different layer orders in both air and water is plotted and shown in **Fig. 5.12 (e-h)**. The characterization of angle-resolved photonic properties of bilayer IO structures and the correlation between experimental and theoretically predicted SBG peak positions confirmed not only the generation of slow photons at multiple spectral regions but also the ability to accurately control the tuning of their wavelengths, particularly in aqueous phase.

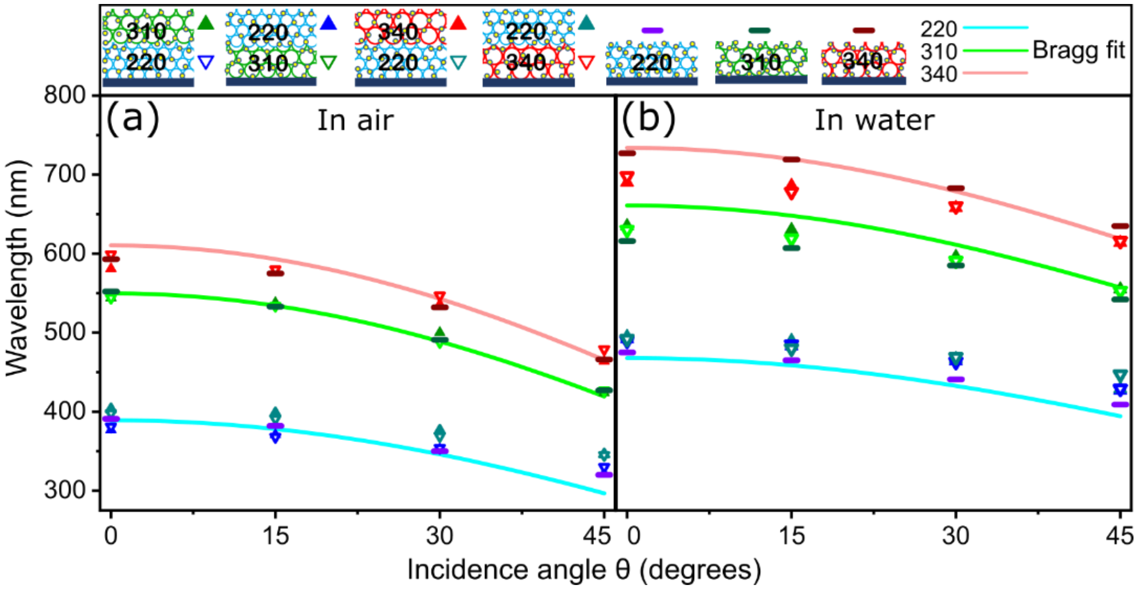

Fig. 5.11: Experimental SBG peak positions (symbols) of top and bottom layers in bilayer IO structures and those of monolayer structures at various incidence angles, along with the corresponding Bragg approximation (lines) in air **(a)** and in water **(b)**.

Table 5.2: Stop Band Gap (SBG) peak positions of the synthesized samples in air and in water.

Sample	Pore size (nm)	SBG peak position (nm)							
		Air				Water			
		0°	15°	30°	45°	0°	15°	30°	45°
ITB-310/220	310	544	538	500	424	635	630	596	555
	220	381	368	354	330	490	485	463	429
ITB-220/310	220	377	371	353	322	492	483	464	427
	310	544	534	488	427	630	619	591	553
ITB-340/220	340	581	576	536	464	690	686	658	614
	220	398	391	369	345	492	480	469	447
ITB-220/340	220	403	398	376	346	495	490	467	429
	340	599	580	547	479	698	678	660	616
ITB-220	220	391	382	350	320	475	465	441	409
ITB-310	310	552	533	491	427	616	607	585	542
ITB-340	340	593	575	532	466	727	719	683	635

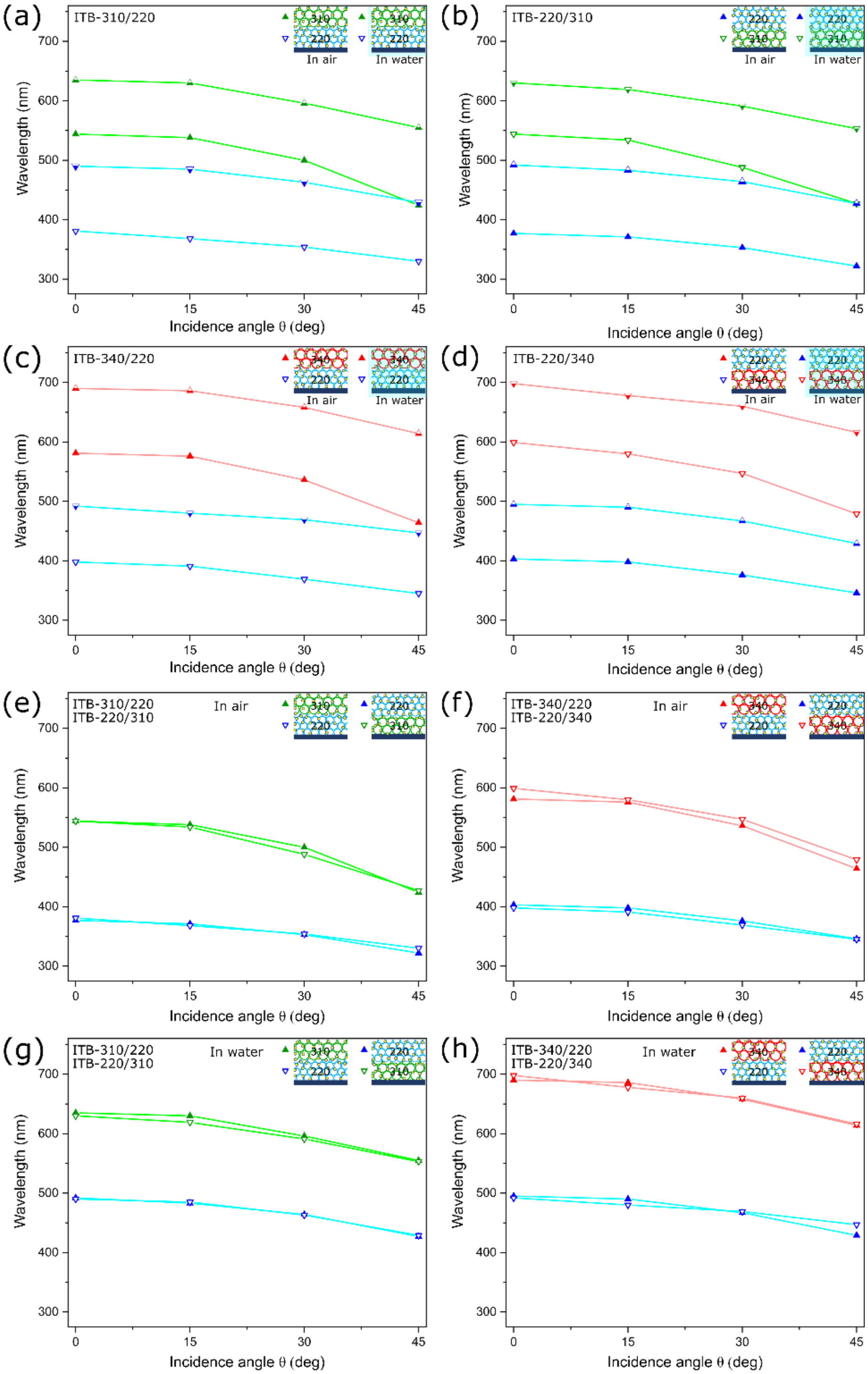

Fig. 5.12: (a-d) Comparison of SBG peak positions in air and in water in each sample: **(a)** ITB-310/220, **(b)** ITB-220/310, **(c)** ITB-340/220, **(d)** ITB-220/340. Full and empty triangles denote the SBG peaks in air while half-full triangles denote those in water. **(e-h)** Comparison of SBG peak positions in samples with inversion of layers in air (e-f) and in water (g-h). Upward-pointing symbols represent top layer while downward-pointing symbols represent bottom layer.

5.3.5. Slow photons at multi-spectral regions for photocatalysis

The effect of slow photons, successfully tuned in bilayer IO TiO_2-$BiVO_4$ structures at multi-spectral regions, was studied by comparing RhB photocatalytic degradation of bilayer samples with that of monolayer samples at varying incidence angles, using the experimental set up schematically shown in **Fig. 5.6 (b)**. In addition, the photocatalytic activities of structured samples were compared with those of the non-structured compact films of $BiVO_4$ (B-NS), TiO_2 (T-NS) and TiO_2-$BiVO_4$ (TB-NS), at different angles, to confirm the slow photon effect. Morphology of the non-structured compact films is shown in **Fig. 5.13**. Comparison was done by normalizing the observed activities based on weight percentage of $BiVO_4$ in the composites, as obtained from EDS elemental analysis.

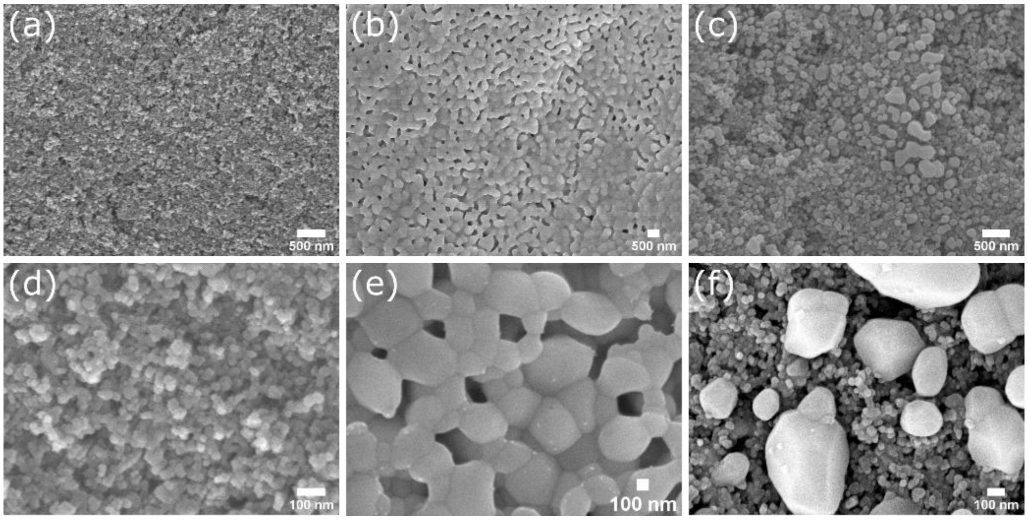

Fig. 5.13: SEM images of **(a, d)** TiO_2 film, **(b, e)** $BiVO_4$ film, **(c, f)** TiO_2-$BiVO_4$ film.

Comparison between photocatalytic activities is shown in terms of degradation efficiency in **Fig. 5.14** and in tabular form in **Table 5.3**. Analysis of the correlation between the tuning of slow photon wavelengths to the electronic absorption of $BiVO_4$ and the corresponding photocatalytic activities was carried out by choosing six representative cases of slow photon tuning **(Fig. 5.15, Table 5.4)**, ranging from that with the highest activity in bilayer samples to that with the lowest activity in monolayer samples. Photoactivities in all other cases can be categorized under one of the above cases. Comparison of photocatalytic activities is also shown as a plot of normalized concentration vs. time **(Fig. 5.16)** and in terms of decrease of RhB absorptance with time (**Fig. 5.17, Fig. 5.18)**.

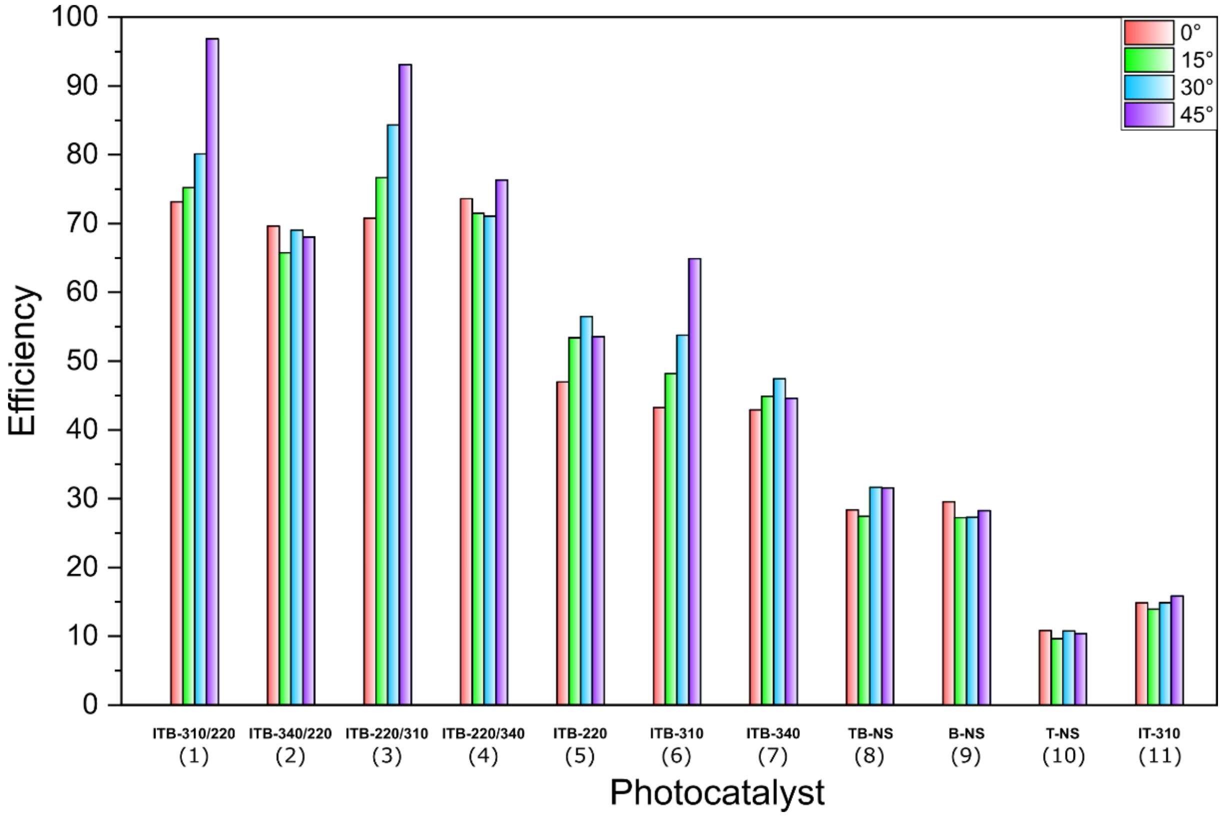

Fig. 5.14: Photocatalytic RhB degradation efficiency of: **(1-4)** bilayer IO photocatalysts **- (1)** ITB-310/220, **(2)** ITB-220/310, **(3)** ITB 340/220, **(4)** ITB 220-340; **(5-7)** monolayer IO photocatalysts **- (5)** ITB-220, **(6)** ITB-310, **(7)** ITB-340; (**8)** TiO_2-$BiVO_4$ non-structured film (TB-NS); **(9)** $BiVO_4$ non-structured film (B-NS); **(10)** TiO_2 non-structured film (T-NS); **(11)** Inverse opal TiO_2 (IT-310).SEM images of **(a, d)** TiO_2 film, **(b, e)** $BiVO_4$ film, **(c, f)** TiO_2-$BiVO_4$ film.

A few general conclusions were deduced from the comparison of activities of all photocatalysts (pcs) **(Fig. 5.14)**. Firstly, the fact that all $BiVO_4$-loaded photocatalysts displayed activities ranging from 24% to 97% (pcs1-9), whereas those without $BiVO_4$ loading showed 11% activity on average (pcs10-11), confirmed that $BiVO_4$ was the active photocatalytic component in the composite, since the light source used was predominantly limited to the visible spectral region. Secondly, comparison between the activities of structured and non-structured samples (pcs1-7 and pcs8-11), revealed that all ordered porous structures exhibited higher photocatalytic efficiencies than their non-structured counterparts, which can be attributed to the slow photon effect in ordered photonic structures. Thirdly, all bilayer photocatalysts (pcs1-4) displayed higher photocatalytic activities than the monolayered photocatalysts (pcs5-7) even after normalization, which confirmed the hypothesis that multiple spectral slow photon regions are responsible for the enhancement of photocatalytic efficiency.

Table 5.3: Normalized photocatalytic efficiencies of the tested photocatalysts

	Photocatalytic efficiency (%)			
Photocatalyst	0°	15°	30°	45°
ITB-310/220	73	75	80	97
ITB-340/220	70	66	69	68
ITB-220/310	71	77	84	93
ITB-220/340	74	71	71	76
ITB-220	47	53	56	54
ITB-310	43	48	54	65
ITB-340	43	45	47	45
TB-NS	28	27	32	32
B-NS	30	27	27	28
T-NS	11	10	11	10
IT-310	15	14	15	16

The effect of utilizing slow photons at multiple spectral regions was further justified by the correlation between photocatalytic activities, the number of slow photon spectral regions and their tuning conditions, grouped under six cases for ease of analysis **(Fig. 5.15, Table 5.3)**. Among all photocatalysts, bilayer sample ITB-310/220 at 45° incidence angle displayed the highest efficiency (97%). As seen in **Fig. 5.15 (a)-Case1**, at 45° incidence angle, slow photons at both red and blue edges of IO 220-layer and those at the blue edge of IO 310-layer were tuned to overlap with the electronic absorption region of $BiVO_4$ (green shaded region). This implies that the group velocity of light was reduced at three wavelength regions within the absorption range of $BiVO_4$, thereby increasing the optical pathlength and lifetime of photons within the photocatalyst and enabling greater light harvesting. Note that the SBG peak of IO-310 layer was tuned to be outside the absorption range (and therefore its red edge as well) to avoid strong reflection of light, which would be detrimental for light harvesting.

For the same sample (ITB-310/220), change of incidence angle to 30° resulted in a lesser activity (80%). In this case **(Fig. 5.15 (b)-Case 2)**, with reduced incidence angle, SBG peaks shifted towards longer wavelengths causing the blue edge slow photons of IO 310-layer to fall outside $BiVO_4$ absorption range. Slow photons were available for assisting light harvesting only at two spectral regions instead of three, namely the blue and red edges of IO 220-layer. Similarly, setting the incidence angle to 0° **(Fig. 5.15 (c)-Case 3)** further reduced the activity (73%) as farther shifting of SBG peaks resulted in slow photon contribution at only one spectral region (blue edge of IO 220-layer). The above considerations revealed that the utilization of slow photons at three spectral regions resulted in 1.2 and 1.3-fold higher activity than those at two and one spectral regions, respectively.

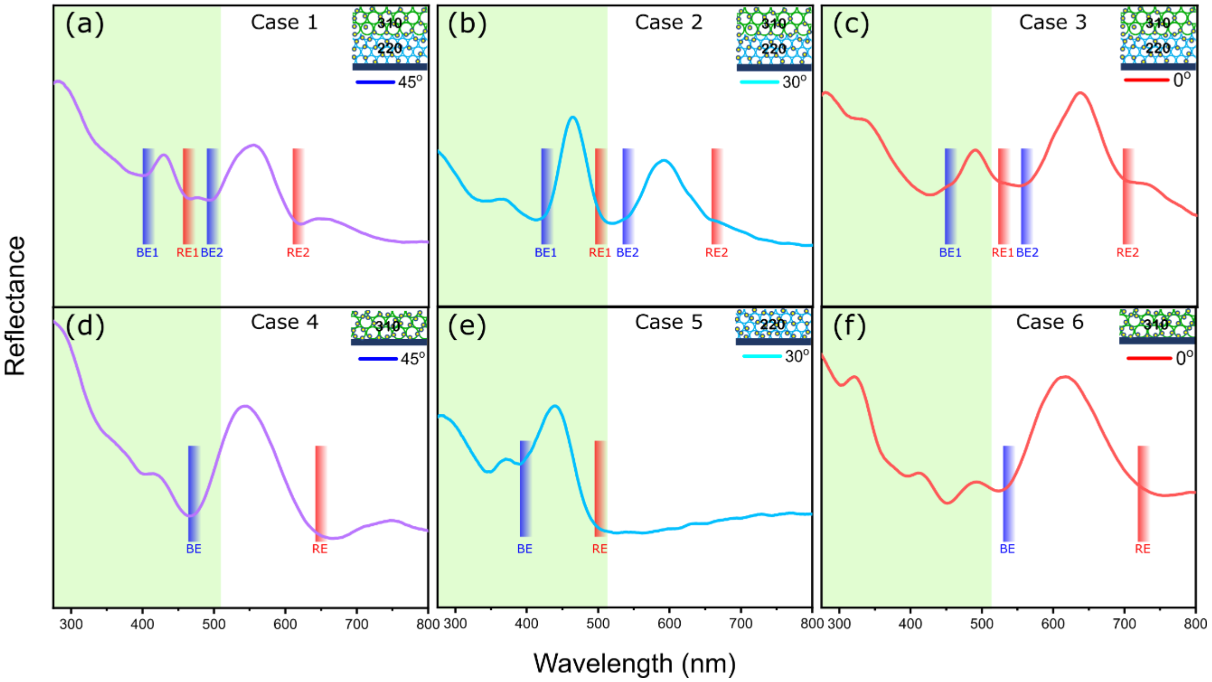

Fig. 5.15: Representative cases of tuning the slow photons at blue edges (BE) (blue shade) and red edges (RE) (red shade) to the electronic absorption edge of $BiVO_4$ (green shade) in bilayer structures **(a, b, c)** with two SBG peaks and four slow photon regions and in monolayer structures **(d, e, f)** with one SBG peak and two slow photons regions. **(a) Case 1:** BE1, RE1, BE2 slow photons within $BiVO_4$ absorption; **(b) Case 2:** BE1, RE1 within $BiVO_4$ absorption; **(c) Case 3:** BE1 within $BiVO_4$ absorption; **(d) Case 4:** BE within $BiVO_4$ absorption and reflection peak outside $BiVO_4$ absorption; **(e) Case 5:** BE and RE within $BiVO_4$ absorption and reflection peak within $BiVO_4$ absorption; **(f) Case 6:** BE and RE outside $BiVO_4$ absorption.

Tuning of slow photons at multiple spectral regions for photocatalytic assistance was also tested on ITB-340/220, a sample with a different combination of IO pore sizes (IO 340-layer and IO 220-layer). The activities of this photocatalyst at different angles were categorized under cases 2 and 3. Due to the larger pore size of the IO 340-layer, the related SBG peaks were shifted towards longer wavelengths and could not be tuned to the electronic absorption of $BiVO_4$ even with increasing incidence angle **(Fig. 5.8 (c))**. As a result, slow photon effect was limited to blue and red edge slow photons of the IO 220-layer. Contrary to ITB-310/220, there was no sharp change in activity with change in incidence angle **(Fig. 5.14)**, which can be explained by the same reason that, at all angles, the slow photons of IO 220-layer were within the spectral range of the electronic absorption of $BiVO_4$ and those of the IO 340-layer were beyond it. The superiority of tuning multi-spectral slow photons to BiVO4 absorption became evident as ITB-310/220 photocatalyst at 45° incidence angle (Case 1 with three well-tuned slow photon regions) displayed an average of 1.4 times higher photocatalytic efficiency than ITB-340/220 photocatalyst.

Table 5.4: Representative cases of tuning the slow photons to the electronic absorption edge of $BiVO_4$ (green shade) in bilayer structures and in monolayer structures

Sample type	Case	Sample and incidence angle	Slow photon tuning conditions	Photocatalytic efficiency (%)
Bilayer IO TiO_2-$BiVO_4$	1	ITB 310-220 (45°)	BE1, RE1, BE2 slow photons within $BiVO_4$ absorption	97
	2	ITB 310-220 (30°)	BE1, RE1 slow photons within $BiVO_4$ absorption	80
	3	ITB 310-220 (0°)	BE1 slow photons within $BiVO_4$ absorption	73
Monolayer IO TiO_2-$BiVO_4$	4	ITB 310 (45°)	BE slow photons within $BiVO_4$ absorption Reflection peak outside $BiVO_4$ absorption	65
	5	ITB 220 (30°)	BE, RE slow photons within $BiVO_4$ absorption Reflection peak within $BiVO_4$ absorption	56
	6	ITB 310 (0°)	BE, RE slow photons outside $BiVO_4$ absorption	45

Photocatalytic efficiencies measured in samples ITB-220/310 and ITB-220/340 with the order of the layers reversed (smaller pore size layer at the top and bigger pore size layer at the bottom) led to similar conclusions. It was observed from reflectance measurements **(Fig. 5.8 (a-b, c-d))** that upon layer inversion, SBG peak positions remained similar, but the intensities of the respective peaks were reversed, as expected. ITB-220/310 showed the highest activity at 45° incidence angle as three slow photon spectral regions overlapped with $BiVO_4$ absorption, followed by those at 30° and 15° incidence angles with the assistance of only two and one slow photon regions respectively. ITB-220/340, on the other hand, did not show significant change in activity with incidence angle as the slow photon regions of IO 340-layer were located far away from $BiVO_4$ absorption at all angles **(Fig. 5.8 (d)**.

When comparison was made between ITB-310/220 and ITB-220/310 (same pore sizes but inverted layers) at 45° incidence angle **(Fig. 5.8 (a-b), Fig. 5.14)**, ITB-310/220 displayed a 1.1-fold higher activity than that of ITB-220/310. This slight decrease in activity in ITB-220/310 can be explained by the fact that the layer responsible for activity change with slow photon tuning (IO 310-layer) was present at the bottom, wherein light entering the second IO layer has already been attenuated while propagating through the first IO layer. On the other hand, ITB-220/340 showed a slightly higher activity than that of ITB-340/220 since the layer responsible for slow photon effect (IO 220-layer) was placed at the top wherein light was not attenuated.

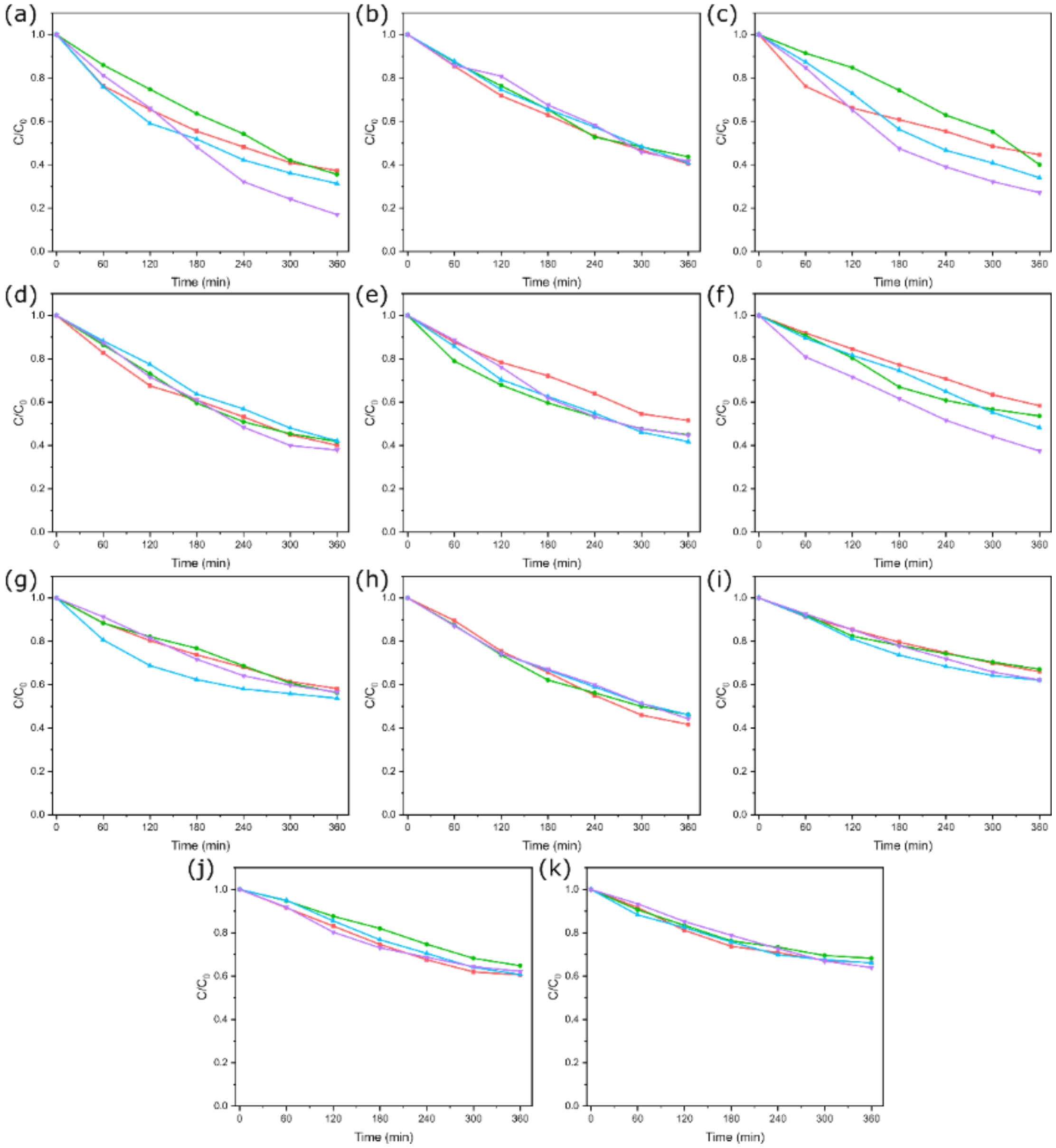

Fig. 5.16: RhB degradation activity plotted in terms of normalized concentration (C/C_0) as a function of time at 0° (red), 15° (green), 30° (cyan) and 45° (blue) incidence angles of **(a-d)** bilayer structures: (a) ITB-310/220, (b) ITB-340/220, (c) ITB-220/310, and (d) ITB-220/340; **(e-g)** monolayer structures: (e) ITB-220, (f) ITB-310, and (g) ITB-340; **(h-k)** non-structured samples: (h) TB-NS, (i) B-NS, (j) T-NS, and (k) IT-310.

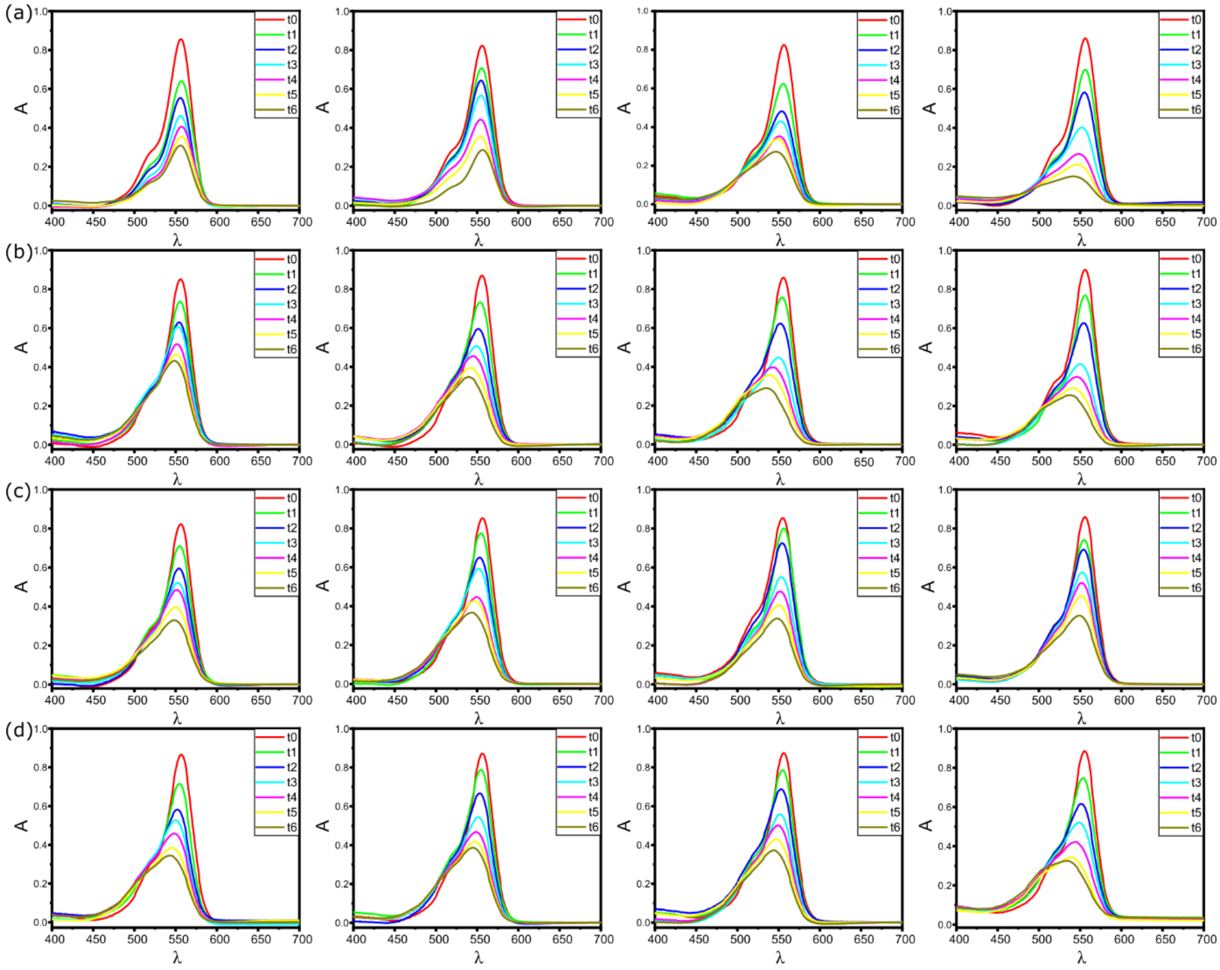

Fig. 5.17: Decrease of RhB absorptance with time due to photocatalytic activity at 0°, 15°, 30° and 45° incidence angles of the photocatalysts (a) ITB-310/220, (b) ITB-220/310, (c) ITB-340/220, (d) ITB-220/340.

When compared with monolayer samples, all bilayer samples showed, on average, 1.8 times higher photocatalytic activity, which is attributed to slow photon effect at multiple spectral regions.

Comparison was made by considering three representative cases of slow photon tuning in monolayer samples, ranging from the highest activity to the lowest **(Fig. 5.15 (d-f))**. ITB-310 at 45° incidence angle showed the highest activity among monolayer samples **(Fig. 5.15 (d)-Case 4)**. Here, the reflection peak was situated outside $BiVO_4$ absorption while the blue edge was within $BiVO_4$ absorption range. As already highlighted above, reduction of light harvesting due to SBG reflectance peak and increase of light harvesting due to blue and red edge slow photons are competing factors for photocatalysis. In this case, tuning was done such that blue edge slow photons contributed to photocatalytic enhancement while simultaneously keeping the reflection peak outside $BiVO_4$ absorption, i.e., an ideal scenario for reaching the highest activity. On the other hand, the variation principle applied to the electromagnetic energy function[13] predicts that slow photons at the red edge contribute to a greater extent to photocatalysis than those at the blue edge since the field intensity at red edge wavelengths is preferably localized in the higher refractive index medium (TiO_2-$BiVO_4$, in this case) whereas the field intensity at blue edge wavelength is preferably localized in the lower refractive index medium (water, in this case). However, previous numerical studies have demonstrated that blue edge slow photons can also be effective in enhancing photocatalysis[61], particularly when the material skeleton is very thin, and hence enables significant overlap with the field intensity distribution lying mostly but not exclusively in IO voids. This consideration validates the justification of photocatalytic enhancement in ITB-310 at 45° incidence angle. The activities in this sample at other angles are significantly lower since the slow photons at both edges were present outside $BiVO_4$ absorption.

When compared with the above case, ITB-220 at 30° incidence angle **(Fig. 5.15 (e)-Case 5)** displayed lower photocatalytic activity. In this case, although slow photons at both edges were within the electronic absorption of $BiVO_4$, the simultaneous presence of reflection peak within $BiVO_4$ absorption was counter-productive for photocatalysis. The activity was not found to vary significantly with angle since at all angles the slow photons at both edges overlapped with $BiVO_4$ absorption. In the case of ITB-310 at 0° incidence angle **(Fig. 5.15 (f)-Case 6)**, slow photons at both edges were outside $BiVO_4$ absorption, which resulted in the lowest photocatalytic activity among all structured TiO_2-$BiVO_4$ samples. ITB-340 at all incidence angles falls under the same category with similar photocatalytic activities since its slow photon regions were located away from $BiVO_4$ absorption **(Fig 5.8 (g))**. Among monolayer samples, ITB-310 at 45° incidence angle (case 4) showed 1.2 times higher activity than ITB-220 at 45° incidence angle having both slow photon effect and reflection peak detrimental effect (case 5) and 1.4 times higher activity than ITB-310 at 0° incidence angle without slow photon effect (case 6).

Slow photon assistance in IO structures was further justified by the absence of variation in photocatalytic activities with light incidence angle in non-IO structures (compact films). These structures do not exhibit a stop band gap **(Fig. 5.7 (h))**, which implies that they do not have slow photon assistance. Varying light incidence angle thereby does not show any significant variation in photocatalytic activity for these samples **(Fig. 5.14, pcs 8-10)**.

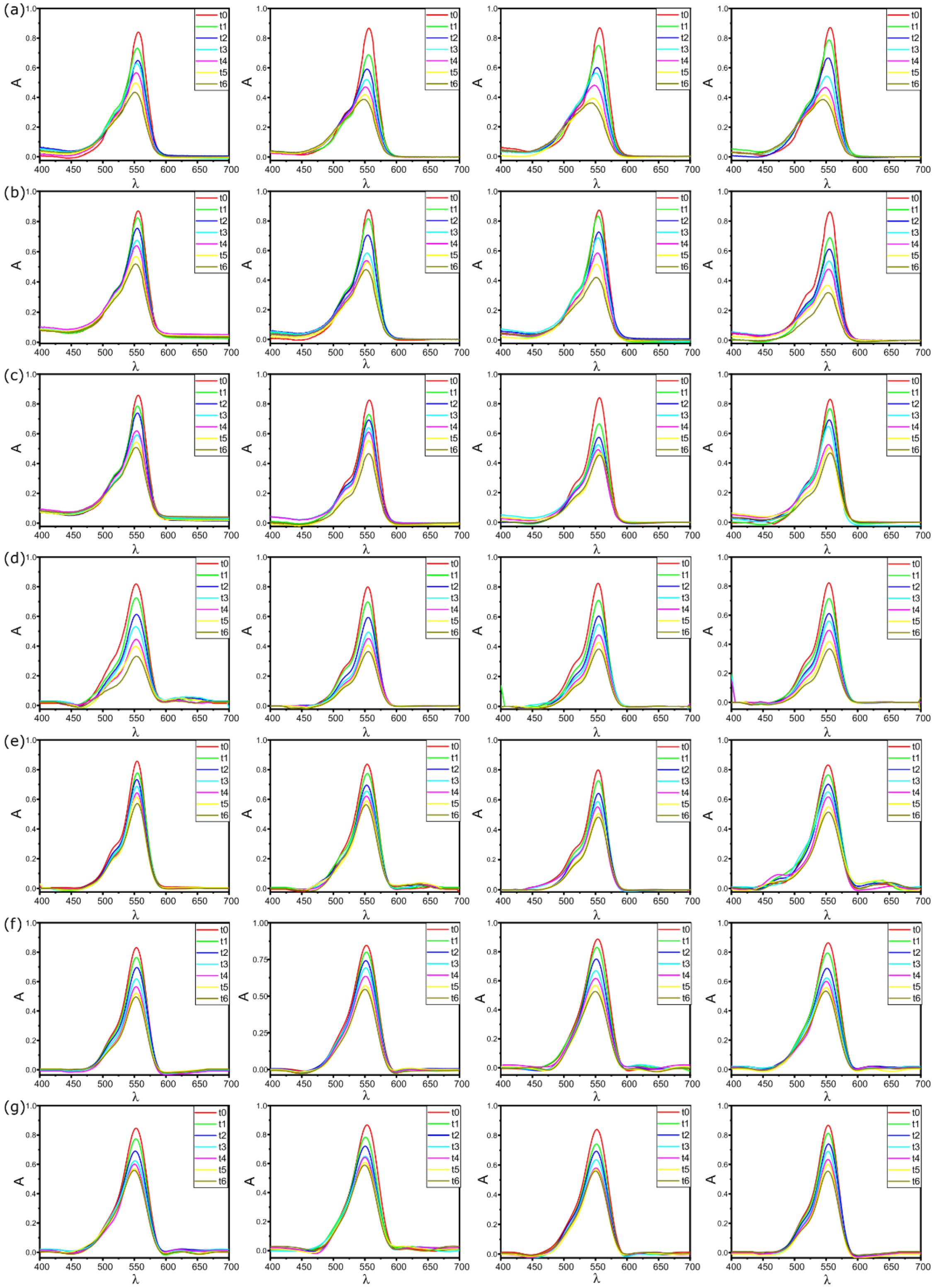

Fig. 5.18: Decrease of RhB absorptance with time due to photocatalytic activity at 0°, 15°, 30° and 45° incidence angles of the photocatalysts (a) ITB-220, (b) ITB-310, (c) ITB-340, (d) TB-NS, (e) B-NS, (f) T-NS and (g) IT-310.

To resume the comparison between bilayer and monolayer samples, all bilayer samples with slow photons generated at four spectral regions showed higher photocatalytic activity than all monolayer samples with slow photons at two spectral regions. The bilayer sample, ITB-310/220, at 45° incidence angle **(Fig. 5.15-case 1, Fig. 5.14-pc 1)**, showed 1.5 times higher activity than the monolayer sample with the highest activity, namely ITB-310 at 45° incidence angle **(Fig. 5.15-case 4, Fig. 5.14-pc 5)**. In the former, three out of the four available slow photon spectral regions were tuned to $BiVO_4$ absorption, while in the latter only one out of the two available slow photon spectral regions overlapped with $BiVO_4$ absorption. It is to be noted that in both cases, the tuning conditions were optimized such that SBG reflections losses were at least partially avoided. When compared to monolayer ITB-220 at 30° incidence angle **(Fig. 5.15-case 4, Fig. 5.14-pc 4)**, the activity of the bilayer sample was 1.7 times higher, since the monolayer sample, despite having slow photon spectral regions available for $BiVO_4$ absorption enhancement, suffered reflection losses from SBG peak. A still higher enhancement factor of 2.2 was observed when compared with monolayer ITB-310 at 0° incidence angle **(Fig. 5.15-case 4, Fig. 5.14-pc 5)**, since both slow photon spectral regions available were tuned away from $BiVO_4$ absorption. The increased activity in bilayer samples compared to that in monolayer samples and the correlation with the number of slow photon spectral regions, confirmed that generating and tuning slow photons at multi-spectral regions can be an effective strategy for improving light harvesting. The influence of multi-spectral slow photons was further justified by comparing the activities of bilayer ITB samples with those of non-structured TiO_2-$BiVO_4$ (TB-NS), $BiVO_4$ (B-NS) and TiO_2 (T-NS) films at varying incidence angles **(Fig. 5.14)**. Bilayer samples exhibited up to a maximum photocatalytic enhancement of 4.0 times and 4.2 times compared to TB-NS and B-NS compact films respectively, while it was 8.5 times higher compared to that of T-NS film. The steep difference in activity, along with the absence of activity variation with incidence angle in non-structured samples, further corroborated the previous justification of slow photon effect in IO structured photocatalysts.

Comparison of photocatalytic efficiencies was also done after normalizing the activities based on the changes in optical path length and Fresnel reflection of light with change in incidence angle. Calculations were similar to those carried out in chapter IV except that in this case the thickness of bilayer samples was 3.5 μm. Normalization based on the specific surface area was also done based on the work previously done. The resulting normalized activities are presented in **Table 5.5** and depicted in **Fig. 5.19**.

Table 5.5: Photocatalytic efficiencies after normalization based on changes in optical path length and specific surface area

Photocatalyst	Photocatalytic efficiency				Normalized with path length				Normalized with surface area			
	0°	15°	30°	45°	0°	15°	30°	45°	0°	15°	30°	45°
ITB-310/220	73.2	75.2	80.1	96.9	73.2	74.2	76.2	87.9	73.2	74.2	76.2	87.9
ITB-340/220	69.6	65.7	69.0	68.0	69.6	64.9	65.7	61.8	69.6	64.9	65.7	61.8
ITB-220/310	70.8	76.7	84.3	93.1	70.8	75.7	80.3	84.5	70.8	75.7	80.3	84.5
ITB-220/340	73.6	71.5	71.1	76.3	73.6	70.6	67.6	69.3	73.6	70.6	67.6	69.3
ITB-220	47.0	53.4	56.5	53.6	47.0	52.7	53.7	48.6	47.0	52.7	53.7	48.6
ITB-310	43.2	48.2	53.7	64.9	43.2	47.5	51.1	58.9	43.2	47.5	51.1	58.9
ITB-340	42.9	44.9	47.4	44.6	42.9	44.3	45.1	40.5	42.9	44.3	45.1	40.5
TB-NS	28.4	27.4	31.6	31.6	28.4	27.1	30.1	28.7	31.4	29.9	33.3	31.7
B-NS	29.5	27.2	27.3	28.2	29.5	26.9	26.0	25.6	32.7	29.7	28.7	28.3
T-NS	10.8	9.7	10.8	10.4	10.8	9.5	10.3	9.4	12.0	10.5	11.3	10.4
IT-220	14.8	13.9	14.9	15.8	14.8	13.7	14.2	14.4	14.8	13.7	14.2	14.4

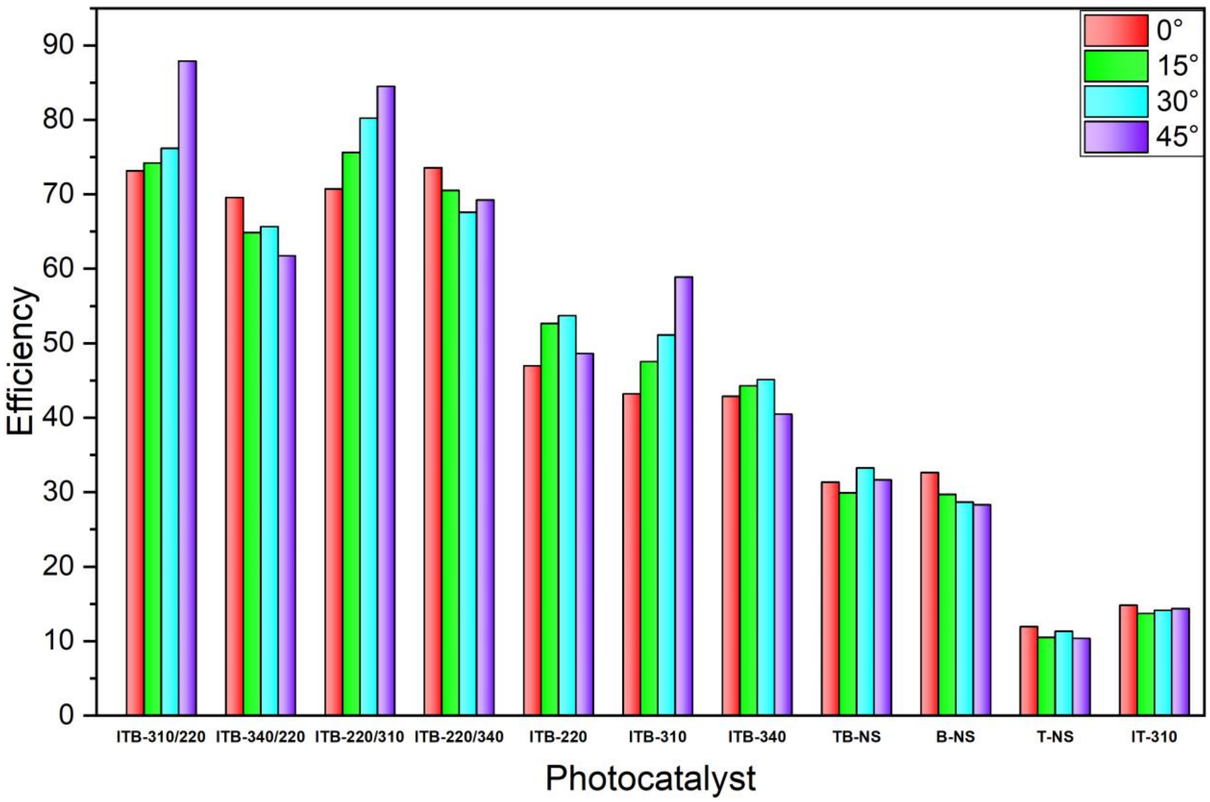

Fig. 5.19: Photocatalytic efficiencies after normalization based on changes in optical path length and specific surface area.

Based on the normalized data, it was observed that the trends in photocatalytic activities remained the same while the enhancement factors were relatively reduced. For instance, in the case of ITB-310/220 at 45° incidence angle (case 1), the enhancement factors with utilization of three slow photon spectral regions were 1.2 and 1.3 compared to the same sample at 30° and 0° incidence angles respectively. These were modified to 1.15 and 1.2 after normalization with changes in optical path length and Fresnel reflection. Similarly, the photocatalytic activities of bilayer IO samples which were 1.8 times higher on average than those of monolayer samples was changed to 1.62 times after the same normalization. In addition, normalization with respect to specific surface revealed that the bilayer samples exhibited up to a maximum of 2.78 times, 3.1 times and 8.4 times higher activity than those of TiO_2-$BiVO_4$, $BiVO_4$, and TiO_2 non-structured films respectively (4.0, 4.2, and 8.5 times before normalization).

Stability of the photocatalyst was determined both by examination of SEM images after photocatalysis **(Fig. 5.20 (a-c))** and activity determination of ITB-310/220 at 0° incidence angle for four continuous cycles **(Fig. 5.20 (d)**. It was noted that the modification in structure was not highly significant, and that the activity remained stable even after 8 cycles (four experimental cycles at different angles and four cycling tests).

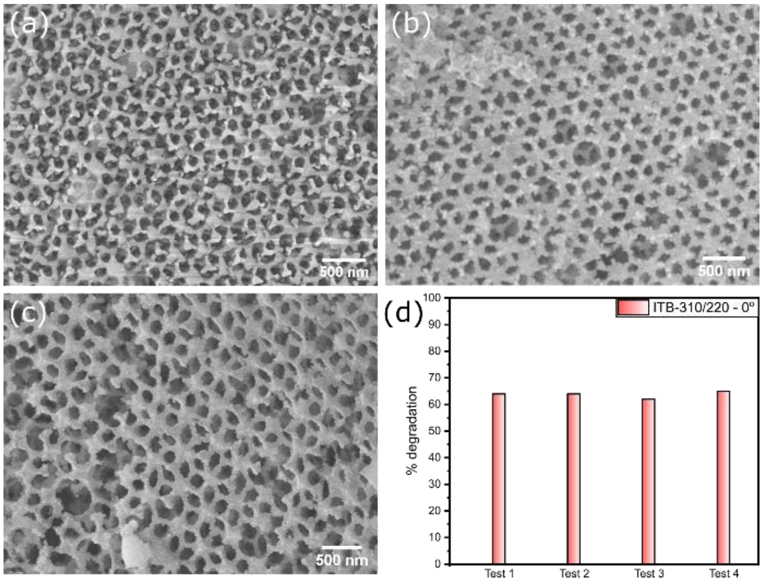

Fig. 5.20: Top-view SEM images, after photocatalysis, of **(a)** ITB-220/310, **(b)** ITB-310/220, **(c)** ITB-340/220; **(d)** photocatalytic degradation efficiency of ITB-310/220 at 0° light incidence angle for four repetitive tests.

To understand better the degradation kinetics of the heterogeneous Fenton-like reaction, the pseudo-first-order (PFO) and the pseudo-second-order (PSO) models were used to predict the experimental data (**Eqs. 5.2** and **5.3**).

$$\ln\left(\frac{C_t}{C_0}\right) = -K_1 t \qquad \textbf{(Eq.5.2)}$$

$$\frac{1}{C_t} = \frac{1}{C_0} + K_2 t \qquad \textbf{(Eq.5.3)}$$

where C_0 and C_t are the concentrations of RhB in aqueous solution at the beginning of the reaction and at t min, respectively; K_1 (min^{-1}) and K_2 ($mg.L^{-1}.min^{-1}$) represent the kinetic rate constants of first-order and second-order models, respectively and t is the reaction time (min). Regression analysis was conducted, and the results are shown in **Table 5.6** and **Fig. 5.21.** It was observed that, in all the experiments considered, the regression coefficients (R^2) based on the pseudo-first-order reaction kinetics were mostly higher than those based on pseudo-second-order reaction kinetics, thereby indicating that the pseudo-first-order model was more suitable for describing RhB degradation kinetics. cycling tests).

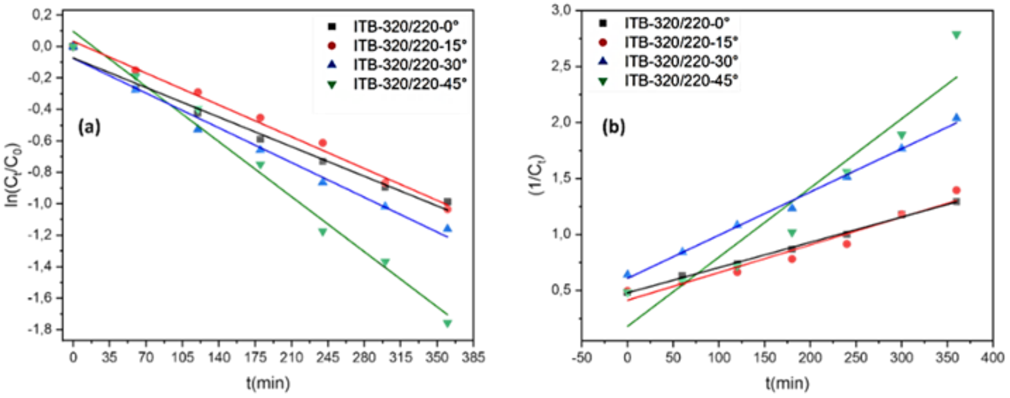

Fig. 5.21: Pseudo-first order **(a)** and pseudo-second order **(b)** kinetic plots for RhB degradation.

Table 5.6: The parameters of pseudo-first-order (PFO) and pseudo-second-order (PSO) kinetic models and correlation coefficients (R^2) for the degradation of RhB using ITB-310/220 at 0°, 15°, 30°, and 45° incidence angles.

	PFO		**PSO**	
	$\boldsymbol{K_1}$ (min^{-1})	$\boldsymbol{R^2}$	$\boldsymbol{K_2}$ ($mg.L^{-1}.min^{-1}$)	$\boldsymbol{R^2}$
Photocatalyst				
ITB-310/220-0°	0.0030	0.996	0.0023	0.992
ITB-310/220-15°	0.0028	0.996	0.0025	0.949
ITB-310/220-30°	0.0034	0.995	0.0039	0.993
ITB-310/220-45°	0.0046	0.993	0.0062	0.909

5.4. Summary

In summary, we have successfully tackled the fundamental issue that restricts enhancement factors in slow photon-assisted photocatalysis, namely the confinement of slow photons to narrow wavelengths. Previous works that utilized slow photon effect for photocatalysis reported a maximum 2 to 3-fold enhancement compared to non-structured counterparts[38-44], which could not be surpassed as they relied on single stop band gap-manifesting photonic structures with limited slow photon spectral ranges at either edge of the stop band gap. In this work, we were able to exceed this enhancement limit by fabricating dual stop band gap inverse opal structures with slow photons at multiple spectral regions. This was realized in a bilayer inverse opal TiO_2 structure, synthesized by following consecutive steps of coassembly in the colloid templating approach, such that each layer having a different pore size manifested a distinct stop band gap, at the edges of which the group velocity of light was reduced and localized within the structure. The wavelengths of these multi-spectral slow photons were tuned through both lattice parameter and incidence angle variation to the absorption range of $BiVO_4$ nanoparticles embedded in the bilayer structure. Under optimal tuning conditions, the bilayer inverse opal TiO_2-$BiVO_4$ heterocomposite photocatalyst displayed 2.2 times higher photocatalytic activity compared to the monolayer inverse opal sample and up to 8.5 times higher activity than the corresponding non-structured compact films. To the best of our knowledge, this is the first scientific work that reports the usage of dual band gap photonic structure to generate and tune slow photons at multiple spectral ranges through lattice parameter and incidence angle variations in a heterocomposite photocatalyst system. We believe that this strategy in slow photon-assisted photocatalysis tested for photodegradation can be successfully employed in other light harvesting applications like water splitting and CO_2 reduction and can even be extended to advanced sensing applications. Further research can be envisaged to improve upon this strategy by tuning slow photons at different wavelengths to different components of the heterocomposite photocatalyst system to obtain optimal light harvesting.

References

1. Liu, J.; Zhao, H.; Wu, M.; Van der Schueren, B.; Li, Y.; Deparis, O.; Ye, J.; Ozin, G. A.; Hasan, T.; Su, B. L., Slow photons for photocatalysis and photovoltaics. *Advanced Materials* **2017,** *29* (17), 1605349.
2. Wang, W.; Qi, L., Light management with patterned micro-and nanostructure arrays for photocatalysis, photovoltaics, and optoelectronic and optical devices. *Advanced Functional Materials* **2019,** *29* (25), 1807275.
3. Djurišić, A. B.; Leung, Y. H.; Ng, A. M. C., Strategies for improving the efficiency of semiconductor metal oxide photocatalysis. *Materials Horizons* **2014,** *1* (4), 400-410.
4. Kundu, S.; Patra, A., Nanoscale strategies for light harvesting. *Chemical Reviews* **2017,** *117* (2), 712-757.
5. Marschall, R., Semiconductor composites: strategies for enhancing charge carrier separation to improve photocatalytic activity. *Advanced Functional Materials* **2014,** *24* (17), 2421-2440.
6. Zhu, S.; Wang, D., Photocatalysis: basic principles, diverse forms of implementations and emerging scientific opportunities. *Advanced Energy Materials* **2017,** *7* (23), 1700841.
7. John, S., Strong localization of photons in certain disordered dielectric superlattices. *Physical Review Letters* **1987,** *58* (23), 2486-2489.
8. Yablonovitch, E., Inhibited spontaneous emission in solid-state physics and electronics. *Physical Review Letters* **1987,** *58* (20), 2059-2062.
9. Cersonsky, R. K.; Antonaglia, J.; Dice, B. D.; Glotzer, S. C., The diversity of three-dimensional photonic crystals. *Nature Communications* **2021,** *12* (1), 1-7.
10. Armstrong, E.; O'Dwyer, C., Artificial opal photonic crystals and inverse opal structures – fundamentals and applications from optics to energy storage. *Journal of Materials Chemistry C* **2015,** *3* (24), 6109-6143.
11. Collins, G.; Armstrong, E.; McNulty, D.; O'Hanlon, S.; Geaney, H.; O'Dwyer, C., 2D and 3D photonic crystal materials for photocatalysis and electrochemical energy storage and conversion. *Science and Technology of Advanced Materials* **2016,** *17* (1), 563-582.
12. Li, Y.; Fu, Z. Y.; Su, B. L., Hierarchically structured porous materials for energy conversion and storage. *Advanced Functional Materials* **2012,** *22* (22), 4634-4667.
13. Joannopoulos, J. D.; Johnson, S. G.; Winn, J. N.; Meade, R. D., *Molding the flow of light*. Princeton Univ. Press: 2008.
14. Joannopoulos, J. D.; Villeneuve, P. R.; Fan, S., Photonic crystals: putting a new twist on light. *Nature* **1997,** *386* (6621), 143-149.
15. Lopez, C., Materials aspects of photonic crystals. *Advanced Materials* **2003,** *15* (20), 1679.
16. Soukoulis, C. M., *Photonic crystals and light localization in the 21st century*. Springer Science & Business Media: 2012; Vol. 563.
17. Baba, T., Slow light in photonic crystals. *Nature Photonics* **2008,** *2* (8), 465-473.
18. Krauss, T. F., Why do we need slow light? *Nature Photonics* **2008,** *2* (8), 448-450.
19. Guo, M.; Yu, X.-Q.; Zhao, J.; Wang, J.-W.; Qing, R.-K.; Liu, J.-D.; Wu, X.; Zhu, L.; Chen, S., Versatile titanium dioxide inverse opal composite photonic hydrogel films towards multi-solvents chip sensors. *Sensors and Actuators B* **2021,** *347*, 130639.
20. Zhou, Q.; Song, Y.; Li, N.; Chen, D.; Xu, Q.; Li, H.; He, J.; Lu, J., Direct dual Z-scheme Bi2WO6/GQDs/WO3 inverse opals for enhanced photocatalytic activities under visible light. *ACS Sustainable Chemistry & Engineering* **2020,** *8* (21), 7921-7927.

21. Ran, L.; Qiu, S.; Zhai, P.; Li, Z.; Gao, J.; Zhang, X.; Zhang, B.; Wang, C.; Sun, L.; Hou, J., Conformal macroporous inverse opal oxynitride-based photoanode for robust photoelectrochemical water splitting. *Journal of the American Chemical Society* **2021,** *143* (19), 7402-7413.
22. Maho, A.; Lobet, M.; Daem, N.; Piron, P.; Spronck, G.; Cloots, R.; Colson, P.; Henrist, C.; Dewalque, J., Photonic Structuration of Hybrid Inverse-Opal TiO_2—Perovskite Layers for Enhanced Light Absorption in Solar Cells. *ACS Applied Energy Materials* **2021,** *4* (2), 1108-1119.
23. Deimling, M.; Kousik, S. R.; Abitaev, K.; Frey, W.; Sottmann, T.; Koynov, K.; Laschat, S.; Atanasova, P., Hierarchical Silica Inverse Opals as a Catalyst Support for Asymmetric Molecular Heterogeneous Catalysis with Chiral Rh-diene Complexes. *ChemCatChem* **2021,** *13* (9), 2242-2252.
24. Kim, O.-H.; Cho, Y.-H.; Kang, S. H.; Park, H.-Y.; Kim, M.; Lim, J. W.; Chung, D. Y.; Lee, M. J.; Choe, H.; Sung, Y.-E., Ordered macroporous platinum electrode and enhanced mass transfer in fuel cells using inverse opal structure. *Nature Communications* **2013,** *4* (1), 1-9.
25. McNulty, D.; Geaney, H.; Ramasse, Q.; O'Dwyer, C., Long cycle life, highly ordered SnO_2/GeO_2 nanocomposite inverse opal anode materials for Li-ion batteries. *Advanced Functional Materials* **2020,** *30* (51), 2005073.
26. Fathi, F.; Monirinasab, H.; Ranjbary, F.; Nejati, K., Inverse opal photonic crystals: Recent advances in fabrication methods and biological applications. *Journal of Drug Delivery Science and Technology* **2022**, 103377.
27. Cai, Z.; Li, Z.; Ravaine, S.; He, M.; Song, Y.; Yin, Y.; Zheng, H.; Teng, J.; Zhang, A., From colloidal particles to photonic crystals: advances in self-assembly and their emerging applications. *Chemical Society Reviews* **2021,** *50* (10), 5898-5951.
28. Moon, J. H.; Yang, S., Chemical aspects of three-dimensional photonic crystals. *Chemical Reviews* **2010,** *110* (1), 547-574.
29. Phillips, K. R.; England, G. T.; Sunny, S.; Shirman, E.; Shirman, T.; Vogel, N.; Aizenberg, J., A colloidoscope of colloid-based porous materials and their uses. *Chemical Society Reviews* **2016,** *45* (2), 281-322.
30. Stein, A.; Wilson, B. E.; Rudisill, S. G., Design and functionality of colloidal-crystal-templated materials—chemical applications of inverse opals. *Chemical Society Reviews* **2013,** *42* (7), 2763-2803.
31. von Freymann, G.; Kitaev, V.; Lotsch, B. V.; Ozin, G. A., Bottom-up assembly of photonic crystals. *Chemical Society Reviews* **2013,** *42* (7), 2528-2554.
32. Hoeven, J. E. v. d.; Shneidman, A. V.; Nicolas, N. J.; Aizenberg, J., Evaporation-induced self-assembly of metal oxide inverse opals: from synthesis to applications. *Accounts of Chemical Research* **2022,** *55* (13), 1809-1820.
33. Curti, M.; Schneider, J.; Bahnemann, D. W.; Mendive, C. B., Inverse opal photonic crystals as a strategy to improve photocatalysis: Underexplored questions. *The Journal of Physical Chemistry Letters* **2015,** *6* (19), 3903-3910.
34. Pietron, J. J.; DeSario, P. A., Review of roles for photonic crystals in solar fuels photocatalysis. *Journal of Photonics for Energy* **2016,** *7* (1), 012007.
35. Aguirre, C. I.; Reguera, E.; Stein, A., Tunable colors in opals and inverse opal photonic crystals. *Advanced Functional Materials* **2010,** *20* (16), 2565-2578.
36. Blanford, C. F.; Schroden, R. C.; Al-Daous, M.; Stein, A., Tuning solvent-dependent color changes of three-dimensionally ordered macroporous (3DOM) materials through compositional and geometric modifications. *Advanced Materials* **2001,** *13* (1), 26-29.

37. Chen, J. I. L.; von Freymann, G.; Choi, S. Y.; Kitaev, V.; Ozin, G. A., Amplified photochemistry with slow photons. *Advanced Materials* **2006,** *18* (14), 1915-1919.

38. Curti, M.; Mendive, C. B.; Grela, M. A.; Bahnemann, D. W., Stopband tuning of TiO_2 inverse opals for slow photon absorption. *Materials Research Bulletin* **2017,** *91*, 155-165.

39. Curti, M.; Zvitco, G.; Grela, M. A.; Mendive, C. B., Angle dependence in slow photon photocatalysis using TiO_2 inverse opals. *Chemical Physics* **2018,** *502*, 33-38.

40. Liu, J.; Jin, J.; Li, Y.; Huang, H.-W.; Wang, C.; Wu, M.; Chen, L.-H.; Su, B.-L., Tracing the slow photon effect in a ZnO inverse opal film for photocatalytic activity enhancement. *Journal of Materials Chemistry A* **2014,** *2* (14).

41. Wu, M.; Jin, J.; Liu, J.; Deng, Z.; Li, Y.; Deparis, O.; Su, B.-L., High photocatalytic activity enhancement of titania inverse opal films by slow photon effect induced strong light absorption. *Journal of Materials Chemistry A* **2013,** *1* (48), 15491-15500.

42. Wu, M.; Liu, J.; Jin, J.; Wang, C.; Huang, S.; Deng, Z.; Li, Y.; Su, B.-L., Probing significant light absorption enhancement of titania inverse opal films for highly exalted photocatalytic degradation of dye pollutants. *Applied Catalysis B* **2014,** *150-151*, 411-420.

43. Xie, H.; Li, Y.; Jin, S.; Han, J.; Zhao, X., Facile fabrication of 3D-ordered macroporous nanocrystalline iron oxide films with highly efficient visible light induced photocatalytic activity. *Journal of Physical Chemistry C* **2010,** *114* (21), 9706-9712.

44. Zhang, L.; Baumanis, C.; Robben, L.; Kandiel, T.; Bahnemann, D., Bi_2WO_6 inverse opals: facile fabrication and efficient visible-light-driven photocatalytic and photoelectrochemical water-splitting activity. *Small* **2011,** *7* (19), 2714-20.

45. Eftekhari, E.; Broisson, P.; Aravindakshan, N.; Wu, Z.; Cole, I. S.; Li, X.; Zhao, D.; Li, Q., Sandwich-structured TiO_2 inverse opal circulates slow photons for tremendous improvement in solar energy conversion efficiency. *Journal of Materials Chemistry A* **2017,** *5* (25), 12803-12810.

46. Zulfiqar, A.; Temerov, F.; Saarinen, J. J., Multilayer TiO_2 inverse opal with gold nanoparticles for enhanced photocatalytic activity. *ACS Omega* **2020,** *5* (20), 11595-11604.

47. Bakhshzadmahmoudi, M.; Jamali, S.; Ahmadi, E., Wettability modification of polystyrene surface by cold atmospheric pressure plasma jet. *Colloid and Polymer Science* **2022,** *300* (2), 103.

48. Guruvenket, S.; Rao, G. M.; Komath, M.; Raichur, A. M., Plasma surface modification of polystyrene and polyethylene. *Applied Surface Science* **2004,** *236* (1-4), 278-284.

49. López, C., Three-dimensional photonic bandgap materials: semiconductors for light. *Journal of Optics A: Pure and Applied Optics* **2006,** *8* (5), R1.

50. Schroden, R. C.; Al-Daous, M.; Blanford, C. F.; Stein, A., Optical properties of inverse opal photonic crystals. *Chemistry of Materials* **2002,** *14* (8), 3305-3315.

51. Choy, T. C., *Effective medium theory: principles and applications*. Oxford Univ. Press: 2015; Vol. 165.

52. Deparis, O.; Ghazzal, M.; Simonis, P.; Mouchet, S.; Kebaili, H.; De Coninck, J.; Gaigneaux, E. M.; Vigneron, J.-P., Theoretical condition for transparency in mesoporous layered optical media: application to switching of hygrochromic coatings. *Applied Physics Letters* **2014,** *104* (2), 023704.

53. Park, Y. R.; Kim, K. J., Structural and optical properties of rutile and anatase TiO_2 thin films: effects of Co doping. *Thin Solid Films* **2005,** *484* (1-2), 34-38.

54. Yuan, Y.; Huang, Y.; Ma, F.; Zhang, Z.; Wei, X., Effects of oxygen vacancy on the mechanical, electronic and optical properties of monoclinic $BiVO_4$. *Journal of Materials Science* **2017,** *52* (14), 8546-855.

CHAPTER VI

Slow photons in photonic plasmonic TiO_2-Au structures sensitized with CdS and Pt nanoparticles for photocatalytic hydrogen generation

Abstract

Slow light in photonic structures is known to increase light harvesting and boost photocatalytic efficiency. However, enhancement factors reported are often low, since slow photons are confined to narrow spectral ranges. Also, their exploitation was limited to particulate photonic structures in which slow light harvesting remains inadequate. In this work, we report the maximized utilization of slow light to achieve high enhancement factors for H_2 evolution over inverse opal (IO) TiO_2 photonic structure film, embedded with CdS, Au and Pt nanoparticles. Slow photons at blue and red edges were harvested such that both the electronic absorption of CdS and the surface plasmon resonance of Au nanoparticles were simultaneously enhanced. The enhancement in light harvesting potential by the synergistic slow photon and surface plasmon-assisted confinement of electromagnetic field in the modified IO TiO_2 photonic structure, along with the increase in photogenerated charge separation efficiency, resulted in a maximum H_2 evolution of 173.16 $mmolh^{-1}g^{-1}$ over IO TiO_2-Au-CdS-Pt (TACP 300 with 295 nm pore diameter) at 45° light incidence angle, 7.78 times higher than the activity of pristine IO TiO_2 photonic structure. The synergy between slow photon and surface plasmon resonance effects was demonstrated by the 3-fold increase in H_2 evolution observed when slow photon frequencies were tuned to Au plasmon resonance, compared to the activity in the absence of Au NPs. This study offers a novel approach to reap optimal benefits from slow light in composite inverse opal photonic film structures to enhance photocatalytic hydrogen evolution.

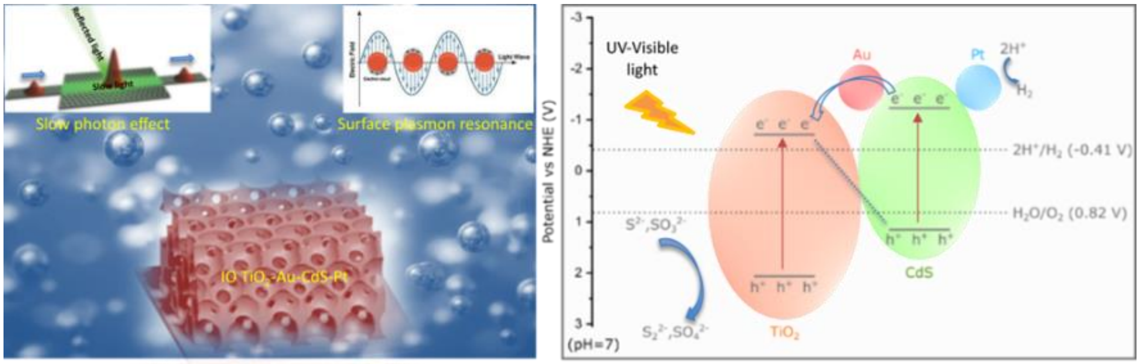

6. Slow photons in photonic plasmonic TiO_2-Au structures sensitized with CdS and Pt nanoparticles for photocatalytic hydrogen generation

6.1. Introduction

Photocatalytic hydrogen generation using sunlight and water is a promising solution for soaring energy demands and dwindling supplies, as it offers clean, renewable, and sustainable fuel[1-3]. Fundamental challenges in this process include light harvesting, photogenerated electron-hole charge separation and charge transfer to the active sites, engineering of valence and conduction band positions relative to water splitting redox potentials, mass transfer of reactants and products, and design of reactor for large scale H_2 production[4-7]. The primary among them, which directly determines the theoretical solar-to-hydrogen conversion efficiency is the capture of sunlight[8]. Several strategies were proposed to improve both the extent and the spectral range of sunlight absorption[9-11], most of which were focussed on the choice, design, and modification of photocatalyst materials[12-16]. However, the strategy of moulding the flow of light[17], as in the case of photonic crystals, to reduce the group velocity of light and localize it within the photocatalyst system, remains relatively underexplored[18].

Photonic crystals are periodic dielectric structures, with periodicity in the order of the wavelength of light[19, 20]. When the refractive index (RI) contrast between their dielectric components is high, photons of a certain wavelength range, termed as photonic stop band gap (SBG), are forbidden from propagating through the material due to coherent Bragg diffraction, while those at either edge of the SBG, termed as blue (i.e., higher frequencies) and red (i.e., lower frequencies) edge slow photons, propagate with highly reduced group velocity[21-24]. High optical gain can be achieved when the wavelengths of slow photons are tuned to the electronic absorption of the photocatalyst, which translates into enhanced photocatalytic efficiency[25-27].

The most employed photonic structure in slow light-assisted photocatalysis is the inverse opal (IO) structure, fabricated by the removal of the opal template containing matrix material in its interstices, to give an ordered macroporous structure[28, 29]. Starting from the early work on slow-photon assistance in IO TiO_2 for the solid-phase photodegradation of methylene blue[30], several researchers successfully established light harvesting enhancement in IO structures, as in those of TiO_2[31, 32], ZnO[33], Bi_2WO_6[34], and Fe_2O_3[35], by demonstrating the variation of photocatalytic activity with light incidence angle. However, in most of the above works, the impact of slow photons was limited to a two-fold photocatalytic enhancement, compared to the activity of the non-structured counterparts. This limitation was mostly due to the narrow spectral region of slow photons. Another reason could be the employment of particulate IO systems, in which the crystal planes are randomly oriented with respect to incident light, resulting either in the absence of SBG or the manifestation of a broad SBG averaged from that of different crystal planes[36-38]. Despite some successful reports[39, 40] of slow-photon assistance in IO particulate photocatalysts, precise tuning of slow-photon frequencies in such systems remains less evident and challenging.

Various strategies were previously employed to improve photocatalytic enhancement in IO structures. These include the synergy of slow-photon effect (SPE) with cocatalyst loading[41], doping[42, 43], heterojunction formation[40, 44], and surface plasmon resonance (SPR)[45-47], successfully investigated mostly in photocatalytic degradation. In chapter V of this work, an alternate approach was provided by fabricating bilayer IO TiO_2-$BiVO_4$ films to generate slow photons at multiple spectral regions for photocatalytic enhancement of rhodamine B degradation. However, the synthesis of such structures remains challenging. Also, in more complex processes like water splitting, SPE and its synergy with a single strategy is insufficient for H_2 evolution enhancement, as it requires the simultaneous optimization of various parameters[13].

In this work, we propose a novel approach to achieve optimal utilization of slow photons in IO TiO_2 photonic film, embedded with Au, CdS, and Pt NPs (TACP), to obtain remarkable H_2 evolution. Initially, H_2 evolution over IO TACP photocatalyst system was compared with IO structures of pristine TiO_2 (T) and binary TiO_2-Au (TA), TiO_2-CdS (TC) and TiO_2-Pt (TP) photocatalyst systems. Synergy between SPE and SPR was established by comparing the activities of IO T and TA photocatalysts and corroborating the interpretation of results through Surface Enhanced Raman Spectroscopy (SERS). This was followed by the comparison with H_2 evolution over ternary TiO_2-Au-CdS (TAC), TiO_2-Au-Pt (TAP) and TiO_2-CdS-Pt (TCP) photocatalyst systems to investigate the synergy between various contributing factors in the composites. In quaternary TACP photocatalyst system, slow-photon utilization was first optimized by lattice parameter (namely, pore size) variation. By varying the pore size in IO-TACP photocatalysts (TACP 300 and TACP 320), slow photons were tuned to Au plasmon resonance absorption that resulted in higher H_2 evolution. An even higher H_2 evolution was obtained by varying light incidence angle such that slow photons at blue and red edges of SBG were tuned to both CdS electronic absorption and Au plasmon resonance. We demonstrate, through this work, a novel multi-pronged strategy to obtain remarkable H_2 production in IO photonic structures by optimizing the exploitation of slow light simultaneously by different components in the composite photocatalyst system and by improving the photogenerated charge separation efficiency.

6.2. Experimental section – synthesis and photocatalytic tests

6.2.1. Synthesis of inverse opal TiO_2-Au-CdS-Pt composites

6.2.1.1. Synthesis of inverse opal TiO_2

Inverse opal TiO_2 (T) photonic structures were synthesized by colloid-templated method, that involved the evaporation-induced simultaneous self-assembly (EISSA) of polystyrene (PS) colloids and TiO_2 NPs on a substrate, followed by the removal of templating colloids by calcination to obtain the IO structure[48]. IO T structures of two different pore sizes were prepared using PS colloids of 397 nm and 425 nm diameters and coded as T 300 and T 320 with the numbers indicating their pore sizes. Sample preparation was done on a single side of the substrates by covering the other side with tape. The area of sample was 1.25×1.25 cm^2 on the glass substrate and 1.25×1.5 cm^2 on FTO substrate.

Phase controlled TiO_2 NPs used in the self-assembly process were prepared by a peptization method involving the hydrolysis and condensation of titanium isopropoxide (TIP) in the presence of tetramethyl ammonium hydroxide (TMAH)[49]. Typically, 2.25 mmol of TMAH was added to 90 ml of water taken in a 250 ml double neck round bottom flask, previously cooled in an ice bath. To this, 3.6 mmol of TIP dispersed in 15 mL of 2-propanol was added drop-by-drop under stirring. The milky white solution was left to stir for 15 min. and later transferred to a silicone oil bath where it was refluxed at 105°C for 6 h. The colourless nanoparticle suspension obtained was cooled and used within an ageing period of 3 to 10 days.

Glass slides were treated with acid piranha (3:1 H_2SO_4:H_2O_2), while FTO slides (2.0×1.5 cm^2) were treated with base piranha (1:1 NH_3:H_2O_2), at 70°C for 1h, to render them hydrophilic (caution: piranha is highly corrosive). The slides were rinsed thoroughly with water and stored in water for further use. The coassembly solution was prepared by mixing 7 mL of PS colloid suspension diluted to 0.1 w/v% and 40 µL/mL of the suspension of TiO_2 NPs in a glass vial. The cleaned substrate was dried under N_2 gas and suspended vertically in the vial using clips. The vial was then placed in an oven at 40°C for 48 h for simultaneous self-assembly of PS colloids and

TiO_2 NPs. The self-assembled opal structure was then calcined at 500°C at a ramp rate of 1°C/min to remove the templating colloids and obtain the IO structure.

6.2.1.2. Synthesis of TiO_2-Au structures

IO TiO_2, with Au NPs loaded *in-situ* in the IO matrix, was synthesized by the evaporation-induced three phase coassembly of PS colloids, TiO_2 NPs and Au NPs on the substrate, followed by the removal of PS colloids by calcination[48].

6.2.1.2.1. Synthesis of Au nanoparticles

Citrate-stabilized Au NPs were prepared by the aqueous reduction of sodium tetrachloroaurate dihydrate ($NaAuCl_4.2H_2O$) by sodium citrate[50]. Typically, 0.063 mmol $NaAuCl_4.2H_2O$ was dissolved in 100 mL water and placed under reflux at 105°C for 15 min, following which a 25 mL solution containing 0.19 mmol sodium citrate was quickly added to it. The reaction was allowed to continue for 15 min. during which the solution turned from light yellow to deep red. After cooling the solution to room temperature, the particles in the suspension were washed by repeated centrifugation at 10000 rpm until all the nanoparticles were collected, and later redispersed in an equal amount of water.

6.2.1.2.2. Coassembly of PS colloids, TiO_2 NPs, and Au NPs

For the coassembly, the pretreated substrate was dried and suspended vertically in a coassembly suspension of 7mL of 0.1 wt% PS colloids containing 40 μL/mL of the suspension of TiO_2 NPs and 100 μL/mL of the suspension of Au NPs. This was left in an oven at 40°C for 48 h, followed by calcination to obtain IO TA structure.

6.2.1.3. Sensitizing inverse opal TiO_2-Au with CdS nanoparticles

CdS NPs were embedded in the IO TA structure by Successive Ionic Layer Adsorption and Reaction (SILAR) method[51, 52]. Initially, the substrate with IO TA was dipped in a solution of 0.1M $Cd(Ac)_2$ in methanol for 1 min. to adsorb Cd^{2+} ions, followed by rinsing in methanol to remove loosely adsorbed ions. The substrate was then dried in an oven at 40°C for 2 min. Later, the substrate was immersed in 0.1 M Na_2S in 1:1 water/methanol solution for 1 min. to adsorb S^{2-} ions followed by rinsing in methanol to remove loosely adsorbed ions and drying in an oven at 40°C for two min. This process was repeated for three cycles, following which the samples were sintered at 100°C for 1h. Reference sample IO TC was prepared by taking IO T and using SILAR method to deposit CdS NPs.

6.2.1.4. Sensitizing inverse opal TiO_2-Au-CdS with Pt nanoparticles

Inverse opal TiO_2-Au-CdS-Pt (TACP) composites were prepared by the photodeposition of Pt nanoparticles on IO TAC using a solution of hexachloroplatinic(IV) acid hexahydrate ($H_2PtCl_6.6H_2O$) in the presence of methanol [53, 54]. Initially, the substrate with IO TAC was immersed in a $1.25x10^{-4}$ M $H_2PtCl_6.6H_2O$ solution (1:1 water/methanol) taken in 10 mL vial. The vial was sealed with a rubber cork and flushed with N_2 gas to remove dissolved oxygen. Inert gas atmosphere was maintained throughout the photodeposition by attaching a balloon containing N_2 gas. The vial was then placed in a photoreactor and irradiated for 1 h with 10 Hg lamps (PL-S 9W/2P) placed at 7 cm around the vial. The substrate was then rinsed with water and dried at 100°C for 1 h. Two samples with different pore sizes, TACP 300 and TACP 320, were thus prepared. Reference samples, IO TP, IO TAP and IO TCP were prepared by the photodeposition of Pt NPs on IO T, IO TA, and IO TC, respectively.

6.2.2. Photocatalytic hydrogen production – experimental set-up and parameters

Photocatalytic H_2 evolution was determined using Merry Change MC-SPB10 commercial photocatalytic reactor equipped with a 300-W PLS-SXE 300D/300DUV Xenon light source with a spectral range of 320-780 nm and an optical power of 50 W (19.6 W in the visible range and 2.6 W in the UV range). The glass substrate with the photocatalyst was fixed on a holder, 10 cm away from the light source, at the bottom of a 150 mL Pyrex chamber containing 100 mL water with 0.1 M Na_2S and 0.1 M Na_2SO_3 as sacrificial agents. The Pyrex chamber was covered with a vacuum-tight quartz lid. The photocatalytic reactor was equipped with a water-circulating system that helped maintain a constant temperature. The amount of H_2 produced during the reaction was measured under auto sampling mode using Agilent Technologies 7890B Gas Chromatograph equipped with a thermal conductivity detector and a 5-Å molecular sieve column using N_2 as carrier gas. The reactor was vacuumized to a reduced pressure before starting the photocatalytic test to minimize backward reaction. Angle-dependent hydrogen production tests were conducted at two angles (30^o and 45^o) by varying the position of the sample holder with respect to the light source. Repeatability tests were conducted each time separately after rinsing the sample with deionized water and drying it in an oven.

6.3. Results and discussion

High quality IO photonic structures of TACP were prepared by a 3-step process as shown schematically in **Fig. 6.1**. The first step involved the synthesis of IO TA photonic structures by the simultaneous self-assembly of PS, TiO_2, and Au particles on the substrate followed by the removal of the colloids. The second and third steps involved the SILAR deposition of CdS NPs and the photodeposition of Pt NPs in the IO structure, respectively. CdS and Pt deposition were optimized by the number of SILAR cycles and the concentration of Pt precursor such that the photonic properties of the IO structure were retained post modification.

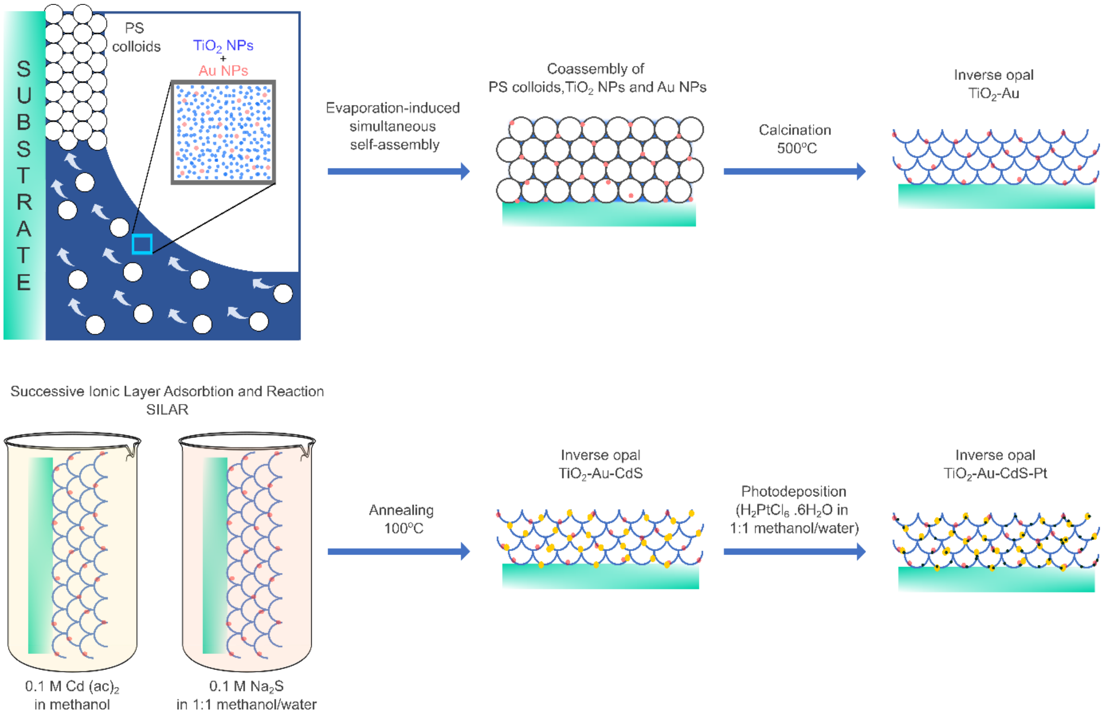

Fig. 6.1: (a) Schematic representation of the synthesis of IO TiO_2-Au-CdS-Pt (TACP) photocatalyst films: (i) Evaporation-induced simultaneous self-assembly of PS colloids, TiO_2 NPs and Au NPs on a glass substrate, (ii) Calcination to remove the templating colloids to get IO TiO_2-Au (TA) structure, (iii) Deposition of CdS NPs over IO TiO_2-Au (TA) by SILAR method to get IO TiO_2-Au-CdS (TAC) composite, (iv) Photodeposition of Pt NPs to get IO TACP photocatalyst.

The mean particle sizes of TiO_2 and Au NPs used in the synthesis were estimated by DLS analysis to be ~14 nm and ~36 nm respectively **(Fig. 6.2, (a-b))**, with TiO_2 NPs having a narrower size distribution than that of Au NPs. The Au NPs suspended in solution displayed their characteristic plasmonic absorption curve with the peak at 524 nm **(Fig. 6.2, (c))**. After synthesis of IO TA, the absorption peak corresponding to Au NPs in the solid sample broadened and red shifted to 554 nm **(Fig. 6.2, (d))**, probably due to the agglomeration of some of the Au NPs into clusters.

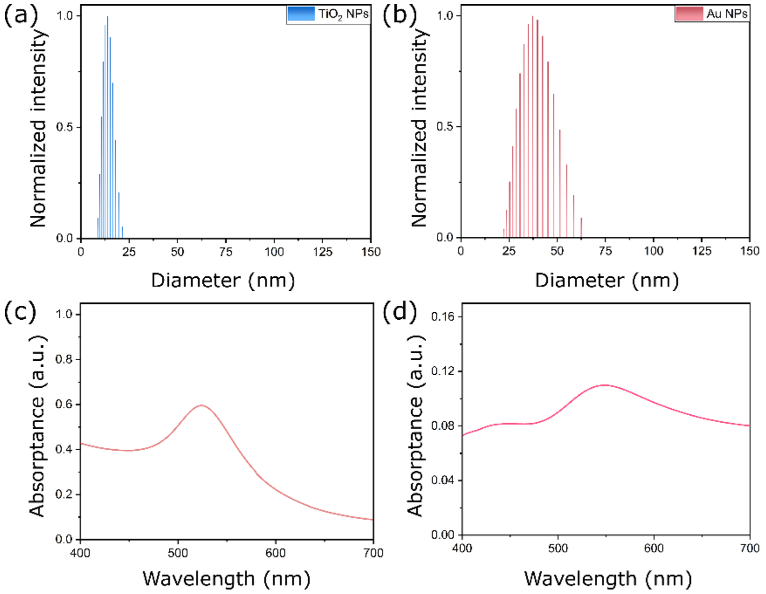

Fig. 6.2: (a-b) Particle size distribution of (a) TiO_2 NPs and (b) Au NPs obtained by Dynamic Light Scattering (DLS) method; **(c-d)** UV-Visible absorption of (c) pre-synthesized Au NPs in suspension and (d) Au NPs in IO TiO_2-Au (solid) photocatalyst.

Top view SEM images showed highly ordered IO structures of TACP 300 and TACP 320 samples, having macropore sizes of 295 nm and 324 nm, respectively **(Fig. 6.3 (a-b))**. PS templating colloids of 397 nm and 425 nm diameters were used to synthesize the two samples, indicating that there was a 26% and 24% shrinkage of the pore size relative to the colloid size in TACP 300 and TACP 320 respectively. The shrinkage, which is in accordance with previous reports of IO synthesis, is attributed to the volume shrinkage caused by both the template removal and the phase transformation of the matrix material. The samples displayed bright structural colours, as seen in the optical microscope images **(inset of Fig. 6.3 (a-b))**, which confirmed their excellent photonic properties, and hence the potential to reduce the group velocity of light. Evaporation-induced simultaneous self-assembly of PS colloids, TiO_2 and Au NPs on the substrate reduced the number of synthesis steps and minimized disorder. SILAR and photodeposition methods, to load CdS and Pt NPs respectively, not only enabled precise control over the amount deposited but also ensured homogeneous deposition while preserving the structural integrity and the photonic properties. The thickness of IO TACP samples was ~1.2 µm, as measured in the cross-section SEM images **(Fig. 6.3 (c-d))**.

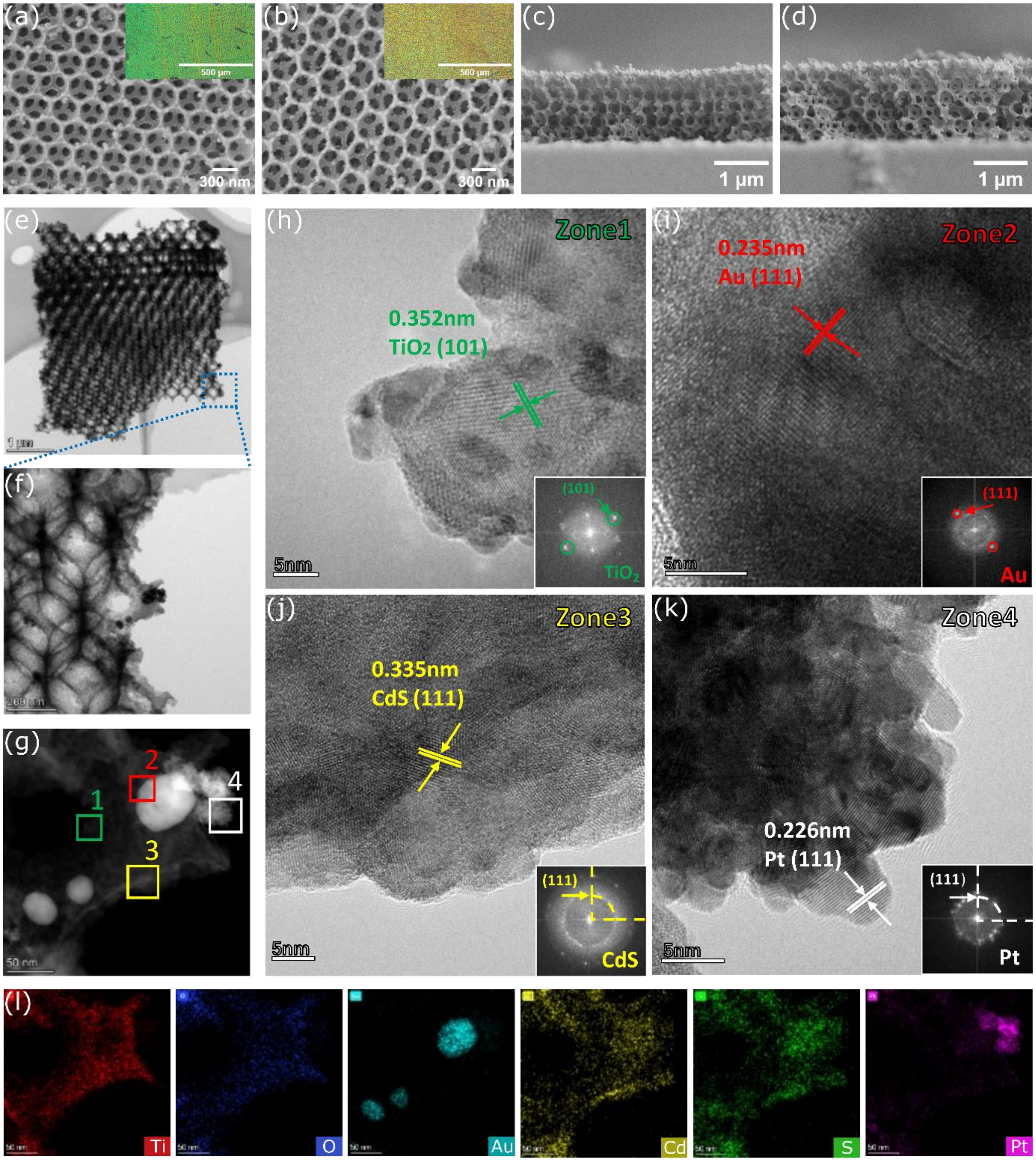

Fig. 6.3: **(a-b)** SEM images of (a) IO TiO_2-Au-CdS-Pt 300 (TACP 300), (b) IO TiO_2-Au-CdS-Pt 320 (TACP 320) with optical microscope images in inset; **(c-d)** Cross section SEM images of (c) TACP 300, (d) TACP 320; **(e-k)** HRTEM and HAADF-STEM images of TACP 300: (e-g) images at low magnification indicating the area of analysis with the four zones in (g) corresponding to TiO_2, Au, CdS, and Pt respectively, **(h-k)** images at high magnification indicating the respective lattice fringes of the exposed planes, with SAED patterns in inset; **(l)** EDX elemental mapping of Ti, O, Au, Cd, S, and Pt in TACP 300 (scale bar is 50 nm).

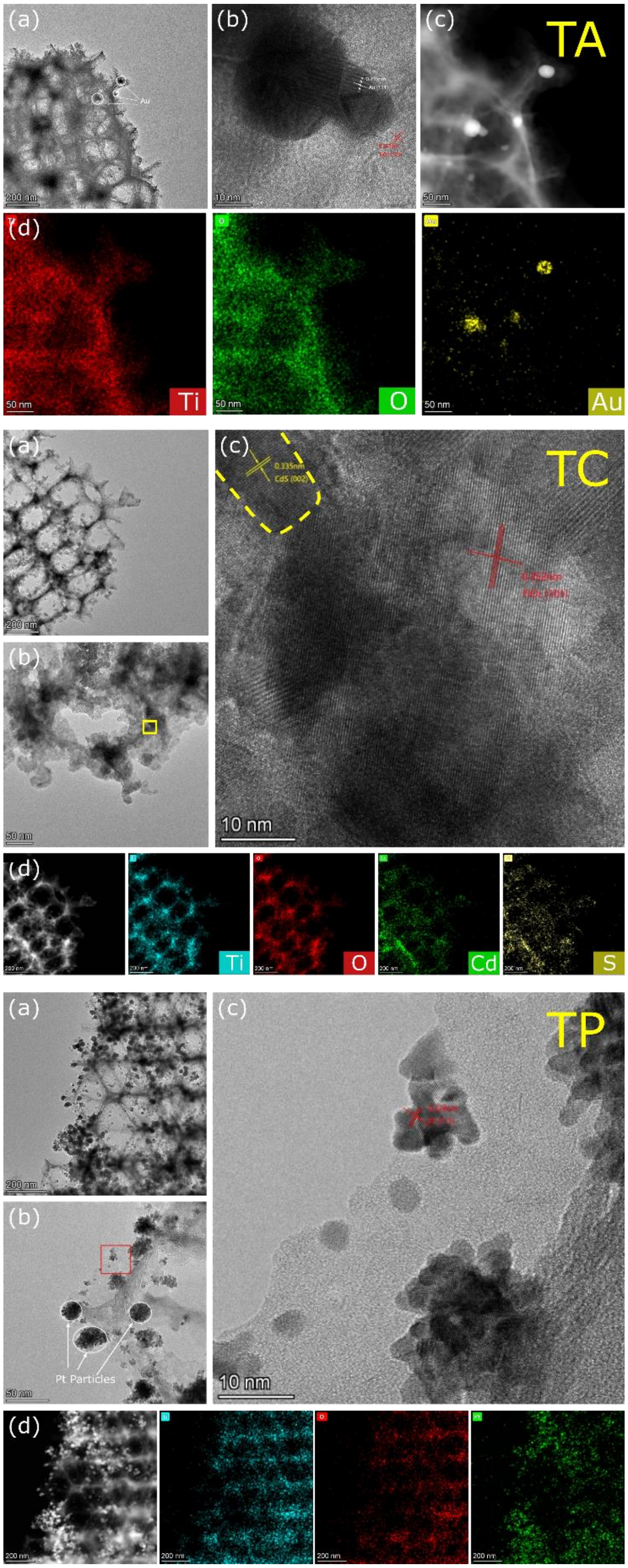

Fig. 6.4: HR-TEM and HAADF -STEM images TA 300, TC 300, and TP 300.

High resolution transmission electron microscope (HRTEM) and high-angle annular dark-field scanning transmission electron microscopy (HAADF-STEM) images **(Fig. 6.3, e-k)** permitted a more detailed structural analysis. Four zones containing TiO_2, Au, CdS, and Pt were identified **(Fig. 6.3, g)** and separately analyzed **(Fig. 6.3, h-k)**. From the lattice fringes observed for TiO_2, Au, Pt, and CdS, reticular inter-distances were measured to be 0.352 nm, 0.235 nm, 0.335 nm, and 0.226 nm, and attributed to the [101], [111], [111] and [111] lattice planes of tetragonal anatase TiO_2, cubic Au, cubic hawleyite CdS, and cubic Pt respectively. Selected area electron diffraction (SAED) patterns, shown in inset of **Fig. 6.3, h-k**, confirmed the above analysis. Structural analysis of each of the components deposited in the IO matrix was carried out from HRTEM and HAADF-STEM images of IO TiO_2-Au (TA 300), IO TiO_2-CdS (TC 300), and IO TiO_2-Pt (TP 300) samples **(Fig. 6.4)**. The average particle sizes of TiO_2, Au, CdS, and Pt NPs were thus determined to be ~12 nm, 35 nm, 12 nm, and 7 nm respectively. Au and Pt NPs were found to agglomerate into clusters in a few random areas. Energy-dispersive X-ray (EDX) elemental mapping **(Figs. 6.3, 6.4)** confirmed the homogeneous distribution of Au, CdS, and Pt NPs in the TiO_2 IO matrix. From EDX elemental analysis **(Table 6.1)**, the average proportions of TiO_2, Au, CdS and Pt in TACP samples were calculated to be 82.4%, 0.6%, 11.7% and 5.3% by weight respectively. The average mass of TACP photocatalysts was ~0.5 mg, determined by measuring the mass of the substrate before and after sample preparation, averaging over five samples. Based on the mass, area of the sample and the EDX elemental analysis, the area density of TiO_2, Au, CdS and Pt in TACP were calculated as 263.68, 1.92, 37.44 and 16.96 μgcm^{-2} respectively.

Table 6.1: Mass percentages of elements in TACP 300 and TACP 320, obtained from EDX elemental analysis.

Sample	Mass percentage					
	Ti	O	Au	Cd	S	Pt
TACP 300	42.64	39.84	0.59	5.50	5.85	5.58
TACP 320	41.38	41.06	0.67	5.85	5.96	5.08

TACP 300 and TACP 320 exhibited bright structural colours (green and greenish yellow respectively), characteristic of photonic structures (**insets of Fig. 6.3 (a-b))**, indicating that the samples retained their structural order and the photonic properties after composite formation. The structural colours resulted from the SBG reflection caused by the coherent diffraction of incident light from the exposed [111] crystallographic planes of the IO *fcc* lattices[55].

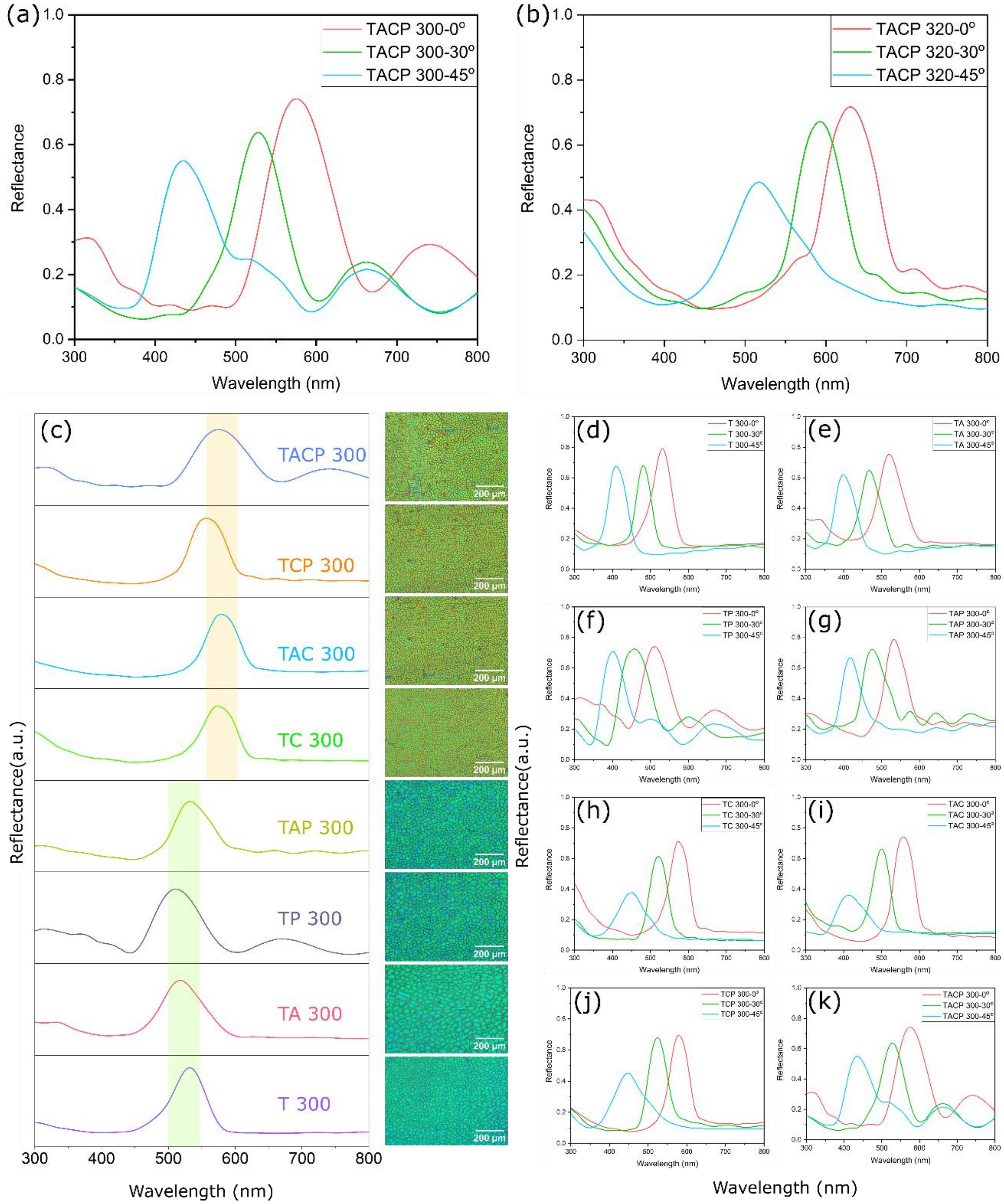

Fig. 6.5: (a-b) Specular reflectance of (a) TACP 300, (b) TACP 320 at 0°, 30° and 45° light incidence angles; **(c)** specular reflectance of samples without CdS deposition – T 300, TA 300, TP 300, TAP 300 – and those of samples with CdS deposition – TAC 300, TAP 300, TCP 300, TACP 300 – indicating the shift in the position of stop band gap (SBG) reflection with CdS deposition (abbreviations: T-TiO_2, A-Au, C-CdS, P-Pt). The corresponding optical microscope images are shown on the right adjacent to each sample. **(d-k)** Angle-resolved specular reflectance at 0°, 30° and 45° of T 300, TA 300, TP 300, TAP 300 (without CdS) and of TC 300, TAC 300, TCP 300, TACP 300 (with CdS).

Specular reflectance measurements of TACP 300 and TACP 320 at 0, 30 and 45° light incidence angles with respect to the normal of the exposed IO [111] plane **(Fig. 6.5 (a-b))**, revealed that the SBG peak position red shifted with increase in pore diameter (580-nm peak in TACP 300 to 630 nm in TACP 320 at 0° incidence angle), and blue shifted with increase in light incidence angle. This shift in SBG position with lattice parameter and light incidence angle variations, which was later employed to tune slow photon wavelengths, is consistent with the optical properties of IO photonic crystals[38], and can be estimated using Bragg's law[56]:

$$\lambda = 2 \cdot \sqrt{2/3} \cdot D \cdot \sqrt{n_{\text{matrix}}^2 \cdot f + n_{\text{void}}^2 \cdot (1-f) - n_{\text{inc}}^2 \cdot \sin^2\theta}$$

where λ is the wavelength of SBG reflection, D is the IO pore diameter, n_{matrix}, n_{void}, and n_{inc} are the RIs of matrix, void of the IO structure, and incidence medium, respectively, f and $1-f$ are their corresponding filling fractions and θ is the light incidence angle. Using the above formula, SBG positions were theoretically calculated by adopting approximations deduced in chapter IV and using the reported RIs of TiO_2 and CdS.

Table 6.2: Stop band gap positions in air and in water of TACP 300 and TACP 320 measured experimentally and calculated theoretically using modified Braggs law.

Sample	**Pore size (nm)**	**PS size (nm)**	**Shrinkage (%)**	**Stop band gap position (nm)**					
				Experimental					
				In air			**In water**		
				0°	**30°**	**45°**	**0°**	**30°**	**45°**
TACP 300	295	397	25.7	576	525	434	654	603	556
TACP 320	324	425	23.8	630	593	517	710	674	628
				Theoretical					
				In air			**In water**		
TACP 300	295	397	25.7	625	577	524	674	629	581
TACP 320	324	425	23.8	687	634	576	761	714	663

Compared with calculated SBG peaks, experimental peaks were ~50 nm lower in all samples both in air and in water **(Tables 6.2, 6.3)**, that could have resulted from the filling fraction of the matrix material being lower than the maximum of 0.26 predicted in ideal *fcc* IO structure. It was also observed from experimental measurements that SBG peak positions red-shifted by ~50 nm after CdS deposition (also reflected by the change in structural colour) but did not change significantly with Au and Pt deposition **(Fig. 6.5 (c), (d-k))**. This could be attributed to the increase in the filling fraction of the matrix material with significantly higher CdS deposition compared to those of Au and Pt NPs.

Table 6.3: Stop band gap positions in air and in water at 0° light incidence angle of T 300, TA 300, TP 300, TAP 300 (without CdS deposition) and of TC 300, TAC 300, TCP 300, TACP 300 (with CdS deposition) measured experimentally and calculated theoretically using Braggs law.

Sample	**Stop band gap position (nm)**			
	Experimental		**Theoretical**	
	In air	**In water**	**In air**	**In water**
T 300	530	610	578	654
TA 300	518	611		
TP 300	512	617		
TAP 300	532	629		
TC 300	574	663	625	714
TAC 300	577	673		
TCP 300	560	654		
TACP 300	576	654		

Ultraviolet-Visible (UV-Vis) absorption spectra of TACP 300 and TACP 320, along with those of the reference IO samples – T, TA, TC, TP, TAC, TAP and TCP 300 – are shown in **Fig. 6.6 (a)**. The spectra revealed that the absorptance range of TACP 300 and TACP 320 increased and extended into the visible range with the deposition of Au, CdS, and Pt NPs. Reference IO T sample (T 300) showed the characteristic absorption of anatase TiO_2 below 387 nm in the UV range. IO T loaded with Au NPs (TA 300) displayed absorption between 520 and 600 nm with the peak at 554 nm, characteristic of the plasmon resonance absorption of Au NPs **(Fig. 6.2 (c-d))**. The low intensity of this absorption peak was due to the low content of Au NPs in the structure (0.6%). Deposition of CdS NPs on T 300 (TC 300) and TA 300 (TAC 300) extended the absorption spectra to 514 nm relative to the narrow band gap of cubic CdS (~2.37 eV)[57, 58]. Additional modification of TAC samples with Pt NPs (TACP 300) further enhanced the absorption of the samples in the visible range. Contrary to Au NPs which exhibited a sharp SPR absorption peak, Pt NPs exhibited a broad absorption peak that extended into the visible region with no distinct peaks[59]. This can be attributed to inter-band transition of *5d* band electrons to *sp* conduction band and intra-band electronic transitions from *sp* band to *sp* conduction band[60, 61]. This is in contrast to the case of Au

NPs with predominantly intra-band transitions of *6sp* band electrons[62]. The inter-band transitions between *sp*, *d*, and hybridized bands in Pt NPs, favoured by the high density of states and high carrier concentration, resulted in an extended inter-band continuum[63], which explains the broad absorption curve that extends into the visible region.

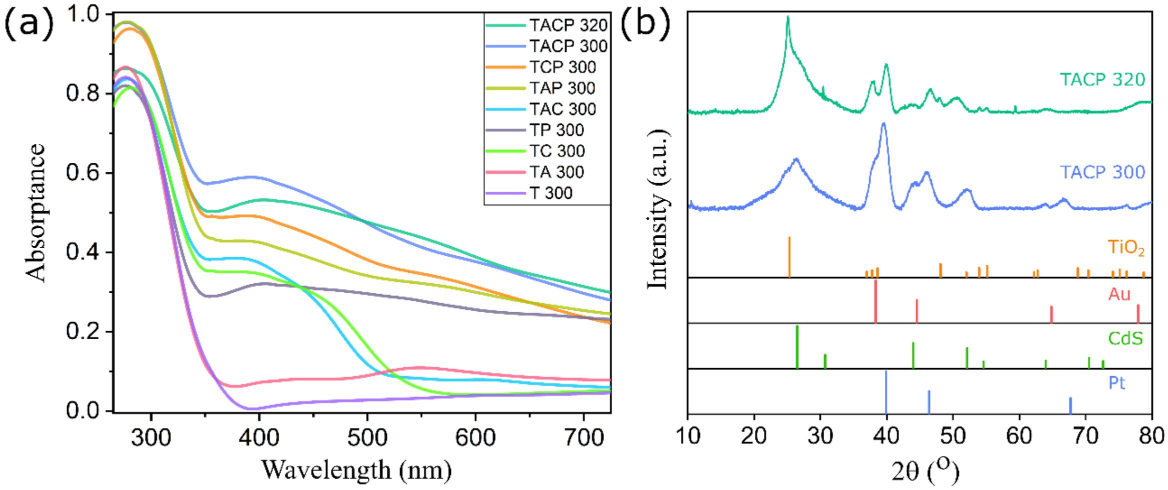

Fig. 6.6: **(a)** UV-Visible absorptance spectroscopy of IO structures T 300, TA 300, TC 300, TP 300, TAC 300, TAP 300, TCP 300, TACP 300, TACP 320 (Abbreviations: T-TiO_2, A-Au, C-CdS, P-Pt); **(b)** XRD spectra of TACP 300 and TACP 320

XRD patterns of TACP 300 and TACP 320 **(Fig. 6.6 (b))** showed distinct diffraction peaks at 2θ = 25.33° corresponding to the [101] plane of tetragonal anatase TiO_2, at 38.27° corresponding to the [111] plane of cubic crystal structure of Au NPs, at 26.82°, 31.04° and 52.81° corresponding to the [111], [200] and [311] planes of cubic Hawleyite CdS, and at 40.12° and 46.57° corresponding to the [111] and [200] planes of cubic crystal structure of Pt NPs (PDF references: TiO_2 - 153-0152, Au - 901-1613, CdS - 900-8840 and Pt - 101-1108).

XRD patterns of reference samples, TA 300, TC 300, TP 300, TAC 300, TAP 300, and TCP 300 IO structures exhibited similar diffraction peaks corresponding to the respective crystalline phases of TiO_2, Au, CdS, and Pt, as in TACP samples **(Fig. 6.7)**. The crystallite sizes of TiO_2, Au, CdS, and Pt NPs, as calculated using Scherrer equation, were 10.1 nm, 21.9 nm, 5.5 nm, and 7.2 nm in TACP 300 while they were 12.3 nm, 18.2 nm, 8.8 nm, and 9.8 nm in TACP 320 respectively. Crystallite sizes of TiO_2, Au, CdS, and Pt NPs were found to be similar across reference samples **(Table 6.4).**

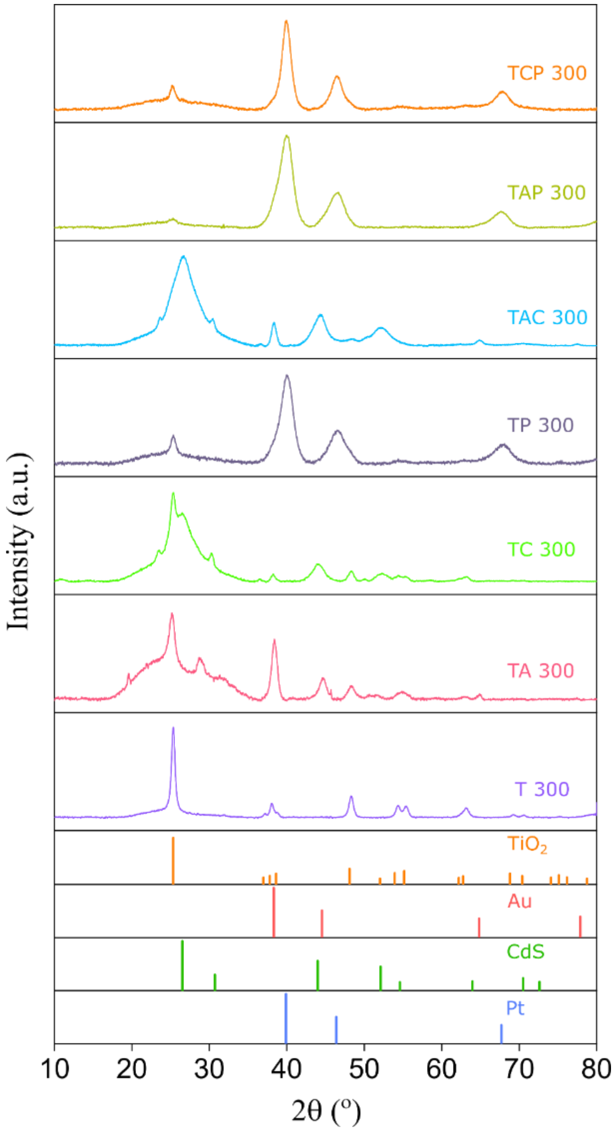

Fig. 6.7: XRD patterns of T 300, TA 300, TC 300, TP 300, TAC 300, TAP 300, TCP 300, along with the standard reference patterns of TiO_2, Au, CdS, and Pt.

Table 6.4: Crystallite sizes of TiO_2, CdS, Au, and Pt in T 300, TA 300, TC 300, TP 300, TAC 300, TAP 300, TCP 300, TACP 300 and TACP 320, as calculated using Scherrer formula.

Sample	**Crystallite size (nm)**			
	TiO_2	**Au**	**CdS**	**Pt**
T 300	10.6	x	x	x
TA 300	11.1	18.8	x	x
TC 300	13.4	x	9.3	x
TP 300	11.0	x	x	8.1

Sample	**Crystallite size (nm)**			
	TiO_2	**Au**	**CdS**	**Pt**
TAC 300	13.0	16.3	7.6	x
TAP 300	9.3	16.4	x	6.1
TCP 300	11.3	x	6.9	7.4
TACP 300	10.1	21.9	5.5	7.2
TACP 320	12.3	18.2	8.8	9.8

The low-resolution XPS full survey spectrum of TACP 300 **(Fig. 6.8 (a))** and TACP 320 **(Fig. 6.9 (a))** revealed distinct peaks pertaining to Ti, O, Cd, S, and Pt elemental (valence) states. Peaks related to Au valence states were relatively less distinct in the survey spectrum due to low concentration of Au NPs. Additional peaks of Si and C were observed which could have resulted from the substrate and the residual carbon after elimination of PS colloids respectively.

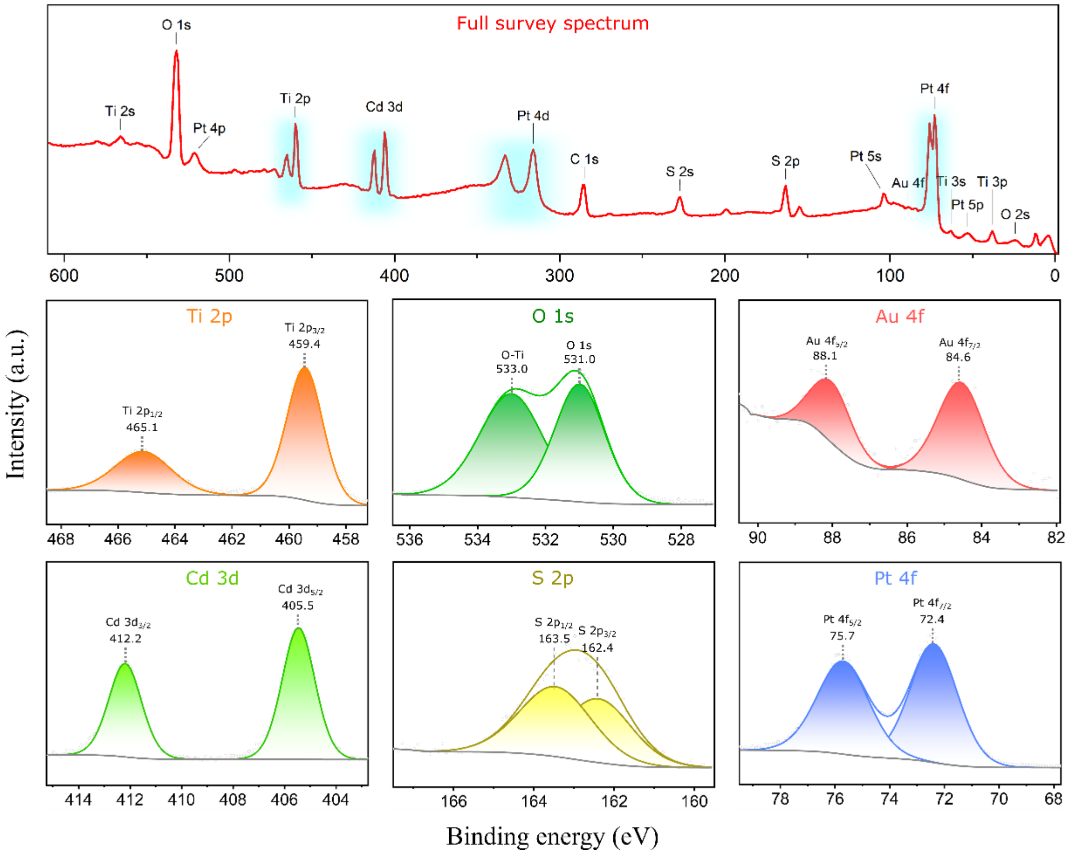

Fig. 6.8: (a) XPS survey scan at low resolution of TACP 300 and **(b-g)** core level spectra of Ti, O, Au, Cd, S, Pt at high resolution.

High resolution XPS spectrum of Ti2p **(Figs. 6.8 (b), 6.9 (b))** revealed two split spin orbit peaks corresponding to $Ti2p_{3/2}$ and $Ti2p_{1/2}$ at 459.4, 465.1 eV in TACP 300 and 459.5, 465.2 eV in TACP 320 respectively, separated by a binding energy (BE) of 5.7 eV, which are attributed to Ti^{4+} species present in tetragonal structure[64]. O1s spectrum **(Figs. 6.8 (c), 6.9 (c))** exhibited a broad peak that included a shoulder peak deconvoluted into peaks at 531.0, 533.0 eV in TACP 300 and 531.0, 533.1 eV in TACP 320, that can be attributed to lattice oxygen in TiO_2 and surface hydroxyl group in Ti-OH respectively[65]. Au4f spectrum **(Figs. 6.8 (d), 6.9 (d))** exhibited two asymmetric peaks pertaining to $Au4f_{7/2}$ and $Au4f_{5/2}$ at 84.6, 88.1 eV in both TACP 300 and TACP 320, which confirmed the presence of Au in metallic state. Cd3d spectrum of **(Figs. 6.8 (e), 6.9 (e))** displayed well separated split spin orbit peaks corresponding to Cd3d$_{5/2}$ and Cd3d$_{3/2}$ at 405.7, 412.6 eV in TACP 300 and 405.9, 412.6 eV in TACP 320, with a spin orbit separation of ~6.8 eV that indicated the presence of Cd^{2+} in CdS. High resolution spectrum of S2p **(Figs. 6.8 (f), 6.9 (f))** revealed a broad peak that was deconvoluted into two spin orbit peaks pertaining to S2p$_{3/2}$ and S2p$_{1/2}$ at 162.4, 163.5 eV in TACP 300 and 162.7, 163.5 eV in TACP 320, indicating the presence of S^{2-} in CdS. The spectrum of Pt4f **(Figs. 6.8 (g), 6.9 (g))** revealed two distinct spin orbit peaks pertaining to Pt4f$_{7/2}$ and Pt4f$_{5/2}$ at 72.4, 75.7 eV in both TACP 300 and TACP 320, which confirmed the presence of Pt in metallic state. XPS spectra of reference samples displayed the corresponding peaks at identical binding energy values, as shown in **Figs. 6.10-6.16**.

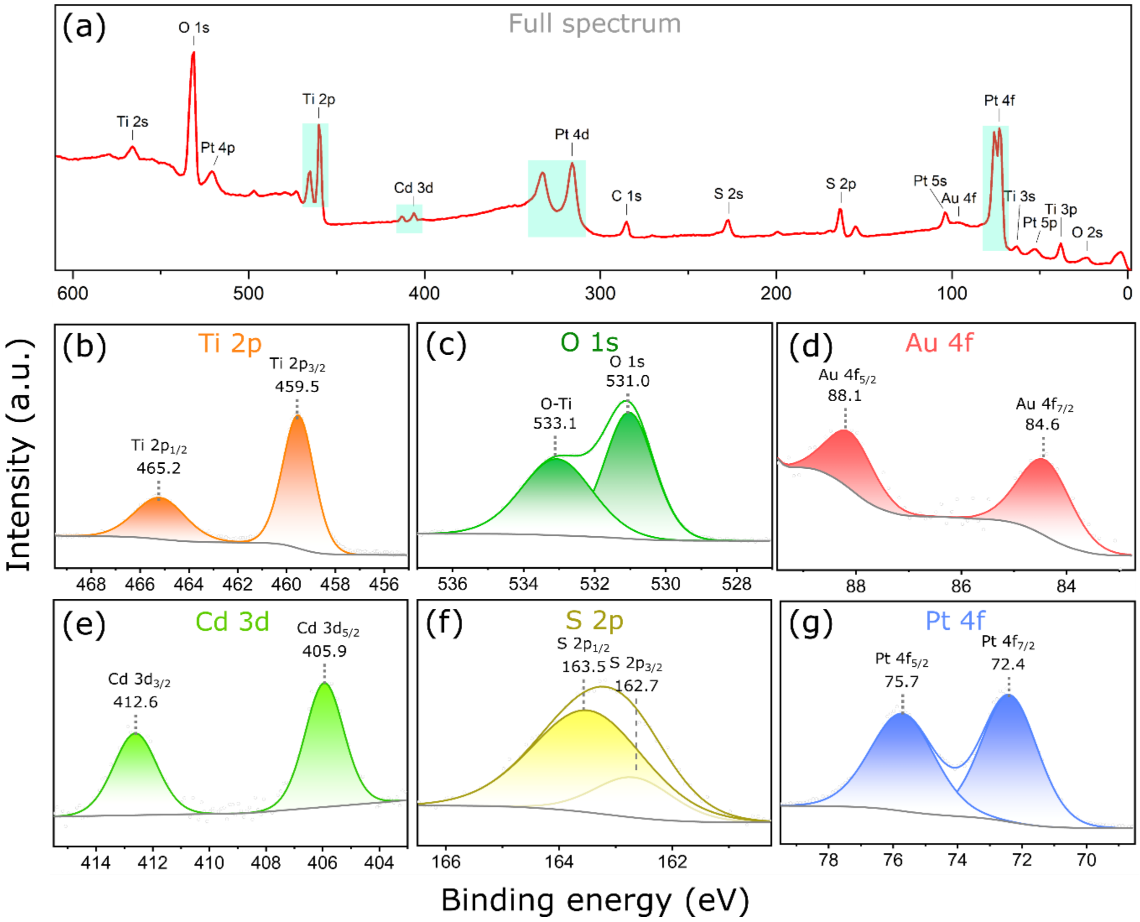

Fig. 6.9: (a) XPS survey scan at low resolution of TACP 320 and **(b-g)** core level spectra of Ti, O, Au, Cd, S, Pt at high resolution.

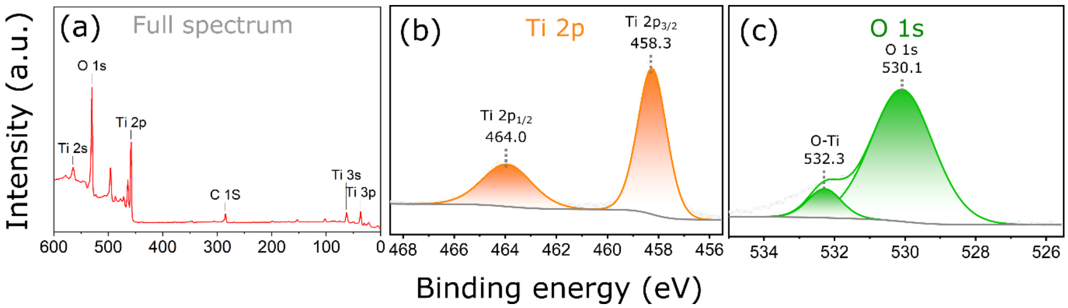

Fig. 6.10: (a) XPS survey scan at low resolution of T 300 and **(b-c)** core level spectra of Ti, O at high resolution.

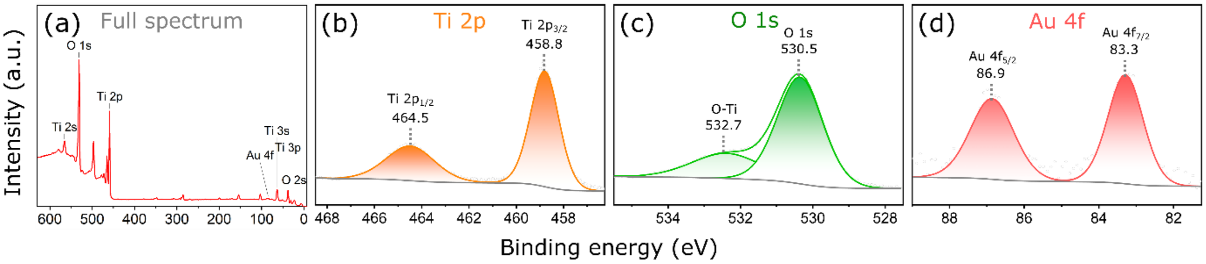

Fig. 6.11: (a) XPS survey scan at low resolution of TA 300 and **(b-d)** core level spectra of Ti, O, Au at high resolution.

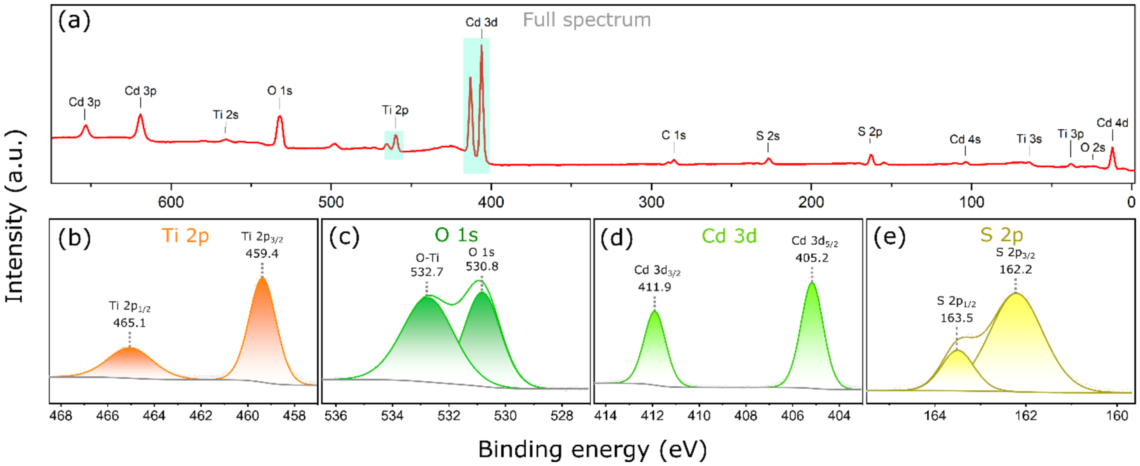

Fig. 6.12: (a) XPS survey scan at low resolution of TC 300 and **(b-e)** core level spectra of Ti, O, Cd, S at high resolution.

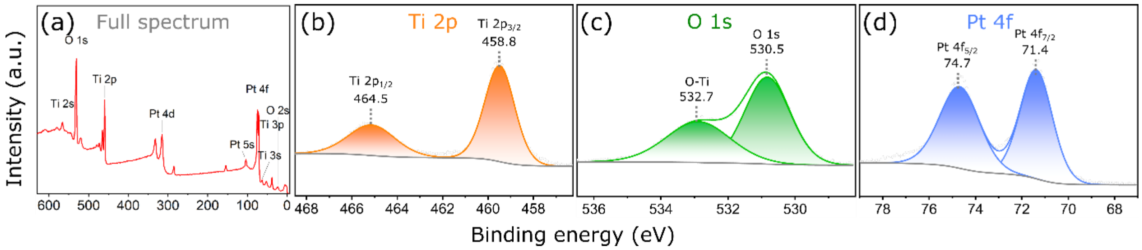

Fig. 6.13: (a) XPS survey scan at low resolution of TP 300 and **(b-d)** core level spectra of Ti, O, Pt at high resolution.

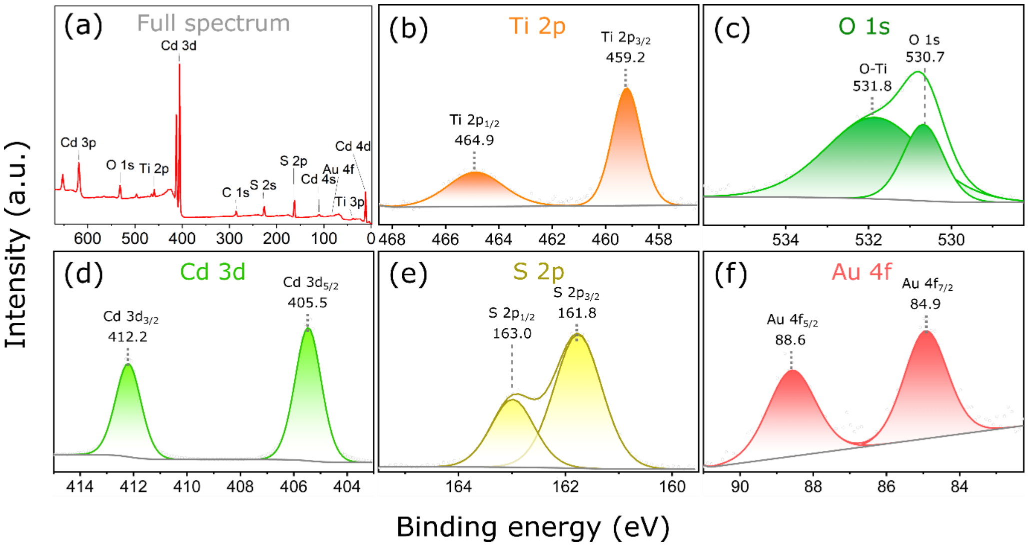

Fig. 6.14: (a) XPS survey scan at low resolution of TAC 300 and **(b-f)** core level spectra of Ti, O, Cd, S, Au at high resolution.

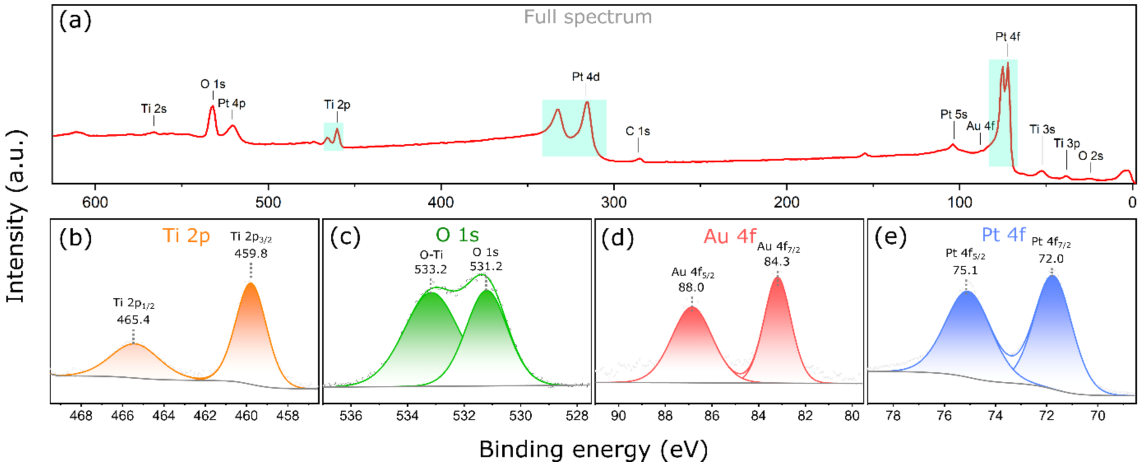

Fig. 6.15: (a) XPS survey scan at low resolution of TAP 300 and **(b-e)** core level spectra of Ti, O, Au, Pt at high resolution.

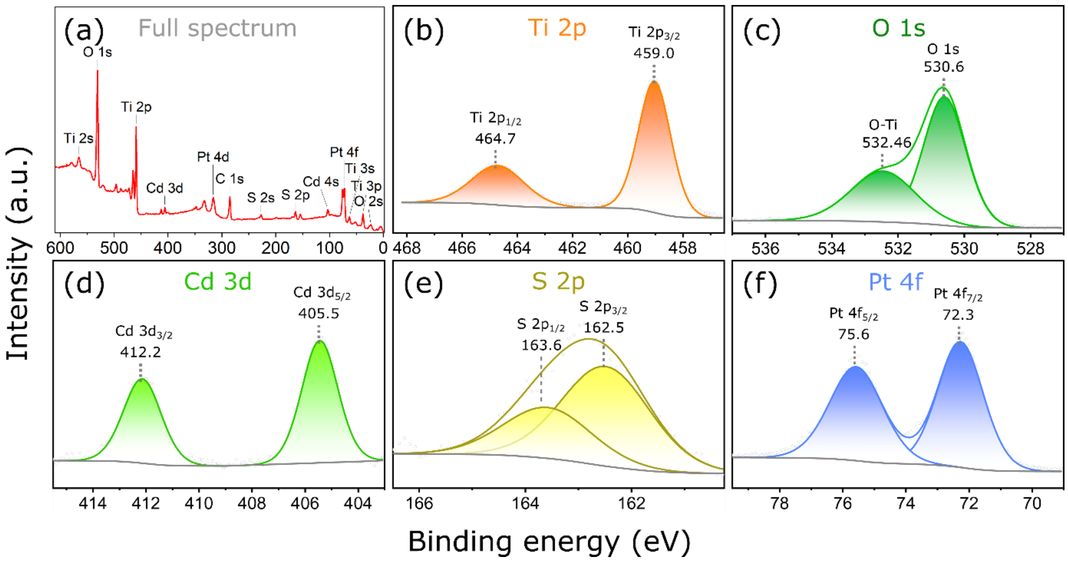

Fig. 6.16: (a) XPS survey scan at low resolution of TCP 300 and **(b-f)** core level spectra of Ti, O, Cd, S, Pt at high resolution.

Photoluminescence (PL) spectra were taken to study the separation of photogenerated electron-hole pairs and the plausible charge transfer dynamics. As shown in **Fig. 6.17 (a)**, all the samples had a similar emission band from ~350-500 nm after being excited over a wavelength of 320 nm.

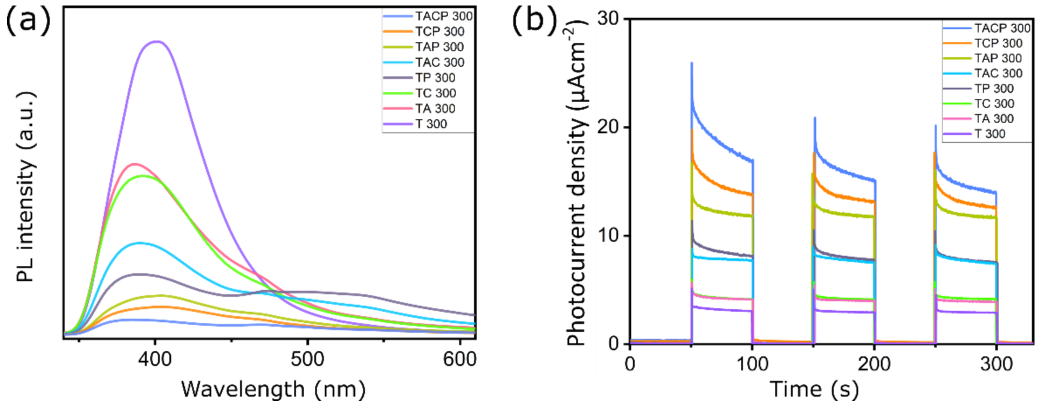

Fig. 6.17: **(a)** Photoluminescence spectra and **(b)** transient photocurrent of T 300, TA 300, TC 300, TP 300, TAC 300, TAP 300, TCP 300, TACP 300 (abbreviations: T-TiO_2, A-Au, C-CdS, P-Pt).

Among all the samples, IO T 300 displayed the highest PL emission intensity, indicating the highest photogenerated charge recombination in TiO_2 that is detrimental to photocatalytic activity[66]. For IO TA 300, a steep dip in PL intensity was observed compared to IO T, which could be attributed to Au NPs serving as a photosensitizer through the localized surface plasmon resonance (LSPR)-induced hot electron transfer[67] that reduces charge recombination. A similar dip in PL intensity was observed in the case of IO TC 300, which could be attributed to the Z-scheme heterojunction between TiO_2 and CdS[68] that promoted efficient charge separation. Compared to the above two samples, IO TP 300 showed a much lower PL intensity, due to the Schottky barrier formed by Pt NPs that resulted in better photogenerated charge separation[69, 70]. This was observed to be lower than that of the combined effect of Au and CdS NPs in TAC 300, probably due to the higher content and the higher efficiency of Pt NPs in charge separation. The PL intensity of TACP 300 was the least among all the samples due to the combined effects of Au, CdS, and Pt NPs in charge separation.

The dynamics of electron-hole pair separation and migration was further investigated by measuring the transient photocurrent response of the samples. As shown in **Fig. 6.17 (b)**, IO TACP 300 exhibited the highest photocurrent density among all the samples, owing to the hot electron transfer from Au NPs, z-scheme heterojunction-assisted charge separation assisted by CdS NPs, and electron transfer mediation offered by Pt NPs. Both photoluminescence and photocurrent measurements confirmed a higher and more efficient charge separation in TACP compared to that in reference samples.

Photocatalytic H_2 production was evaluated in the presence of 0.1 M Na_2S and 0.1 M Na_2SO_3 sacrificial agents, under a 300 W Xenon light source emitting a spectral range of 320-780 nm. Initially, the effect of modifying IO T with Au, CdS, and Pt NPs on photocatalytic H_2 evolution was investigated. H_2 evolved over each photocatalyst is shown in terms of mmol evolved **(Fig. 6.18 (a))**, mmol$h^{-1}g^{-1}$ **(Fig. 6.18 (c))**, and mmol$h^{-1}cm^{-2}$ **(Fig. 6.18 (c))**.

H_2 evolution was observed to be the highest over quaternary IO TACP photocatalysts (103.96 mmol h^{-1} g^{-1} over TACP 300 and 91.29 mmol h^{-1} g^{-1} over TACP 320) among pristine IO T, binary IO TA, TC, TP photocatalysts and ternary TAC, TAP, TCP photocatalyst systems **(Fig. 6.18 (a, c-d) and Tables 6.5-6.6)**. Also, it was observed that all ternary photocatalysts showed higher H_2 evolution than binary photocatalysts, which were in turn higher than that of pristine IO T. The effect of slow photons in each of the above photocatalysts towards photocatalytic H_2 evolution was studied by correlating the photocatalytic activity with the corresponding spectral positions of slow photons in aqueous medium, indicated by blue and red shades at either edge of their SBGs in **Fig. 6.18 (b)**, with respect to CdS electronic absorption, indicated by yellow shade and Au plasmon resonance absorption, indicated by purple shade.

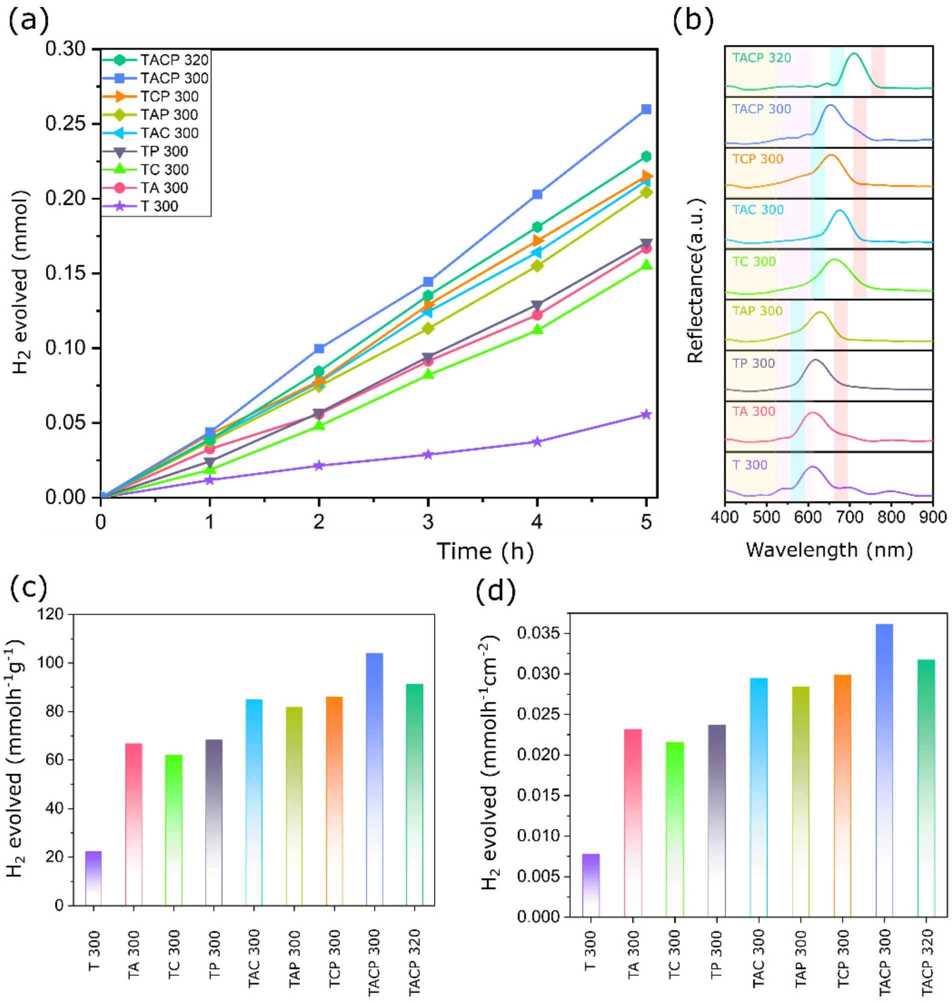

Fig. 6.18: **(a)** H_2 evolution in mmol over T 300, TA 300, TC 300, TP 300, TAC 300, TAP 300, TCP 300, TACP 300, TACP 320; **(b)** Specular reflectance spectra of the samples in water - representation: yellow region - CdS electronic absorption, purple region - Au plasmon resonance absorption, blue shade - blue edge slow photons, red shade - red edge slow photons; **(c-d)** H_2 evolution over the same samples in (c) mmolh^{-1}g^{-1} and (d) mmolh^{-1}cm^{-2}.

Table 6.5: H_2 evolved in mmol after each hour over T 300, TA 300, TC 300, TP 300, TAC 300, TAP 300, TCP 300, TACP 300 and TACP 320.

Time (h)	H_2 evolved (mmol)								
	T 300	TA 300	TC 300	TP 300	TAC 300	TAP 300	TCP 300	TACP 300	TACP 320
0	0.0000	0.0000	0.0000	0.0000	0.0000	0.0000	0.0000	0.0000	0.0000
1	0.0118	0.0326	0.0187	0.0243	0.0392	0.0375	0.0425	0.0438	0.0389
2	0.0214	0.0559	0.0479	0.0568	0.0772	0.0746	0.0780	0.0997	0.0846
3	0.0288	0.0914	0.0820	0.0943	0.1243	0.1132	0.1291	0.1444	0.1352
4	0.0374	0.1222	0.1119	0.1292	0.1642	0.1551	0.1719	0.2029	0.1811
5	0.0557	0.1668	0.1552	0.1706	0.2121	0.2043	0.2151	0.2599	0.2282

Table 6.6: H_2 evolved represented in mmol h^{-1}, mmol h^{-1} g^{-1} and mmol h^{-1} cm^{-2} over T 300, TA 300, TC 300, TP 300, TAC 300, TAP 300, TCP 300, TACP 300 and TACP 320

Photocatalyst	**H_2 evolved**		
	mmol h^{-1}	**mmol h^{-1} g^{-1}**	**mmol h^{-1} cm^{-2}**
T 300	0.0111	22.267	0.0077
TA 300	0.0334	66.713	0.0232
TC 300	0.0310	62.085	0.0216
TP 300	0.0341	68.241	0.0237
TAC 300	0.0424	84.832	0.0295
TAP 300	0.0409	81.732	0.0284
TCP 300	0.0430	86.055	0.0299
TACP 300	0.0520	103.956	0.0361
TACP 320	0.0456	91.294	0.0317

IO T loaded *in situ* with Au NPs (TA 300) showed a sharp 3-fold increase in H_2 evolution (66.71 mmol h^{-1} g^{-1}) compared to that of pristine IO T (22.27 mmol h^{-1} g^{-1}) **(Fig. 6.18 (a, c))**. This increase, despite a very low Au content of 0.6%, can be attributed to the synergy between slow photon effect (SPE) and surface plasmon resonance (SPR). As seen in **Fig. 6.18 (b)**, blue edge slow photons of TA 300 overlapped with the plasmon resonance absorption peak of Au NPs. This could have resulted in enhancement of SPR by the reduced group velocity of light, contributing towards increased light harvesting in the visible range and towards increased 'hot electron' generation that favoured charge separation and transfer efficiency. In pristine IO T 300, on the other hand, slow photons located in the visible range could not be efficiently utilized by TiO_2, the absorption of which lies in the UV range. IO T loaded with CdS NPs (TC 300) showed a slightly lower enhancement factor for H_2 evolution (2.8-fold) compared to that over TA 300. In this case, slow photons, which were located at spectral ranges far away (> 600 nm) from CdS absorption (< 514 nm), as shown in **Fig. 6.18 (b)**, could not be utilized for improving light absorption. However, the extension of light absorption to the visible range by CdS and the formation of z-scheme heterojunction between TiO_2 and CdS that assisted in charge separation, could have contributed to the enhancement. IO T loaded with Pt NPs (TP 300) showed a high H_2 evolution (68.24 mmol h^{-1} g^{-1}), which is similar to that over TA 300 **(Fig. 6.18 (c))**. Despite slow photons not being utilized in this case, the higher Pt content at 5.58% and its efficiency as a cocatalyst with high work function, high redox potential, and favourable Fermi level for accepting photogenerated electrons to provide active sites for proton reduction, could have contributed to higher H_2 evolution.

Compared to the binary photocatalysts (TA 300, TC 300, TP 300), all ternary photocatalysts (TAP 300, TAC 300, TCP 300) showed higher photocatalytic H_2 evolution **(Fig. 6.18 (a, c))** due to synergistic effects. A noteworthy observation among the activity of the ternary photocatalysts is the slightly lower H_2 evolution over TAP 300 (81.73 mmol h^{-1} g^{-1}) compared to those over TAC 300 (84.83 mmol$h^{-1}g^{-1}$) and TCP 300 (86.10 mmol h^{-1} g^{-1}), despite the utilization of slow photons to enhance Au plasmon resonance **(Fig. 6.18 (c))**. In TAP 300, blue-edge slow-photon spectral region overlapped with the plasmon-resonance absorption peak of Au NPs whereas in TAC 300 and TCP 300, due to the loading of CdS NPs, SBG peaks red shifted placing the blue-edge slow photons to the far edge of the plasmon resonance region **(Fig. 6.18 (b))**. This highlights the importance of CdS photocatalyst in the system that offers the significant advantages of efficient charge transfer pathway and favourable band gap positions required for redox reactions in H_2 evolution. Also, as noted in HR-TEM images and EDX analysis **(Fig. 6.3 (h))**, CdS was homogeneously deposited at a higher loading of 11.4% that assisted in better charge separation.

H_2 evolution over TACP photocatalyst was further enhanced by tuning slow photons to both CdS and Au absorption by varying lattice parameter (pore diameter) and light incidence angle. Lattice parameter variation was investigated by comparing the activities of two TACP samples with different pore sizes (TACP 300 and TACP 320), while incidence angle variation was probed by comparing the activity of the same TACP sample at three different light incidence angles (0, 30 and 45°). The results of H_2 evolution in these two photocatalyst systems at different angles are shown in **Fig. 6.19**. and in **Tables 6.7-6.8**.

Table 6.7: H_2 evolved in mmol after each hour over TACP 300 and TACP 320 at 0°, 30° and 45° light incidence angles.

Time (h)	**H_2 evolved (mmol)**					
	TACP 300			**TACP 320**		
	0°	**30°**	**45°**	**0°**	**30°**	**45°**
0	0.0000	0.0000	0.0000	0.0000	0.0000	0.0000
1	0.0438	0.0455	0.0615	0.0389	0.0356	0.0488
2	0.0997	0.1134	0.1446	0.0846	0.0859	0.0925
3	0.1444	0.1969	0.2516	0.1352	0.1275	0.1431
4	0.2029	0.2834	0.3469	0.1811	0.1753	0.1967
5	0.2599	0.3726	0.4329	0.2282	0.2285	0.2562

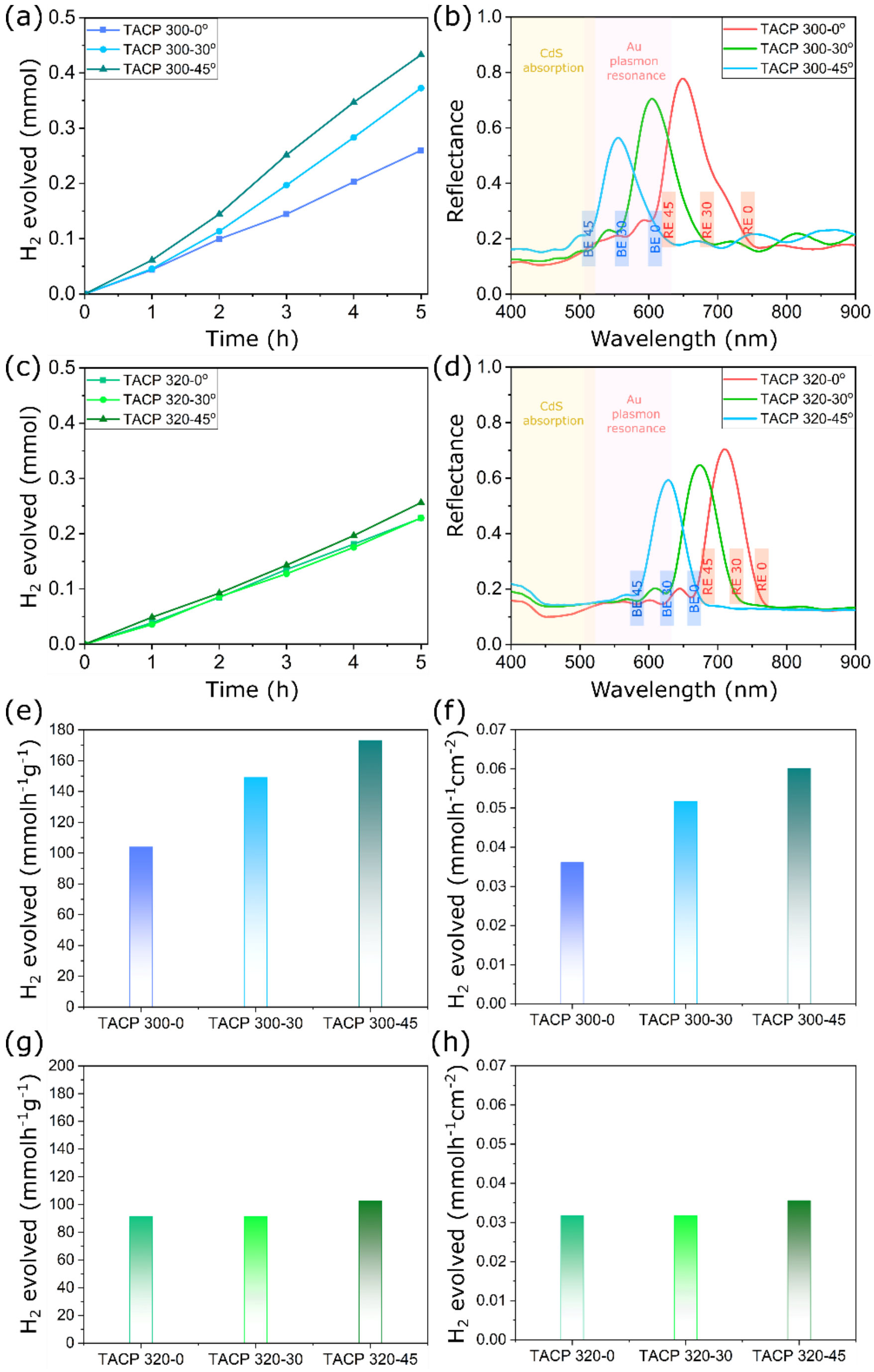

Fig. 6.19: **(a)** H_2 evolution in mmol over TACP 300 at 0°, 30° and 45° incidence angles and **(b)** its angle-resolved reflectance spectra in water; **(c)** H_2 evolution in mmol over TACP 320 at 0°, 30° and 45° incidence angles and **(d)** its angle-resolved reflectance spectra in water, (representation of shades: yellow – CdS absorption, purple – Au plasmon resonance, blue – blue-edge slow photons, red – red-edge slow photons); **(e-f)** H_2 evolution over TACP 300 at 0°, 30° and 45° incidence angles in (e) $mmolh^{-1}g^{-1}$ and (f) $mmomh^{-1}cm^{-2}$; **(g-h)** H_2 evolution over TACP 320 at 0°, 30° and 45° incidence angles in (g) $mmolh^{-1}g^{-1}$ and (h) $mmolh^{-1}cm^{-2}$.

Table 6.8: H_2 evolved represented in mmol h^{-1}, mmol h^{-1} g^{-1} and mmol h^{-1} cm^{-2} over TACP 300 and TACP 320 at 0°, 30° and 45° light incidence angles.

Photocatalyst	**H_2 evolved**		
	mmol h^{-1}	**mmol h^{-1} g^{-1}**	**mmol h^{-1} cm^{-2}**
TACP 300-0°	0.0520	103.956	0.0361
TACP 300-30°	0.0745	149.057	0.0518
TACP 300-45°	0.0866	173.158	0.0601
TACP 320-0°	0.0456	91.294	0.0317
TACP 320-30°	0.0457	91.381	0.0317
TACP 320-45°	0.0512	102.471	0.0356

A significant difference in H_2 evolution was observed between TACP 300 (103.96 mmol h^{-1} g^{-1}) and TACP 320 (91.29 mmol h^{-1} g^{-1}) **(Fig. 6.19 (a, c, e-h), Tables 6.7-6.8)**. In the case of TACP 300, at normal incidence, blue edge slow photon spectral region falls within the Au plasmon absorption region at the far edge as seen in **Fig. 6.19 (b)** (BE 0 blue shade overlapping with the purple shade corresponding to Au absorption). This overlap could result in the slow photons in TACP 300 further enhancing the plasmon resonance of Au NPs. In the case of TACP 320, at normal incidence, blue edge slow photons were located away from Au plasmon absorption region as seen in **Fig. 6.19 (d)** (BE 0 blue shade), which implies that slow photons could not be harvested to improve light absorption.

In the above cases, with lattice parameter variation, slow photons were tuned only to the plasmon resonance of Au NPs, but they were still located far away from CdS absorption region (< 514 nm). Hence, to utilize slow photons optimally, their frequencies were further tuned by light incidence angle variation. It was observed that in the case of TACP 300, H_2 evolution increased from 103.96 mmol h^{-1} g^{-1} to 173.16 mmol h^{-1} g^{-1}, when the incidence angle increased from 0 to 45° **(Fig. 6.19 (e), Table 6.8)**. This marked increase can be explained from angle-resolved reflectance measurements in aqueous medium **Fig. 6.19 (b)**. It was observed that blue edge slow photons, located at the far edge of Au plasmon absorption at 0° incidence angle, were blue shifted to overlap with Au plasmon absorption peak at 30° incidence angle. The increased synergy between SPE and SPR resulted in an increase of H_2 evolution from 103.96 mmol h^{-1} g^{-1} to 149.06 mmol h^{-1} g^{-1}. When incidence angle was increased to 45°, slow photon wavelengths further blue shifted such that blue edge slow photon spectral region overlapped with both CdS absorption and Au surface plasmon absorption while that of red edge slow photons overlapped with the far edge of Au plasmon absorption. H_2 evolution in this case was 173.16 mmol h^{-1} g^{-1}, 1.67 times higher than that of the same sample at 0° incidence angle where there was limited slow photon assistance, and 1.90 times higher than that of TACP 320 at 0° incidence angle where there was no slow photon assistance.

Angle-dependency of H_2 evolution was also evaluated over TACP 320 photocatalyst system. The difference in H_2 evolution observed in this case was minimum **(Fig. 6.19 (c, g-h)**. This can be justified by the spectral positions of slow photons at different angles **(Fig. 6.19 (d))**. At 0 and 30° incidence angles, slow photons at blue and red edges were far away from both CdS and Au absorption ranges. Slow photons, although present, could not be utilized for improving CdS absorption or enhancing Au plasmon resonance. H_2 evolution at these angles was 91.29 mmol h^{-1} g^{-1} and 91.38 mmol h^{-1} g^{-1}, respectively. At 45° incidence angle, blue edge slow photon spectral region overlapped with the plasmon resonance absorption region of Au NPs, which resulted in H_2 evolution being slightly increased to 102.47 mmol h^{-1} g^{-1} due to slow photon-assisted enhancement of surface plasmon absorption.

Comparison of photocatalytic H_2 evolution was also done after normalizing the activities based on change in optical path length with change in light incidence angle. The calculations were similar to those done in chapters IV and V. The difference was that the effective refractive index was 1.596 in this case, while the optical path length at normal incidence (thickness of sample) was 1.2 µm. Normalization based on specific surface area was not done in this work as the comparison was made only between IO samples and not with compact films. The data showing the comparison of normalized activities for TACP 300 and TACP 320 at different light incidence angles is presented in **Table 6. 9** and depicted in **Fig. 6. 20**.

Table 6.9: Normalized photocatalytic H_2 evolution over TACP 300 and TACP 320 at different light incidence angles based on the change in optical path length with incidence angle.

Photocatalyst	**H_2 evolved (mmol h^{-1} g^{-1})**				**Normalized with path length**		
	0°	**30°**	**45°**		**0°**	**30°**	**45°**
TACP 300	103.96	149.06	173.16		103.96	141.79	157.11
TACP 320	85.50	91.38	102.47		85.50	86.93	92.97

Based on the normalized data, it was observed that the trends in photocatalytic H_2 evolution remained the same after normalization, while the enhancement factors were relatively minimized. In the case of TACP 300, with increase in light incidence angle from 0° to 45°, the enhancement factor which was 1.66 decreased to 1.51 after normalization with optical path length. Similarly, the activity of TACP 300 at 45° light incidence angle (slow light utilized by both CdS and Au NPs), which was 2.02 times higher than that of TACP 320 at 0° light incidence angle, was reduced to an EF of 1.84 after normalization.

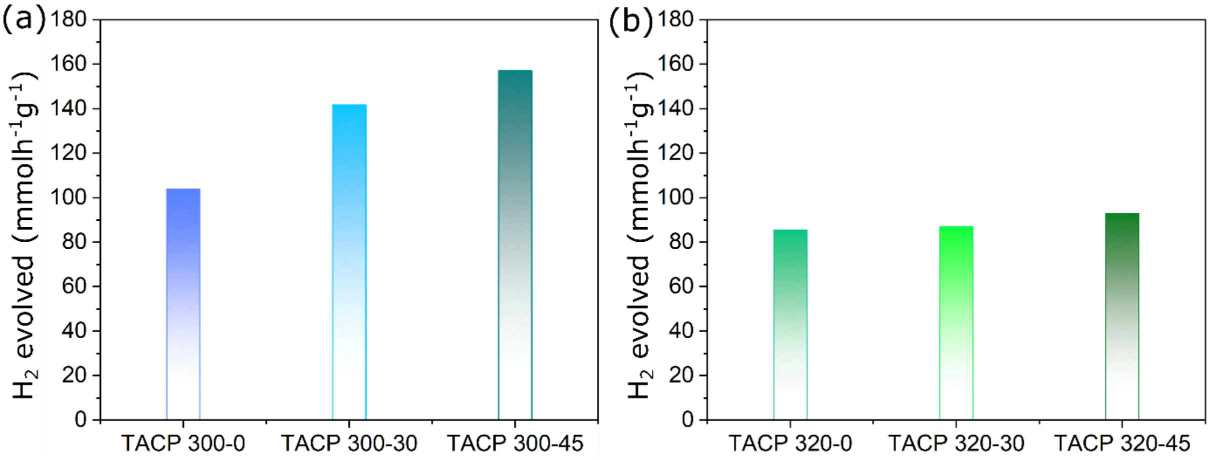

Fig. 6.20: Normalized photocatalytic H_2 evolution over **(a)** TACP 300 and **(b)** TACP 320 at different light incidence angles based on the change in optical path length with incidence angle

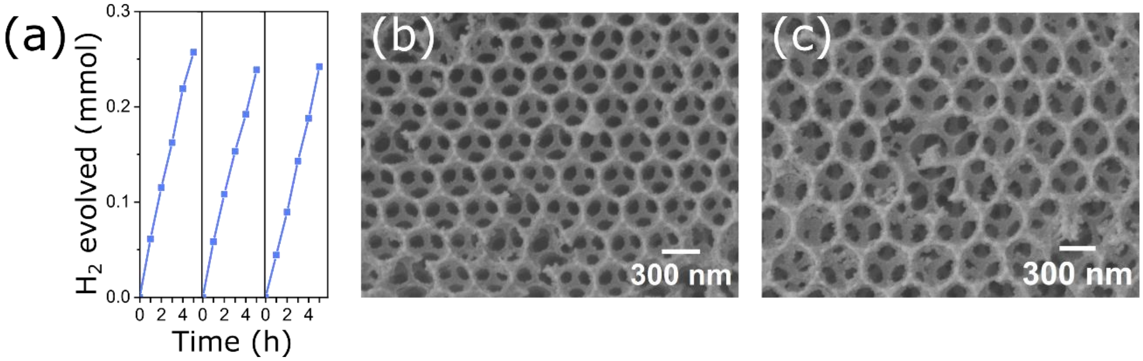

Fig. 6.21: (a) Repeatability tests for H_2 evolution over TACP 300 at 0° incidence angle for 3 cycles; **(b-c)** SEM images after H_2 evolution tests of (b) TACP 300 and (c) TACP 320.

Repeatability tests were conducted over TACP 300 at 0° incidence angle for three cycles (after it was tested at three different angles). The difference in H_2 evolution in the repeated cycles was insignificant, as shown in **Fig. 6.21 (a)**. SEM images of TACP 300 and TACP 320 taken after photocatalysis **(Fig. 6.21 (b-c))** revealed that there was very little structural damage in the IO structure after photocatalysis.

Photocorrosion is acknowledged to be one of the common problems faced while using CdS photocatalyst[71]. This could lead to the degradation and loss of the photocatalyst resulting in a reduced efficiency in H_2 evolution over time. Hence, photocorrosion of CdS was studied by XPS analysis of the photocatalyst after photocatalytic H_2 evolution experiments. Photocorrosion mechanism of CdS is usually attributed to the photogenerated holes that accumulate on the surface of sulfides[72]. When CdS is irradiated with visible light, electrons from CB are excited to VB generating photoexcited electrons and holes. Photoexcited electrons are transferred to the surface of the photocatalyst while the holes are concentrated on the outer surface of the sulfide ions. Resultantly, sulfide ions are oxidized to either elemental sulfur and/or sulfate. Meanwhile, Cd^{2+} ions are either leached into the solution[73] or converted into Cd^0 elemental state[74], resulting in a gradual loss of photocatalyst. The reactions involved are presented below:

$CdS + h\nu \rightarrow e^- + h^+$

$CdS + 2h^+ \rightarrow Cd^{2+} + S$

$CdS + 4h^+ + 2H_2O + O_2 \rightarrow Cd^{2+} + SO_4^{2-} + 4H^+$

$O_2 + 4e^- + 2H^+ \rightarrow 2OH^-$

$CdS + 2O_2 \rightarrow Cd^{2+} + SO_4^{2-}$

$Cd^{2+} + 2e^- \rightarrow Cd$

To determine the extent of CdS photocorrosion in our experiments, XPS analysis was conducted on TACP 300 after six cycles of photocatalytic tests. The high-resolution spectra of Ti 2p, O 1s, Au 4f, Cd 3d, S 2p, and Pt 4f are presented in **Fig. 6.22**. No significant change in binding energy peak positions was observed in the case of Ti 2p, O 1s, Au 4f, and Pt 4f. The low-resolution spectrum of Cd 3d showed peaks at nearly identical positions to those in the spectrum of unused photocatalyst. This confirmed that Cd^{2+} was not reduced to Cd^0 after photocatalysis. However, a slight reduction in the peak intensity was observed, which led us to the hypothesis that Cd^{2+} ions would have partially leached into the solution during photocatalysis. The low-resolution spectrum of S 2p provided further insights into the changes in CdS during photocatalysis. In addition to the two S 2p spin orbit peaks corresponding to S^{2-} in CdS (deconvoluted into S $2p_{3/2}$ and S $2p_{1/2}$ at 162.9 eV and 164.1 eV respectively), two additional peaks at 169.7 eV and 167.1 eV were observed. The peak at 169.7 eV is attributed to the S^{6+} valence state in SO_4^{2-} formed as a result of photocorrosion[75]. The formation of S^0 state however could not be ascertained as the peak pertaining to S^0 $2p_{3/2}$ between 163 eV and 164 eV is indistinguishable from those of S^{2-} 2p. The peak at 167.1 eV can be attributed to S4+ valence state in SO_3^{2-} ions. In this work, Na_2S + Na_2SO_3 sacrificial agents were used as hole scavengers for photocatalytic H_2 evolution. This could have resulted in a small amount of SO_3^{2-} ions remaining adsorbed on the surface despite rinsing the photocatalyst several times with deionized water.

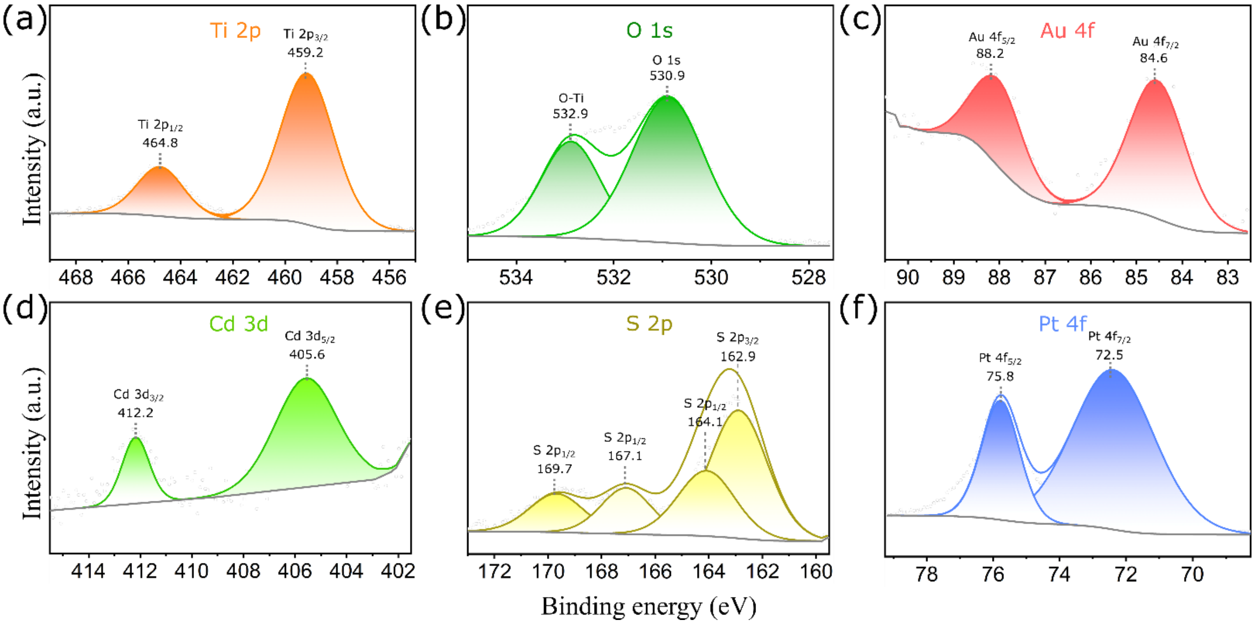

Fig. 6.22: High-resolution XPS spectra of **(a)** Ti 2p, **(b)** O 1s, **(c)** Au 4f, **(d)** Cd 3d, **(e)** S 2p, and **(f)** Pt 4f after photocatalytic H_2 evolution tests

To have an estimate of the different valence states, the peaks were quantified. It was observed that peaks pertaining to S^{2-} constituted 83.3% while those pertaining to S^{6+} and S^{4+} in SO_4^{2-} and SO_3^{2-} constituted 7.9% and 8.8% respectively. This indicated that photocorrosion of CdS, although present, was significantly low, which explains the retention of stable photocatalytic H_2 evolution evidenced in recyclability and repeatability tests **(Fig. 6.21)**. The low extent of CdS photocorrosion can be explained based on two factors: (i) the presence of hole-scavenging sacrificial agents reduces the availability of photogenerated holes for CdS photocorrosion[75], (ii) the heterojunction formed between CdS and TiO_2, Au, Pt facilitates a more efficient charge transfer that minimizes the accumulation of photogenerated holes on the surface of sulphide ions and inhibits CdS photocorrosion[72].

Table 6.10: H_2 evolved in inverse opal photocatalyst systems reported in comparison with that in the present work (*p* stands for particulate photocatalyst, *f* stands for photocatalyst film).

IO Photocatalyst system	Max. H_2 evolution	Light source	Sacrificial agent	Ref.
TiO_2-Pt - *p*	24.7 mmol h^{-1} g^{-1}	500-W Xe lamp < 400 nm	CH_3OH	79
TiO_2-Au-(Pd) - *p*	0.12 mmol h^{-1} g^{-1}	100-W UV lamp 1.2 mWcm^{-2}	C_2H_5OH	83
WO_3-CdS-Au - *p*	1.73 mmol h^{-1} g^{-1}	300-W Xe ≥ 420 nm	Na_2S+ Na_2SO_3	77
TiO_2-Pt - *p*	6.0 mmol h^{-1} g^{-1}	9-W UV light 365 nm	HCOOH+ HCOONa	81
TiO_2-Au-CdS - *p*	2.28 mmol h^{-1} g^{-1}	UV+Visible, 250-780 nm 34+158 mWcm^{-2}	Na_2S+ Na_2SO_3	40
$SrTiO_3$-Pt - *p*	3.599 mmol h^{-1} g^{-1}	300-W Xe lamp	CH_3OH	84
$SrTiO_3$-Au-CdS-Pt - *p*	5.46 mmol h^{-1} g^{-1}	300-W Xe > 420 nm	Na_2S+ Na_2SO_3	44
TiO_2-Au-CdS - *p*	3.5 mmol h^{-1} g^{-1}	Visible 158 mWcm^{-2} ≥ 420 nm	Na_2S+ Na_2SO_3	64
$TiO_2(Ti^{3+})$-Au-Pt - *p*	181.77 mmol h^{-1} g^{-1}	200-W Hg/Xe lamp, 350-700 nm, 100-150 mWcm^{-2}	C_2H_5OH	80
TiO_2-CuO - *p*	1.2 mmol h^{-1} g^{-1}	100-W Hg lamp (UV)	C_2H_5OH	78
TiO_2-$BiVO_4$ - *p*	1.64 mmol h^{-1} g^{-1}	100-W Hg lamp (UV)	C_2H_5OH	78
TiO_2-Ag - *f*	0.0329 mmol h^{-1} cm^{-2}	300-W Xe arc lamp 100 mWcm^{-2}	-NO-	82
TiO_2-Au-CdS-Pt - *f*	**0.0601 mmol h^{-1} cm^{-2}** **173.158 mmol h^{-1} g^{-1}**	**300-W Xe lamp 320-780 nm**	**Na_2S+ Na_2SO_3**	**This work**

Finally, we compared these results over IO TACP photocatalyst film with previously reported results of H_2 evolution over IO photocatalyst systems[40, 44, 64, 76-84], although comparisons are inadequate due to the differences in photocatalytic conditions and materials. Firstly, we found no reports of this quaternary photocatalyst system used for H_2 evolution, and secondly, we found that in most of the reports, IO particulate systems were used for photocatalytic H_2 evolution instead of films. Despite the difficulties in comparing results, we observed that this photocatalyst system with optimal slow-photon utilization in IO TACP photonic film was one among the best for H_2 evolution **(Table 6.10)**.

6.4. Summary

To conclude, we propose a novel approach to derive maximum benefit from slow photons in an inverse opal TiO_2-Au-CdS-Pt photocatalyst system. Multiple strategies have been employed in this approach, which include slow photon effect, localized surface plasmon resonance, heterojunction-assisted charge separation and transfer, and cocatalyst. Each of these effects was initially investigated by comparing the photocatalytic hydrogen evolution activities of IO structures over single component TiO_2, binary TiO_2-Au, TiO_2-CdS, TiO_2-Pt, ternary TiO_2-Au-CdS, TiO_2-Au-Pt, TiO_2-CdS-Pt, and quaternary TiO_2-Au-CdS-Pt. The synergy of multiple strategies in the quaternary photocatalyst resulted in a 5-fold increase in H_2 evolution compared to that of the IO TiO_2 photocatalyst. We further improved the activity of this photocatalyst system by tuning the slow photons using lattice parameter (pore size) and incidence angle variations such that slow photons at both blue and red edges were aligned with both the electronic absorption of CdS and the plasmon resonance absorption of Au NPs. This optimized utilization of slow photons enabled us to achieve a maximum of 7.78-fold increase in H_2 evolution compared to that over pristine IO T and a 1.9-fold increase in H_2 evolution under optimal slow-light harvesting conditions compared to conditions where slow light was not harvested. We believe that this approach could be extended to other light harvesting applications involving IO photonic structures.

References

1. Acar, C.; Dincer, I.; Naterer, G. F., Review of photocatalytic water-splitting methods for sustainable hydrogen production. *International Journal of Energy Research* **2016,** *40* (11), 1449-1473.

2. Chen, X.; Shen, S.; Guo, L.; Mao, S. S., Semiconductor-based photocatalytic hydrogen generation. *Chemical Reviews* **2010,** *110* (11), 6503-6570.

3. Dale, S., BP statistical review of world energy. *BP Plc: London, UK* **2021**, 14-16.

4. Kim, J. H.; Hansora, D.; Sharma, P.; Jang, J.-W.; Lee, J. S., Toward practical solar hydrogen production–an artificial photosynthetic leaf-to-farm challenge. *Chemical Society Reviews* **2019,** *48* (7), 1908-1971.

5. Maeda, K.; Domen, K., Photocatalytic water splitting: recent progress and future challenges. *The Journal of Physical Chemistry Letters* **2010,** *1* (18), 2655-2661.

6. Samanta, B.; Morales-García, Á.; Illas, F.; Goga, N.; Anta, J. A.; Calero, S.; Bieberle-Hütter, A.; Libisch, F.; Muñoz-García, A. B.; Pavone, M., Challenges of modeling nanostructured materials for photocatalytic water splitting. *Chemical Society Reviews* **2022,** *51* (9), 3794-3818.

7. Villa, K.; Galán-Mascarós, J. R.; López, N.; Palomares, E., Photocatalytic water splitting: advantages and challenges. *Sustainable Energy & Fuels* **2021,** *5* (18), 4560-4569.

8. Qi, J.; Zhang, W.; Cao, R., Solar-to-hydrogen energy conversion based on water splitting. *Advanced Energy Materials* **2018,** *8* (5), 1701620.

9. Afroz, K.; Moniruddin, M.; Bakranov, N.; Kudaibergenov, S.; Nuraje, N., A heterojunction strategy to improve the visible light sensitive water splitting performance of photocatalytic materials. *Journal of Materials Chemistry A* **2018,** *6* (44), 21696-21718.

10. Fajrina, N.; Tahir, M., A critical review in strategies to improve photocatalytic water splitting towards hydrogen production. *International Journal of Hydrogen Energy* **2019,** *44* (2), 540-577.

11. Kundu, S.; Patra, A., Nanoscale strategies for light harvesting. *Chemical Reviews* **2017,** *117* (2), 712-757.

12. Kudo, A.; Miseki, Y., Heterogeneous photocatalyst materials for water splitting. *Chemical Society Reviews* **2009,** *38* (1), 253-278.

13. Takanabe, K., Photocatalytic water splitting: quantitative approaches toward photocatalyst by design. *ACS Catalysis* **2017,** *7* (11), 8006-8022.

14. Tao, X.; Zhao, Y.; Wang, S.; Li, C.; Li, R., Recent advances and perspectives for solar-driven water splitting using particulate photocatalysts. *Chemical Society Reviews* **2022,** *51* (9), 3561-3608.

15. Wang, Q.; Domen, K., Particulate photocatalysts for light-driven water splitting: mechanisms, challenges, and design strategies. *Chemical Reviews* **2019,** *120* (2), 919-985.

16. Wang, Z.; Li, C.; Domen, K., Recent developments in heterogeneous photocatalysts for solar-driven overall water splitting. *Chemical Society Reviews* **2019,** *48* (7), 2109-2125.

17. Joannopoulos, J. D.; Johnson, S. G.; Winn, J. N.; Meade, R. D., *Molding the flow of light*. Princeton Univ. Press: 2008.

18. Liu, J.; Zhao, H.; Wu, M.; Van der Schueren, B.; Li, Y.; Deparis, O.; Ye, J.; Ozin, G. A.; Hasan, T.; Su, B. L., Slow photons for photocatalysis and photovoltaics. *Advanced Materials* **2017,** *29* (17), 1605349.

19. Joannopoulos, J. D.; Villeneuve, P. R.; Fan, S., Photonic crystals: putting a new twist on light. *Nature* **1997,** *386* (6621), 143-149.

20. Soukoulis, C. M., *Photonic crystals and light localization in the 21st century*. Springer Science & Business Media: 2012; Vol. 563.

21. Baba, T., Slow light in photonic crystals. *Nature Photonics* **2008,** *2* (8), 465-473.

22. Ho, K.; Chan, C. T.; Soukoulis, C. M., Existence of a photonic gap in periodic dielectric structures. *Physical Review Letters* **1990,** *65* (25), 3152.

23. John, S., Strong localization of photons in certain disordered dielectric superlattices. *Physical Review Letters* **1987,** *58* (23), 2486.

24. Yablonovitch, E., Inhibited spontaneous emission in solid-state physics and electronics. *Physical Review Letters* **1987,** *58* (20), 2059.

25. Dowling, J. P.; Scalora, M.; Bloemer, M. J.; Bowden, C. M., The photonic band edge laser: A new approach to gain enhancement. *Journal of Applied Physics* **1994,** *75* (4), 1896-1899.

26. Vlasov, Y. A.; Luterova, K.; Pelant, I.; Hönerlage, B.; Astratov, V., Enhancement of optical gain of semiconductors embedded in three-dimensional photonic crystals. *Applied physics letters* **1997,** *71* (12), 1616-1618.

27. Zhang, X.; John, S., Enhanced photocatalysis by light-trapping optimization in inverse opals. *Journal of Materials Chemistry A* **2020,** *8* (36), 18974-18986.

28. Armstrong, E.; O'Dwyer, C., Artificial opal photonic crystals and inverse opal structures–fundamentals and applications from optics to energy storage. *Journal of Materials Chemistry C* **2015,** *3* (24), 6109-6143.

29. Stein, A.; Wilson, B. E.; Rudisill, S. G., Design and functionality of colloidal-crystal-templated materials—chemical applications of inverse opals. *Chemical Society Reviews* **2013,** *42* (7), 2763-2803.

30. Chen, J. I.; von Freymann, G.; Choi, S. Y.; Kitaev, V.; Ozin, G. A., Amplified photochemistry with slow photons. *Advanced Materials* **2006,** *18* (14), 1915-1919.

31. Curti, M.; Mendive, C. B.; Grela, M. A.; Bahnemann, D. W., Stopband tuning of TiO2 inverse opals for slow photon absorption. *Materials Research Bulletin* **2017,** *91*, 155-165.

32. Wu, M.; Jin, J.; Liu, J.; Deng, Z.; Li, Y.; Deparis, O.; Su, B.-L., High photocatalytic activity enhancement of titania inverse opal films by slow photon effect induced strong light absorption. *Journal of Materials Chemistry A* **2013,** *1* (48), 15491-15500.

33. Liu, J.; Jin, J.; Li, Y.; Huang, H.-W.; Wang, C.; Wu, M.; Chen, L.-H.; Su, B.-L., Tracing the slow photon effect in a ZnO inverse opal film for photocatalytic activity enhancement. *Journal of Materials Chemistry A* **2014,** *2* (14), 5051-5059.

34. Zhang, L.; Baumanis, C.; Robben, L.; Kandiel, T.; Bahnemann, D., Bi2WO6 inverse opals: facile fabrication and efficient visible-light-driven photocatalytic and photoelectrochemical water-splitting activity. *Small* **2011,** *7* (19), 2714-2720.

35. Xie, H.; Li, Y.; Jin, S.; Han, J.; Zhao, X., Facile Fabrication of 3D-Ordered Macroporous Nanocrystalline Iron Oxide Films with Highly Efficient Visible Light Induced Photocatalytic Activity. *The Journal of Physical Chemistry C* **2010,** *21* (114), 9706-9712.

36. Li, Z. Y.; Zhang, Z., Photonic Bandgaps in Disordered Inverse-Opal Photonic Crystals. *Advanced Materials* **2001,** *13* (6), 433-436.

37. Li, Z.-Y.; Zhang, Z.-Q., Fragility of photonic band gaps in inverse-opal photonic crystals. *Physical Review B* **2000,** *62* (3), 1516.

38. Schroden, R. C.; Al-Daous, M.; Blanford, C. F.; Stein, A., Optical properties of inverse opal photonic crystals. *Chemistry of Materials* **2002,** *14* (8), 3305-3315.

39. Jovic, V.; Idriss, H.; Waterhouse, G. I., Slow photon amplification of gas-phase ethanol photo-oxidation in titania inverse opal photonic crystals. *Chemical Physics* **2016,** *479*, 109-121.

40. Zhao, H.; Hu, Z.; Liu, J.; Li, Y.; Wu, M.; Van Tendeloo, G.; Su, B.-L., Blue-edge slow photons promoting visible-light hydrogen production on gradient ternary 3DOM TiO_2-Au-CdS photonic crystals. *Nano Energy* **2018,** *47*, 266-274.

41. Chen, J. I.; Loso, E.; Ebrahim, N.; Ozin, G. A., Synergy of slow photon and chemically amplified photochemistry in platinum nanocluster-loaded inverse titania opals. *Journal of the American Chemical Society* **2008,** *130* (16), 5420-5421.

42. Cai, J.; Wu, M.; Wang, Y.; Zhang, H.; Meng, M.; Tian, Y.; Li, X.; Zhang, J.; Zheng, L.; Gong, J., Synergetic enhancement of light harvesting and charge separation over surface-disorder-engineered TiO2 photonic crystals. *Chem* **2017,** *2* (6), 877-892.

43. Qi, D.; Lu, L.; Xi, Z.; Wang, L.; Zhang, J., Enhanced photocatalytic performance of TiO_2 based on synergistic effect of Ti3+ self-doping and slow light effect. *Applied Catalysis B: Environmental* **2014,** *160*, 621-628.

44. Chang, Y.; Yu, K.; Zhang, C.; Yang, Z.; Feng, Y.; Hao, H.; Jiang, Y.; Lou, L.-L.; Zhou, W.; Liu, S., Ternary CdS/Au/3DOM-$SrTiO_3$ composites with synergistic enhancement for hydrogen production from visible-light photocatalytic water splitting. *Applied Catalysis B: Environmental* **2017,** *215*, 74-84.

45. Liu, Y.; Xu, G.; Ma, D.; Li, Z.; Yan, Z.; Xu, A.; Zhong, W.; Fang, B., Synergistic effects of g-C_3N_4 three-dimensional inverse opals and Ag modification toward high-efficiency photocatalytic H_2 evolution. *Journal of Cleaner Production* **2021,** *328*, 129745.

46. Meng, S.; Li, D.; Fu, X.; Fu, X., Integrating photonic bandgaps with surface plasmon resonance for the enhancement of visible-light photocatalytic performance. *Journal of Materials Chemistry A* **2015,** *3* (46), 23501-23511.

47. Zhang, X.; Liu, Y.; Lee, S.-T.; Yang, S.; Kang, Z., Coupling surface plasmon resonance of gold nanoparticles with slow-photon-effect of TiO_2 photonic crystals for synergistically enhanced photoelectrochemical water splitting. *Energy & Environmental Science* **2014,** *7* (4), 1409-1419.

48. Phillips, K. R.; Shirman, T.; Shirman, E.; Shneidman, A. V.; Kay, T. M.; Aizenberg, J., Nanocrystalline precursors for the co-assembly of crack-free metal oxide inverse opals. *Advanced Materials* **2018,** *30* (19), 1706329.

49. Chemseddine, A.; Moritz, T., Nanostructuring titania: Control over nanocrystal structure, size, shape, and organization. *European Journal of Inorganic Chemistry* **1999,** *1999* (2), 235-245.

50. Turkevich, J.; Stevenson, P. C.; Hillier, J., A study of the nucleation and growth processes in the synthesis of colloidal gold. *Discussions of the Faraday Society* **1951,** *11*, 55-75.

51. Nicolau, Y., Solution deposition of thin solid compound films by a successive ionic-layer adsorption and reaction process. *Applications of Surface Science* **1985,** *22*, 1061-1074.

52. Zhou, R.; Zhang, Q.; Tian, J.; Myers, D.; Yin, M.; Cao, G., Influence of cationic precursors on CdS quantum-dot-sensitized solar cell prepared by successive ionic layer adsorption and reaction. *The Journal of Physical Chemistry C* **2013,** *117* (51), 26948-26956.

53. Herrmann, J. M.; Disdier, J.; Pichat, P., Photoassisted platinum deposition on TiO_2 powder using various platinum complexes. *The Journal of Physical Chemistry* **1986,** *90* (22), 6028-6034.

54. Jiang, Z.; Zhang, Z.; Shangguan, W.; Isaacs, M. A.; Durndell, L. J.; Parlett, C. M.; Lee, A. F., Photodeposition as a facile route to tunable Pt photocatalysts for hydrogen production: on the role of methanol. *Catalysis Science & Technology* **2016,** *6* (1), 81-88.

55. López, C., Three-dimensional photonic bandgap materials: semiconductors for light. *Journal of Optics A: Pure and Applied Optics* **2006,** *8* (5), R1.

56. Blanford, C. F.; Schroden, R. C.; Al-Daous, M.; Stein, A., Tuning solvent-dependent color changes of three-dimensionally ordered macroporous (3DOM) materials through compositional and geometric modifications. *Advanced Materials* **2001,** *13* (1), 26-29.

57. Kim, D.; Yu, Y.-M.; Lee, J.; Choi, Y., Investigation of energy band gap and optical properties of cubic CdS epilayers. *Applied Surface Science* **2008,** *254* (22), 7522-7526.

58. Yuan, Y.-J.; Chen, D.; Yu, Z.-T.; Zou, Z.-G., Cadmium sulfide-based nanomaterials for photocatalytic hydrogen production. *Journal of Materials Chemistry A* **2018,** *6* (25), 11606-11630.

59. Creighton, J. A.; Eadon, D. G., Ultraviolet–visible absorption spectra of the colloidal metallic elements. *Journal of the Chemical Society, Faraday Transactions* **1991,** *87* (24), 3881-3891.

60. Shiraishi, Y.; Tsukamoto, D.; Sugano, Y.; Shiro, A.; Ichikawa, S.; Tanaka, S.; Hirai, T., Platinum nanoparticles supported on anatase titanium dioxide as highly active catalysts for aerobic oxidation under visible light irradiation. *ACS Catalysis* **2012,** *2* (9), 1984-1992.

61. Zhang, N.; Han, C.; Xu, Y.-J.; Foley IV, J. J.; Zhang, D.; Codrington, J.; Gray, S. K.; Sun, Y., Near-field dielectric scattering promotes optical absorption by platinum nanoparticles. *Nature Photonics* **2016,** *10* (7), 473-482.

62. Shiraishi, Y.; Sakamoto, H.; Sugano, Y.; Ichikawa, S.; Hirai, T., Pt–Cu bimetallic alloy nanoparticles supported on anatase TiO_2: highly active catalysts for aerobic oxidation driven by visible light. *ACS Nano* **2013,** *7* (10), 9287-9297.

63. Hao, Q.; Juluri, B. K.; Zheng, Y. B.; Wang, B.; Chiang, I.-K.; Jensen, L.; Crespi, V.; Eklund, P. C.; Huang, T. J., Effects of intrinsic fano interference on surface enhanced raman spectroscopy: comparison between platinum and gold. *The Journal of Physical Chemistry C* **2010,** *114* (42), 18059-18066.

64. Zhao, H.; Wu, M.; Liu, J.; Deng, Z.; Li, Y.; Su, B.-L., Synergistic promotion of solar-driven H_2 generation by three-dimensionally ordered macroporous structured TiO_2-Au-CdS ternary photocatalyst. *Applied Catalysis B: Environmental* **2016,** *184*, 182-190.

65. Yuan, W.; Zhang, Z.; Cui, X.; Liu, H.; Tai, C.; Song, Y., Fabrication of hollow mesoporous CdS@ TiO_2@ Au microspheres with high photocatalytic activity for hydrogen evolution from water under visible light. *ACS Sustainable Chemistry & Engineering* **2018,** *6* (11), 13766-13777.

66. Guo, Q.; Zhou, C.; Ma, Z.; Yang, X., Fundamentals of TiO_2 photocatalysis: concepts, mechanisms, and challenges. *Advanced Materials* **2019,** *31* (50), 1901997.

67. Furube, A.; Hashimoto, S., Insight into plasmonic hot-electron transfer and plasmon molecular drive: new dimensions in energy conversion and nanofabrication. *NPG Asia Materials* **2017,** *9* (12), e454-e454.

68. Meng, A.; Zhu, B.; Zhong, B.; Zhang, L.; Cheng, B., Direct Z-scheme TiO_2/CdS hierarchical photocatalyst for enhanced photocatalytic H_2-production activity. *Applied Surface Science* **2017,** *422*, 518-527.

69. Cui, E.; Lu, G., Modulating photogenerated electron transfer and hydrogen production rate by controlling surface potential energy on a selectively exposed Pt facet on Pt/TiO_2 for enhancing hydrogen production. *The Journal of Physical Chemistry C* **2013,** *117* (50), 26415-26425.

70. Wang, Y.; Wang, Y.; Xu, R., Photochemical deposition of Pt on CdS for H_2 evolution from water: markedly enhanced activity by controlling Pt reduction environment. *The Journal of Physical Chemistry C* **2013,** *117* (2), 783-790.

71. Cheng, L.; Xiang, Q.; Liao, Y.; Zhang, H., CdS-based photocatalysts. *Energy & Environmental Science* **2018,** *11* (6), 1362-1391.

72. Ning, X.; Lu, G., Photocorrosion inhibition of CdS-based catalysts for photocatalytic overall water splitting. *Nanoscale* **2020,** *12* (3), 1213-1223.

73. Tang, Y.; Hu, X.; Liu, C., Perfect inhibition of CdS photocorrosion by graphene sheltering engineering on TiO_2 nanotube array for highly stable photocatalytic activity. *Physical Chemistry Chemical Physics* **2014,** *16* (46), 25321-25329.

74. Chen, Y.; Zhong, W.; Chen, F.; Wang, P.; Fan, J.; Yu, H., Photoinduced self-stability mechanism of CdS photocatalyst: The dependence of photocorrosion and H_2-evolution performance. *Journal of Materials Science & Technology* **2022,** *121*, 19-27.

75. Wei, L.; Guo, Z.; Jia, X., Probing photocorrosion mechanism of CdS films and enhancing photoelectrocatalytic activity via cocatalyst. *Catalysis Letters* **2021,** *151*, 56-66.

76. Chang, Y.; Xuan, Y.; Quan, H.; Zhang, H.; Liu, S.; Li, Z.; Yu, K.; Cao, J., Hydrogen treated Au/3DOM-TiO_2 with promoted photocatalytic efficiency for hydrogen evolution from water splitting. *Chemical Engineering Journal* **2020,** *382*, 122869.

77. Cui, X.; Wang, Y.; Jiang, G.; Zhao, Z.; Xu, C.; Wei, Y.; Duan, A.; Liu, J.; Gao, J., A photonic crystal-based CdS–Au–WO_3 heterostructure for efficient visible-light photocatalytic hydrogen and oxygen evolution. *RSC Advances* **2014,** *4* (30), 15689-15694.

78. Fiorenza, R.; Bellardita, M.; Scirè, S.; Palmisano, L., Photocatalytic H_2 production over inverse opal TiO_2 catalysts. *Catalysis Today* **2019,** *321*, 113-119.

79. Liu, J.; Liu, G.; Li, M.; Shen, W.; Liu, Z.; Wang, J.; Zhao, J.; Jiang, L.; Song, Y., Enhancement of photochemical hydrogen evolution over Pt-loaded hierarchical titania photonic crystal. *Energy & Environmental Science* **2010,** *3* (10), 1503-1506.

80. Rahul, T. K.; Mohan, M.; Sandhyarani, N., Enhanced solar hydrogen evolution over in situ gold–platinum bimetallic nanoparticle-loaded Ti^{3+} self-doped titania photocatalysts. *ACS Sustainable Chemistry & Engineering* **2018,** *6* (3), 3049-3059.

81. Sordello, F.; Minero, C., Photocatalytic hydrogen production on Pt-loaded TiO_2 inverse opals. *Applied Catalysis B: Environmental* **2015,** *163*, 452-458.

82. Temerov, F.; Pham, K.; Juuti, P.; Mäkelä, J. M.; Grachova, E. V.; Kumar, S.; Eslava, S.; Saarinen, J. J., Silver-decorated TiO_2 inverse opal structure for visible light-induced photocatalytic degradation of organic pollutants and hydrogen evolution. *ACS Applied Materials & Interfaces* **2020,** *12* (37), 41200-41210.

83. Waterhouse, G.; Wahab, A.; Al-Oufi, M.; Jovic, V.; Anjum, D. H.; Sun-Waterhouse, D.; Llorca, J.; Idriss, H., Hydrogen production by tuning the photonic band gap with the electronic band gap of TiO_2. *Scientific Reports* **2013,** *3* (1), 2849.

84. Yu, K.; Zhang, C.; Chang, Y.; Feng, Y.; Yang, Z.; Yang, T.; Lou, L.-L.; Liu, S., Novel three-dimensionally ordered macroporous $SrTiO_3$ photocatalysts with remarkably enhanced hydrogen production performance. *Applied Catalysis B: Environmental* **2017,** *200*, 514-520.

CHAPTER VII

Conclusion and perspectives

Overview

This chapter concludes the thesis with a summary of the entire work and perspectives for future research. The summary collates the results of the individual research works that were undertaken, which are in tune with the overall objective and the three sub-objectives. A brief critical self-appraisal follows the summary, which highlights the strengths and limitations of this thesis. In the section on perspectives, the challenges that continue to persist in the research on slow light in photocatalysis are enumerated. In addition, perspectives for future research are presented.

7. Conclusions and perspectives

7.1. Conclusions

In this research work, the group velocity of light was successfully reduced using inverse opal photonic structures, and the frequencies of these 'slow photons' were efficiently tuned to improve light harvesting in photocatalytic applications. Initially, the hypothesis of slow light assistance was validated as proof of concept in photocatalytic dye degradation. Later, this strategy was further improved by reducing the group velocity of light at multiple spectral ranges and utilizing them for enhanced light harvesting. Finally, slow light was successfully utilized for photocatalytic hydrogen generation, which is a solution for renewable and sustainable energy sources. Research undertaken in each of the three sections is summarized below.

(i) In the first part, high quality IO TiO_2 photonic structures were synthesized as a film on glass substrates using the 2-step coassembly approach, that involved the evaporation-induced simultaneous self-assembly of PS colloids and TiO_2 NPs, followed by calcination. $BiVO_4$ NPs were embedded in IO TiO_2 structure using SILAR approach, to render the photocatalyst responsive in the visible region. The structures exhibited distinct SBGs with slow photons at either edge of the SBG. Slow photon wavelengths were tuned by both lattice parameter and light incidence angle variations to the electronic absorption of $BiVO_4$. Under accurate tuning conditions, the photocatalytic RhB dye degradation efficiency of this IO photocatalyst system reached up to 7 times higher than that of non-IO compact films. Light absorption enhancement due to slow photons was justified by RCWA simulations of reflectance and absorptance.

(ii) In the second part, light absorption enhancement due to slow photon assistance was further improved by generating slow photons at multiple spectral regions. Bilayer IO TiO_2 structures with each layer having a different pore size were synthesized by the coassembly of the first layer of PS colloids and TiO_2 NPs, followed by plasma treatment of the first layer to improve its hydrophilicity, the coassembly of the second layer and calcination. $BiVO_4$ NPs were loaded in the bilayer structure by SILAR method. The bilayer photocatalyst exhibited two distinct SBGs with slow photons at the blue and red edges of either of them. Slow photons were tuned by lattice parameter and light incidence angle variations. Under optimal tuning conditions, a 2.2-fold and 8.5-fold increase in photocatalytic RhB dye degradation was manifested compared to the activities of monolayer inverse opal and non-inverse opal counterparts.

(iii) In the third part, slow light strategies optimized in the previous sections were applied, in conjunction with other strategies like localized surface plasmon resonance and cocatalyst assistance, for photocatalytic H_2 generation from water. To realize LSPR, Au NPs were loaded *in situ* in the IO TiO_2 structure by a three-phase coassembly approach that involved the simultaneous self-assembly of PS colloids, TiO_2 NPs, and Au NPs, followed by calcination. The IO TiO_2-Au structure was sensitized with CdS NPs by SILAR method to absorb light in the visible region, to efficiently separate photogenerated charges by the formation of heterojunction with TiO_2, and to facilitate surface redox reactions, thanks to its band gap positions that satisfy the thermodynamic requirements of water splitting. The structure was further modified with Pt NPs that served as cocatalyst for the electrocatalytic reactions. The optimized synthesis methods enabled the simultaneous modification of the photocatalyst and the preservation of photonic properties. Precise tuning of slow photon wavelengths resulted in a 7.8-fold increase in H_2 evolution compared to that over IO TiO_2 structures, and a 1.9-fold increase in H_2 evolution compared to that over the same composite under sub-optimal tuning conditions.

Thus, in this thesis, slow photons were successfully generated in IO TiO_2-based photonic structures and tuned to the electronic absorption of the photocatalyst to achieve highly enhanced photocatalytic dye degradation and photocatalytic hydrogen generation from water.

7.2. Perspectives

Despite the success reported on slow photon assistance in IO photonic structures for photocatalytic applications, many challenges continue to exist.

The primary challenge concerns the synthesis of highly ordered pPBG-manifesting structures. Given that ~40% of the total solar energy is concentrated in the visible spectral region, materials that harvest visible light need to be moulded into photonic structures for maximum slow photon utilization. So far, TiO_2, which absorbs light in the UV region has been the most extensively researched light harvesting material for photonic structures. Numerous other visible light responsive materials have been synthesized into photonic structures; however, they are plagued by poor structural quality that undermines their photonic properties. Hence, research can be oriented towards developing synthesis strategies to obtain highly ordered photonic structures of visible light-responsive materials through approaches like coassembly colloid templated method.

Most photoconversion processes require composites involving more than one material for improving efficiency. This implies that photonic structures need to be functionalized and modified to suit specific applications. However, photonic properties deteriorate with each post-modification step. Hence, strategies like one-pot synthesis using mixed precursors or mixed pre-synthesized materials need to be further developed to create the required composite structures. Alternatively, optimization strategies can be developed through methods like SILAR to achieve controlled post-modification, for simultaneously achieving functionality and preserving photonic properties. In addition, simulating energy or field energy maps for composite materials may help understanding the fundamental mechanisms underlying the interaction between the incident light and the materials.

Inverse opals are by far the photonic structures the most explored to exploit slow photon effect. Research has shown that other photonic structures can also be highly effective for slow photon-assisted light harvesting. However, research remains limited in this regard. Research on SPE could be extended to other photonic structures that could manifest rich and diverse photonic properties. Innovative designs like layered structure and spherical structures can be further explored. Advances in technology like 3D printing and laser writing could be incorporated in the synthesis process to create such novel designs.

Numerical optimizations relying e.g. on evolutionary algorithms[1, 2] for optimization of photonic structures with respect to their simulated optical properties and their predicted photocatalytic activity. These methods are often used in the photonics community and novel slow photon enhanced photocatalytic applications could be designed based on such optical simulations. Parameters such as the lattice symmetry, the geometrical dimensions, the crystallographic orientations, the incidence angle, or the refractive indices could, for instance, be optimized.

Disorder is inevitable in PCs synthesized by wet chemical methods. Numerous efforts are being made to create highly ordered structures with minimum defects. However, studies that analyse and quantify the impact of disorder on SPE in actual light harvesting applications are negligible. More efforts could be devoted to systematic studies on the correlation between disorder in PC’s and light harvesting efficiency. Numerical simulations are important tools to employ to this end. They can take defects into account and are also able to assess the level of defect that could be tolerated for given photocatalytic applications. To a further extent, they could even verify whether some levels of defects could enhance any photocatalytic activity. Also, novel strategies aimed at controlling disorder formation, also called disorder engineering, could be further explored.

The reduction of group velocity of light in PCs has been theoretically established and experimentally measured using techniques like white light interferometry. Besides, it has been experimentally tested and proved in real-time applications using various strategies. However, claims are far from being foolproof and many factors need to be taken into consideration. Firstly, SPE is only one of the light-harvesting effects observed when light interacts with photonic crystals. Effects like scattering and internal reflection could be other contributing factors. Secondly, improving light harvesting efficiency is only one of the steps in photoconversion process. The role of other factors like surface area, interconnected porosity, charge transfer and mass transport need to be considered while interpreting photoconversion efficiencies. As it is highly implausible to study SPE independently of the accompanying effects, it is recommended to justify claims of slow photon assistance by adopting more than one of the strategies detailed above.

The most common approach to demonstrate SPE involves reflectance or transmission measurements that indicate the pPBG spectral position. However, the accurate location of slow photons is far from being obvious and spectrophotometry provides only an estimate of the wavelength range of slow photons. Hence, advanced techniques to measure in-situ group velocity is another approach that could be employed to accurately pinpoint the magnitude of the reduction in group velocity of light, the exact wavelengths at which it occurs, and its impact in the specific photoconversion application. Also, concerning whether blue edge slow photons or red edge slow photons have a greater impact in photoconversion applications, experimental observations remain divided, although it is intuitive to deduce from theoretical principles that red edge slow photons localized in the higher dielectric material are more efficient in photoconversion. More comparative studies need to be undertaken especially considering the scenario when both pPBG reflection and slow photon regions fall within the absorption range of the photoactive material.

The limiting factor of SPE in photoconversion is that slow photons are confined to narrow spectral ranges. To go beyond this limitation, new promising strategies like layered structures, multi band gap structures and synergistic effects like that involving surface plasmon resonance can be further researched. There are a growing number of reports on synergy between SPE and SPR for photoconversion. However, systematic theoretical studies and experimental studies on these coexisting photonic properties mutually influencing each other were not undertaken, which calls for more detailed research.

Slow light in photonic structures has been used for two decades as a strategy for enhancing photocatalytic activity. As discussed in the introduction, other physical methods allow to slow down photons. These avenues could be explored for photocatalytic applications. In addition, some of these methods are also able to generate fast light. Using optical methods that can generate slow and fast light on demand could allow to control in real time the photocatalytic activity of a given reaction and hence the speed of reaction.

In addition to the above perspectives, it is important to note the contribution of theoretical and simulation studies in understanding the interaction of light in PC's, particularly in the presence of an absorbing material. Simulation can be a valuable tool not only to justify SPE but also to optimize and improve slow photon assistance in light harvesting applications. Hence, a greater research investment is required to optimize light harvesting efficiency in PCs.

Finally, it can be concluded that slow photon effect in PCs for light harvesting enhancement is not fully explored. The scope for further research on slow photon effect in inverse opal photonic crystals is vast as new materials are being explored and new synergistic strategies are being tried out for novel applications. One can hope that new frontiers will be created, and old frontiers redrawn to better utilize slow light in light harvesting applications.

References

1. Cohoon, J.; Kairo, J.; Lienig, J., Evolutionary algorithms for the physical design of VLSI circuits. *Advances in Evolutionary Computing: Theory and Applications* **2003**, 683-711.
2. Vikhar, P. A. In *Evolutionary algorithms: A critical review and its future prospects*, 2016 International conference on global trends in signal processing, information computing and communication (ICGTSPICC), IEEE: 2016; pp 261-265.

Annex

Inverse opal TiO_2-based heterocomposite photonic structures for slow photon-assisted visible light photocatalysis*

Abstract

Manipulation of light was proved to be an efficient strategy to improve light harvesting efficiency in solar energy conversion. Inverse opal (IO) photonic structures are among the most promising materials, which permit light manipulation, thanks to their ability to slow down light at specific wavelengths and localize it within the dielectric structure. However, the generation, the control and, in particular, the practical utilization of these narrow spectral range ‘slow photons’ remain highly challenging and relatively underexplored. In this work, we report the ability not only to generate slow photons in the visible range by synthesizing highly ordered IO TiO_2 photonic structures, but also to control and tune their wavelengths, by varying lattice parameters (pore sizes), such that they can be efficiently utilized by the composite $BiVO_4$ semiconductor for visible light photocatalysis. Photocatalytic experiments revealed a 70% increase in efficiency in all IO structures compared to the corresponding non-structured compact film. In addition, a 20% increase in efficiency was observed when the photonic stop band gap as well as its blue and red edges were accurately tuned to match the electronic absorption of the $BiVO_4$ photocatalyst. Our choice of IO synthesis parameters and tuning strategies enabled us to generate, control and transfer the energy of slow photons from IO TiO_2 to the composite visible light-responsive photocatalyst for highly amplified photoactivity. This work opens new possibilities for the practical utilization of slow photon effect under visible light in various solar energy conversion applications.

---

*This part of the work has been published in the *Proceedings of SPIE, Photonics for Solar Energy Systems IX* **2022**, 12150, 1215004.

A 1. Inverse opal TiO_2-based heterocomposite photonic structures for slow photon-assisted visible light photocatalysis

A.1.1. Introduction

‘Sustainable and CO_2-emission-free energy’ has garnered extensive research interest and financial investment in the past few decades as the global drive towards reducing fossil-fuel dependency and minimizing carbon dioxide emissions continues to expand. Photocatalysis, a process involving photon-to-chemical energy conversion, is one of the most promising routes towards achieving this objective since sustainable solar energy can be harvested for ‘clean’ energy-related applications like water splitting for H_2 production and CO_2 reduction. Various approaches have been followed by researchers in photocatalysis in order to improve different aspects of photocatalysis like light harvesting, electron-hole pair separation, electron transport and mass transport. These approaches include synthesis of novel photocatalyst systems, modification of chemical composition of photocatalyst, modification of morphology, reaction-specific ‘band gap engineering’ and development of efficient photoreactors[1,2].

Although significant progress has been made using the above methods, alternative and synergistic approaches involving the manipulation of light to improve photocatalytic efficiency have not been sufficiently explored. Photonic crystals are among the promising materials that permit the control of the flow of light, thanks to their periodic structures with alternating refractive indices[3,4]. Under suitable conditions of high refractive index (RI) contrast and the size of periodicity corresponding to the wavelength of light, these structures reflect light within a specific wavelength range, giving rise to a photonic stop band gap (SBG), while simultaneously reducing the group velocity of light at both the blue and red edges of the SBG to nearly zero i.e., standing waves of light. The blue edge slow photons are preferentially localized in the lower RI medium, while the red edge slow photons are preferentially localized in the higher RI medium[5]. These slow photons, due to their increased optical path length and lifetime within the photocatalyst, can be utilized to improve energy conversion, specifically light harvesting, and photocatalytic efficiency, provided the wavelengths of slow photons are accurately tuned to the electronic band gap of the photocatalyst. The tuning of slow photon wavelengths can be achieved by modifying various parameters like Bravais lattice type, lattice constant, refractive index, filling fraction, crystallographic orientation, and light incident angle[6].

Various efforts have been made to exploit slow photons in photocatalysis starting from the initial work to demonstrate slow photon effect using IO TiO_2 (IOT) for the solid phase photodegradation of methylene blue by varying both lattice parameters (pore sizes of the IOs) and incidence angle[7]. Ever since, efforts have been made to utilize inverse opal (IO) structures of various semiconductors like ZnO, WO_3, Fe_2O_3, gC_3N_4 for photocatalytic applications[8]. However, in most cases, the slow photon effect was claimed but not sufficiently established[9]. Moreover, most of the above cited works were limited either to UV-responsive photocatalysts, single-component photocatalysts or non-aqueous phase photocatalysis. In this work, we report, in a composite inverse opal TiO_2-$BiVO_4$ (IOTB) semiconductor photocatalyst, not only the possibility to generate slow photons by synthesizing highly ordered structures but also to tune their wavelengths to the electronic absorption edge of the visible-light-responsive photocatalyst in aqueous phase. The results of our experiments indicated a 70% increase in photodegradation efficiency of all IO photocatalyst with respect to the non-structured compact film. In addition, a further 20% increase in activity under accurate tuning conditions confirmed that slow light can be efficiently utilized for photocatalysis using IO photonic semiconductors and that this approach can be extended to other applications of photonics for energy conversion.

A.1.2. Experimental methods and synthesis

This section describes the synthesis process of the photocatalysts used in this work as well as the characterization methods and the photocatalytic test we performed.

Synthesis of IOT photonic structures

IOT films were synthesized by a colloidal templating strategy that includes a two-step process of simultaneously assembling the colloids and the phase-controlled TiO_2 nanoparticles on a glass substrate by Evaporation-Induced Simultaneous Self-Assembly (EISSA) method and the subsequent removal of the template by calcination[10]. In a typical process, 0.1 % dispersion of monodisperse polystyrene (PS) colloids in water and a previously prepared dispersion of phase controlled TiO_2 nanoparticles in water were mixed together at a 25:1 ratio. A glass substrate previously treated with piranha solution (H_2SO_4 + H_2O_2) to render it hydrophilic, was suspended in the colloid-TiO_2 mixture for 48 hours so that the evaporation of the solvent resulted in an ordered face-centered cubic (*fcc*) assembly of the colloids with the interstices filled with the phase-controlled TiO_2 material. The self-assembled opal structures were then calcined at 500°C at a ramp rate of 1°C/min to remove the colloidal template and obtain the IO structure. Three samples, IOT 300, IOT 400 and IOT 500, with different pore sizes were prepared by using colloids of 300 nm (PS 300), 400 nm (PS 400) and 500 nm (PS 500), respectively.

Synthesis of IOTB heterocomposites

In order to render the photocatalyst responsive to visible light, the IOT films were deposited with $BiVO_4$ semiconductor nanoparticles by Sequential Ionic Layer Adsorption Reaction (SILAR) method[11], wherein the films were sequentially dipped in the anionic and cationic precursors prepared at a 1:2 molar ratio, followed by calcination in order to obtain the crystalline phase of the IOTB films.

Synthesis of TiO_2 heterocomposite compact films

A TiO_2 compact film with a similar thickness to that of the IOT films was synthesized by optimizing a previously reported sol-gel dip coating method[12]. The film was then deposited with the $BiVO_4$ semiconductor nanoparticles using the same method as described above to obtain non-IO compact TiO_2- $BiVO_4$ (CTB) hetero-composite film.

Characterization methods

A JEOL JSM-7500F Scanning Electron Microscope (SEM) was used for electron microscopy observation and Energy Dispersive X-ray Spectroscopy (EDS) for quantitative analysis. An Olympus BX 61 microscope fitted with an Olympus XC50 camera was used to carry out optical microscopy observation. X-ray diffraction (XRD) patterns were taken using PANalytical X'PERT PRO Bragg-Brentano diffractometer using Cu Kα radiation (λ = 1.54184 Å) measured in 2θ angle range 20°-60°. Perkin Elmer 750S UV/Vis/NIR spectrophotometer was employed for absorptance measurements at 8° incidence, while an Avantes AvaSpec-2048-2 spectrophotometer coupled with an AvaLight-DH-S-BAL deuterium-halogen light source was used for reflectance measurements at normal incidence and detection wherein incident and reflected light were channeled through a bifurcated optical fiber.

Photocatalytic tests

The IOTB (with different pore sizes) and CTB samples were tested for photocatalytic activity by the degradation of Rhodamine-B (RhB) in aqueous phase using a 300 W ELDIM-RFLX-ET101-01 EZ Reflex light source emitting a spectral range of 390-770 nm. Light was channeled through an Avantes FC-UV-200 optical fiber mounted on Avantes AFH-15 fiber holder onto the photocatalyst immersed in 4 ml of 2.0 μM RhB solution. After leaving the sample in the dark for 60 min to reach equilibrium, the test was allowed to continue for 6 hours, during which the photocatalytic degradation was analyzed every 60 min. by measuring the absorptance of the RhB solution using Analytik Jena-Specord 205 UV-VIS spectrophotometer.

A.1.3. Results and discussion

Highly ordered and homogeneous IO photonic structures are essential in order to exhibit a distinct SBG, at the edges of which the group velocity of light is reduced nearly to zero. In order to obtain ordered IO structures, a novel one-step co-assembly of template colloids and phase controlled TiO_2 nanoparticles **(Fig. 1 (a))** was preferred to the conventional two-step process of assembling the colloids and then backfilling the interstices with the semiconductor material. The conventional process was often found to result in higher defect formation since the fragile opal template tends to get structurally disturbed during matrix material infiltration. Also, incomplete, or excessive infiltration often tends to result in either a collapse of the photonic structure or a formation of overlayer.

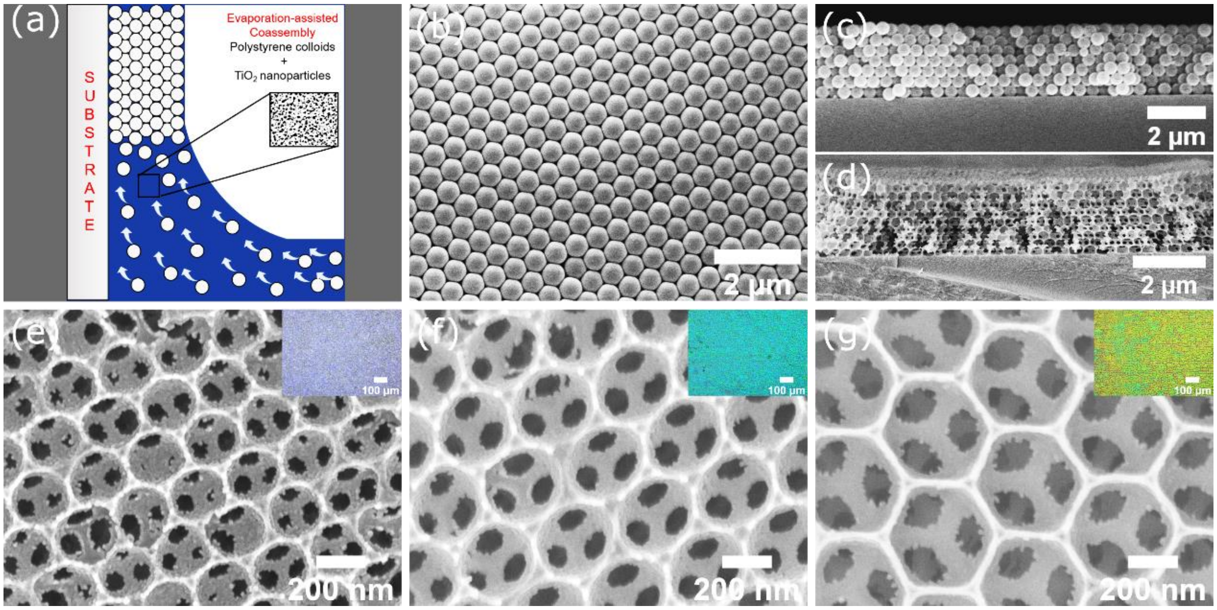

Figure 1. (a) Schematic illustration of the co-assembly of PS colloids and phase-controlled TiO_2 nanoparticles; **(b)** SEM image of PS 500 colloids-TiO_2 co-assembly; **(c)** Cross-section SEM image of the PS 500 colloid-TiO_2 co-assembly; **(d)** Cross section SEM image of IOT 500 obtained after calcination; **(e-g)** SEM images of IO photonic structures of IOT 300 (e), IOT 400 (f), IOT 500 (g), with their corresponding optical microscope images shown in the insets.

The co-assembly process adopted in this work avoided the delicate infiltration step, thus forming an ordered co-assembly **(Fig. 1 (b))**, that resulted in ordered IO structures after template removal **(Fig. 1 (e-g)).** Also, the use of phase-controlled crystalline-amorphous TiO_2 matrix material provided additional advantage striking the right equilibrium between providing stability to the structure (due to crystalline phase) and accommodating the stress arising from shrinkage during template removal by calcination (due to amorphous phase). Cross-section SEM images revealed that the film thickness was around 2 µm **(Fig. 1 (c, d))**.

SEM images of IOT 300, IOT 400 and IOT 500 **(Fig. 1 (e- g))** reveal homogeneous structures with pore sizes of 238 nm, 320 nm, and 445 nm, respectively. This corresponds to a 15-20% shrinkage compared to the related colloid sizes. This is in accordance with previously reported results[13]. The corresponding optical microscope images shown in the insets with distinct colors corresponding to the SBG reflection confirm the high quality of the synthesized photonic structures. Since TiO_2 absorbs light only in the UV region, the IOT structures were deposited with $BiVO_4$ nanoparticles (25% by weight of TiO_2) in order to shift the absorptance of the photocatalysts to the visible region. SEM image shown in **Fig. 2 (a)** confirms the homogeneous deposition of the $BiVO_4$ semiconductor nanoparticles, while **Fig. 2 (b)** shows the shift in absorptance from UV region to the visible region after depositing the IOT structures with the visible light-responsive semiconductor. For comparison of photocatalytic activities, a non-structured compact TiO_2-$BiVO_4$ composite (CTB) film was synthesized **(Fig. 2 (c))**, with a similar quantity of $BiVO_4$ nanoparticles deposited as in the IO structures.

Reflectance spectral measurements in air **(Fig. 2 (d))** show that IOTB 300, IOTB 400 and IOTB 500 samples exhibit distinct SBG reflection peaks at 392, 487 and 597 nm, respectively. This corresponds to a gradual red shift of the SBG peak wavelength with an increase in the lattice parameter and pore size. The reflection peak positions can be theoretically estimated by Bragg's equation[14]:

$$\lambda = 2 \cdot \sqrt{2/3} \cdot D \cdot \sqrt{n_{matrix}^2(f) + n_{void}^2(1-f) - \sin^2\theta} \qquad (1)$$

where λ is the wavelength of the reflection peak, D is the lattice parameter (here corresponding to the pore diameter), n_{matrix} is the average refractive index (RI) of TiO_2 host material and $BiVO_4$ nanoparticles, n_{void} is the RI of the medium filling the pores (namely, air or water), f and (1-f) are the filling fractions of the matrix and pores, respectively, while θ is the angle between the incident light and the surface normal. It was observed that the experimentally determined positions of the SBG reflection peaks were lower than the theoretical predictions, which was probably due to a lower filling fraction of the host material, as reported in previous works[15], compared to the ideal filling fraction of f = 0.26 in a close-packed *fcc* arrangement. Since photocatalytic degradation tests were done in aqueous phase, reflectance measurements were also performed after the pores were filled with water **(Fig. 2 (e))**. In water medium, the SBG reflection peaks red shifted due to the increase in refractive index of the filling medium from 1.0 (RI of air) to 1.33 (RI of water). It was also noted that the reflection peaks were lower in intensity and broader compared to those in air due to the lower RI contrast between the matrix and the pores filled with water.

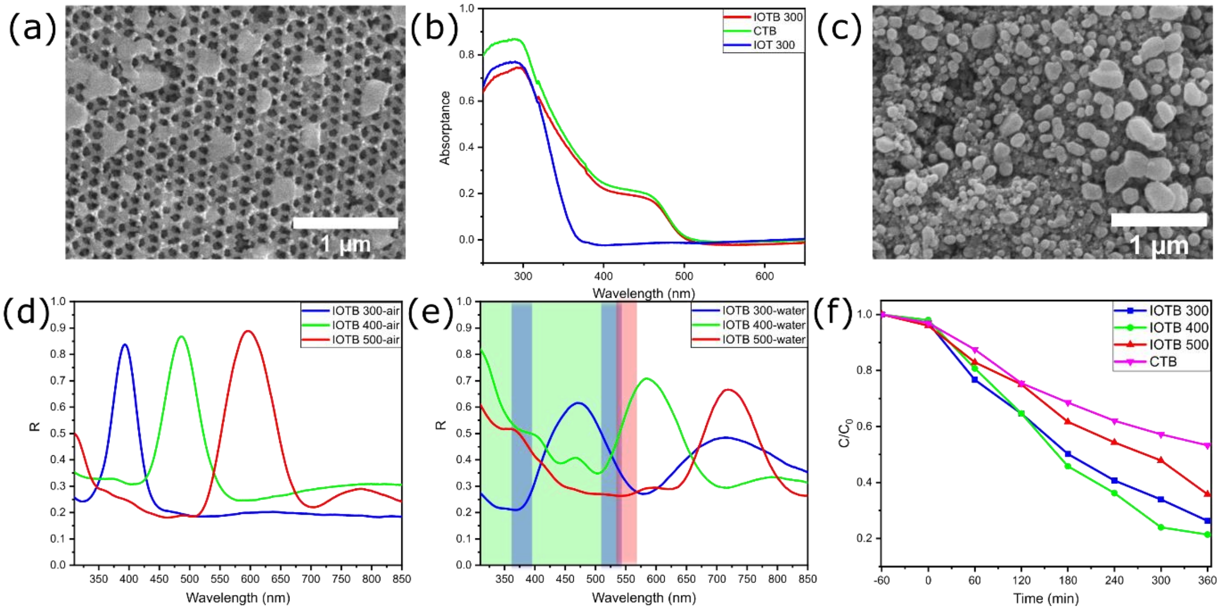

Figure 2. (a) SEM image of IOT 300 deposited with $BiVO_4$ nanoparticles (IOTB 300); **(b)** UV-Visible absorptance spectra of IOTB 300, CTB and IOT 300; **(c)** SEM image of a CTB sample; **(d)** Reflectance spectra in air of IOTB 300 (blue), IOTB 400 (green) and IOTB 500 (red); **(e)** Reflectance spectra in water of IOTB 300 (blue), IOTB 400 (green) and IOTB 500 (red); **(f)** Normalized concentration (C/C_0) as a function of time indicating the RhB degradation activity of IOTB 300 (blue), IOTB 400 (green), IOTB 500 (red) and CTB (magenta).

The three IOTB samples were tested for photocatalytic RhB dye degradation and their activities were compared to that of non-structures CTB film. The comparison of photocatalytic efficiencies is represented in **(Fig. 2 (f))** in terms of normalized concentration (C/C_0) as a function of time of degradation, where C_0 is the initial concentration of RhB, while C is the concentration of RhB at time ‘t’. All the IO photocatalysts exhibited higher activity than that of the compact film. The comparison of degradation efficiencies of the photocatalysts ($(C_0$-$C)/C_0$×100%), after being normalized with respect to the amount of the visible light-responsive photocatalyst, revealed an average 70% increase in activity in IOTB samples compared to the non-structured CTB film. This can be justified by the assistance of slow photons in IO photonic structures in enhancing photocatalytic activity.

Among the three IOTB samples, IOTB 400 was found to exhibit the highest activity followed by IOTB 300 and then by IOTB 500. This difference in activity establishes the importance of accurately tuning the wavelengths of slow photons to the electronic absorption of the visible-light responsive $BiVO_4$ photocatalyst, in order to increase photocatalytic activity. In the case of IOTB 300, both the blue and red edge slow photon wavelengths (blue and red shades in **Fig. 2 (e)**) at ~325 nm and ~520 nm, respectively) were tuned in such a way that they overlap with the electronic absorption of the visible light photocatalyst (green shade in **Fig 2 (e)**). However, the absorption of visible light was reduced by the strong SBG reflection, which also fell within the absorption of the $BiVO_4$ photocatalyst, which explains its reduced photocatalytic activity compared to that of IOTB 400. In the case of IOTB 400, the blue edge slow photons (blue shade at ~510 nm in **Fig. 2 (e)**) were tuned to the electronic absorption of the $BiVO_4$ photocatalyst, while, at the same time, the SBG reflection peak remained outside the absorption of the visible light photocatalyst. This explains the highest activity of IOTB 400 compared to the other two samples (20% and 10% higher than IOTB 500 and IOTB 300, respectively). Blue edge slow photons, although localized primarily in the lower RI medium (water), can still be utilized by the matrix material (photocatalyst) for enhancement of photocatalytic activity, as demonstrated through Rigorous Coupled Wave Analysis (RCWA) simulation studies[16]. The least activity of IOTB 500 can be explained by the fact that both blue and red edge slow photons are located far away from the electronic absorption of $BiVO_4$ photocatalyst, which reduces the impact of slow photons to a minimum. These results indicate that slow photons, when properly tuned to match with the electronic absorption of the photocatalyst, while simultaneously avoiding SBG reflection, can result in highly enhanced photocatalytic activity in IO photonic photocatalysts. films.

A.1.4. Conclusion

Slow photons in IO structures, originating from the reduction of group velocity of light at either edge of the photonic stop band gap, have immense potential in enhancing the photocatalytic activity of the nanostructured semiconductors. The challenges in benefitting fully from this potential lie firstly in synthesizing highly ordered photonic structures capable of generating a distinct SBG with slow photons at its edges and secondly in tuning the wavelengths of slow photons in such a way that they overlap with the electronic absorption of the photocatalyst. In this work, the first challenge was overcome by using a co-assembly method that resulted in ordered IO structures. The second challenge was overcome by varying the lattice parameter (and pore diameter), that resulted in the wavelengths of the slow photons being tuned to the electronic absorption of the $BiVO_4$ semiconductor nanoparticles, thereby enhancing light absorption and photocatalytic activity. In the present work, the activity of all IO structures, assisted by slow photons, was found to be around 70% higher than the non-structured composite. In addition, accurate tuning of the slow photons to the electronic absorption of the photocatalyst, while simultaneously avoiding SBG reflection resulted in a further 20% increase in photocatalytic activity. This work realized for a heterocomposite photocatalytic system in aqueous phase throws new light on the tuning strategies in aqueous phase and opens new possibilities for utilizing the slow photon effect in other solar energy conversion processes like water splitting and CO_2 reduction.

References

1. Kubacka, A.; Fernandez-Garcia, M.; Colon, G., Advanced nanoarchitectures for solar photocatalytic applications. *Chemical Reviews* **2012,** *112* (3), 1555-1614.
2. Xu, C.; Anusuyadevi, P. R.; Aymonier, C.; Luque, R.; Marre, S., Nanostructured materials for photocatalysis. *Chemical Society Reviews* **2019,** *48* (14), 3868-3902.
3. Yablonovitch, E., Inhibited spontaneous emission in solid-state physics and electronics. *Physical Review Letters* **1987,** *58* (20), 2059-2062.
4. John, S., Strong localization of photons in certain disordered dielectric superlattices. *Physical Review Letters* **1987,** *58* (23), 2486-2489.
5. Joannopoulos, J. D.; Johnson, S. G.; Winn, J. N.; Meade, R. D., *Photonic crystals*. Princeton Univ. Press: 2011.
6. Collins, G.; Armstrong, E.; McNulty, D.; O'Hanlon, S.; Geaney, H.; O'Dwyer, C., 2D and 3D photonic crystal materials for photocatalysis and electrochemical energy storage and conversion. *Science and Technology of Advanced Materials* **2016,** *17* (1), 563-582.
7. Chen, J. I. L.; von Freymann, G.; Choi, S. Y.; Kitaev, V.; Ozin, G. A., Amplified photochemistry with slow photons. *Advanced Materials* **2006,** *18* (14), 1915-1919.
8. Pietron, J. J.; DeSario, P. A., Review of roles for photonic crystals in solar fuels photocatalysis. *Journal of Photonics Energy* **2016,** *7,* (1).
9. Liu, J.; Zhao, H.; Wu, M.; Van der Schueren, B.; Li, Y.; Deparis, O.; Ye, J.; Ozin, G. A.; Hasan, T.; Su, B. L., Slow photons for photocatalysis and photovoltaics. *Advanced Materials* **2017,** *29* (17), 1605349.
10. Phillips, K. R.; Shirman, T.; Shirman, E.; Shneidman, A. V.; Kay, T. M.; Aizenberg, J., Nanocrystalline precursors for the co-assembly of crack-free metal oxide inverse opals. *Advanced Materials* **2018,** *30* (19), 1706329.
11. Kumbhar, V. S.; Lee, H.; Lee, J.; Lee, K., Interfacial growth of the optimal $BiVO_4$ nanoparticles onto self-assembled WO_3 nanoplates for efficient photoelectrochemical water splitting. *Journal of Colloid and Interface Science* **2019,** *557*, 478-487.
12. Kim, D. J.; Hahn, S. H.; Oh, S. H.; Kim, E. J., Influence of calcination temperature on structural and optical properties of TiO_2 thin films prepared by sol–gel dip coating. *Materials Letters* **2002,** *57* (2), 355-360.
13. Wu, M.; Liu, J.; Jin, J.; Wang, C.; Huang, S.; Deng, Z.; Li, Y.; Su, B.-L., Probing significant light absorption enhancement of titania inverse opal films for highly exalted photocatalytic degradation of dye pollutants. *Applied Catalysis B* **2014,** *150-151*, 411-420.
14. Likodimos, V., Photonic crystal-assisted visible light activated TiO_2 photocatalysis. *Applied Catalysis B* **2018,** *230*, 269-303.
15. Wu, M.; Jin, J.; Liu, J.; Deng, Z.; Li, Y.; Deparis, O.; Su, B.-L., High photocatalytic activity enhancement of titania inverse opal films by slow photon effect induced strong light absorption. *Journal of Material Chemistry A* **2013,** *1* (48), 15491-15500.
16. Deparis, O.; Mouchet, S.; Su, B.-L., Light harvesting in photonic crystals revisited: why do slow photons at the blue edge enhance absorption? *Physical Chemistry Chemical Physics* **2015,** *17* (45), 30525-30532.

List of publications and conference presentations

Articles published:

1. Madanu, T. L., Mouchet, S. R., Deparis, O., Liu, J., Li, Y.; Su, B.-L., Tuning and transferring slow photons from TiO_2 photonic crystals to $BiVO_4$ nanoparticles for unprecedented visible light photocatalysis. *Journal of Colloid and Interface Science* **2023,** *634*, 290-299.
https://doi.org/10.1016/j.jcis.2022.12.033

2. Madanu, T. L., Chaabane, L., Mouchet, S. R., Deparis, O., Su, B.-L., Manipulating multi-spectral slow photons in bilayer inverse opal TiO_2@ $BiVO_4$ composites for highly enhanced visible light photocatalysis. *Journal of Colloid and Interface Science* **2023,** *647*, 233-245.
https://doi.org/10.1016/j.jcis.2023.05.124

3. Madanu, T. L., Mouchet, S. R., Deparis, O., Su, B.-L., Inverse opal TiO_2-based heterocomposite photonic structures for slow photon-assisted visible light photocatalysis, *Proceedings of SPIE, Photonics for Solar Energy Systems IX* **2022**, volume 12150, 1215004.
https://doi.org/10.1117/12.2625327

Articles under submission:

1. Madanu, T. L., Chaabane, L., Mouchet, S. R., Chen, J., Deparis, O., Liu, J., Li, Y., Su, B.-L., Blue and red edge slow photons in inverse opal TiO_2 photonic structure tuned to CdS and plasmonic Au nanoparticles in the presence of Pt cocatalyst for remarkable photocatalytic hydrogen evolution **2024** (Article).

2. Madanu, T. L., Mouchet, S. R., Chaabane, L., Zheng, R., Deparis, O., Li, Y., Su, B.-L., Slow photons in photonic structures for photocatalysis – recent advances, challenges, and strategies, **2024** (Review).

3. Chaabane, L., Madanu, T. L., Trendafilova, I., Lakshmidevi, R., Su, B.-L., Harmonizing plasmonic effect to boost photocatalytic hydrogen production over 628 $mmolh^{-1}g^{-1}$, **2024** (Article).

Conference presentations

o – oral presentation *p – poster presentation* *i – invited talks*

1. Madanu, T. L., Su, B.-L., Inverse opal photonic crystals for photocatalysis, *bePOM, Belgian Photonics Online Meetup*, **2020**. (Belgium)^{p}.

2. Madanu, T. L., Su, B.-L., Slow photon manipulation in inverse opal photonic crystals for solar energy conversion, *International Invited Lectures – Online meeting agenda, Wuhan University of Technology*, **1 December 2021**[i].

3. Madanu, T. L., Mouchet, S. R., Deparis, O.; Su, B.-L., Inverse opal TiO_2-based heterocomposite photonic structures for slow photon-assisted visible light photocatalysis, *Photonics for Solar Energy Systems IX, SPIE Photonics Europe, Strasbourg* **2022**; 12150-20. (Strasbourg, France)[o].
   https://doi.org/10.1117/12.2625327

4. Madanu, T. L., Mouchet, S. R., Deparis, O., Su, B.-L., Tuning and transfer of slow photons from TiO_2 inverse opal photonic crystals to $BiVO_4$ nanoparticles for visible light photocatalysis, *Photosensitive Materials and their Applications II, SPIE Photonics Europe* **2022**; 12151-44. (Strasbourg, France)[o].

5. Madanu, T. L., Mouchet, S. R., Deparis, O., Su, B.-L., Tuning and transfer of slow photons in inverse opal TiO_2-$BiVO_4$ hetero-composite photonic crystal for visible light photocatalysis, *Nanoengineering: Fabrication, Properties, Optics, Thin Films, and Devices XIX*, *SPIE Nanoscience + Engineering,* **2022**; 12202-20. (Presented by Mouchet, S. R., on behalf of Madanu, T. L.). (San Diego, California, USA)[o].
   https://doi.org/10.1117/12.2625468

6. Madanu, T. L., Mouchet, S., Deparis, O., Su, B.-L., Slow photon manipulation in inverse opal TiO_2-based hetero-composite photonic crystals for photocatalysis, *SPEA 11, 11th European Photocatalysis: Conference on Solar Chemistry and Environmental Applications* **2022**, O/3-OR 22. (Turin, Italy)[o].

7. Madanu, T. L., Mouchet, S. R., Deparis, O., Su, B.-L., Slow photon-assisted enhancement of visible light photocatalysis using colloid-templated TiO_2-$BiVO_4$ photonic crystals, *bePOM, Belgian Photonics Online/Onsite Meetup*, **2022**. (Belgium)[o].

8. Madanu, T. L., Mouchet, S. R., Deparis, O., Su, B.-L., Generating and tuning slow photons at multiple wavelength regions using colloid-templated bilayer inverse opal TiO_2-$BiVO_4$ photonic structures for highly enhanced visible light photocatalysis, *12th International Colloids Conference* **2023**. (Palma, Mallorca, Spain)[p].

9. Madanu, T. L., Mouchet, S., Chaabane, L., Deparis, O., Su, B.-L., Generating and tuning slow photons at multiple spectral regions in bilayer inverse opal TiO_2-$BiVO_4$ photonic structures for highly enhanced visible light photocatalysis, *Nanoengineering: Fabrication, Properties, Optics, Thin Films, and Devices XX, SPIE Nanoscience + Engineering* **2023**; 12653-22. (San Diego, California, USA)[o].
   https://doi.org/10.1117/12.2676857

Other scientific articles not included in thesis:

1. Zhang, X., Xing, P., Madanu, T. L., Li, J., Shu, J., Su, B.-L., Aqueous batteries: from laboratory to market. *National Science Review* **2023,** *10* (11), nwad235. https://doi.org/10.1093/nsr/nwad235
2. Oger, M. J.; Vermeulen, O.; Lambert, J.; Madanu, T. L.; Kestemont, P.; Cornet, V., Down to Size: Exploring the Influence of Plastic Particle Dimensions on Physiological and Nervous Responses in Early-Stage Zebrafish. *Environmental Pollution* **2024**, 124094. https://doi.org/10.1016/j.envpol.2024.124094

Biographic note

Thomas Lourdu Madanu is a native of Phirangipuram, Andhra Pradesh, India. He received his bachelor's degree in science from Andhra Loyola College, Acharya Nagarjuna University, Vijayawada, Andhra Pradesh, in 2003, and his master's degree in chemistry from Loyola College, University of Madras, Chennai, Tamil Nadu, in 2009. Before undertaking research at the Chemistry of Inorganic Materials (CMI) laboratory, University of Namur, Belgium in 2019, he worked in the field of administration as Assistant Director of Andhra Loyola Institute of Engineering and Technology (affiliated to Jawaharlal Nehru Technological University, Kakinada), Vijayawada, for four years, while at the same time giving courses on Applied Chemistry and Basic Engineering Chemistry. Besides academics, he is a member of the Society of Jesus (also called Jesuits), a religious order committed to the promotion of faith, service, and social justice. As a Jesuit, he is oriented towards working in the field of education, wherein he is committed to the holistic formation of youth that includes academic excellence, personality development, and social commitment. As a researcher, his interests include solar energy conversion, photocatalysis, photoelectrocatalysis, nanomaterials, photonic structures, plasmonic structures, colloids and self-assembly processes.